UAB
Universitat Autònoma de Barcelona

UAB

Universitat Autònoma de Barcelona

Departamento de Ingeniería Electrónica y de Telecomunicación

Novel Printed Electroactive Devices for Environmental Monitoring

Autor:	Marc Alique Garcia
Directores:	Dr. Claudia Delgado Simao
	Dr. Ana Moya Lara
	Dr. Gonzalo Murillo Rodríguez
Tutor	Dr. Gabriel Abadal Berini

Memoria de Tesis
presentada para optar al título de

Doctor en Ingeniería Electrónica y de Telecomunicación

Septiembre 2022

UAB
Universitat Autònoma
de Barcelona

Department of Electronic Engineering and Telecommunications
Av. de Serragalliners
Bellaterra (Cerdanyola del Vallès), 08080

eurecat

Unit of Functional Printing & Embedded Devices
Av. de Ernest Lluch, 36
Mataró, 08302

Dr. Claudia Delgado Simao, Group Leader of the FPED Unit from Fundació Eurecat, Dr. Ana Moya Lara, Researcher of the FPED Unit from Fundació Eurecat, Dr. Gonzalo Murillo Rodriguez, Group Leader and Senior Research Fellow from IMB-CNM (CSIC) and Dr. Gabriel Abadal Berini, associate professor from the Department of Electronic Engineering of the Universitat Autònoma de Barcelona (UAB) CERTIFIED that the Thesis Memory "*Novel Printed Electroactive Devices for Environmental Monitoring*" submitted by Marc Alique Garcia to qualify for the title of Doctor in Electronic and Telecommunication Engineering has been carried out under his direction at Fundació Eurecat, Technological Center of Catalonia and has been supervised by the Department of Electronic Engineering of UAB.

Dr. Claudia Delgado Simao, Cap de línia de la Unitat de FPED de la Fundació Eurecat, Dr. Ana Moya Lara, Investigadora de la Unitat FPED de la Fundació Eurecat, Dr. Gonzalo Murillo Rodriguez, Cap de línia i investigador sènior de IMB-CNM (CSIC) i Dr. Gabriel Abadal Berini Professor associat en el Departament d'Enginyeria Electrònica de la Universitat Autònoma de Barcelona (UAB) CERTIFIQUEN que la Memòria de Tesis "*Novel Printed Electroactive Devices for Environmental Monitoring*" presentada per Marc Alique Garcia per optar al títol de Doctor en Engenyeria Electrònica i de Telecomunicació s'ha realitzat sota la seva direcció a Fundació Eurecat, Centre Tecnològic de Catalunya i ha sigut tutelada en el Departament d'Enginyeria Electrònica de la UAB.

Dr. Claudia Delgado Simao, Líder línea de la Unitad de FPED de la Fundació Eurecat, Dr. Ana Moya Lara, Investigadora de la Unitat FPED de la Fundació Eurecat, Dr. Gonzalo Murillo Rodriguez, Líder línea e investigador senior de IMB-CNM (CSIC) y Dr. Gabriel Abadal Berini, Profesor asociado en el Departamento de Ingeniería Electrónica de la Universitat Autònoma de Barcelona (UAB) CERTIFICAN que la Memoria de Tesis "*Novel Printed Electroactive Devices for Environmental Monitoring*" presentada por Marc Alique Garcia para optar al título de Doctor en Ingeniería Electrónica y de Telecomunicación se ha realizado bajo su dirección en Fundació Eurecat, Centre Tecnològic de Catalunya y ha sido tutelada en el Departamento de Ingeniería Electrónica de la UAB.

Thesis supervisor	Thesis Co-supervisor	Thesis Co-supervisor	Thesis Tutor
Dr. Claudia Delgado Simao	Dr. Ana Moya Lara	Dr. Gonzalo Murillo Rodríguez	Dr. Gabriel Abadal Berini
SIGNATURE	SIGNATURE	SIGNATURE	SIGNATURE

A mi Familia

Shoot for the moon.
Even if you miss, you will land among the stars.

Norman Vincent Peale

Agradecimientos

Como bien sabéis todos a los que van dedicados estos agradecimientos, soy una persona un poco manca en palabras, pero no quería dejar pasar esta oportunidad que tengo de dejar algo por escrito para poder plasmar lo que siento por cada uno de vosotros y cuan agradecido me siento de teneros a mi lado durante esta etapa de mi vida, así que coged palomitas, pañuelos y espero no ser muy pesado y enrollarme mucho.

En primer lugar, me gustaría agradecer a mis dos directoras, siendo a su vez amigas, mentoras e incluso consejeras en algún momento. A Claudia Delgado, por darme la oportunidad de realizar esta tesis, sabiendo como guiarme y dirigirme a lo largo de este camino y ayudarme a en todo lo que he necesitado. M'has ensenyat molt més del que pot quedar plasmat en aquesta tesis i m'has introduït en el món que hi ha després de la universitat, confiant en mi inclús per portar projectes junts i t'estic més que agraït. A Ana Moya, que ha estado a mi lado desde un primer momento, presentándome a su querida Dimatix y a sus preciosos sensores electroquímicos. Tanto tu forma de ser como de enseñar me han ayudado a dar lo máximo de mí y cortas se me quedan las palabas para poder expresar lo mucho que me has aportado durante estos años y lo mucho que aún te queda por aportar. Del mismo modo, me gustaría darle las gracias a mi tercer director, Gonzalo Murillo por acogerme en su grupo del CNM y guiarme en gran parte del estudio de los materiales piezoeléctricos, ojalá poder hacer más cosas juntos en un futuro. También me gustaría agradecer a Gabriel Abadal, que como tutor me ha aportado todo lo que he necesitado durante este periodo.

En esta misma línea, me gustaría agradecer tanto a Paul Lacharmoise como a toda la Dirección Científica de Eurecat por darme la oportunidad de realizar esta tesis mediante la beca Vicente López, queda más que claro que sin su apoyo y soporte durante este viaje esto no se hubiera podido realizar.

A la siguiente persona me gustaría agradecer es a Ale, por todo lo que me ha aportado durante esta etapa, tanto en el laboratorio como fuera de él, sabiéndome apoyar y ayudar en todo momento que he necesitado y por todas las más que necesarias charlitas. Del mismo modo, quiero dar las gracias a todos mis compañeros que han formado parte de PSA durante estos años; David, Urbez, Diogo, Miki, Matías F., Matías J., Luciano, Cristina, Van, Laura, Ignasi, Paula, Estanis, Iván, Gerard, Ismael y Pablo, que me han aguantado todos estos años y siempre me han ayudado en todo lo que han podido, así como a Saeed y Karell, que, aunque su estancia fue corta, también les agradezco toda su ayuda. Laura, moltes gràcies pels cafès, les cerveses i les estonetes de xerrada,

desde que éramos unos críos, así como a mis compañas lanzadoras Julia, Zaynab y Cristina, amenizando los entrenos haciendo que sean mucho más entretenidos.

No me quiero olvidar de mis amigos de Alcantud, mi segunda familia. Jesús, Álvaro, Adri M., Adri P., David A., David B., Raúl, Maria, Iris, Irene, Lydia, Sara, Ainhoa, Álex, Jaime, Mario, Dani, Ana, Alberto, Santi, Jonathan. Tenía la necesidad de nombraros a todos, porque me habéis acompañado y apoyado a lo largo de mi vida desde que tengo uso de razón. Gracias a vosotros los veranos se pueden llamar veranos. Las rutas, los ríos, los partidos, las fiestas, las noches bajo las estrellas, los paseos; siempre que he necesitado una desconexión ahí habéis estado. Ojalá estar más cerca y poder disfrutaros más a menudo.

Dejo para el final a los más importantes, a mi familia. Quiero dar las gracias a mi hermano Albert, el lanzador bueno de la familia. A medida que te has ido haciendo mayor te has ido convirtiendo en una persona excepcional, ya no solo en ser alto y fuerte, pudiéndote coger "prestada" ropa que, indiscutiblemente, me queda mejor a mí, si no por tu enorme corazón y por la voluntad que tienes de preocuparte por los demás. Tienes la capacidad de convertirte en lo que quieras ser. Y por último dejo a mis dos pilares, mis padres Manolo y Geni. Sois mis referentes en esta vida y de vosotros he heredado todo lo que soy, tanto en carácter como en la pasión por la investigación y el deporte. Si no fuera por todo vuestro apoyo y sacrificio, nada de lo que he dicho hasta ahora tiene sentido y esto jamás hubiera sido una realidad. Aunque no os lo diga tanto como debería, os quiero muchísimo.

Resumen

La necesidad de monitorización de sistemas ambientales se ha establecido en nuestra sociedad desde que el aumento de la industrialización global ha provocado una mayor producción de contaminantes. Estos se pueden encontrar en distintos ámbitos del ecosistema como el aire, agua tierra o biota y su detección puede facilitar un mayor control de la salud en la sociedad. A medida que aumenta la complejidad de los parámetros a detectar, aumenta la necesidad de analizar y monitorizar su respuesta. Sin embargo, el poder controlar un gran rango de parámetros implica la necesidad de implementar una red de dispositivos conectados entre ellos capaces de, no solo monitorizar, sino de ser capaces de dar una respuesta frente a una anomalía, lo que provoca el aumento en la complejidad y por lo tanto en el coste, siendo inviable en muchos ámbitos. Además, el uso de sistemas de medida convencionales suele estar limitado en su rango de operación, por lo que su aplicabilidad es limitada.

Es en este contexto en el que esta tesis busca investigar y obtener nuevas herramientas para la monitorización de parámetros ambientales en tiempo real mediante técnicas de fabricación aditiva por impresión funcional, en cualquier tipo de sustratos, tanto rígidos como flexibles. Esta metodología de fabricación es una estrategia valiosa para el desarrollo de sensores a bajo coste en comparación a los sensores convencionales, con la facilidad de personalizar el diseño y su versatilidad en la integración. Con este fin, y para el desarrollo en el campo de sensores impresos para monitorización ambiental, se propone estudiar dos familias distintas de dispositivos para la monitorización de parámetros físico-químicos relevantes, no solo del ámbito medioambiental, sino también en el ámbito de salud.

La primera familia investigada son los dispositivos piezoeléctricos como sensores de parámetros físicos como el movimiento, y dada la naturaleza de la reversibilidad del efecto piezoeléctrico, también se investigará sus propiedades como actuadores y recolectores de energía. Concretamente, se ha enfocado el estudio en una serie de dispositivos basados en el copolímero de fluoruro de polivinilideno con trifluoroetileno (PVDF-TrFE) sobre distintos sustratos plásticos y se ha caracterizado y validado su versatilidad como sensor, actuador o generador de energía. La segunda familia investigada se basa en el uso de sensores electroquímicos impresos para monitorizar distintos parámetros de calidad de sistemas acuosos. El principal reto común a todos los dispositivos investigados en esta tesis doctoral consiste en el estudio de las propiedades de los materiales funcionales depositados mediante tecnologías de impresión, y de la funcionalidad de

los dispositivos, obteniendo así las reglas de diseño de los sistemas multicapa con los diferentes materiales, y estudiando la interacción y compatibilidad en cada capa y en las interfases.

Un paso más allá, para dotar de autonomía y automatización de la medida, se han incorporado y validado los sensores en un sistema "Lab-on-a-Chip" que permite una calibración automática y la monitorización de parámetros de carácter amperométrico; como el cloro libre y oxígeno disuelto, potenciométrico; como el pH y el redox, impedimétrico como la conductividad, resistivo como la temperatura y vibracional, para monitorizar el flujo en canales microfluídicos. Dichos parámetros son clave para controlar la calidad y bioactividad de los medios acuosos en un gran rango de aplicaciones y sistemas. Ambas estrategias investigadas en esta tesis tienen una amplia aplicabilidad, y gracias a la versatilidad que proporciona la fabricación mediante técnicas de impresión en cuanto a diseño, sustratos y forma, tienen un alto potencial de implementación disruptiva en una elevada cantidad de sistemas de gran utilidad para sistemas de monitorización en tiempo real, continuo y al "Point-Of-Need".

Abstract

The need to monitor environmental systems has been established in our society since the increase in global industrialization has caused a bigger pollutant generation. These can be found in different areas of the ecosystem such as air, water, soil or biota, and their control can facilitate better control of society's health. As the complexity of the parameters to be detected increases, the need to analyze and monitor their response also increases. However, being able to control a wide range of parameters implies the need to implement a network of connected devices capable of not only monitoring but also of being able to respond against an anomaly, which causes an increase in complexity and therefore also in cost, being unfeasible in many areas. In addition, the use of conventional measurement systems is usually limited in their range of operation, so their applicability is limited.

It is in this context that this thesis seeks to investigate and obtain new tools for monitoring environmental parameters in real-time through functional printing additive manufacturing techniques, on any type of substrate, both rigid and flexible. This sensor preparation methodology is a valuable strategy for the development of sensors with a reduced cost compared to conventional ones, with a customizable design and versatile integration. To this end, and to advance in the field of printed sensors for environmental monitoring, it is proposed to study two different families of devices for monitoring relevant physical-chemical parameters, not only in the environmental field but also in the health field.

The first family investigated are piezoelectric devices as sensors of physical parameters, such as movement, but given the reversibility nature of the piezoelectric effect, their properties as actuators and energy collectors are also investigated. Specifically, the study has focused on a series of devices based on the polyvinylidene fluoride copolymer with trifluoroethylene (PVDF-TrFE) on different plastic substrates, and their versatility as a sensor, actuator or energy harvester has been characterized and validated. The second family investigated is based on the use of printed electrochemical sensors to monitor different quality parameters of aqueous systems. The main challenge common to all the devices studied in this thesis consists in the study of the properties of the functional materials deposited by means of printing technologies, and of the functionality of the devices, thus obtaining the design rules of the multilayer systems with the different materials, and studying the interaction and compatibility in each layer and the interfaces.

One step further, to provide autonomy and automation of the measurement, the sensors have been incorporated and validated in a "Lab-on-a-Chip" system that allows an automatic calibration and the monitoring of amperometric parameters such as free chlorine and dissolved oxygen, potentiometric such as pH and redox, impedimetric such as conductivity, resistive such as temperature, and vibrational, to monitor the flow in microfluidic channels. These parameters are key to controlling the quality and bioactivity of aqueous media in a wide range of applications and systems. Both strategies studied in this thesis have wide applicability, and thanks to the versatility provided by manufacturing through printing techniques in terms of design, substrates and shape, they have a high potential for disruptive implementation in a large number of highly useful systems for real-time, continuous and " Point-Of-Need" monitoring systems.

List of Acronyms

Contents

1. Dissertation Summary

In this chapter, an extended abstract of this thesis work is presented, where the most relevant aspects of the research carried out are briefly introduced and summarized.

1.1. Motivation of the thesis work

The concern for environmental monitoring (EM) has been increasing in society along with the technological growth produced in the last century. The rise of industrialization causes an increase in the number of pollutants present in the environment, accelerating the risk of contamination.[1], [2] These pollutants are not only referred to as air contaminants, water and soil are also affected by this industrialization.[3]–[5] Water is one of the fields from which a greater source of data can be obtained for society healthcare. Health or environmental problems arise from pollutants or pathogens such as microplastics, or bio-organisms, affecting the whole ecosystem equilibrium. Therefore, the monitoring of key parameters to follow the occurrence of such species directly or indirectly, with different sensors presents as an important tool to understand and control their propagation. Among the universal range of chemical and biochemical parameters found in aqueous environments, two key chemical species are especially relevant for bioactivity growth, free chlorine (FC) and dissolved oxygen (DO).[6], [7] Notwithstanding chemical parameters that can be monitored in water and soil, physical measurements are also key indicators for EM,[8] such as vibrations or movements related to mass flow in rivers owing to the melting glaciers or produced by geothermal activity that can affect the structural health of the near infrastructures.[9] For example, the monitoring of the vibrations produced by geothermal activity can help us to register movement patterns and associate to wear, friction or cleavage that is generated, allowing predictive and personalized maintenance of conducts, and lower costs due to possible fatigue or accidents that may appear due to its use.[10], [11]

Therefore, EM can be applied to any environment, both natural and anthropogenic and demands continuous research in novel reliable monitoring systems, able to monitor multiple parameters, being autonomous, compact and sustainable. One important open challenge is the study and development of new sensors that can monitor all the different and continuous new parameters that appear related to EM. As observed, sensors play a very important role in several application fields, and nowadays are very present in our society, being able to be found in all the different aspects of the population. Nonetheless, one sensor usually can only provide continuous information from one specific area, if located in the environment as Point-of-Need (PoN) application. If more information is required, the sensor must be placed in another place, the sample can be collected for later analysis or more sensors can be located in different positions.

The way to develop and understand the sensing mechanisms systems has notably evolved since the emerging of printing electronics (PE) in the mid-20th century.[12] The need to be able to obtain a large amount of data autonomously means that the use of conventional technology is not efficient enough. The excellent capabilities of PE for the deposition of different materials have

become an attractive alternative to be used in several applications, being EM one of the most promising.[13], [14] The advantages of PE include the reduction of the complexity in the fabrication steps, the compatibility with various substrates and the minimization of waste material, obtaining a technology that reduces the cost of production and increases the eco-compatibility, becoming very suitable for low-cost applications.[15] Furthermore, PE is capable of testing new materials and designs, and, in combination with rapid prototyping techniques, plays an important role in the fabrication of customized devices. Among them, electroactive materials are in the set of those accessible components with very high interest to be processed with PE, being piezoelectric and electrochemical devices with better and interesting properties to be investigated for their application in EM. Moreover, the compatibility of PE with Lab-on-a-Chip (LoC) technology and Internet-of-Things (IoT) systems makes piezoelectric and electrochemical devices gain autonomy, versatility, relevance and competitiveness compared to conventional systems.[16] Figure 1.1 schematically elucidates the approach of the printed electroactive devices (ED) for EM systems.

Figure 1.1 | Schematic illustration for the environmental monitoring approach with printed electroactive devices.

As result, in this thesis work, new sensing systems based on fully printed devices are proposed, upon the convergence of dissimilar technologies such as printed electronics, materials science, environmental science and artificial intelligence (AI), to advance high-resolution mapping of concentration levels, and distribution pathways of environmental exposures in any location,

creating an early warning for environmental control. It is in this sense that the motivation of this thesis dissertation appears for the accomplishment of this ambitious goal.

1.2. Main contribution of the thesis work

In the EM field, the ability to analyze and monitor in real-time the different responses is of paramount importance. For this reason, **this thesis work brings new insights in devices for EM and proof-of-concept of novel functional electroactive sensors and actuators based on printing techniques as disruptive tools for EM**. In the first stage, it has been studied and fabricated two novel printed piezoelectric devices using a combination of printing techniques to obtain their design rules for the different monitoring study cases, and in the second stage, it has been developed different fully printed electrochemical device platforms, incorporating multiparametric sensors for the water quality measurement in a LoC configuration, as a reliable continuous and real-time water quality control. The fabrication study of all constructed sensors was performed by using printing techniques and rapid prototyping techniques (RPTs) to prepare cost-effectively the different sensors and actuators.

In the following section are described the main and specific objectives of this thesis work to obtain the final goal. After this, it is presented the list of publications that comprise this work in which Marc Alique is the first author of all of them and are published in first-quartile journals. The section finishes with the outline of this dissertation presenting a summary of each chapter.

1.2.1. Objectives of the dissertation

In general terms, the main goal is to study and define a methodology based on printed electronics to achieve novel functional, reliable and cost-effective systems to solve current and future EM problems in real analysis. Inside this main goal, two types of devices are going to be investigated: the first one involves the study of the piezoelectric effect on printed systems, and the second is the study of electrochemical sensors. The two specific objectives are:

- **To develop a reliable and functional piezoelectric device for EM by using printing techniques.** To achieve this objective, the following specific sub-objectives are proposed:

  o To investigate and construct a fully printed polyvinylidene fluoride trifluoroethylene (PVDF-TrFE) piezoelectric device on polymeric substrates, by means of inkjet printing (IJP) and screen printing (SP), characterizing the

interaction of the different inks within the multilayer printed structure and with the polymeric substrates.

o To understand and control the mechanism underlying poling of the PVDF-TrFE layer by means of electrical and thermal stimuli, explore its reversibility and correlate these parameters to the morphological and electrical activity of the printed piezoelectric device, in both poled and non-poled forms.

o To investigate the printed piezoelectric single device as a multifunctional platform by measuring the response of the single device in three modes: sensor, actuator and energy harvester.

o To investigate the preparation methodology of a single device and an array of printed piezoelectric devices in a highly stretchable substrate for wearable applications, study the correlation of the morphological and electrical characteristics with the strain applied, investigate the reversible and irreversible stretchability ranges and determinate their maximum stretchability.

- **To develop a printed multisensing platform for water quality monitoring in environmental applications.** To achieve this objective, the following sub-objectives have been addressed:

o To investigate the preparation of an Iridium Oxide (IrOx)-based pH sensor fully fabricated through printing technologies on polymeric substrates and to study their functionality and electrochemical response.

o To study the fabrication of a printed FC electrochemical sensor on polymeric substrates understanding the behavior behind the electrochemical system.

o To study, fabricate and characterize a multisensing platform using polymeric substrates for the measurement of pH, redox, FC, DO, conductivity, temperature and flow in the water quality monitoring.

o To integrate the multisensing platform in a LoC system to increase their stability, lifetime and autonomy.

1.2.2. List of publications

The publications included in this list shall be considered for the evaluation of this thesis dissertation. A reproduction of each publication can be found in the indicated chapter summarized below.

Paper I. M. Alique, C. D. Simao, G. Murillo and A. Moya. Fully Printed Piezoelectric Devices for Flexible Electronics Applications. Adv. Mater. Technol. 6, (2021), 2001020. doi:10.1002/admt.202001020 (Q1, IF:8.856)

* The author's contribution: first author, leading finding, reading and analyzing the state-of-the-art of publications related to printing techniques for printed electronics and printed piezoelectric devices in the last years and writing the main parts of the manuscript.

Paper II. M. Alique, A. Moya, M. Kreuzer, P. Lacharmoise, G. Murillo, and C. D. Simao. Controlled poling of fully printed piezoelectric PVDF-TrFE device multifunctional platform with inkjet-printed silver electrodes. J. Mater. Chem. C, 2022, doi:10.1039/D2TC01913B (Q1. IF: 8.067)

* The author's contribution: first author, planning and performing the design of the printed device, its characterization, calibration and experimentation, and writing the main parts of the manuscript.

Paper III. M. Alique, A. Moya, D. Otero, M. Kreuzer, P. Lacharmoise, G. Murillo, and C. D. Simao. Multiparametric sensing electronic skin based on seamless fully printed stretchable piezoelectric devices. The article has been SUBMITTED to Advanced Science journal in July 2022. (Q1, IF:17.521).

* The author's contribution: first author, planning and performing the design of the printed device, its characterization, calibration and experimentation, and writing the main parts of the manuscript.

Paper IV.* M. Alique, P. Lacharmoise, C. D. Simao, and A. Moya. Large-scale fully printed iridium oxide-based pH sensor. The article has been SUBMITTED to Advanced Materials Technologies journal in September 2022. (Q1, IF: 8.856).

* The author's contribution: first author, planning and performing the design of the printed device, its characterization, calibration and experimentation, and writing the main parts of the manuscript.

Paper V. * <u>M. Alique,</u> P. Lacharmoise, C. D. Simao, and A. Moya. Fully printed novel approach for Lab-on-a-Chip smart water monitoring. The article has been SUBMITTED to Chemical Engineering Journal in September 2022. (Q1, IF:16.744).

* The author's contribution: first author, planning and performing the design of the printed device, its characterization, calibration and experimentation, and writing the main parts of the manuscript.

* Paper IV and Paper V are derived from an European patent application number EP22382764.3 entitled "Additive manufacturing of sensors", by A. Moya, M. Alique, M. Berenguel, D. Fernández, C.D. Simao and P. Lacharmoise filed in July 2022 by Fundació Eurecat.

1.2.3. Thesis outline

With regards to the objectives that steered the course of this thesis work and the articles pointed out in the previous section, the dissertation is organized into five well-defined chapters which are summarized below.

<u>*Chapter 1*</u> entitled "*Dissertation Summary*" presents the dissertation overview, where the most relevant aspects of this thesis work are briefly introduced.

<u>*Chapter 2*</u> entitled "*Introduction to Printed Sensors and Actuators for Environmental Monitoring*" presents the technology used for the fabrication and investigation of the devices presented in this thesis. This chapter has a short introduction to EM, focusing on the use of ED for PoN applications. In there, a brief introduction to the piezoelectric and electrochemical sensors is performed, as well as the introduction to the Lab-on-a-Chip (LoC) technology. Following is explained the importance of study and manufacture these. Next, the potential of the different printing techniques is demonstrated, pinpointing the main capabilities of printed electronics for the fabrication of piezoelectric and electrochemical devices.

<u>*Chapter 3*</u> entitled "*Fully Printed Piezoelectric Devices*" is focused on one of the main objectives of the thesis work; first, an overview of the main concepts of piezoelectricity is presented, followed by a review of the needs and requirements to construct these piezoelectric devices with printing technologies. Finally, the investigation of two printed piezoelectric devices on polymeric substrates is shown. The first is based on the study of a PVDF-TrFE device with inkjet-printed electrodes, demonstrating its capabilities as a versatile sensor, actuator and energy harvester. The second one is the investigation of a stretchable piezoelectric single sensor and a sensing matrix

fabricated on an elastic polymeric substrate for wearable applications, to understand their correlation with stretchability.

Chapter 4 entitled "*Fully Printed Electrochemical Sensors for Water Quality Monitoring*" is dedicated to the second main objective of the thesis; the study and integration of printed electrochemical sensors for environmental monitoring. A first introduction to electrochemical devices and their miniaturization by printed electronics is explained. Then, the study of two different electrochemical devices with printed electronics is presented. The first is a novel, fully printed, scalable fabrication route for an IrOx-based pH sensor on a polymeric substrate. The second is the integration of all the knowledge acquired in this thesis for the fabrication of a multisensing platform for scalable and automatic smart water monitoring through the LoC approach.

Chapter 5 entitled "*Conclusions and Future Work*" summarizes the main conclusions of this thesis work, as well as an open issue and potential future research directions and the research area.

1.3. Thesis framework

Marc Alique has received a "*Vicente López*" pre-doctoral scholarship granted by *Fundació Eurecat- Centre Tecnològic de Catalunya*. The main part of this thesis work has been carried out in the facilities of *Fundació Eurecat*, within the department "Functional Printing and Embedded Devices" supervised and co-supervised by Dr. Claudia Simao and Dr. Ana Moya, respectively. The work in piezoelectric was partially carried out in a scientific collaboration with the *Institut de Microelectrònica de Barcelona* (IMB-CNM) del *Consejo Superior de Investigaciones Científicas* (CSIC), within the group of Dr. Gonzalo Murillo, and co-supervisor of this thesis work.

Throughout his *Vicente López* scholarship, Marc Alique carried out its research, where he produced the 5 presented articles that compose this thesis, the submission of one European patent and several contributions to scientific conferences

2. Introduction to Printed Sensors and Actuators for Environmental Monitoring

In this chapter it is presented a brief introduction and description of electroactive devices (ED) in environmental monitoring systems, pinpointing the materials capable to be fabricated through scalable and low-cost techniques, including an introduction to Point-of-Need (PoN) applications and Lab-on-a-Chip (LoC) devices. Following, a description of printing electronics is presented, explaining the different substrates and materials in form of ink and their characteristics. Finally, the main fundamentals and characteristics of the different printing technologies used in this thesis dissertation are presented.

2.1. Environmental monitoring techniques

The importance and need for integrated environmental monitoring (EM) systems is fundamental for human society since its onset.[8] The increase of urbanization and industrialization areas has led to a continuously increasing list of parameters that need to be monitored, either for being dangerous for human health, or simply to control natural or anthropogenic events. On the other side, sustainable growth of the human society depends on a balanced and respectful intercorrelation of economy, environmental and social dimensions, and chemical and physical parameters may be used to monitor factors transversely affecting these dimensions, in particular, controlling the quality of natural resources, and the state of human health or wellbeing.[16] Two specific groups of parameters are thus categorized and addressed depending on their nature: *physical* (e.g. noise, vibrations, electromagnetic fields…)[17] and *chemical* (e.g. metal ions in water resources, pesticides, pharmaceuticals…).[18] If these parameters are monitored in air or water in natural or anthropogenic milieus it is referred to as EM, and if it is used to monitor internal or external parameters in the human body, it is referred to as healthcare monitoring. Thus, discrete measurements of such parameters offer the opportunity to know the present state and understand future tendencies found in Point-of-need (PoN) applications.

2.1.1. Printed Point-of-Need applications

The concept of EM includes the use of an array of discrete or multiparametric sensors to obtain broader and more precise monitoring, controlling all the areas and parameters that may influence it. However, the difficulty of measuring at certain points with conventional sensors, their laborious data processing and transmission, as well as, their high cost, require the use of more viable techniques for this sensing procedure. Traditional EM approaches are based upon discrete sampling methods followed by laboratory analysis. However, the measurement of different environmental parameters requires a sample treatment or adaptation, to eliminate the background noise, identify the disease and respond according with.

This performance can be only achieved in laboratory conditions with highly advanced diagnosis, due to the need for complex and expensive devices. Just as Point-of-Care (PoC) describes the identification of pathogens near the patient with a fast turn-around time, and the potential to immediately change the health management in human patients and samples, the term PoN has a broader meaning, and also includes on-site testing of environment, animals, and food samples, being a more adequate term for EM.

At this point, the manufacture of measuring devices using printing technologies emerges with great energy. The concept of printed electronics (PE) has been on the rise since the middle of the last century, owing to its capability to manufacture several types of devices on large scale at a low cost. Therefore, the use of printing techniques in the manufacturing process for devices in EM is very promising and its characteristics are detailly explained in Section 2.2.

Printed sensors for environmental monitoring
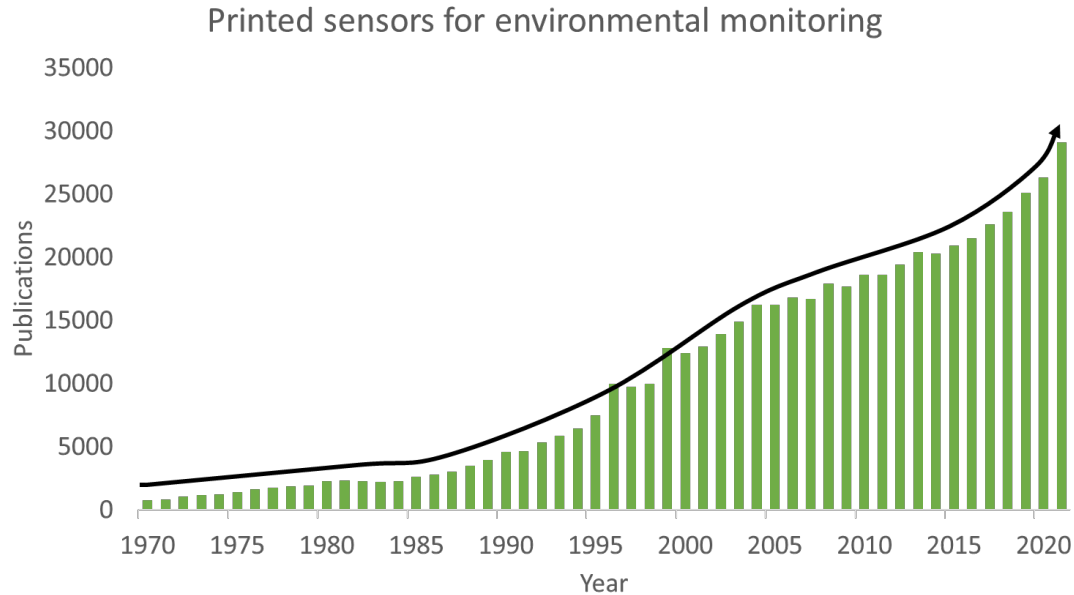
| **Figure 2.1** | Graphical representation of the number of publications per year about printed sensors for environmental monitoring. Search carried out 06/08/2022. |

Figure 2.1 elucidates the reported publication number of the use of printed sensors and actuators for their use in EM. As observed, two clear trends can be differentiated: in the middle 80's, the concept of EM started winning attention amongst scientists, which began to detect the need for EM to guarantee the quality of life. This is the case until the beginning of the 21st century when this EM trend continued to increase, but at a slower rate. And it was not until a few years later that printing technology began to gain importance among researchers, offering the possibility of using functional materials, converted into inks, to obtain printed devices at a low cost but, with great features and the capacity to be used in a wide range of applications.

Beyond the state of the art, the research for EM systems of air, water, land and biota quality lay in reliable, continuous measurement, autonomous, sustainable and lightweight systems, able to measure multiple parameters at the same time, in real-time and *in situ*. Such systems lay the grounds for the acquisition of reliable datasets with high spatial and time resolution, crucial to build environmental or healthcare models.[19], [20] With the recent advances in science and technology, especially artificial intelligence (AI) and machine learning, EM becomes smart EM

owing that the recent technology methods enable a more precise measurement, with optimal control and avoiding interferent, being able to anticipate the maintenance due to wear and offer a response at the time of the detected problem.[21]

Wireless networks or wireless sensor networks (WSNs) comprise modern sensors which operate on AI-based monitoring and controlling methods. Internet-of-thing (IoT) devices are employed in WSNs for effective waste management, vehicle marking and temperature and pollution control. Therefore, modern methods of EM are known as smart EM systems, due to the use of IoT, AI and wireless sensors.[16] An example of this type of smart EM can be easily understood with the scheme illustrated in Figure 2.2. In this example, different types of sensors and actuators are distributed along a discrete space. Thanks to wireless transmission, these devices can be controlled and monitored with the help of IoT, being able to monitor in real-time the desired parameters.
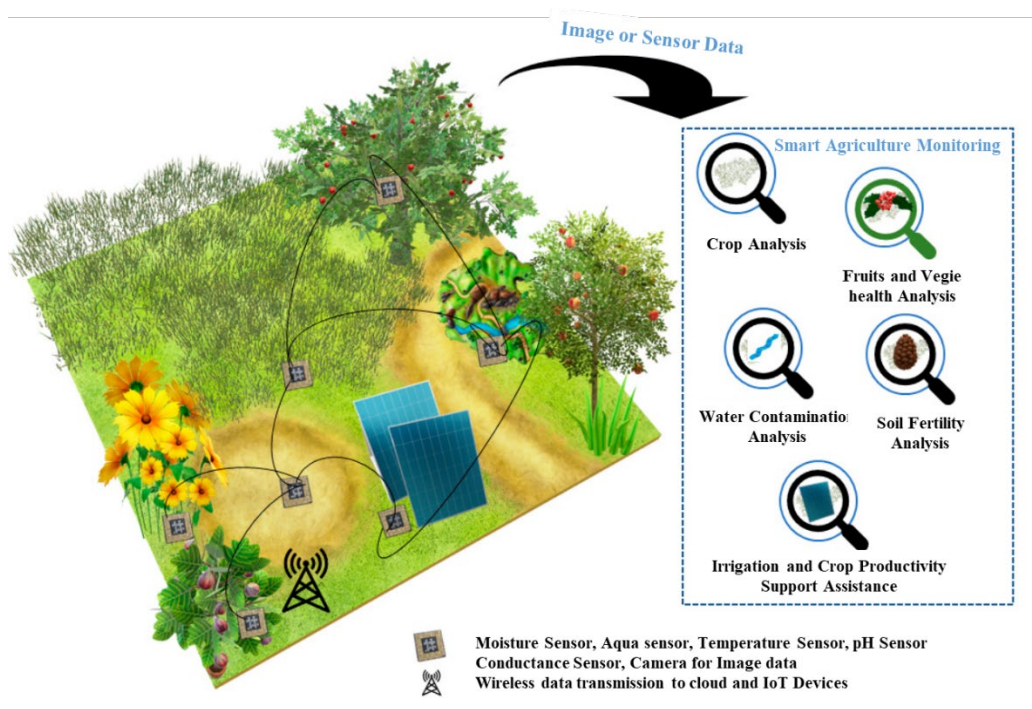
Figure 2.2 | Smart environment monitoring system using IoT devices and sensors. Scheme adapted from [16].

This EM approach can be further increased thanks to the use of the cloud, by connecting and controlling all the IoT devices as graphically illustrated in Figure 2.3. In the represented scheme, different parameters from water to the environment are monitored with WSN in a smart city example. These sensors can measure the desired parameters like pollution, contaminants, temperature, or vibrations; and the obtained data is wirelessly transmitted to the cloud, where it

is analyzed and processed. Once the information is processed, the required actions are sent to the same environmental devices to fix the situation or to the population to be conscient of the detected problem.

This smart EM can be even enhanced as we increase the number of devices, thus increasing the knowledge network. Therefore, the greater the ability to obtain and manufacture the devices needed for EM, the more precise and accurate will be the sensing and intervention. This is why, in the last decades scientists are making a great effort to fabricate these types of devices with large-scale manufacturing with printing techniques as further explained in Section 2.2, to obtain these devices at low cost.
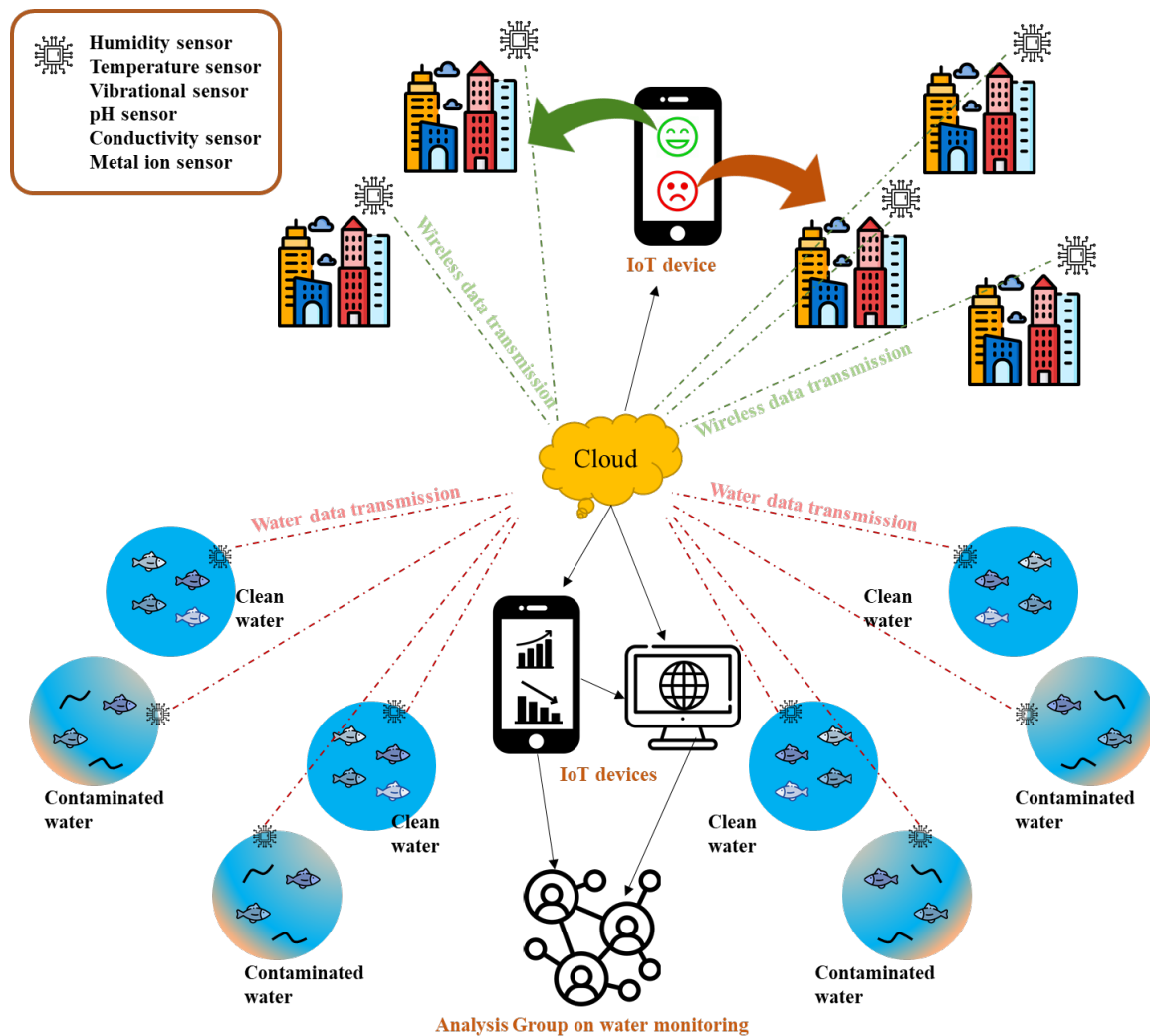
Figure 2.3 Scheme of a smart environment monitoring system using the cloud, connecting IoT with a wireless sensor network. Scheme adapted from [16].

2.1.2. Electroactive devices

In the EM communication chain, we can classify different device types depending on their role in the system. Those devices are directly or indirectly related to electrical signals, since they are capable to detect them, or they work with them. Therefore, from now on we are going to call these systems electroactive devices (ED). The most important ones that can be distinguished are sensors, actuators and generators:

- **Sensors**: The devices that are in charge of the monitoring performance, obtaining all the needed information, by detecting and responding to inputs from the environment, and generating a readable output signal. Depending on the nature of the target, physical and bio/chemical sensors are distinguished (if chemical species are biomolecules). The quality of the sensors is defined by their selectivity, sensitivity, precision and response time. The fact of responding to the precise evaluated parameter makes the device much more accurate, being therefore more selective.

- **Actuators**: They are the responsible for converting energy into an action to fix, regulate or optimize the environmental conditions when required. We can differentiate several types of actuators depending on the action they perform, being them mechanicals, chemicals, thermals and electrics.

- **Generators**: Their main function is to obtain energy from the environment to be supplied onto an electrical system, that may comprise sensors and actuators, being the power source of the system. In some environments where monitoring is necessary but there is not enough energy to afford this system, the capability to collect energy from the environment to supply it, makes generators the most important devices in this system. Among them we can distinguish solar, thermal, wind and motion as the most important ones.

Low-cost, integrable EDs are particularly important for EM, to be employed as extended arrays placed on the same network, to improve the accuracy of data acquisition.[22] By increasing the number of EDs present in the same network, more amount of data can be obtained, and outlier values can be properly analyzed, obtaining more reliable and accurate data from the environment. Also, this massive amount of data can be properly treated, thanks to AI-driven electronics. This allows obtaining behavior patterns, being able to better understand the environment and thus adapting the generated response. The most used sensors in resource quality control in PoN applications are chemical and physical sensors, devices capable to transform the information from

a chemical or physical change produced in a media into an analytically useful signal. Chemical sensors can be differentiated depending on their transduction mechanism in optical, electrochemical, electric, mass, magnetic, thermometric and radiometric sensors, while physical sensors can be differentiated depending on position, pressure, temperature, force, vibration, piezoelectric, fluid, humidity, strain gauges, photo optic and flow.

A type of physical device that has been attractive in EM are piezoelectric devices owing to its high sensitivity to a broad range of vibration frequencies that can be used for monitoring different events, from mass flow to acoustic emission.[23], [24] Also, thanks to their versatility, they are capable to be used as sensor, actuator and energy harvester with the same structure composition.[25] Therefore, piezoelectric and electrochemical sensors are in the set of accessible devices with promising results. Their different transduction mechanisms, characteristics and opportunities will be treated in detail in the next sections.[26]

2.1.2.1. Piezoelectric Devices

Piezoelectricity is a property that is exhibited by some non-centrosymmetric materials called piezoelectric materials. The piezoelectric effect occurs when the charge balance within the crystal lattice of those materials is disturbed.

The interest in piezoelectric devices stumble upon their ability to generate electrical signals as outputs in response to mechanical stress, vibrations, or deformations, and vice versa, reversibly. This duality sets the basis for their application in devices, such as sensors, actuators, or energy harvesters (i.e., direct and indirect piezoelectric effects).[27]–[29] The generated electrical power arises from changes in the internal charge distribution of the piezoelectric material, produced by random or environmental-driven mechanical movements that can deflect the device structure, e.g., contact from airstreams or liquid flow, or triggered by vicinity vibrations, or also by human motion in their everyday life. Likewise, the application of an external electric field (EF) along a piezoelectric material induces a redistribution of its internal structure, obtaining a controlled mechanical strain.[15]

Table 2.1 shows a summary of the main important applications of piezoelectric devices[30] and a deep description of the piezoelectric properties and materials are explained in Section 3.1. A suitable selection of piezoelectric materials can be affordable depending on the target mechanical stress electrical signal ratio. For example, in sensors; inorganic piezoelectric materials like lead zirconate titanate (PZT), show large sensitivity owing to their large piezoelectric constant. However, its rigid shapes and difficult processing manufacturing make their integration on a mass

scale difficult and expensive. Another option for the fabrication of piezoelectric devices is the use of piezoelectric organic materials, such as polymers like Polyvinylidene fluoride (PVDF) with a low piezoelectric constant, but with the advantage that can be biocompatible and flexible. Furthermore, these types of piezoelectric materials are suitable to be fabricated with scalable techniques with the versatility to be adhered to any type of surface such as with PE.

Table 2.1. Piezoelectricity, innovation fields, and important applications. Reproduced from [30].

Category	Innovation field	Materials and shaping	Main applications
Frequency control and signal processing	**Frequency/time standards**	Quarts single crystal plates	Precise frequency control
	Mechanical frequency filters	Ceramic plates of specially tailored PZT	Inexpensive frequency control and filtering
	Surface acoustic wave devices	LiNbO$_3$, LiTaO$_3$, Quarts single crystal substrates	Passive signal processing for wireless communication, identification, sensing…
	Bulk acoustic wave devices	Ceramic plates of hard PZT, AlN, ZnO thin films	
Sound and ultrasound	**Buzzer**	Ceramic tapes of soft PZT	Sonic alerts
	Microphones and speakers	Ceramic tapes of soft PZT, PZT thin films	Telephone, blood pressure
	Ultrasonic imaging	Diced plates of soft PZT or PZNT single crystals	Medical diagnostics
	Hydrophonics	Hard PZT of various shapes soft PZT composites	Sources and detectors for sound location
	High power transducers and shockwave generation	Ceramic discs of hard PZT	Machining, US cleaning, lithotripsy
	Atomizer	Ceramic discs of soft PZT	Oil atomizers, humidifiers, aerosols
	Air ultrasound	Ceramic discs of soft PZT	Distance meter, intrusion alarm
Actuators and motors	**Printers**	Bars, tubes, multilayer ceramics of soft PZT, PZT thin films	Needle drives and inkjet
	Motors and transformers	Rings, plates or hard PZT soft PZT multilayer ceramics PZT thin films	Miniaturized, compact motors and transformers

	Bimorphs actuators	PZT multilayer ceramics	Pneumatics, micropumps, braille for the blind
	Multilayer actuators	Multilayer stacks of soft PZT	Fine positioning and optics
	Injection systems	Multilayer stacks of soft PZT	Automotive fuel valves
Sensors	Acceleration sensors	Rings, plates of soft PZT	Automotive, automation, medical
	Pressure and shock-wave sensors	LiNbO$_3$ substrates PVDF foils	
	Flow sensors	Soft PZT discs	
	Mass sensitive sensors	Quartz discs, Quartz substrates ZnO, AlN thin films	
Ignition	**Ignition**	Hard PZT cylinders	Gas and fuel ignition
Adaptronics	Adaptive devices	Various shapes of soft PZT, multilayer stacks of soft PZT	Active noise and vibration cancellation, adaptive control, airmail filter control

2.1.2.2. Electrochemical sensors

As previously mentioned, the main sensors for pollution detection are based on chemical methods. These types of sensors provide an electrical signal when a change in the analyte composition or quality is detected.[31] The International Union of Pure and Applied Chemistry (IUPAC) defines a chemical sensor as "a device that transforms information, ranging from the concentration of specific sample component to total composition analysis, into an analytically useful signal. The chemical information may be originated from a chemical reaction of the analyte or from a physical property of the system investigated".[32]

The electrochemical sensors are one classification of chemical sensors, being differentiated by the transduction mechanism. Furthermore, there are 3 types of electrochemical sensors and thus are classified depending on the nature of the electrical signal: amperometric, potentiometric or impedimetric. Further information about the nature of electrochemical sensors and their functional materials is provided in Section 4.1. Table 2.2 shows the electrochemical sensors classification regarding the measurement technique.[33] The common electrochemical sensor transducers and the usual analytes for each type of measurement are also shown.

Table 2.2. Electrochemical sensors classification regarding the measurement technique including the common transducer type and the usually measured electrodes.

Measurement type	Transductor	Usual analyte
Amperometric	Metal or carbon electrode	O_2, sugars, alcohols, FC, DO
	Chemically modified electrodes (CME)	Sugar, alcohol, phenols, oligonucleotides
Potentiometric	Liquid junction ion selective electrode	K^+, Cl^-, Ca^{2+}, F^-
	Glass electrode	H^+, Na^+
	Solid-state ion selective electrode	H^+, Na^+, K^+
	Ion-sensitive field-effect transistor (ISFET)	
Impedimetric	Interdigitated electrode (IDE)	Urea, charged species, oligonucleotides
	Metal electrode	

The structure type of these sensors in a liquid state can be miniaturized to a solid-state sensor, with more versatility in design, and with the capacity to make it flexible and low-cost thanks to scalable and reproducible techniques such as PE, with the advantage and possibility to be fabricated as a standard device or for single use in medical applications, where the importance of an isolated system it is required.

2.1.2.3. Lab-on-a-Chip systems

The different monitoring techniques described until this point have been designed upon discrete sampling methods. As previously explained, sometimes it is necessary to perform a sophisticated sample treatment before the measurement or calibration of the sensors with different buffers to increase resolution. With the emergence of microfluidic technology, a new challenge appears to combine the integration of microfluidics and printed sensors without disturbing them.[34]–[36] It is therefore when the concept of Lab-on-a-Chip (LoC) system appears, being a very accurate definition for PoC and PoN systems for EM.

This miniaturizing sensing approach was first introduced by Manz et al. in 1990, creating new opportunities for sample preparation and processing in a single platform.[37] In there, the concept of miniaturized and automated sensing platforms was explained. The capability of this system allows chemical sensing through a flow injection analysis method.

Microfluidic systems offer a route forward in that the sensing device can be housed within a protective environment and only occasionally exposed to the sample, which is drawn into the fluidic manifold through a filter interface from the external environment. Between measurements, the instrument can perform automated calibration routines to detect and compensate for baseline drift and changes in sensitivity.[38] This miniaturization sensing concept has several advantages such as cost efficiency, parallelization, compactness, diagnostic speed and sensitivity, opening the possibility of performing in situ, real-time measurements, being ideal for PoN diagnosis. Figure 2.4 schematically illustrates this LoC concept, where all the different procedures for the measurement of a sample are located in a single chip.[39]
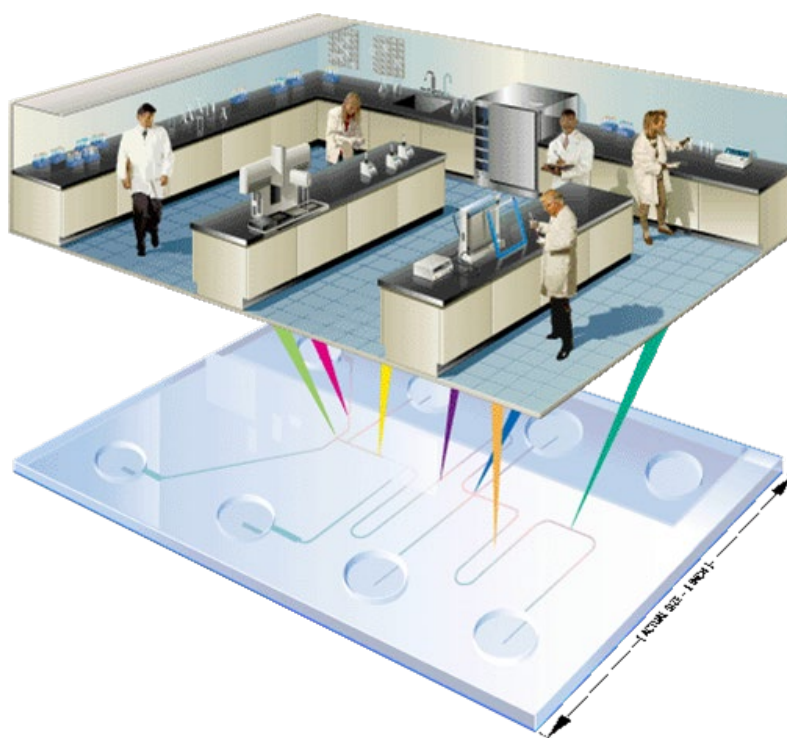
Figure 2.4 | Schematic approach of the Lab-On-a-Chip concept. Source [39]

Although LoC systems have several advantages, it still has limitations that we have to investigate to minor or deal with them. Table 2.3 depicts the main advantages and limitations of the LoC systems compared with conventional sensing tools.

For EM the most important sensors that better works with LoC systems are the electrochemical sensors.[40]–[45] As explained in the previous section, its working principle is based on an electrical signal produced by an interaction between the analyte and the electrode surface.

Table 2.3. Advantages and limitations of a Lab-on-a-Chip system compared with conventional tools. Reproduced from [46].

LoC Advantages	LoC Limitations
Low Cost: Numerous tests are performed on the same chip, reducing the cost of each individual analysis.	**Industrialization:** Most LoC technologies are not yet ready for industrialization. Currently, fabrication technologies are not standard.
High parallelization: Their capacity for integrating microchannels, LoC allows that several analyses can be performed simultaneously.	**Signal/noise ratio:** When miniaturization increases the signal/noise ratio also increases. LOC provides poorer results than conventional techniques.
Ease of use and compactness: Diagnostics using LoC requires a lot less handling and complex operations.	**Ethics and human behavior**: Without regulations, real-time processing may generate some fears of the untrained public diagnosing potential infections at home.
Reduction of human error: Since it strongly reduces human handling, automatic diagnoses reduce the risk of human error compared with classical analytical processes.	**Needs an external system**: Even if LoC devices can be small and powerful, they require specific machinery such as electronics or flow control systems to work. External devices increase the final size and cost of the overall system.
Faster response time and diagnosis: At the micrometric scale, diffusion of chemicals and flow switch is faster.	
Low volume samples: Because LoC systems only require a small amount of sample for each analysis, decreasing the cost of analysis by reducing the use of expensive chemicals.	
Real-time control and monitoring: One can control in real-time the environment of a chemical reaction, leading to more controlled results.	
Expendable: Due to their low price, automation and low energy consumption, LoC devices be able to be used in outdoor environments without the need for human intervention.	
Sharing the health with everybody: LoC will reduce diagnostic costs, the training of medical staff and the cost of infrastructure. As a result, LoC technology will make modern medicine more accessible to developing countries at reasonable costs.	

Microfluidic technology allows the analysis and use of reduced volume samples, chemicals, and reagents, minimizing the material and waste managed. However, the major challenge in environmental analysis is the need for sufficient device robustness to perform unattended high throughput sampling in the field with complex matrices. Another challenge for LoC systems is their need for external energy to control the fluidic pumps that control the sample and reactive, as well as the monitoring electronic system.[47] Therefore, the integration of these pumps and the generation of energy in a LoC system are challenges that scientists are focused on.

The combination of LoC with printed electrochemical sensors performs an ergonomic and user-friendly interface, with the facilities to be easily adapted to perform the desired analysis just by simply modifying the design of the printed materials and the pattern of the fluidic channels. Furthermore, the integration of LoC devices with wireless communication becomes a very powerful tool for EM with the possibility of remotely modifying acquisition parameters as well as enabling data transfer.

2.1.2.4. Rapid prototyping techniques

Standard manufacturing techniques may be required for the fabrication of microfluidic channels, components, or interfaces to isolate the sensors from the environment and only interact with the desired sample. These techniques are mainly related to the cut, the mill, the drill, the subjection or the bonding of different materials such as glass, silicon and polymers.

Rapid prototyping techniques (RPTs) are used to reduce the time and cost of ad-hoc fabrication and it is a good system to design new structures. In this thesis work, different manufacturing techniques are used for the encapsulation of the studied sensors with their microfluidic channels and for the connections, which are described below.

Milling

It is the oldest technique for manufacturing objects, being very suitable for the production of any flow system, from microfluidic to electrolytic cells. A rotary tool carves structures from the material delimiting the desired shape (Figure 2.5 (a)). The use of this technique was introduced in the 90's for the fabrication of fluidic channels. [37] Milling can be performed on almost any type of substrate, being polymethylmethacrylate (PMMA), polytetrafluoroethylene (PTFE), or cyclic olefin copolymers (COC) mainly used for microfluidic applications. Its precision allows the fabrication of very small channels down to 35 μm, with the qualified equipment, being a very useful technique for the fabrication of microfluidic prototypes.

Blade Cutting

It is a contact technique, where thanks to a movable blade mounted on a plotter hand, cuts can be made on a wide variety of substrates, including paper and polymers (Figure 2.5 (b)). This technique is mainly used in graphical arts, where it is widely used for vinyl cutting and adhesive films. The rotating head axis facilitates the orientation of the cutting edge in the cutting direction, enabling resolution down to 200 μm. Their use in printing electronics is enhanced since they can be used for the cutting of adhesive tapes on the manufacturing of microfluidic devices or the production of spray coating (SC) masks.[48]

Laser Cutting

Their work functionality is by melting and vaporizing material using a laser beam (Figure 2.5 (c)). This technique is mainly used for realizing microstructures in polymeric materials. It is based on an ablation mechanism, which significates that some chemical bonds of the substrate are broken directly during the process of photon absorption while others are broken thermally by the released heat of those excited molecules that do not break up photochemically.[49] Prototype laboratory lasers are based on CO_2 and they emit infrared radiation at a wavelength of 10.6 mm, photothermally ablating the underlying material. It is a non-contact technique; therefore the substrate does not suffer from mechanical stress during the cutting, being faster than the contact techniques.

Hot press

This prototyping procedure consists of two metal plates mounted onto pneumatic support which have the capability of applying a controlled pressure while heating (Figure 2.5 (d)). Is a very useful and interesting technique for the lamination process of polymeric substrates. By playing with the glass transition temperature (Tg) of these polymers we can obtain monolithic structures, being one of the most important techniques for the fabrication of microfluidic devices in the laboratory scale of prototyping

3D Printing

This manufacturing technique is a manufacturing process that allows the fabrication of 3D objects with the desired shape from a model or any electronic data. The main working approach is that successive layers of materials are deposited under electronic control. There are different types of 3D printers depending on the technology and materials behind the deposition process; those can be differentiated on soften materials (fused deposition) and cure liquid materials (stereolithography). In the first case, the printed material is melted inside a nozzle and deposited onto a platen, where is rapidly cooled, with the desired shape (Figure 2.5 (e)). In the second approach, UV light cures a liquid photosensitive polymer layer by layer creating the final 3D

structure (Figure 2.5 (f)). [48] The resolution of this technique is directly related to their capability to perform thin layers.
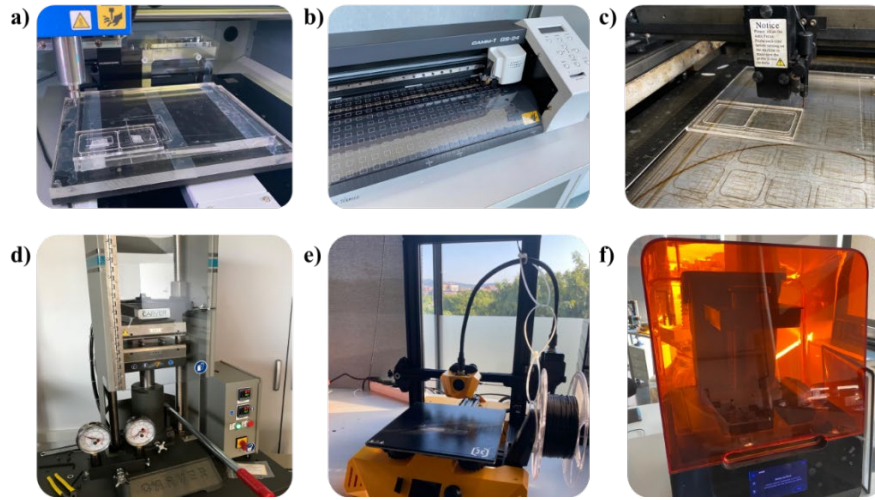
Figure 2.5 Rapid prototyping techniques: a) milling technique, b) blade cutting, c) laser cutting, d) hot-press embossing, and 3D printing e) fused deposition f) stereolithography.

2.2. Overview of printed electronics

In today's society, the concept of printing technologies is well established, being a key step of several processes in the industry, from newspapers to packaging, with the graphic arts as the commonly known extended worldwide. Over the past decades, the fast-growing pace of printing technology accompanied the emergence of the concept of PE, where electronic circuits or devices may be printed through an additive manufacturing technique.[50] Since its emerging in the mid-20th century, the field of PE has witnessed tremendous progress in the electronic technology concept with the appearance of new materials syntheses,[51] novel device concepts,[52] new functionalities, and new production techniques.[53]

PE combines electronics manufacturing with text/graphic printing, leading to high-quality products that can be thin, flexible, wearable, lightweight, of varying sizes, ultra-cost-effective, and environmentally friendly, being a revolution in the microelectronics industry, that was mainly focused on silicon and microfabrication techniques.[54]

PE technology uses an ensemble of additive manufacturing techniques,[2],[5] where stacked layers of functional materials are deposited on a substrate with a certain design or pattern. It is considered relatively simple to implement because it is built over mature technology, which is

less time-consuming, versatile, and customizable, and has less materials waste than typical microfabrication,[54] being suitable to produce cost-effective devices, aiming for niche applications in high-volume market segments where the high performance of conventional electronics is not required.

Most printed devices target the use of flexible and potentially low-cost substrates to enable large area and/or more rugged products, enabling higher freedom of design, seamless integration, use of sustainable materials, even recycled or biodegradable,[55] and reduction of metal content in electronic circuits.

2.2.1. Printing technologies

Historically, a wide range of printing techniques have been employed for PE, operating in a different manner owing to their different physic principles, such as the physical and chemical properties of the deposited functional inks, and the selected substrate characteristics, being lithography or flexography the first one to be employed.[56] However, there are two main groups of techniques that can be differentiated for the manufacturing of PE, with and without the use of a printing mask, also called analog and digital printing, respectively.[57] An overview of the commonly used printed techniques can be observed in Figure 2.6. Each printing technique operates inks and substrates differently, limiting the application of one technique or other to the interface relations concerning the materials used and designed pattern structure (thickness and resolution requirements), the physical and chemical properties of the deposited functional inks, and the selected substrate characteristics.
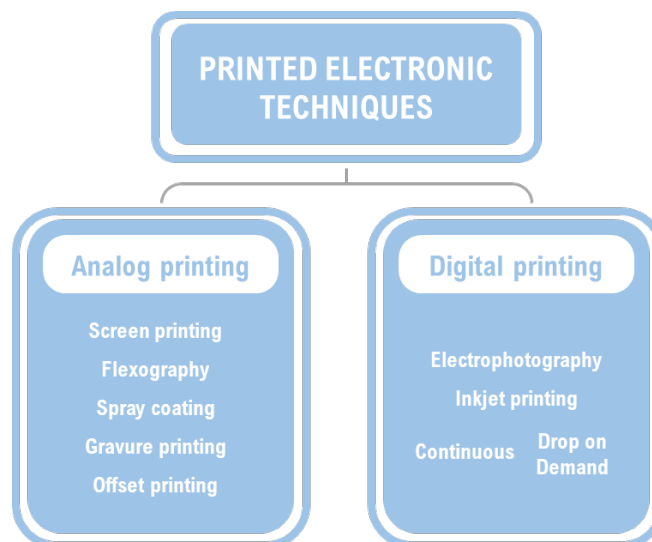
Figure 2.6   Schematic overview of the different technologies for PE dividing the selection between analog and digital printing techniques.

Analog printing

On one hand, the PE techniques that require a mask can be called analog printing, and include techniques like screen printing (SP),[58] offset,[59] flexography,[60] and gravure.[61] All these techniques share a common feature: the pattern to be printed is embodied in a physical form such as a mask, roll, plate, or screen. This template is transferred during the act of printing through direct or indirect contact with the substrate. Changes in the patterns can only be achieved by changing the master pattern, which involves making physical changes to the template within the printing machine, meaning time-consuming and increase the device fabrication cost and consequently, variability to some extent. These master patterns can be produced with different mesh sizes depending on the type of ink used and the weight of their components to regulate the size of the printed layer. This technique allows a high-volume production based on a roll-to-roll (R2R) approach, being offset, gravure, flexography, spray coating and SP the mainly used. These last techniques can be also used in the sheet-based method, for low-volume production and high-precision work.

Digital printing

On the other hand, some techniques do not require a physical, pre-manufactured mask, known as digital methods. This term means that the design is controlled by a computer, therefore the printing head is electronically controlled making a translational movement that follows the digital pattern. This results in a contactless selective transfer of the ink into the substrate without extra waste, and without force applied onto the substrate or sublayer. The basic premise of digital printing is the accurate positioning of a liquid droplet with a small volume directly correlated under digital control with the presence of information at each binary unit of the image to be reproduced. This technique allows the obtaining of thinner layers and a very easy superposition of the deposited ones without masking, being these two the main advantages of the technique. As a result, digital printing does not have the key disadvantage of analog printing, related to the investment to generate the masters, with in-line variable data. However, digital printing has certain drawbacks especially concerning average throughput when compared to high-end analog printing technologies. Inkjet printing (IJP) [62] is the dominant digital technique, but other techniques, like electrophotography,[63] are also used with less reproducibility in industry.

2.2.1.1. Comparison among printing techniques

The most suitable techniques for almost any application related to the PE field are SP (analog) and IJP (digital). Although SP and IJP have different system specifications and requirements, they have both matured in the graphic arts sector before becoming electronic devices manufacturing

techniques. Furthermore, their enhanced properties allow the fabrication of customized patterns with complex shapes at low-cost production, making PE very attractive for industrial adoption.[64]

There are different required bases to work with the PE methods, but among all, there are a reduced number of steps that are always needed: the deposition of the functional material in a form of ink and the post-processing of the ink to obtain their functionality, generally related with the sintering or curing of the ink. Figure 2.7 shows an example of the different necessary fabrication steps to pattern a layer over a substrate comparing both fabrication approaches. For analog printing (Figure 2.7 (a)), the deposition of the printed layer requires more fabrication steps to fabricate the same pattern than just an additive manufacturing technology such as digital printing (Figure 2.7 (b)). As explained before, this additional step in analog printing is provided by a common feature; the deposition of the pattern through a printing mask to define the different areas.

a) Analog printing

Substrate ➤ **Mask printing** ➤ *Sintering* ➤ **Printed layer**

b) Digital printing

Substrate ➤ **Printing** *Sintering* ➤ **Printed layer**
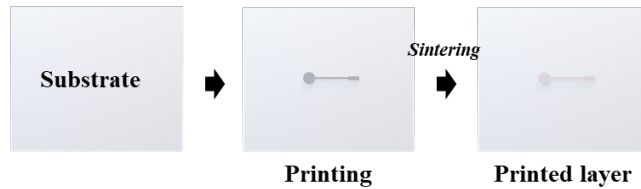
Figure 2.7 | Schematic diagram depicting the fabrication steps for the deposition of a metallic layer electrode with PE with a) analog and b) digital printing approaches.

Special characteristics of the most common scalable printing techniques for PE are summarized in Figure 2.8. Regarding their resolution, each printing technique has its constraints, and in general, a process with high resolution has smaller throughput and vice versa as shown in Figure 2.9. The lateral resolution of the printing techniques (the smaller feature that can be printed) typically goes from 3 to 100 µm depending on the process, throughput, substrate and ink properties.[65] Deposited thickness can range from well under tens of nm up to tens of µm. Each process has its advantages, e.g. SP is excellent for stacking multiple layers, while IJP allows a more precise deposition of the desired amount of material without any type of waste. Furthermore,

the SC technique combines such as both advantages, allowing the easy multiple stack formation with a small material deposition through a printing mask to obtain more resolution.

The increase of the resolution in mass production for PE has continued growing year by year, and lines down to 20 µm are now obtainable with SP with a special metallic screen and using new lattice material. SC combines a medium resolution with a medium throughput, owing to its capability to obtain very thin layers over a large surface in a short period with the possibility of using a mask to increase the resolution defining the printing area.

SP and SC are two of the printing techniques selected to work in this thesis and will be further explained in Section 2.2. and 2.3. respectively.

Screen printing

- Printing pattern defined by Surface relied (raised features) of master.
- Thick layers (> 10 µm) possible; low resolution (100 µm).
- Broad dynamic viscosity range; from 0.05 to 150 Pa·s.
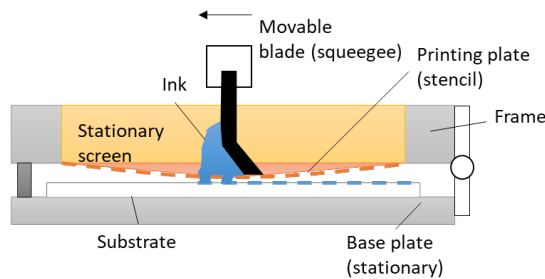
Inkjet printing

- Master-less; droplet size determined by nozzle diameter and waveform.
- Thin layers down to 100 nm possible; moderate resolution (10-50 µm).
- Dynamic viscosity of ink; 1 to 20 mPa·s.
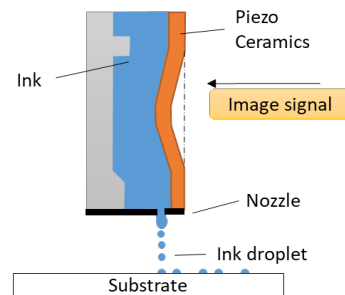
Spray coating

- Pattern can be defined with mask to increase resolution.
- Thin layers down to 100 nm possible; low resolution (100 µm).
- Dynamic viscosity of ink; 1 to 20 mPa·s.
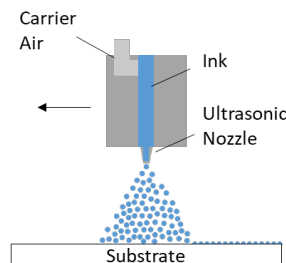
Figure 2.8 | General specifications of the most common scalable printing techniques in the industry.

Among digital patterning processes, the technique that has focused attention on the deposition of functional materials is IJP. Being a digital printing process, it allows greater versatility in the manufacturing process, managing to make live corrections. Their resolution is provided by their

finer printheads, whose developers continue to improve to obtain much more precise depositions, as well as adding multi-heads to increase their performance substantially. On a lab scale, new superfine inkjet printers can form features down to 1 μm, but these have not yet been scaled up to production. IJP is the last technique selected and used for the construction of this work and will be further explained in Section 2.5.
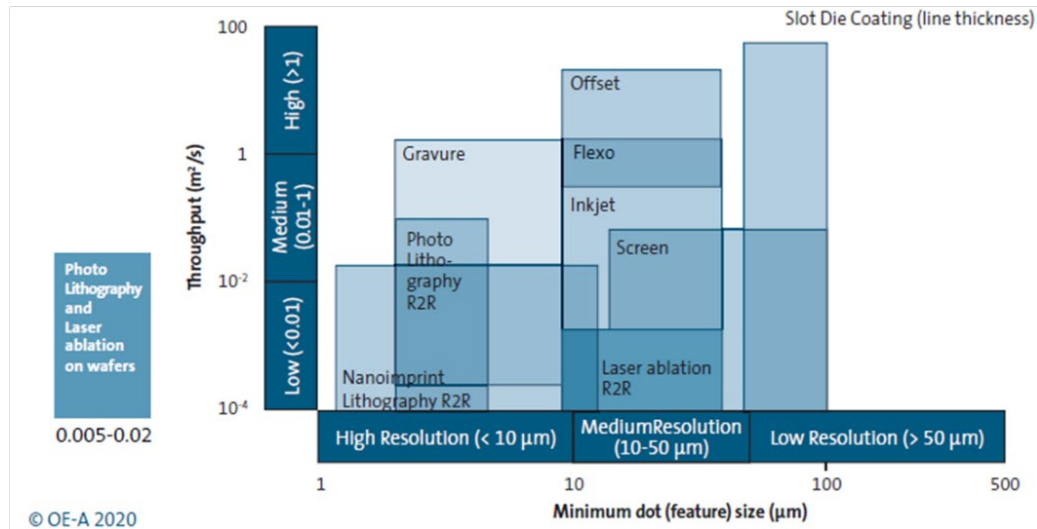
Figure 2.9 | Resolution and throughput for different printing techniques. Source: OE-A 2020 [65].

2.2.2. Substrates and functional inks for printed electronics

The resolution of the deposited design is one of the most important factors in PE, which will determine the application limitations and the requirements of the printing technique. The printable substrates and the rheological properties of the functional inks are the most important points to ensure high precision and resolution. Therefore, the adhesion of printed films into targeted substrates has to be optimized to obtain the maximum resolution.

2.2.2.1. Substrates

The fact of working with PE also requires the use of advanced materials for the printable substrates. The vast majority of PE devices target the use of flexible and low-cost substrates suitable for mass production and suitably applied to a R2R process to increase the scalability of the printing process. The compatibility of the selected substrates with the functional inks and curing conditions is a key and critical point to obtain a stable product. The main requirements for the substrates to be used in flexible electronics are flexibility, transparency in many cases, surface

wetting and smoothness, thin and lightweight, low thermal expansion, stiffness, heat resistance, and low cost amongst others.[50] Therefore, the selected substrates vary widely depending on the application requirements.

Table 2.4 lists different materials commonly used in PE and different important properties. From the vast majority, polymeric substrates have received the main attention in PE, offering a broad range of parameters, as well as material and surface chemical properties that enable micrometric design features that cannot be realized by any other class of materials.[66] Furthermore, due to their low cost and stable structural properties, polymeric materials became perfect for disposable devices, which minimize issues of sterilization, clogging and drift.

The different polymers that can be used as substrates in PE can be divided depending on their glass-transition temperature (Tg), which can be described as the critical temperature at which amorphous polymers increased their molecular mobility resulting in significant structural changes.

The polymers that cannot be reshaped once cured are called **thermosets**, and when these materials are heated further directly decomposes or burns instead of melting, being the polyesters, such as polyethylene terephthalate (PET), the most representative of this section, with very high optical transparency near to 90 %. However, one of the main drawbacks is its poor heat resistance, being necessary that the entire manufacturing process must be performed at low temperatures below 130 ˚C under low tension. This heat resistance gets better for polyethylene naphthalate (PEN), while transparency decreases and cost increases, and much better for polyimide (PI), increasing the process temperature to 300 ˚C, but with no transparency and increasing the cost.

Table 2.4. Variety of flexible substrates and selected valued properties for PE

	Thickness (μm)	Density (g·cm⁻³)	Transparency (%)	Haze (%)	Tg (˚C)	Process temperature limit (˚C)
PET	16-125	1.4	90	Approx. 0.3	80	130
PEN	12-250	1.4	87	Approx. 0.8	120	155
PI	12-125	1.4	-	-	410	300
PC	5-500	1.5	89	1	147	130
PMMA	20-500	1.3	93	7.2	105	130
TPU	20-250	1.2	-	-	107	160
Glass	50-700	2.5	90	0.1	500	400
Paper	100	0.6-1.0	-	-	-	130
Steel	200	7.9	-	-	-	600

On the other side, the polymers that can be structured when softening at Tg, which makes them processable at this temperature, are called **thermoplastics**. These materials include technical polymers, which can be structured using replication methods like injection molding or hot embossing. The most typical thermoplastics used in PE are PMMA and polycarbonate (PC), which have very high transparency, but like PET, the printing process must be done under 130 ˚C.[67] Within this substrate group, we can also find thermoplastic polyurethane (TPU), which stretchable characteristics and compatibility with textiles, make them perfect for wearable applications.[68]–[70]

Glass and steel are also attractive substrates for PE owing to their reliable barrier properties make them widely used for photonic applications. The transparency of the glass above 90 %, with a haze far below 1 provides great characteristics to applications such as photovoltaics, displays and lightings.[71]–[73] However, their high brittleness and their cost are their main drawbacks compared with plastics. The big heat-resistant qualities of the steel make them also suitable for printed photovoltaic cells.[74], [75] Since metallic substrates are conductive, a passivation treatment to isolate the surface is also needed for PE.

Recently, there has also been growing interest to use paper as a substrate. The fact of being a biocompatible and low-cost material made them perfect for single-use applications that have high impact on PoC devices. Furthermore, the unique properties of the paper, such as its capillarity, and its compatibility with several chemical and biochemicals, makes it an ideal substrate to be used in 2D microfluidics.[76], [77] Microfluidic paper-based analytical devices are targeting healthcare-related diagnostics, where the impact of cost reduction and simplicity is deemed to be highest, in other fields of applications, such as EM, explosives detection, or screening for food. Furthermore, disposable devices such as radio frequency identification (RFID) antennas on paper substrates without a Si chip are increasingly popular in the graphic paper industry, being one of the biggest PE application markets.[78], [79]

The main parameters to consider for good printing are the surface free energy and the surface tension of the ink. These parameters will define the wettability and adhesion between ink and substrate. When the surface tension of the ink is lower than the surface energy of the substrate the printing will be adequate.[80] If the surface energy of the substrate is higher than the surface tension of the ink different treatment methods can decrease the surface energy of the substrate and increase its wettability. As observed in Figure 2.10, the good and bad wetting of an ink onto a printable substrate can be differentiated through the contact angle of the ink. When the angle is higher than 90˚ (Figure 2.10 (a)), we can consider that the wetting is appropriate, however, when

the contact angle is lower than 90° (Figure 2.10 (b)) treatment to decrease the surface energy of the substrate is needed.

a) High Surface Energy

Good Wetting

Surface tension (Fs)

> 90°

Hydrophilic substrate

Metals, Kapton, Polyester, Polyurethane, Polycarbonate, Acrylic

b) Low Surface Energy

Poor Wetting

Surface tension (Fs)

< 90°

Hydrophobic substrate

Polyvinyl Acetate, Polystyrene, Acetal, Powder paints, Polyethylene, Polypropylene
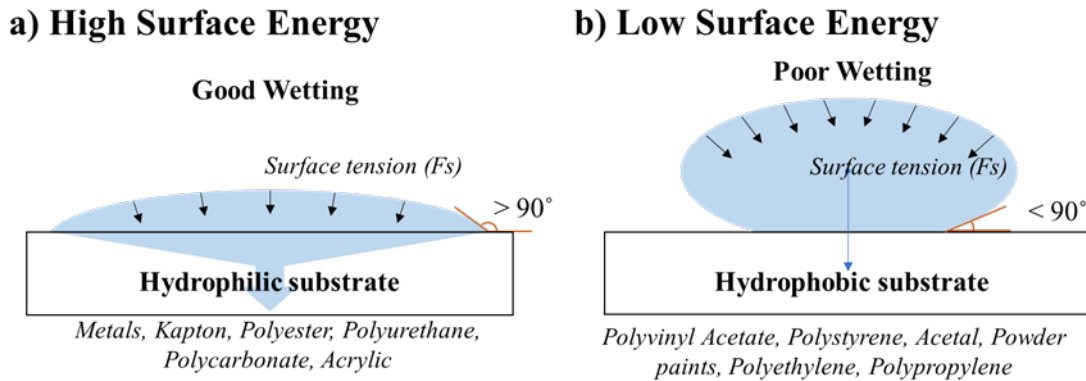
Figure 2.10 | Effect of the surface tension on the wetting of the a) hydrophobic and b) hydrophilic substrates. Reproduced from [81].

There are different pre-treatments than can be performed on a substrate prior to a printing process and those are mainly focused on facilitating and improving the complete printing process. The pre-treatments that can be performed on the substrate are structural or superficial.

The **structural** treatments involve a temperature treatment to avoid deformations between printed layers. Before the printing procedure, the printed substrate is heated at the maximum curing temperature of the ink (which in the temperature at the functional inks achieve their properties) to provoke a pre-shrinking of the structure in the oven for a certain time. After this shrinking procedure, it will be possible to print all the necessary layers of functional material, with their respective curing steps, avoiding problems of deformation of the printing design between layers.

The **surface** treatments are focused to decrease the surface energy of the printable substrate and increase the affinity with the deposited functional ink by improving the adhesion in the interlayer. This can be performed through corona or plasma discharge treatments (CDT) and with chemical modifications, introducing functional groups onto the surface that increases its wettability.[82]–[84] Plasma is the fourth state of the matter, generated by a discharge induced in a partial vacuum. It is an excited gas that consists of atoms, ions, molecules, free radicals, electrons and metastable species. Their interactions with the solid surface placed in the plasma lead to the desired surface properties depending on the nature of the gas used. The effect of the CDT is widely reported: it starts with the formation of radicals on the top layer of the surface which can react with each other to cause cross-linking or branching polymerization, with the O_2 molecule or with the O atomic, then the surface is oxidized and the wettability is increased.[85]–[89]

2.2.2.2. Functional inks

Over the last decades, the number of functional materials that have been adapted and used as functional inks for PE has widely increased, being the decorative inks based on pigments or dyes the first used for graphic arts. Nowadays these inks are also used in PE as decorative, but with the emergence of printed devices manufactured by printing means, a wide range of conductive, semiconductor and dielectric materials have been performed as inks for the different available printed techniques.[53] Electroactive polymers are some of the most promising materials for flexible PE,[22] and among them, piezoelectric materials are in the set of these accessible printed substances.[90] These materials will be further explained in Section 3.1.

The most restrictive property that enables the use of one technique for PE is the rheological behavior of the functional ink, owing to it has to be liquid enough to go through a 10 pL inkjet nozzle and balance of the ink viscosity is needed for SP; the ink has to be liquid enough to slide and pass through the mesh of the mask, but dense enough to be adhered to the substrate surface.

The most important materials that are used in PE are **conductive**. Those inks are typically based on metal nanoparticles, organometallic compounds and carbon nanostructures. Metal inks based on nanoparticles or precursors are commonly employed as conductive elements in PE due to their reliable and stable conductivity, being silver the most common printable metal conductor, with several different formulations that enable its deposition through different printing techniques, as well as inks that are more flexible or stretchable when sintered. Gold, platinum and copper inks are also available for PE, but their elevated price and sintering conditions make them not very compatible with polymetric substrates. However, the use of polymeric materials is on the rise enabling a wide range of electronic components to be made through low-cost printing processes, opening up the possibility of a range of new products and applications, including organic photovoltaics, organic light-emitting diodes, and organic thin-film transistors, which can be integrated into RFID tags, display backplanes, memory and sensor devices, and so forth, being the PEDOT:PSS the main representative. The material composition and the particle size allowed for these inks can vary depending on the printing technique, owing to each one has its limitations as explained in the next sections.

A strong factor for PE is the use of **semiconducting** materials.[91] Semiconductive ink manufacturing has different alternatives to meet the electrical requirements and the material restriction. A semiconductor resistivity falls as its temperature rises, against metal behavior; and its resistivity value as its name implies is between a conductor and dielectric. As with conductive materials, inorganic semiconductors generally show better electrical performances and stabilities,

being the transparent oxide conductors the called next-generation semiconductors for thin-film transistors,[91] nevertheless, organic semiconductors generally ensure cost-effectiveness, easier synthesis, and higher mechanical bending strength, however, they are sensitive to the environment and it is more difficult to achieve a homogeneous layer.[92]

A key point in many types of devices is the **dielectric** material, which allow the passivation of the printed conductive layers in multi-stack structures, avoiding possible short-circuits or defining the exposure area such as in electrochemical sensors. Additionally, due to their easy processability for ink formulation, they enhance the capacitance of PE for the fabrication of electronic devices such as capacitors or transistors. Printable dielectric materials can be classified as inorganic materials, polymers and organic/inorganic hybrid materials, being, like with the other material types, the polymeric materials the more compatible with the printing techniques.[53]

2.3. Screen printing technology

SP is one of the most versatile processes for transferring ink and technical coatings, ranging from artistic application to PE, being the most mature technique in this sector. It is a 2D low-cost manufacturing process able to coat large surface areas, and it is the simplest, most popular, and most economical technique in PE. SP is a push-through process, a special type of stencil printing, which means that during the printing process the ink passes through the screen and is adhered to the substrate. A blade, or squeegee, forces the desired ink transfer through the open areas (mesh) of the designed pattern of the mask onto the substrate. It is possible to apply a thick layer of ink in the SP process (normal values are around 20–100 μm, and offset printing values are typically around 0.5–2 μm).[57] The thickness of the stencil (the distance that the stencil stands above the screen) determines the thickness of the layer of ink. A balance of the ink viscosity is needed; the ink must be liquid enough to slide and pass through the mesh of the mask, but dense enough to be adhered to the substrate surface.

The main advantage of SP is based on its suitability. This technology allows a wide range of production scales, with a lower initial investment than other printing techniques. The fact of being a 2D technique requires the presence of a designed pattern, which provides more versatility than other analog printing tools. However, this technique has its disadvantages. The need for a printing mask also implies that the design cannot be easily modified, and therefore, any small change in the composition requires a new printing mask. Another drawback of this technique is the ink consumption. A large amount of minimal ink is needed to make a print and only a small amount is deposited on the substrate, thus having a loss of ink that remains attached to the screen and cannot be recovered.

2.3.1. Screen printing technique

For the SP technique the deposition of the material is through a printing mask, and this is composed by three parts: the frame, the screen fabric and the stencil, containing the printed information. Print masks can be created with an external editor, such as Inkscape or Adobe Illustrator, and the .pdf file obtained is sent to an external company where is stamped with de desired conditions. In Figure 2.11 (a) a scheme of a printing mask can be observed with the main parts differentiated.

There are diverse types of **frames** for the SP masks, but aluminum is the most commonly used. The frame provides stability to the mask, clamping the fabric in a specific arrangement, which is vital for the quality and the aspect of the printing to avoid distortions in the pattern.[57] Low frame weight is expedient for ease of handling, especially in the craft work sector.

The type of **fabric** to be used is a key point for the SP technique and depends only on the requirements arising from the process. The fabric's material must allow a good connection to the stencil material and must not be affected by the ink solvent or cleaning agents. It must be sufficiently abrasion-resistant to withstand the stress created when the squeegee is brought into contact with the substrate. The mesh width must be sufficiently large if coarse-pigmented inks or coating materials are going to be used, and on the other hand sufficiently fine to provide safe anchoring for the smallest parts of the stencil during halftone printing. The main parameter is the fabric count, which corresponds to the number of threads/cm, and will determine the **mesh width**. The mesh determines the open screen area as a percentage of the total surface and is determined by the fabric count in threads/cm and the diameter of the thread in μm. A scheme of the mesh calculation is explained in Figure 2.11(b). Fabrics can be obtained in levels of fineness from 10 to 200 fibers/cm. The most frequently used fabrics in PE are those between 60 and 120 fibers/cm.

$$\text{Open screen area } [\%] = \frac{w^2}{a^2} * 100$$

d = Thread thickness (diameter)
a = Thread spacing
w = Mesh width

Frame   Screen fabric   Stencil
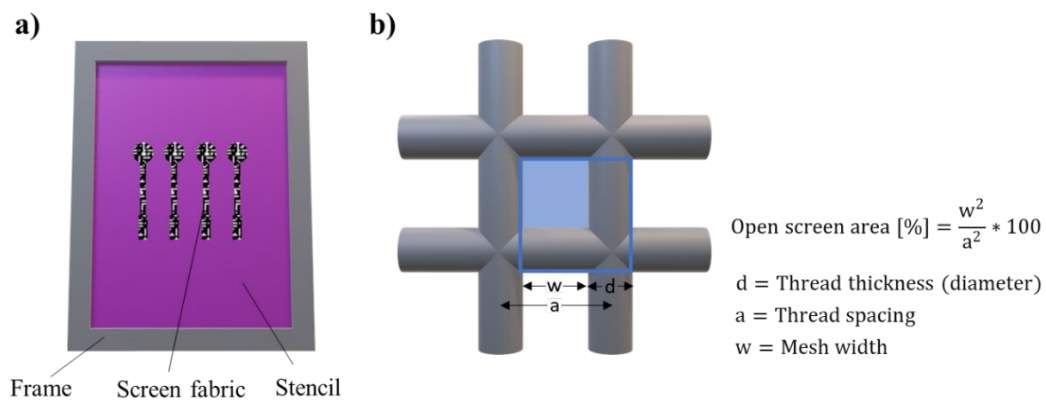
Figure 2.11 | a) Printing mask seed from the print side and b) geometry of the fabric mesh.

Finally, the **stencil** of the mask defines the actual printable area. It is made of patterned light-sensitive material and located on the opposite side of the screen on which the squeegee works, to avoid damage. This pattern is usually done by optical lithography.

There are three different assemblies of SP techniques that can be used in 2D R2R manufacturing based on flatbed and rotary mechanics and a hybrid mechanism mixing both techniques:
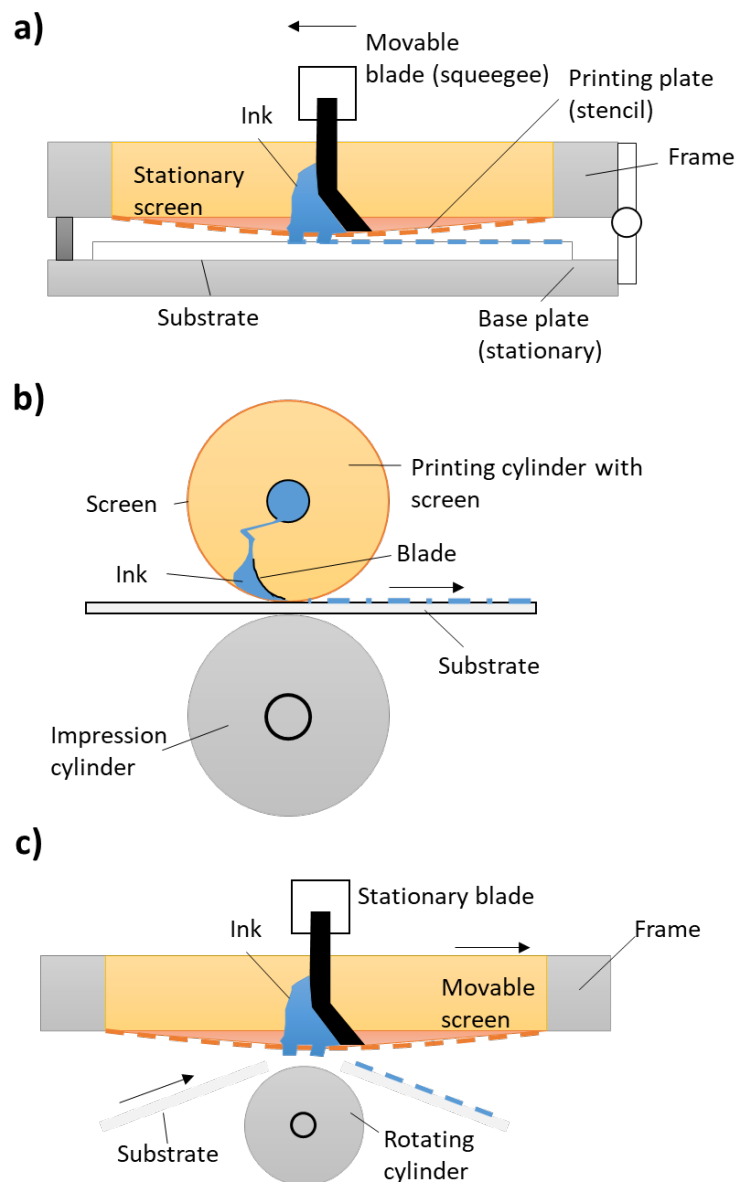
Figure 2.12 | Simplified views of a) flat-to-flat, b) round-to-round and c) flat-to-round SP mechanics

- **Flat-to-flat method** (flatbed): Both printing mask and printable substrate are flat, parallel to each other. The base plate holds the substrate by vacuum and a movable squeegee force the ink to pass through the screen apertures and deposited onto the printing substrate

(Figure 2.12 (a)). This mechanism allows the R2R production when mass scale is needed, however also has the capacity to perform sheet-to-sheet production, when a low-volume of production and a high precision work is needed. This will be the method selected to use in this thesis work.

- **Round-to-round** (rotary printing): The printing screen is cylindrical with ink inside the printing cylinder. Printing mask, substrate, and impression cylinder moves at the same time taking place the ink transfer to the printable substrate (Figure 2.12 (b)).

- **Flat-to-round**: Mixture of both previous techniques. The printing mask is flat and the printing onto the substrate is done by a rotating impression cylinder that moves synchronously. A static blade adapts to the substrate surface transferring the ink meanwhile the mask moves (Figure 2.12 (c)).

2.3.1.1. Inks, squeegee and printers for screen printing

The patterning resolution is one of the most important factors on SP, which mainly depends on mesh conditions. However, the printable substrates and the rheological properties of the functional inks are also key points to ensure high precision and resolution. Furthermore, the adhesion of printed films is influenced by surface tension and wettability of printable inks to targeted substrates, which could be adjusted by the used solvents and binders.

Inks

The ink viscosity can be adapted to the printed application, with a balance between viscosity and wettability to slide and pass through the mesh of the mask and to be adhered to the substrate surface with the maximum resolution.

The SP inks are typically composed of fillers, binders and solvents, which can be combined in different proportions to guarantee a proper viscosity to be adhered on different substrates. In PE these inks also have functional particles such as metals or polymers, which are the materials that provide the functionality of the ink. In SP the metal content of the ink could be up to 90 wt% with a particle size usually ranging from some hundred nanometers up to several micrometers. In SP, the dynamic viscosity of the ink may vary from 0.05 to 150 Pa·s, which allows a wide range of formulations to be used with this technique. The ink drying properties during the printing are also important. If the solvent evaporates too fast it can modify the viscosity of the ink and it will cause damages to the printing process.

The squeegee speed and the pressure of the squeegee are also very important variables in the printing process, being both correlated with the viscosity of the ink. The higher the viscosity of the ink, the slower the speed of the squeegee, owing to the increase of time needed for the ink to pass through the screen onto the printed substrate. Similarly, when the ink has low viscosity, the speed should be higher so the ink will not pass uncontrollably through the screen. When the speed of the squeegee increases, the pressure must be increased to pass through the screen fabric and to maintain the thickness of the printed layer.

Squeegee

The printing squeegee plays a very important role in SP. The combination of their material, the contact angle with the mask, the hardness and edge shape will determine the resolution and the thickness of the printed layer.

Table 2.5. *Mechanical properties of the squeegee material.*[93]

	Hardness (˚ Shore A)	Tensile strength (MPa)	Elongation (%)	Modulus 300% (MPa)	Tear resistance	Absorption resistance
Polyurethane	50-95	8000	700	200-4000	Excellent	Superior
Neoprene	30-90	3200	700	100-1480	Good	Excellent
Butyl rubber	35-90	2500	500	840-1280	Very Good	Good
Nitrile rubber	40-90	3000	650	2600	Good	Good
Silicone	20-90	1500	750	-	Poor	Poor
Floro carbon	60-90	2700	300	1300	Fair	Good
Polysulphide	20-80	1250	400	800-1200	Good	Poor

Table 2.6. *Solvent resistance of the squeegee material.*[93]

	Aliphatic hydrocarbon	Aromatic hydrocarbon	Alcohols and ketones	Oil and gasoline	Acid resistance
Polyurethane	Excellent	Good	Fair	Excellent	Excellent
Neoprene	Good	Fair	Poor	Good	Good
Butyl rubber	Poor	Poor	Good	Poor	Very Good
Nitrile rubber	Excellent	Fair	Poor	Excellent	Good
Silicone	Poor	Fair	Fair	Fair	Poor
Floro carbon	Excellent	Good	Poor	Excellent	Fair
Polysulphide	Excellent	Excellent	Good	Excellent	Good

The principal **materials** with which rubbers are made are elastomers, being polyurethane (PU) the one with the best characteristics to be used as squeegee. Table 2.5 and Table 2.6 summarizes

the mechanical and chemical properties of the different elastomeric materials which are suitable to be used as squeegee in SP for PE.

As observed in Table 2.5, the **hardness** and stiffness of the squeegee play an important role in SP, the harder the squeegee, the more it will maintain the angle of attack, cuts off the ink sharply, cleans the screen surface and has a longer life. The hardness in a squeegee is measured with a durometer, and the shore A hardness scale measures the hardness of flexible mold rubbers that range in hardness from very soft and flexible, to medium and somewhat flexible, to hard with almost no flexibility at all. Semi-rigid plastics can also be measured on the high end of the Shore A Scale. A 'Shore Hardness' gauge has a needle on a spring protruding from one end. The needle is placed against the rubber or plastic and pressure is applied. Once the gauge is pressed firmly against the material and the needle has penetrated as far as it can go, the measurement needle will indicate the corresponding hardness measurement. Figure 2.14 (a) elucidates an example of the established color for all the available ranges in the PU squeegees. Shore A hardness values from 50 to above 90 (modulus 200-4000 p.s.i.) can be obtained without losing elongation and while retaining good resiliency.

The modulus (300 % elongation) is also a very important property of elastomers, which is another parameter to choose the best material for squeegees. Higher modulus keeps the attack angle constant, being the PU the material with a large working range.

The squeegee material must have very high resistance to the main chemicals used in ink formulations and the cleaning process. Again, as observed in Table 2.6, the PU is not affected by the chemical elements listed, obtaining a very good resistance. The other material options may have some resistance better than PU, but all of them are very sensitive to some of the chemicals, therefore they would not be viable to use in these conditions.

The squeegee rubbers are available in many end **shapes**, and each one of them is suitable for different purposes. Figure 2.14 (b) elucidates the most typical ones and their principal characteristics and applications:[93], [94]

- **Rectangular**: is the most used in the printing processes, and therefore also in PE. The flat axis removes the surplus ink maintaining the pressure on the mask. Is usually used for printing on flat surfaces**.**

- **Diamond**: the contact angle of 45° leads on a very accurate printing line. It is very popular on applications with extremely fine line detail.

- **Single cut**: is generally used when printing on glass or irregular surfaces. Depending on the orientation this squeegee is used with an upright or angled attack, but owing to its small thickness at the end, it deflects at slight pressure.

- **Round**: mainly used for textile applications. The rounded corners allow more amount of material to pass underneath the squeegee, leading to an extra ink deposition.

- **Double cut**: used for upright printing circular shapes. Mainly applied for ceramic and glass substrates.

a) Hardness

SOFT			MEDIUM		HARD		
50-60°	60-65°	65-70°	70-75°	75-80°	80-85°	85-90°	90-95°
Yellow	Red	Red	Green	Blue	Brown	Fawn	Pink

More ink ←――――――――――――――→ *Less ink*

b) Shape

Rectangle	**Diamond**	**Single cut**	**Round**	**Double cut**
Widely applicable for different substrates, inks. Generally used.	Very accurate printing lines. Popular in printed intelligence processes.	Uneven or irregular substrates.	Textile printing. Maximum ink transfer.	Glass or plastic cylinder-shaped surfaces.

c) Angle effect

> 60° — *Poor filling, good definition*

= 60° — *Good filling and definition*

< 60° — *Good filling, poor definition*

Figure 2.13 | a) Schematic illustration of the hardness of the squeegee correlated with their characteristic colors and the amount of material deposited, b) different squeegee rubber shapes and their main purpose and c) schematic illustration of the squeegee contact angle effect with the substrate.

Finally, the **contact angle** that generates the squeegee with the printing mask will determine the precise amount of ink deposited onto the substrate.[95], [96] As observed in Figure 2.14 (c), with the ideal contact angle of 60° only the necessary amount of material will be deposited, obtaining the required resolution for the application. However, if the contact angle is > 60° the ink will try to lift off the mesh and will not transfer adequately to the substrate, obtaining a better resolution but with a smaller amount of ink that can cause the track to be cut off. Furthermore, if the contact angle < 60°, the squeegee will pass a larger amount of ink that will be deposited on the substrate, overflowing layout tracks and thus losing resolution.

ATMA screen printer

The printer used in this work is a semi-automatic flat screen printer AT – 60PD from ATMA, model shown in Figure 2.15. It is a versatile system for SP deposition mainly used in research area, but allow some large-scale production in comparison to manually operated SP equipment. The printer is equipped with a high pneumatic system that serves to keep the substrate on the vacuum bed during registration and printing. It also controls the motion of the squeegee, flood bar, and screen during the operation. Their semi-automatic meaning comes from the fact that the screen is raised and lowered automatically. Because of a combination of two squeegees, the screen flooding and the actual printing process where ink is pressed through the screen take place automatically, being able to program multiple squeegee operations if a particular large amount of ink is needed. However, the feeding of the substrate and delivery of the printed substrate is still done manually on a vacuum printing table. More information about this printer can be obtained in [97].
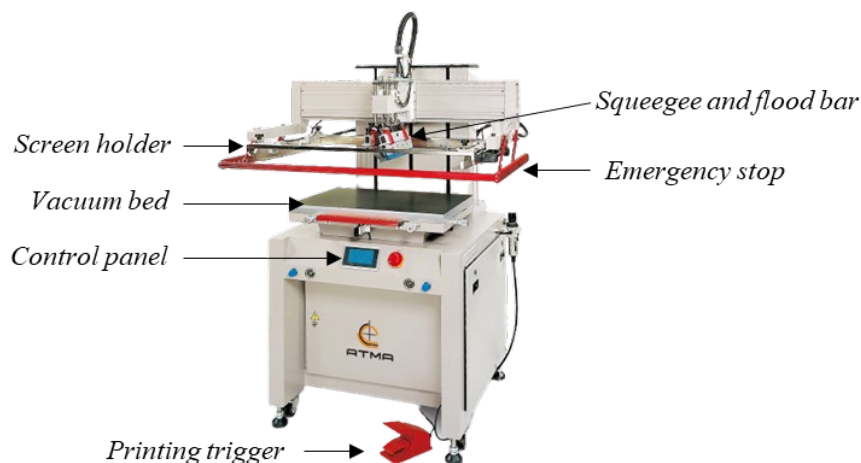
Figure 2.14 | ATMA-60PD Digital Electric semi-automatic flat screen printer.

2.3.2. Screen printing process

The different types of SP technologies have the same working principle and more or less have similar requirements concerning substrate and inks. These requirements are addressed in this section. Figure 2.15 shows a general schematic of the SP procedure to print the desired pattern, and Figure 2.16 schematically illustrates the different steps for the printing of one functional material.
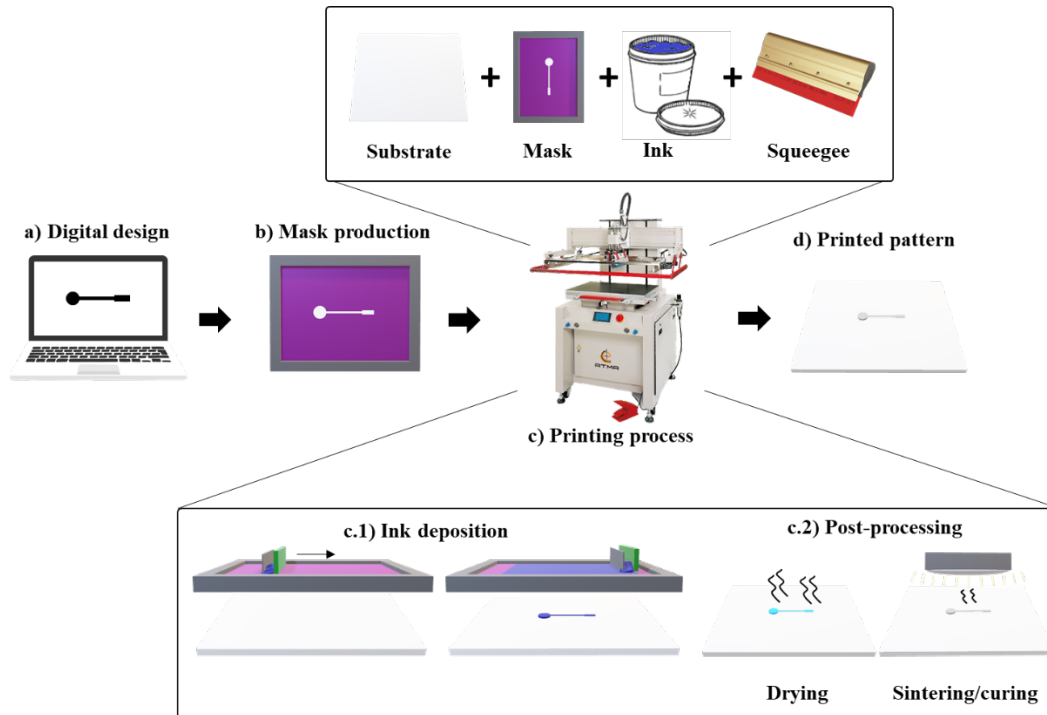
| *Figure 2.15* | Simplified image of the basis of a SP complete printing process starting with a) the digital design, b) the mask production c) the printing process which implies c.1) the ink deposition through the mask and c.2) the post-processing of the material, until c) the final printed device. |

Once all the printing designs and material types for the printing procedure are selected, a series of steps to carry out the printing process must be followed:

Starting with a fundamental step, we must ensure that the working area is completely clean. This is a very basic, but important, concept that we must follow, because if it is not the case, irregularities, such as fingerprints, can appear in the printed design. Then, we must perform the surface and structural pre-treatments of the printed substrate, as already explained in the previous sections, to ensure that after the first layer has cured, the following ones are not affected by the shrinking of the substrate. Afterward, we must choose the desired ink and squeegee that we are

going to use for the printing procedure. From the same material, different inks with different viscosities, binders and solid contents can be found, therefore we must choose the one that better fits with the printing substrate and design to obtain the best resolution. Consequently, the selected squeegee will also be in accordance with the ink and the application.

After the pattern was digitally designed (Figure 2.15 (a)) the printing mask is prepared with the necessary mesh according to the ink parameters (Figure 2.15 (b)). Then, the tension of the screen must be checked with a tension meter, and it has to be the same compared with the reading measurement in the first inspection. This monitoring is needed to know when the condition of the screen is weakened during the different printing cycles. Afterward, the screen has to be firmly placed on the adapters of the machine. Subsequently, the printing squeegee is inspected to ensure that its structure has not been worn with the use and is also placed in the printer, adjusting the height concerning the printing mask. Prior to depositing the ink onto the printer, it has to be carefully shaken with a glass jar or an electric shaker to mix all the components that may have been deposited at the bottom of the container during the storage. After adjusting all the parameters of the printer according to the design and the ink used and making sure both the screen and the squeegee are in good condition, we proceed to place the substrate in the printer and print the number of layers needed (Figure 2.15 (c)).

Roughly, the printing process in PE can be simplified into two main steps: the ink deposition onto de printing substrate and the material post-processing. In SP, the ink deposition step is observed in Figure 2.15 (c.1), the printed material is deposited in the screen mask and with the squeegee is transferred onto the substrate. In this step, the user needs to define different important printing parameters to deposit a homogeneous material layer, such as the squeegee conditions, their angle and speed, the pressure it exerts on the mask and the distance it travels. After the functional printable material is deposited, the second step is to provide them with its properties and functionalities removing all the external materials that make the ink suitable for PE such as surfactants, dispersants, humectants, adhesion enhancers, etc. (Figure 2.15 (c.2)). This process is done in two steps; the drying, which is mainly used to evaporate the solvent, and the sintering/curing, where the dried structure achieves its functionality. Typically, it can also be performed with temperature but other sintering techniques such as UV, plasma treatment, photonic or microwave are also available. Finally, the printed pattern is obtained (Figure 2.15 (d)).

Every printed material should be recognizable; therefore, it is important to keep the information management of the entire process with all the conditions related to the manufacturing process that could be retrieved afterward.

Screen printing procedure

01 — Cleaning of the laboratory surfaces
02 — Pretreatment of the printing substrates
03 — Process parameters and materials selection
04 — Condition check of the screen
05 — Preparation of the print machine
06 — Inks preparation
07 — Printing and curing the materials
08 — Washing off the screen and equipment
09 — Documentation

Figure 2.16 | Roadmap of the different steps for the SP procedure.

2.4. Spray coating technology

SC is a well-established technology in graphic arts, industrial coatings, and paintings. This high-throughput large-area deposition technique ensures ideal coatings on a variety of surfaces with different morphologies and is often used for in-line production, making this technique very promising for large-scale printing in PE.[98]–[100] Moreover, the fluid waste is reduced to minimal quantities by the use of a controlled pump that injects the ink at the desired speed through a nozzle where an aerosol is formed and deposited with the help of a carrier gas. This aerosol deposition can be patterned by a simple shadow masking with a millimeter detail resolution. [101]

The main advantage of the SC technique is the versatility it offers to print several materials onto many different substrates. SC can access a broad spectrum of fluids with different rheology, offering very high adaptability of the system to deposit virtually any kind of solution on any surface and obtain the desired film properties.[100] Furthermore, owing to its easy printability, it makes a very interesting technique to functionalize electrode surfaces. These surfaces are quite rough, but thanks to the SC technique they can be functionalized more simply with the possibility of being applied in large-scale manufacturing.

However, the usage of SC in the production of PE has not been given much attention, owing to some unstable parameters. The formation of the aerosol and the evaporation of some of the solvent is complex, and even in principle the SC technique is R2R compatible, involves a difficulty concerning the homogeneous control of deposition thickness and roughness, as well as the complexity of the multilayer printing owing to the mask pattern when details are needed. [101], [102]

2.4.1. Spray coating technique

As mentioned, the deposition of functional materials with the SC technique can be performed with and without a shadowing mask. For this technique, the printing mask is necessary when a resolution over the millimeter scale is needed. A large number of materials and methods have been suggested for the fabrication of shadow masks for other applications than SC such as Si,[103], [104] nanostencils for metal deposition[105] and polymers such as SU-8,[106] Parylene,[107] Polydimethylsiloxane (PDSM)[108] or PI.[109] Si masks are very fragile, especially when the stencil design has high hole density, not being suitable for multiple depositions and the subsequent cleaning steps, therefore, polymeric masks are more suitable for this type of application.

In addition to printing techniques, standard manufacturing techniques may be required for the fabrication of regular shadowing masks for SC, fluidic components and interfaces and no extra equipment is needed like in the SP screens. These RPTs mainly involve cutting operations and are also used to reduce the time and cost of fabrication. A detailed explanation of the RPTs is explained in Section 2.1.2.4 In this thesis work different RPTs are used, but for the fabrication of the SC masks, the laser cutting of a PEN substrate has been employed.

Different assemblies can be employed when the SC technique is used in PE and the main technical difference between them is the droplet formation reported. The scheme of both printing methodologies can be observed in Figure 2.17.

- **Airbrush SC**: This is the most basic approach for the SC technique and allows the deposition of several materials with very simple equipment. This equipment contains an ink container where the functional material is stored while pressurized air enters to the system forming the droplets at the end. Also, it has a manual trigger that allows the formed spray to exit the system and be deposited on the substrate.[99], [110], [111] Its main disadvantage is its difficulty to control small ink flows and a greater amount is spent on each print, in addition to its larger droplet size, given its technical limitations (Figure 2.17 (a)).
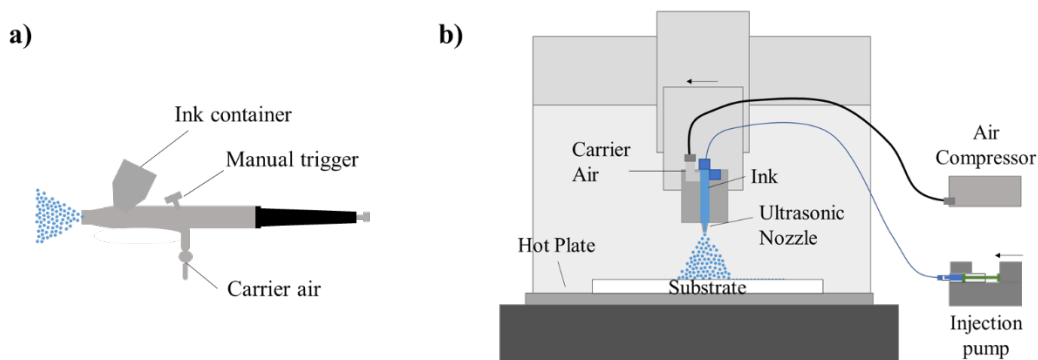
Figure 2.17 | Schematic diagram of the SC machine with a) air-brush spray coater and b) electro spray coater.

- **Electro SC**: Advanced airbrush approach. In this case, the drops are generated thanks to an ultrasonic nozzle (Figure 2.17 (b)). A cross-section of the ultrasonic nozzle is represented in Figure 2.18 (a). As observed, the ink enters to the nozzle and this operates by converting high-frequency sound waves into mechanical energy that is transferred into a liquid, creating standing waves. As the liquid exits the atomizing surface of the nozzle, it is broken into a fine mist of uniform micron-sized droplets (Figure 2.18 (b)). Unlike pressure nozzles, ultrasonic nozzles do not force liquids through a small orifice using high pressure to produce a spray. The liquid is fed through the center of a nozzle with a relatively large orifice, without pressure, and is atomized due to ultrasonic vibrations in the nozzle.[100], [101] Thanks to ultrasonic technology, the average size of drop generation can be controlled by modifying the vibration frequency of the nozzle. As elucidated in Figure 2.18 (c), the increase of the nozzle frequency generates the increase in the drop size. Another great advantage that has the ultrasonic nozzle is that this drop generation is more controlled than the regular air-brush spray coater, obtaining a very narrow average size of the drops (Figure 2.18 (d)). Also, as it does not need as much volume of ink for the formation of the drops, it can be supplied in a controlled way by

means of injection pumps, allowing it to work with flow rates of the order of µL/min.[112]

a) Ultrasonic Nozzle Cross Section
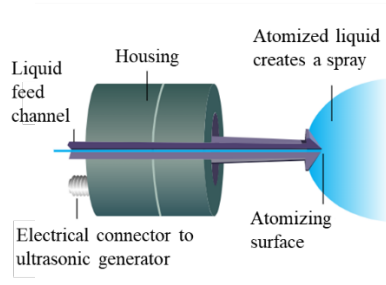
b) Ultrasonic Nozzle drop generation
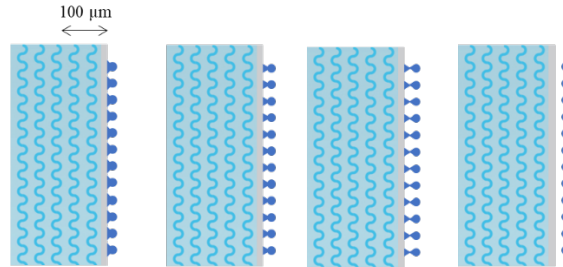
c) Ultrasonic nozzle median drop size
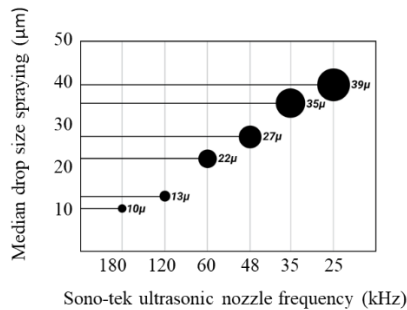
c) Drop size comparison Sono-tek vs pressure nozzles
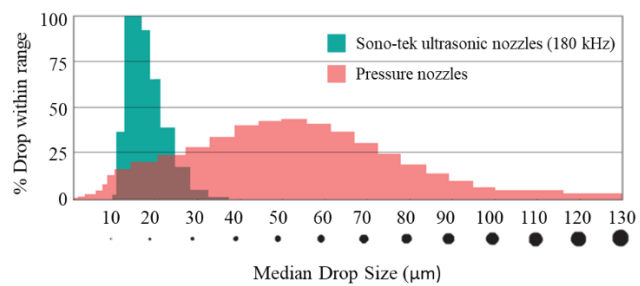
Figure 2.18	Schematic diagram of a) the cross section of the ultrasonic nozzle and b) the drop generation at the ultrasonic nozzle. Graphical representation of c) the size of the generated drop at each different frequency and d) drop size distribution comparison between the ultrasonic nozzle and a regular pressure nozzle. Source from [112].

2.4.1.1. Inks and nozzles for spray coating

As previously explained, the SC technique allows a wide range of functional inks owing to its working principle, including polymers, such as PEDOT:PSS, metallic nanoparticles, metal oxides or carbon-based solutions. However, there are a few parameters for SC that has been called crucial to obtain homogeneous printing, however, the distance between sample and nozzle is one of the parameters that had a bigger impact on the morphology of the obtained layer. It has been identified three different regions between the nozzle and the substrate:[102], [113]

- **Wet**: If the distance is too small, the ink is deposited as a solution, dissolving the previously deposited material, obtaining a weak relationship between spray time and the material thickness. Also, irregular surfaces are obtained.

- **Dry**: If the distance is too far from the substrate, the material was scarcely deposited. The solvent of the polymer solution was completely dried before reaching the substrate and the material became a dust.

- **Intermediate**: This distance is perfect for a more stable deposition. When the ink solution arrives at the substrate it still has the necessary amount of solvent to have a good deposition of the substrate, but it dries fast enough to be able to continue adding material on top without ruining the previous layer.

With the optimum distance between the nozzle and substrate, there are other key parameters that will affect the SC process. The modification of these parameters will modify the thickness of the deposited material and thus will depend on the application, the functional ink and the printable substrate. Those parameters are:[101], [111], [114]

- **Flow rate and pressure**: as higher the flow rate, the airbrush will have a higher pressure, arriving with a higher density of drops on the substrate, therefore the modification of these values implies the modification of the distance between the nozzle and substrate to obtain a stable deposition. However, when obtained, the amount of ink deposited increases.

- **Temperature**: the temperature of the heating plate, and therefore of the substrate must be optimized to be in the range that evaporates de solvent slow enough to lay down the printed material well but fast enough so that solvent does not accumulate and damage the printed layer.

- **Concentration**: as higher the concentration of the ink, more material will be deposited on the printed substrate, however, an excess of concentration must be avoided, owing that in the atomization process in the nozzle, material can accumulate and clog it.

- **Spray duration**: it is a key parameter to obtain a reproducible and homogeneous layer. If the duration is too short, the deposited layer will be very thin and pinholes can appear, therefore, more layers will be necessary to obtain a homogeneous surface. In the same way, if the duration is too long a lot of solvent will accumulate in the same area, thus deteriorating the printed layer

- **Solvent**: the choice of the ink solvent is very important since it will affect the choice nozzle–substrate distance for thickness optimization and film morphology.[114] As

explained, the concept behind choosing a solvent is to choose a fast drying solvent to prevent droplets from re-dissolving sublayers but not so fast to allow for a homogenous and pin-hole-free film to form. Besides, by controlling the phase evaporation, by means of substrate heating or mixed solvents, the homogeneity of the thin films is assured

With all the previous parameters optimized to obtain the best printing resolution for the required application, the ultrasonic nozzle spray shaping can be modified in order to meet the need of several applications, from high precision to uniform deposition to cover the largest area possible. Several patented air shaping technologies have been developed and patented by Sono-Tek [112] to shape the atomized spray into defined patterns that can be precisely controlled using low-pressure air to entrain the atomized spray.

PicoMist™

Very low volume applications. Fine lines as thin as 0.5mm.

MicroMist™

With ultrasonic atomic nozzle. Fine lines as thin as 0.5mm.

AccuMist™

Highly focused beam of small drops. The lines varies from 1.78 – 25 mm.

Vortex

Low velocity, rotational air/gas to produce a conical spray pattern that is 50 – 100 mm in diameter.

Impact

Fan-shaped spray pattern. Spray patterns up to 15 cm, with unlimited widths possible in wide area.

Propel™

Uniform wide spray pattern up to 25 cm per nozzle.

WideTrack™

Two jets of air/gas that pulse alternately to direct the spray as it emerges from the nozzle. The position of the jets can be adjusted, creating a pattern up to 61 cm.
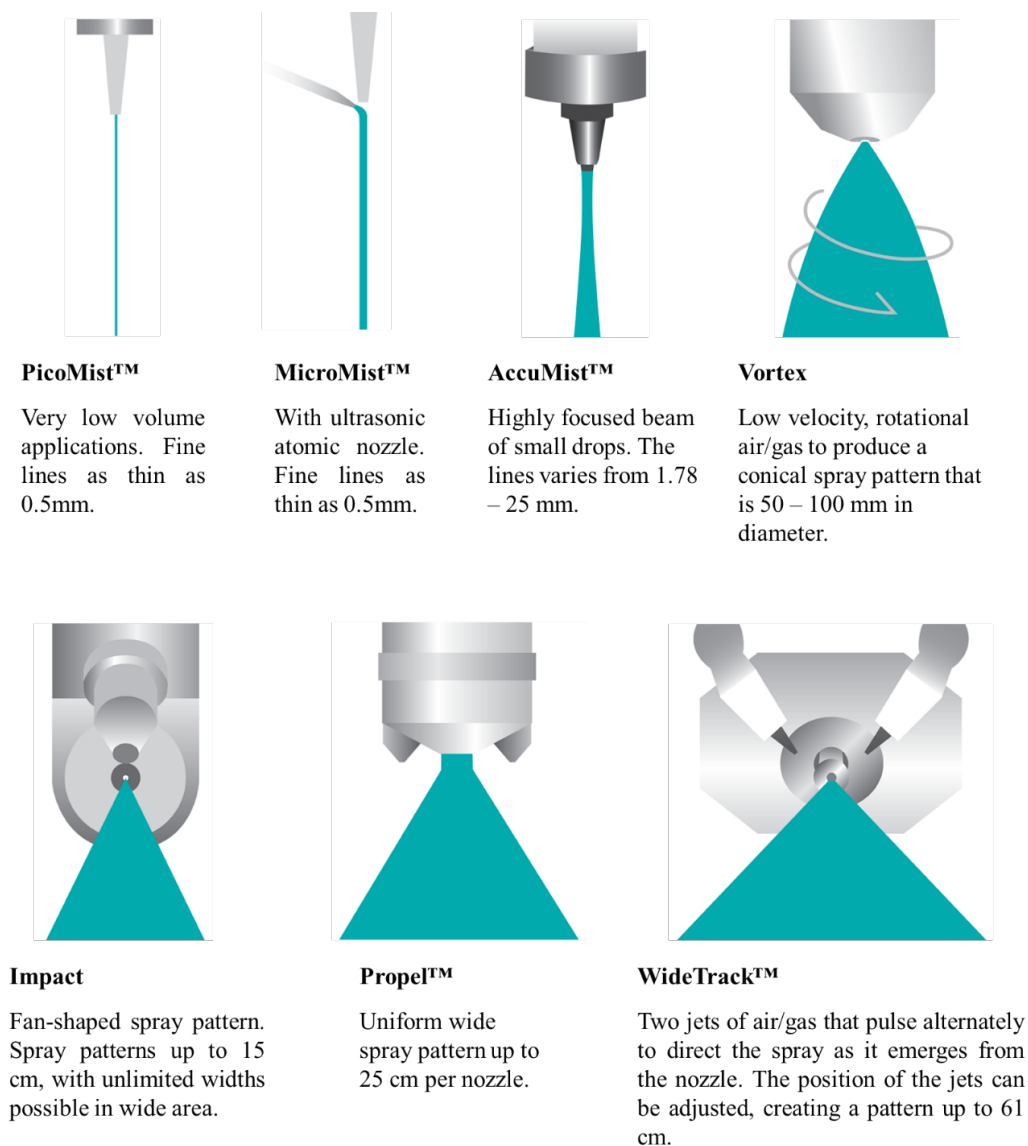
Figure 2.19 | Schematic representation of the different ultrasonic nozzles provided by Sono-tek and their main characteristics and working application. Source from [112].

Figure 2.19 shows a schematic representation of the different ultrasonic nozzles and their main characteristics. As can be observed, a wide range of applications can be covered by all the different ultrasonic nozzles, since very high precision with a line thickness of 0.5 mm to the homogeneous deposition of large substrate areas with lines up to 61 mm thick, passing through different intermediate lengths that cover the entire spectrum of possible applications.

This wide range operational of the ultrasonic nozzle is available owing to their technology, by adapting, increasing, reorientating or duplicating the direction of the air pressure that is focused on the drops beam, as well as the vibration frequency of the nozzle, allowing to modify the size of the formed drop.

In this thesis work, the equipment used to print through the SC technique was the SelectaFlux system from Sono-Tek (Figure 2.20 (a)). This ultrasonic selective fluxing system offers the highest accuracy degree and fine line control. It can control the spray velocity, which gives maximum top side fill and lower maintenance, being also compatible with all fluxes. The SelectaFlux system is connected to a precision syringe pump, which works in parallel with the ultrasonic nozzle to obtain a stable drop formation and a constant spray flux.
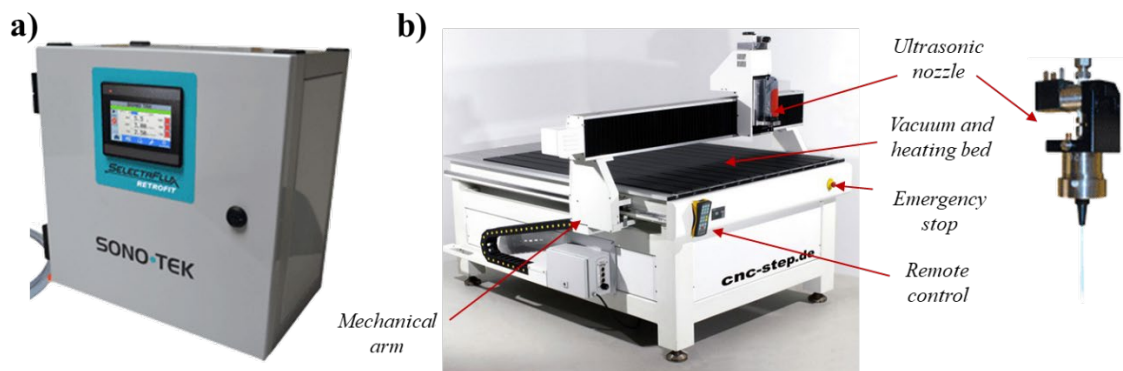
Figure 2.20 a) Sono-tek spray coating equipment and b) CNM T-Rex machine with the ultrasonic nozzle for the automatic deposition.

The SelectaFlux was equipped with the AccuMist^{TM} Ultrasonic Spray Shaping from Sono-Tek to perform the SC deposition. The AccuMist^{TM} system combines Sono-Tek's unique MicroSpray ultrasonic atomizing nozzle with low-pressure air to produce a soft, highly focused beam of small spray drops. Compressed air, typically at 1 psi, is introduced into the diffusion chamber of an air shroud, which surrounds the nozzle, producing a uniformly distributed flow of air/gas around the nozzle stem. The ultrasonically produced spray at the tip of the stem is immediately entrained in the low-pressure air stream. An adjustable focusing mechanism on the air shroud allows complete

control of spray width. The spray envelope is very narrow and hourglass-shaped. The width of the shape is controlled by adjusting the nozzle distance to the substrate and varies from 1.78 – 25 mm, which enables very high control of the deposited material resolution. To increase the deposition automation, the AccuMist™ was mounted on an adapted CNC machine provided with a vacuum and hot plate (Figure 2.20 (b)). This machine allows loading the head path to carry out the deposition of the spray with the desired pattern and head speed.

2.4.2. Spray coating process

The different types of SC technologies previously mentioned have very similar working principle and requirements respecting to substrate, printing distance and inks. These requirements are addressed in this section. Figure 2.21 shows a general schematic of SP procedure to print a desired pattern. After the pattern was digital designed (Figure 2.21 (a)) the shadow mask was prepared with the necessary RPT according to the applications specifications (Figure 2.21 (b)). Once the mask is fabricated it is placed in the printed with the selected substrate. Then the ink is placed on the peristaltic pump and the rate conditions are set. After stablishing the working conditions of the ultrasonics nozzle according to the application requirements, and after verifying that the deposition by SC is optimal, it is possible to proceed to the deposition of the functional material through the printing process (Figure 2.21 (c)) to obtain the desired printed pattern (Figure 2.21 (d)).

As with the SP, the printing process in SC can be simplified in two main steps: the ink deposition onto de printing substrate and the material post-processing. In SP, the ink deposition step observed Figure 2.21 (c.1), the printed material is deposited to the substrate through the shadowing mask with the ultrasonic nozzle. In this step, the user needs to define different important printing parameters to deposit a homogeneous material layer, such as the distance between nozzle and substrate, the spray duration, the temperature of the heating table or the flow of the peristaltic pump. These parameters will be related to the application requirements. After the functional printable material is deposited, the second step is to provide them with its own properties and functionalities removing all the external materials that make the ink suitable for PE such as surfactants, dispersants, humectants, adhesion enhancers, etc. (Figure 2.21 (c.2)). This process is done in two steps; the drying, which is mainly used to evaporate the solvent and is done while the deposition process is made thanks to the heating table where the substrate is deposited, and the sintering/curing, where the dried structure achieves its functionality. Depending on the material characteristics this process will be performed with temperature or UV, plasma treatment, photonic or microwave.
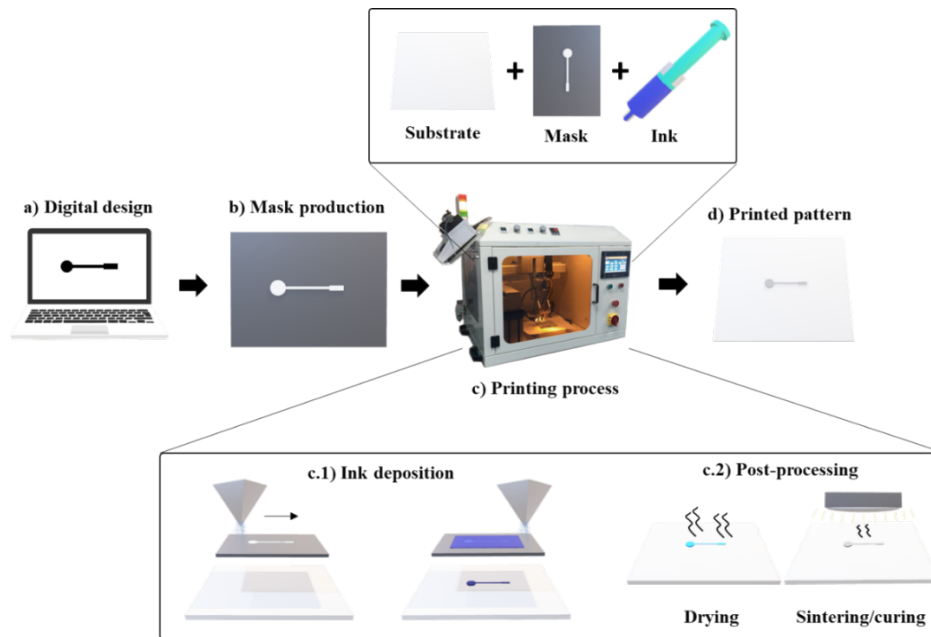
Figure 2.21 | Simplified image of the basis of a SC complete printing process starting with a) the digital design, b) the mask production c) the printing process which implies c.1) the ink deposition through the mask and c.2) the post-processing of the material, until c) the final printed device.

2.5. Inkjet printing technology

Like the previously explained printing techniques, IJP it is mainly established in graphic and art application, however, owing to the high resolution that is capable to achieve is winning a lot of interest in PE. It is a digital and noncontact printing technique that allows the direct patterning of large substrate areas without the needed of a physical mask, owing to the precise control of picolitre volumes of material in form of ink.

The main advantage of IJP remains in its digital patterning, reducing the manufacturing cost and allowing a fast change in the printing design without a need for a new set of masks, which enables a more flexible processing flow and an easy superposition of printed layers. It is a suitable technology for a wide range of production scales, with a lower initial investment than the others printing techniques.

The main drawback of IJP is the narrow properties that inks for inkjet needs to feed since a very specific rheological requirements are allowed, such as viscosity or surface tension, obtaining more restrictions in materials than the other printing techniques, and commercial functional inks are

scarce, expensive, and have very limited shelf-life. So, more investigation into inks development is required.

2.5.1. Inkjet printing technique

IJP techniques can be broadly classified into two categories based on their droplet generation mechanism: continuous inkjet (CIJ) and drop-on-demand IJP (DOD). DOD technique is in turn classified into three types since it can be modulated by thermal, piezo, or electrostatic regulators. **CIJ** was the first existing IJP technology (Figure 2.22 (a)). A constant flow of selectively charged droplets is generated according to the image and the electronic pattern. The ones that are charged are deflected by an EF, and the uncharged flow onto the substrate. So, only a fraction of the droplets is adhered. Is mainly used for very low-cost systems where no need for resolution is needed. For CIJ we can consider the arrangement of single-jet nozzles to obtain a multiple-jet, where each jet is associated with its charging electrode.[115]

DOD is the evolution of CIJ, being the predominant mechanism for IJP technology. A single drop is ejected by the cartridge nozzle when required by the image. DOD IJP can be classified into three types according to the drop formation; **thermal**, when is generated by vaporization of the liquid in the ink chamber (Figure 2.22 (b)), **piezoelectric**, when is generated by a mechanical deformation produced by piezoelectric material under a controlled EF (Figure 2.22 (c)), or **electrostatic**, when an electrostatic force generated by an EF between the ink and the substrate, pushes the drop through the nozzle (Figure 2.22 (d)).[57]

- **Thermal**: This method is still used in a large proportion of home and office inkjet printers. A small resistive heater is in contact with the ink cavity, and a rapid heating up to 400 ˚C (within few micro-seconds) causes vaporization of a thin ink layer near the heater, creating a bubble that rapidly expands generating a fluid movement. When the drop is ejected the heater then cools down and a vacuum is produced that refills de ink chamber with fresh ink for a new ejection.[115] One advantage of this technique is the facility of the heater integration since the resistive tracks can be fabricated with a large number of manufacturing techniques. On the other hand, the main disadvantage of thermal jets is that nozzles typically suffer from a short lifetime owing to the residue generated on the resistive heater; also, this technique requires special ink that supports the high temperature needed for the bubble generation, therefore is not suitable for the functional materials. Thermal jets also have a limitation work for the generate drops owing to the cooling step needed after the generation.
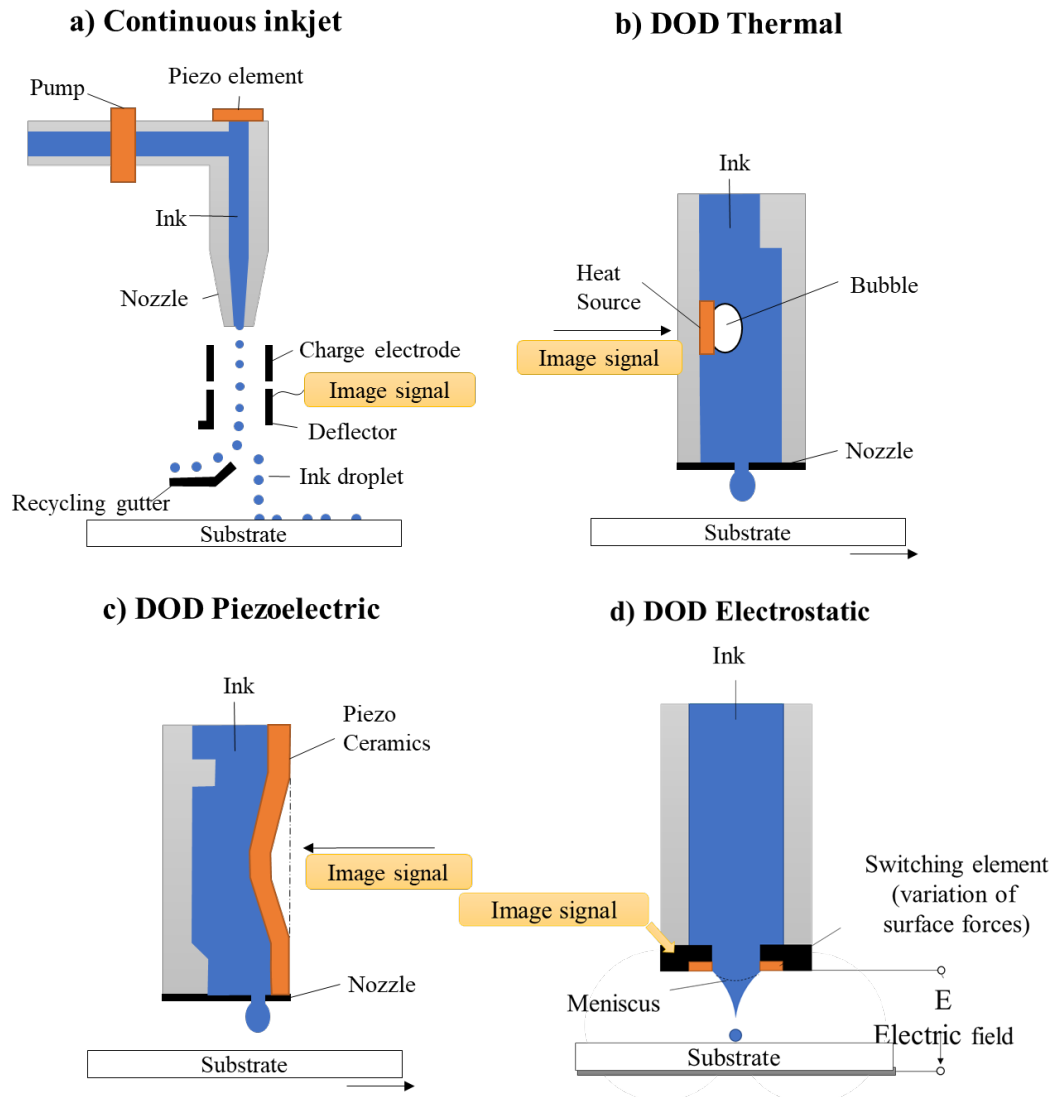
Figure 2.22 Schematic representation a) Continuous IJP, drop-on-demand b) thermal, c) piezoelectric and d) electrostatic IJP systems. Reproduced with permission from [57].

- **Piezoelectric**: It is the predominant method for industrial application. A piezoelectric piece of lead zirconate titanate (PZT) is placed in the ink chamber. When a voltage pulse is applied to the PZT plate it causes a deflection, creating an acoustic wave that propagates inside the chamber and ejects the droplet. Unlike thermal actuators, piezoelectric DoD allows a low-pressure pulsed by negative deflecting increasing the exit-channel volume. This property is used to improve ejection performance and drop shape and allows the use of inks with low viscosity and low surface tension. Due to the quick response of the piezoelectric actuator, this technology is faster than the thermal, one since it needs a cooling time of the heater after the ejection. This fast actuation of the piezoelectric plate also increases its resolution, since in IJP is defined by the drop ejection

volume. The 1 pL generated drop creates spots around 15 μL or higher in diameter on the substrate, highly depending on the contact angle, flying time and surface tension, among other conditions of the substrate and ink. To increase the printing surface and reduce the printing time, industrial inkjet printheads utilize hundreds to thousands of nozzles via parallelization.

2.5.1.1. Piezoelectric Drop-on-Demand working principle

In this thesis work the printer used is based on a PZT piezoelectric system. The deflection of the PZT is controlled by a voltage pulse called waveform. The waveform is responsible for the ink jetting performance. A typical waveform is composed of four segments as shown in Figure 2.23. Each segment has three main properties: duration (time), level, and slew rate.

The 100% of the applied voltage relates directly to the volume of the pumping chamber. The level value in phase **Start** (Figure 2.23 (a)) and **Phase 1** (Figure 2.23 (b)) have the most impact on the jetting process. Changing the duration of phase **Start** and slew rate and/or duration of phase 1 has a strong influence on drop formation. Faster changes in voltage modify the volume faster, and bigger amplitudes in voltage level cause bigger volume changes. And the slew rate determines how fast the volume changes. Published works demonstrate a clear dependence between waveform characteristics and drop formation process and ejection.[116]–[118]

Short rise and fall times are needed to have jet formation. More in detail, the **Start** phase brings the piezoelectric to a relaxed position with the chamber at its maximum volume capacity (**Phase 1**). Immediately a decreased voltage is applied to retract the piezoelectric drawing fluid into the pumping chamber and followed by a settling time (**Phase 2**, Figure 2.23 (c)). In this phase, the fluid is pulled into the chamber through the inlet and two in-phase acoustic waves are created at both ends of the chamber traveling in opposite directions. The end of this phase needs to be aligned with the beginning of the next one to expand the piezoelectric precisely when the two waves meet at the center of the pumping chamber to push out a droplet with its maximum energy (**Phase 3**).[116] During the last phase (**Phase 4**, Figure 2.23 (d)), the piezoelectric retracts slightly breaking the droplet from the chamber and the voltage returns to the standby state. However, waveform generation and drop ejection are highly dependent on the functional ink properties, such as viscosity and surface tension.[117]
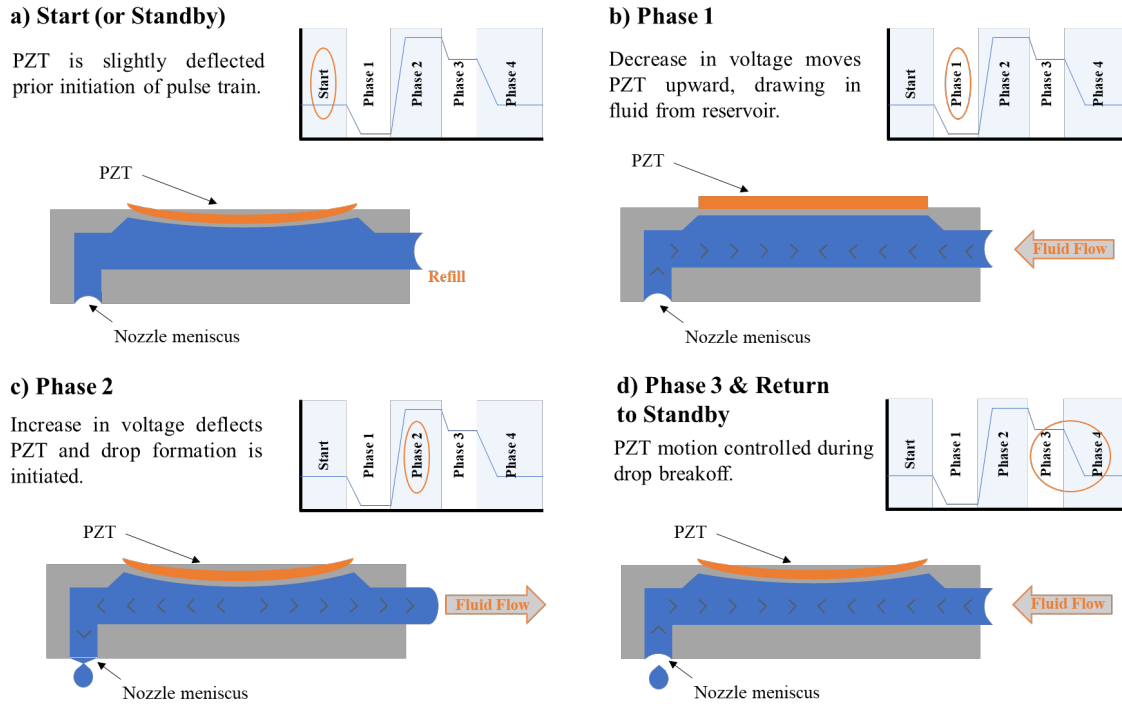
a) Start (or Standby)

PZT is slightly deflected prior initiation of pulse train.

PZT

Refill

Nozzle meniscus

b) Phase 1

Decrease in voltage moves PZT upward, drawing in fluid from reservoir.

PZT

Fluid Flow

Nozzle meniscus

c) Phase 2

Increase in voltage deflects PZT and drop formation is initiated.

PZT

Fluid Flow

Nozzle meniscus

d) Phase 3 & Return to Standby

PZT motion controlled during drop breakoff.

PZT

Fluid Flow

Nozzle meniscus

Figure 2.23 | Schematic representation of the waveform steps for a drop ejection with controlling piezoelectric deflection, a) Start, b) Phase 1, c) Phase 2, d) Phase 3 & return. Source from. Source [119].

2.5.1.2.   Printer and inks for inkjet printing

For this thesis work the printer used was the piezoelectric Dimatix DMP-2831 shown in Figure 2.24 (a). This is a versatile desktop IJP system mainly used in the research area and the use of ink jetting technology for new manufacturing and analytical processes. It is designed to be convenient and easy to use to carry out "proof of concept" and development work using inkjet technology. It have extensive capabilities to allow increased experimental sophistication to optimize process parameters for the user's applications as the user gains familiarity with the system, allowing the deposition of materials on substrates up to A4 size.[119]

Print patterns can be created using the editor program provided or derived from images to create complex structures. The substrate platen can be heated up to 60 ˚C. The use of substrate heating can be used to slightly enhance the drop drying to improve the film formation. It also incorporates two cameras; a drop watcher system, that has the capability to characterize the ejected materials, examining the drop formation and progression from each of the nozzles; and a fiducial camera placed on the print carrier. This fiducial camera allows the inspection and alignment of the printed layer across all the printable substrate areas. The movable carrier also incorporates a swivel holder where the ink cartridge is placed (Figure 2.24 (b)).
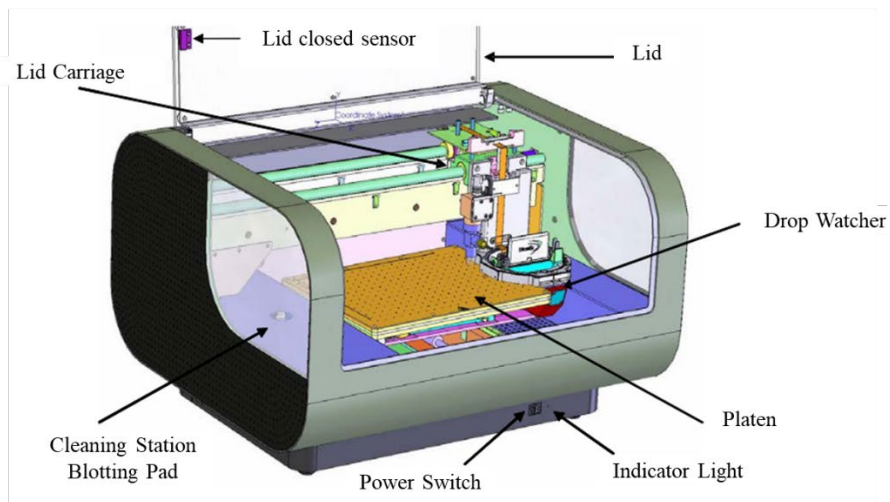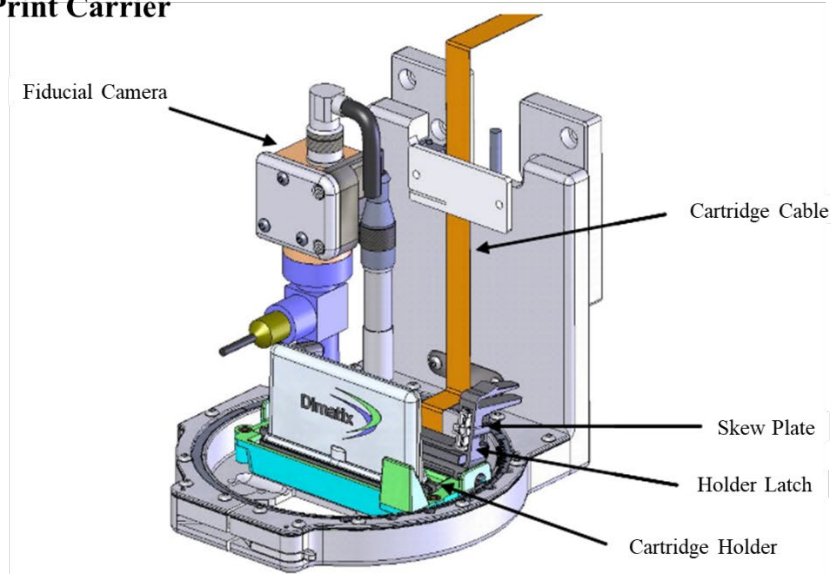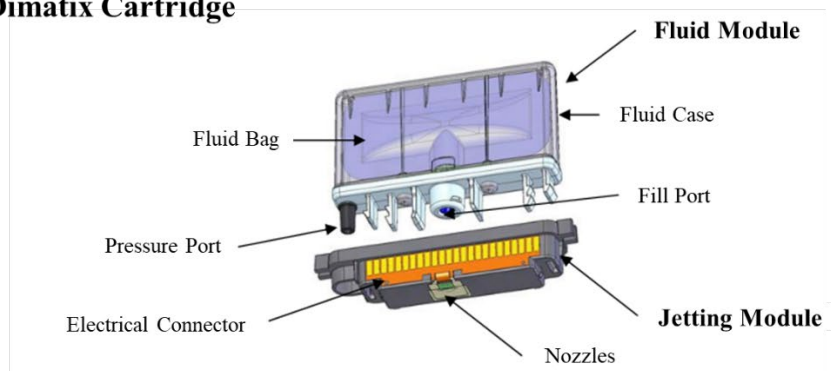
Figure 2.24 Schematic representation of the a) Dimatix DMP-2831 inkjet printer, b) the print carrier and c) the printhead and cartridge. Source [119].

The piezoelectric cartridges used with this printer are composed of two principal parts: the jetting and the fluid modules (Figure 2.24 (c)). The jetting module is composed of 16 printing nozzles, with 254 μm spacing, for the ink deposition, which mainly can deliver a volume drop of 10 pL, and their electronic control. Small nozzle printheads up to 1 pL nozzles are also available. These smaller printheads allow the increasing of the printing resolution owing to the small drop volume; however, the small nozzle makes difficult the printing of nanoparticle-based inks due to the high evaporation rate at the meniscus, causing frequent clogging of the nozzles. The fluid module is the part of the cartridge where the ink is placed and stored. This module is capable to be user-filled with up to 1.5 mL of the desired functional ink.

In the Dimatix system, a drop velocity of 6-10 m·s^{-1} is desired; therefore, inks with viscosity below 15 cP and surface tension of 28-33 dyn·cm^{-1} are recommended to obtain stable jetting. More information of the Dimatix printer is available in [119].

Owing to the complex nature of inkjet inks, their design and preparation are often very sophisticated. It is therefore that inks have many different properties that can influence the jetting process and drop formation.[115] These properties are mainly depending on operating conditions and the nature of fluid molecules. The most dominating ones are the surface tension and the viscosity. The surface tension should be an intermediate lower that water's surface tension value of 72.8 mN·m^{-1} meanwhile the viscosity must be below 20 mPa·s.[120] The study of new inks for IJP plays an important role, the reason why a huge effort has been done in this field. However, and as explained, the design and preparation of these inks are not often very simple, as it is mentioned above inks must have physiochemical properties that allow an appropriate printing process:

- **Surface Tension**: reflects the fact that atoms or molecules at a free surface have higher energy than those in the bulk. When a liquid is deposited, the shape it acquires depends on the relative strengths of the adhesive and attractive forces between molecules. As previously explained in Figure 2.10, if the surface tension of the substrate dominates, the ink will tend to lift, producing a bad adhesion. However, if the surface tension of the ink dominates the ink will be pulled onto the substrate obtaining good wettability.[121]

- **Viscosity**: is the measure of the resistance of a liquid to a gradual deformation by shear stress or flow. Depends on the attractive force between molecules and the momentum interchange between molecules in adjacent layers of fluid as they move relative from one to another.[122] This molecular interaction dominates the viscosity, directly depending on the temperature. As the temperature increases, molecules in a liquid become more

energetic and separated. Thus, the cohesive force decreases, and so does viscosity.[121], [123] Piezoelectric printheads usually function at ink viscosity in the range of 8–15 cP,[124] while thermal printheads require viscosities below 2 cP. Proper selection of the ink vehicle is also very important. Such selection can be affected tremendously not only by the requirements regarding the quality of the printed pattern on a specific substrate but also by the final application and the printing environment.

To obtain a proper jettability of the functional material, the generated droplet needs to be thin and break up after leaving the nozzle. An illustration of this droplet formation can be observed in Figure 2.25. This thinning, which is driven by surface tension forces, is balanced by viscous and inertial forces. For Newtonian liquids with a sufficiently high viscosity, the surface tension that induces jet squeezing is opposed by the viscous stresses within the filament. On the other hand, for liquids of low viscosity, the inertia of the accelerating fluid within the jet is the one opposing the thinning of the jet.[121]
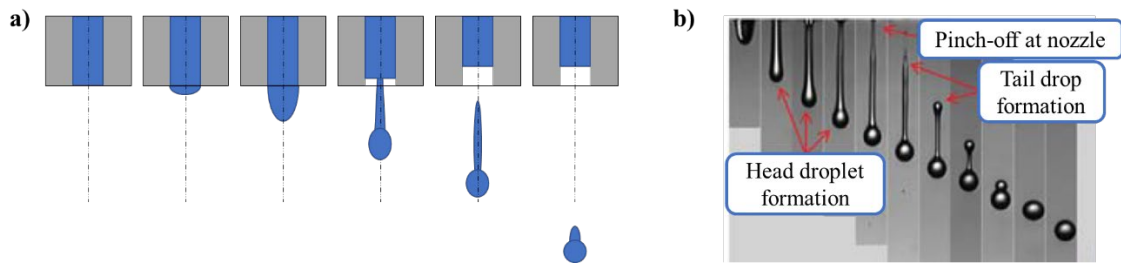
Figure 2.25 a) Schematic procedure showing the drop formation and b) sequence of photographs showing the drop formation procedure. Source [125].

Before the obtention of IJP, Wolfgang von Ohnesorge introduced a dimensionless grouping of numbers to understand and define different regimes found for jet breaking after it leaves the nozzle [126] using the Weber number (We) and Reynolds number (Re). The Ohnesorge number (Oh) (Equation 2.1) eliminates the speed of the drop and therefore only depends on the intrinsic physical properties of the fluid and the dimensions of the ejecting nozzle (which usually is similar to the drop diameter):

$$Oh = \frac{\sqrt{We}}{Re} = \frac{\eta}{\sqrt{\gamma \rho \alpha}}$$

Equation 2.1

Where η is the viscosity, γ the surface tension, ρ the density of the fluid and α the diameter of the nozzle orifice. A stable drop ejection typically takes place between 0.1 and Oh numbers. This set

of limits for Oh, We and Re dimensionless numbers allows us to limit the properties of the printable fluids using IJP as illustrated in Figure 2.26.
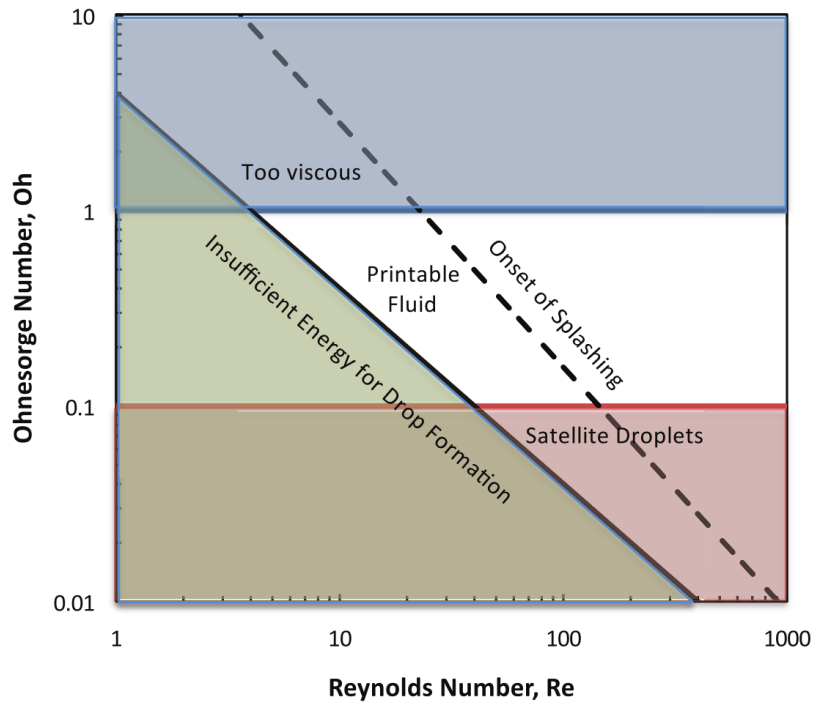
Figure 2.26 | Parameter space of inkjet printable fluids. Source [126].

The science of the IJP is far more than drop formation; their impact and deposition on the substrate and their evaporation/curing are key points in industry to manufacture inkjet print heads and printing machines. As explained, factors such as ink rheology, substrate properties, patter geometries or interface interaction can influence the final structure.
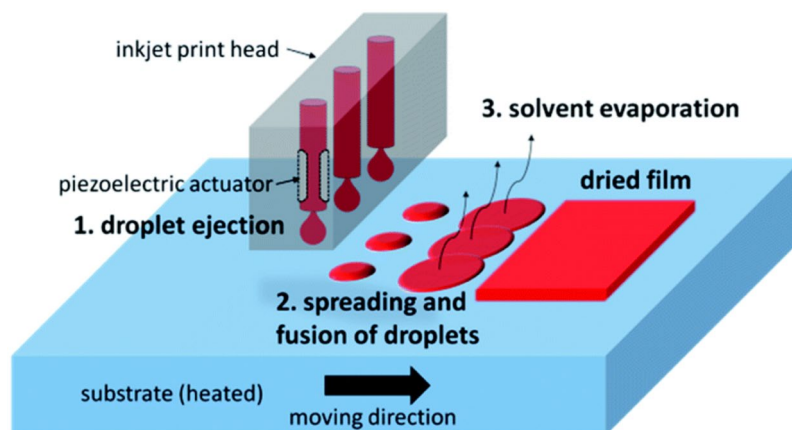
Figure 2.27 | Inkjet printing processes: (1) drop ejection, (2) spreading and fusion of droplets and (3) solvent evaporation. Source [127].

Briefly, the working principle of a drop deposition consist of three steps: 1. Droplet formation, 2. Positioning, spreading and ink coalescence on a substrate and 3. Solvent evaporation and curing.[127] An image of this printing process is illustrated in Figure 2.27.

After leaving the nozzle, the droplet flies until it contacts with the target substrate. The spreading of the drop when reaches the substrate and its underlying mechanism after impact can be again understood by performing non-dimensional analysis using We, Re and Oh numbers, being the inertial and capillary forces the dominant in this interaction.[126] A typical value of a drop diameter a impacting with the substrate is about tens of micrometers, therefore the gravitational effects can be neglected, no expecting a splashing of the ink. This drop interaction can be divided in two steps, depending on the predominant forces. First the drop spreads just after the impact with the surface being this behavior controlled with the inertial forces and the kinetic energy of the drop is transformed into surface energy spreading into de substrate. Second and last, the spread drop suffers a retraction owing the surface tension, followed by drop oscillations in which the energy is dissipated by the viscous forces, wining importance the capillary forces until the deposited drop reaches the stationary shape. Therefore, the size printed drop, and therefore the resolution of IJP, is a combination of the size of the ejected drop in equilibrium with the contact angle of the ink with the substrate.

After the ink deposition a drying phase occurs, in which the solvent contained in the droplet evaporates and a solid layer with the functional material remains on the substrate. Depending on the conditions of the ink drying, different effects can be observed in the material deposition. The main, and the most important one is the coffee ting effect. This effect was first explained by Deegan et al. in 1997 [128], where owing to a fast evaporation of the solvent at the outer edges of the deposited drop, an outward convective flow is produced to replenish this loss of solvent resulting in the accumulation of functional material at the edges, as observed in Figure 2.28 (a). This effect can be reduced by different methods, such as changing the substrate temperature[129] or with the incorporation of a co-solvent with a higher boiling point and a lower surface tension.[130] The solution through this principle is schematically illustrated in Figure 2.28 (b). Due to the higher evaporation at the edges, the solvent composition becomes mainly the solvent with high boiling point. As a result, the solvent at the edges has a lower surface tension than in the center, resulting in a surface tension gradient appearing the Marangoni flow that carries out the material inward to the center. This Marangoni effect can be summarized as the mass transfer along an interface between to fluids due to a gradient of the surface tension.[131]
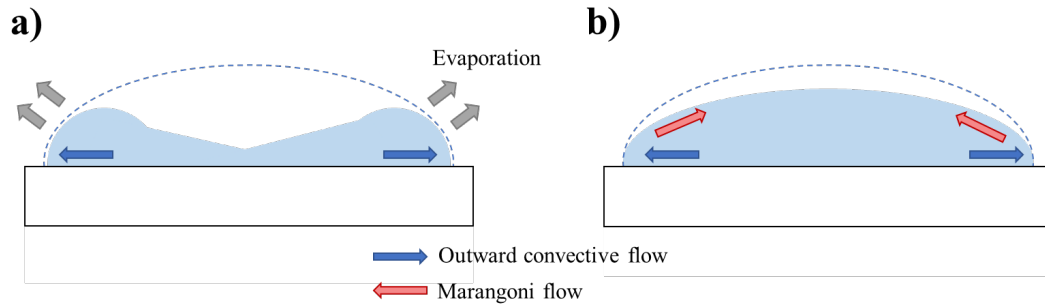
Figure 2.28 | Drop drying process after ink deposition with inkjet printing: a) Coffee ring formation and b) coffee ring suppressed by Marangoni flow.

Aside of isolated drops, PE is mainly based on functional devices with continuous printed tracks or areas, therefore individual droplets must be overlapped, and the resultant features should be stable to maintain their shape and functionality. The distance between two consecutive printed drops is the one called drop spacing (DS), and it has to be optimized for each ink and substrate combination owing to their surface interaction. As elucidated in Figure 2.29, when varying this distance between drops, their interaction also variates. For large distances between drops, where they do not interact, an individual printed pattern it is observed (Figure 2.29 (a)). As the distance becomes smaller the drops collide forming a line with a rounded contour (Figure 2.29 (b)). If DS is even more decreased a parallel side edge appears, and a perfect straight line is observed (Figure 2.29 (c)). This DS is the one that better fits with this ink and substrate combination and the one we must achieve every time we make a new combination. If the DS is further decreased, a wide line can occur, however this increase of ink makes the line more unstable, and some regions can outflow the line and uniformities through the line can appear (Figure 2.29 (d)).
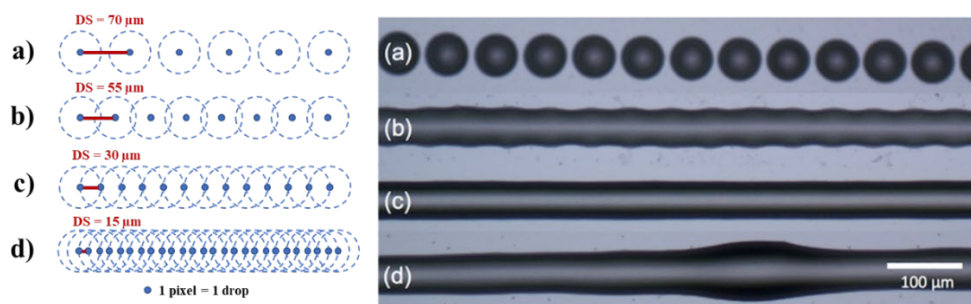

Figure 2.29 | Droplets deposited along a line with different drop spacing, showing different behaviors: a) isolated dots, b) line with rounded contour, c) line with straight contour and b) line bulging. Source [46], [125].

2.5.2. Inkjet printing process

The different types of IJP technologies mentioned earlier have the same working principle and similar requirements concerning substrate and inks. These requirements are addressed in this section. Figure 2.30 shows a general schematic of the IJP procedure to print a desired pattern and a schematic approach to carry out the printing procedure is illustrated in Figure 2.31.

As mentioned with the previous printing techniques, a key and basic step when printing functional materials is the cleaning of the working area. For IJP this step is even more important, owing to the deposited small volume, where a little impurity can lead to a big damage in the final printed design. Then, it is need to perform the surface and structural pre-treatments of the printed substrate, as explained in the previous sections, to ensure that the shrinking of the substrate does not affect the printing process. After the pattern is digitally designed (Figure 2.30 (a)) the printer is equipped with the selected materials (Figure 2.30 (b)). It is choose the desired ink that is going to use for the printing procedure; from the same material, different ink with different viscosities, binders and solid contents can be found, therefore it is necessary to choose the one that better fits with the printing substrate and design to obtain the best resolution. After choosing the desired materials the preparation of the ink must be done. This step includes their cooling down to room temperature if it is stored in cold, the mixing of their components to homogenize the solution composition and the filling of the printing cartridge. Afterward, the cartridge is placed in the printer with the selected substrate. The selected printing temperature is loaded together with the waveform composition. With the fiducial camera, the orientation of the substrate can be corrected, and the starting place to deposit the printing design is selected. When the printer conditions are ready, the drop ejection conditions are checked, and optimized if needed, in the drop-watching camera.

After adjusting all the parameters of the printer according to the design and the ink used and making sure that the ejected drop is stable, it can be proceeded to print the number of layers needed. Sometimes is needed an automatic cleaning of the printing cartridge to stabilize the printing procedure and avoid the nozzles clogging. Then, the printed layer is placed in an oven and the ink is cured at the required temperature and time. Finally, it is proceed to clean the cartridge nozzles using the solvent recommended by the manufacturer, making sure that no ink is left to dry and could clog them.
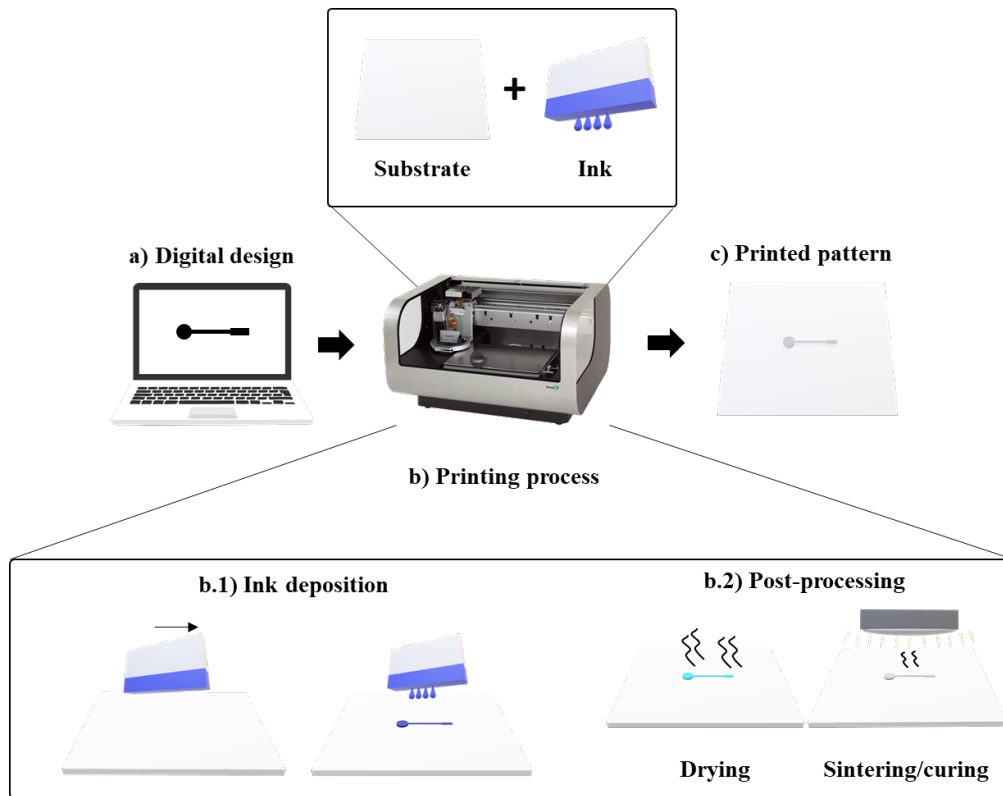
Figure 2.30 | Simplified image of the basis of an IJP complete printing process starting with a) the digital design, b) the printing process which implies b.1) the ink deposition, b.2) the post-processing of the material, until c) the final printed device.

Like in the other printing techniques, the printing process can be simplified in the two main steps previously explained: the ink deposition onto de printing substrate and the material post-processing. In IJP, the ink deposition step is observed in Figure 2.30 (b.1), the printed material is deposited with the DOD by means of a digital pattern. In this step, the user needs to define different important printing parameters to deposit a homogeneous material layer, such as the waveform applied, the working frequency or the DS. The second step is the post-processing of the printed material (Figure 2.30 (b.2)), and like in the other printing techniques, the curing of the material to give their properties with temperature or UV, plasma treatment, photonic or microwave is performed after the evaporation of the solvent to obtain the desired printed pattern (Figure 2.30 (c)).

As previously mentioned, every printed material should be recognizable; therefore, it is important to keep the information management of the entire process with all the conditions related to the manufacturing process, such as the used waveform with the applied voltages that could be useful afterward.

Figure 2.31 | Roadmap of the different steps for the IJP procedure.

3. Fully Printed Piezoelectric Devices

The main purpose of this chapter is to study and characterize the performance of printed piezoelectric devices. The chapter starts with a brief introduction to the history of the piezoelectric effect followed by an introduction to the macroscopic and microscopic effects which explain the piezoelectricity. Later on, a Progress Report explaining the characteristics of printing piezoelectric materials and their deposition techniques it is included, summarizing the most important works with the different available configurations. With the results of this study, two printed piezoelectric devices were studied following different approaches. The first one includes their fabrication through different printing techniques to obtain the best electrical and morphological characteristics as well as to evaluate their performance as sensors actuators and energy harvesters. The second approach deals with the integration of these devices in a stretchable substrate for their implementation in wearable applications, validated with the monitoring of different body movements and including the study of a sensor matrix as e-skin.

3.1.   Overview of piezoelectric devices

The increase of materials technology has led to a big impact on the evolution of human civilization, being the base to the rinse of wearables technology that improve our quality or life. Nowadays, our society is identified by synthetic and lightweight engineering materials with tailor enhanced performance over traditional materials. However, their responses are only better when optimized to fulfill the range of scenarios where the material is exposed.[132]

With the advancement of manufacturing technologies that can process different materials, 21st century witnessed the emergence of smart materials.[132] The essential idea of these materials is to produce non-biological systems that will achieve the optimum functionality observed in biological systems through the emulation of their adaptive capabilities and integrated design. By definition, smart materials consist of systems with sensors and actuators that are either embedded in or attached to the system to form an integral part of it and have the intrinsic and extrinsic capabilities, first, to respond to stimuli and environmental changes and, second, to activate their functions according to these changes.[133] This system mechanism is schematically illustrated in Figure 3.1. Piezoelectric materials emerge as one of the most promising materials for environmental monitoring (EM), being able to interact with the environment.
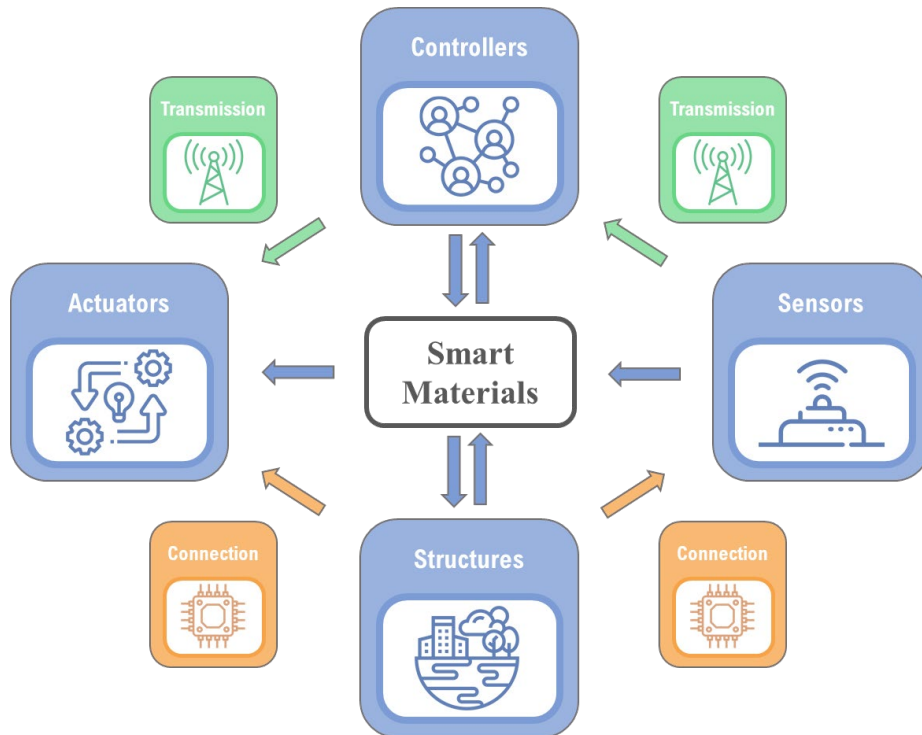

Figure 3.1 | Schematic mechanism procedure for the smart materials. Source [134].

3.1.1. Piezoelectric effect

As described in Section 2.1.2.1, piezoelectric materials are those that are mainly dominated by the piezoelectric effect. This effect is produced when the charge balance within the crystal lattice of those materials is disturbed by some external stimuli or *stress*. When there is no *stress* applied to the material, the positive and negative charges are equally distributed with a potential equilibration along the material. When a strain is applied to the material, for instance, by the human interaction of by an external agent from the environment such as wind, water or soil, its internal distribution changes, leading to the appearance of charge generation owing to a potential difference between the electrodes (Figure 3.2). This stress can be applied from different directions to the material, leading to a change in the intensity of the measured signal, depending on the piezoelectric coefficient matrix. When this stress is released, the dipoles come back to the initial position, leading to a generation of an electric signal of the opposite sign than the first one.

a) No stress   **b) z-stress**   **c) x/y-stress**
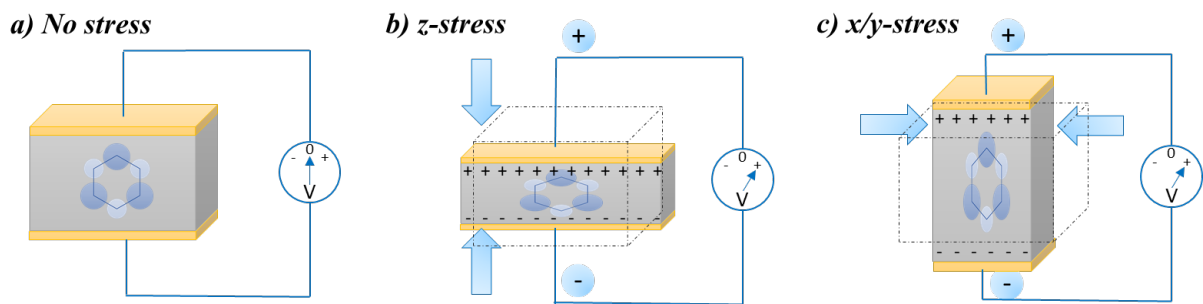
| **Figure 3.2** | Schematic representation of the direct piezoelectric effect in a sandwich structure with the top and bottom electrodes when a) no stress is applied, b) the stress is applied in the z-direction and c) the stress is applied in the x/y direction. |

This electrical impulse can be processed as a signal or can be used as an electrical generation source. This use of piezoelectric materials as sensors is one of the different sections of the chemical sensors available for EM, being differentiated and fitted in the group by the transduction mechanism as mass sensors.

Also, an enormous advantage of these materials is that the piezoelectric effect can be used with the inverse mode; when an external electric field (EF) is applied it causes a realignment of the internal charges of the piezoelectric material and a mechanical deformation is produced proportional to the intensity of this field (Figure 3.3). If the applied EF is in only one direction using a direct current, the material will expand in the direction of the field, however, if the EF is

applied through an alternate current, the charges continuously change their direction, causing the piezoelectric material to deform in different directions of the same axis.
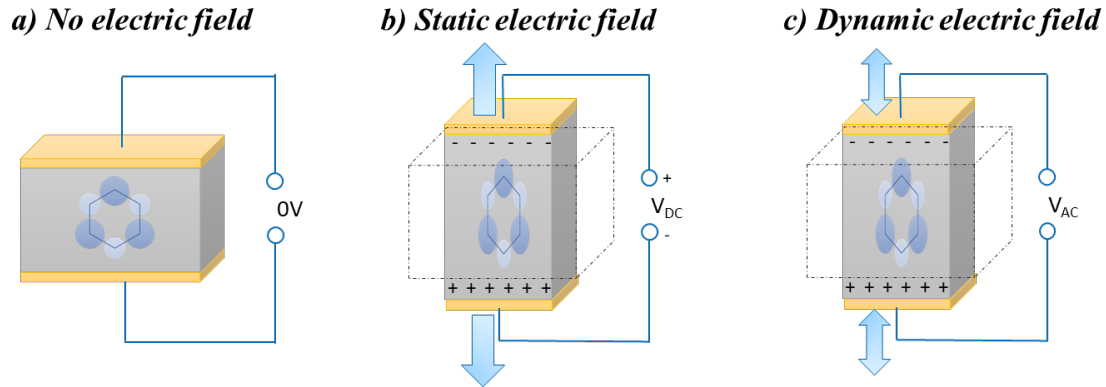
a) No electric field　　　　**b) Static electric field**　　　　**c) Dynamic electric field**

Figure 3.3 | Schematic representation of the inverse piezoelectric effect in a sandwich structure when a) no EF is applied, b) the EF is applied in direct current c) the EF is applied in alternate current.

Therefore, thanks to the duality property of the piezoelectric effect to generate electrical signals or mechanical movements, piezoelectric device performances can be divided into three groups: **sensors**, **actuators** and **generators**.

Sensors and generators belong to the group of devices that use the direct piezoelectric effect, either only reading the generated electrical signal, as in the case of sensors, or using this signal to power any electrical elements such as capacitors or other sensors in the case of generators. Actuators, nevertheless, are based on the inverse piezoelectric effect. Thanks to an external EF, they can generate a movement, being very used in motors, buzzers or speakers applications.[132], [135], [136]

The property of piezoelectricity was first discovered by Pierre and Jacques Curie in 1880 while studying the mechanical properties of quartz. When it was subjected to a mechanical change, the material shows positive and negative charges across the surface, being these proportional to the applied pressure and disappearing when the pressure ceases.[137] After this achievement, with the help of Lippmann in 1881, they also demonstrate that when an EF was applied to this quartz material, its structure expands, elucidating the concept of the inverse piezoelectric effect.[48]

This piezoelectric effect is an intrinsic property of the piezoelectric material and is provided by its crystalline structure. The origin of this effect is related to an asymmetry in the cell unit and the resultant generation of electric dipoles due to the mechanical dispersion, leading to a net

polarization on the surface. This effect is practically linear and direction-dependent, requiring that the dipoles of the same crystalline region of the material are oriented in the same direction to generate this piezoelectric effect. In some piezoelectric materials the dipoles must be oriented to induce the piezoelectricity in a mechanism called poling.[25], [138], [139] This poling procedure is mainly needed by polycrystalline ferroelectric materials such as lead titanate zirconate (PZT)[138] or polyvinylidene fluoride (PVDF),[140] meanwhile the dipoles of nonferroelectric piezoelectric materials such as aluminum nitride (AlN)[141] cannot be realigned after their deposition, being highly dependent on the crystal orientation.

The entire poling procedure is performed by applying a high EF in combination with an elevated temperature, to aligning (at the nanoscale) all the dipoles with the EF, which is what is eventually recognized as piezoelectricity. Figure 3.4 elucidates the poling mechanism for a piezoelectric material. In the first stage, the dipoles are randomly oriented across the structure. When an EF is applied between the electrodes, with the help of temperature, the dipoles align themselves in the field direction. By heating the piezoelectric material above the Curie temperature, the dipole movement will be produced easily, and maintaining the applied EF while cooling the piezoelectric layer the oriented dipoles can keep their position after removing the EF achieving a remaining polarization that gives the piezoelectric activity to the ferroelectric material.
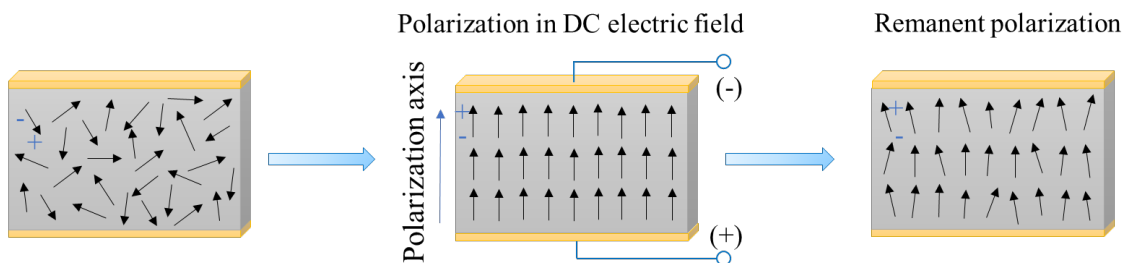
Figure 3.4 | Poling mechanism process of a piezoelectric material.

3.1.2. Dielectric hysteresis curve

Polarization is related to the electric displacement or an electric flux density, but owing to the resistance to domain switching in ferroelectric materials, this polarization maintains a hysteretic behavior, which means that the electric density and the polarization are non-linear functions of the applied EF. More specifically, polarization is a double-valued function of the applied EF, and so it is not precisely reversible with the field. Figure 3.5 shows the relation between polarization and EF for a ferroelectric material. This curve is known as dielectric hysteresis curve.
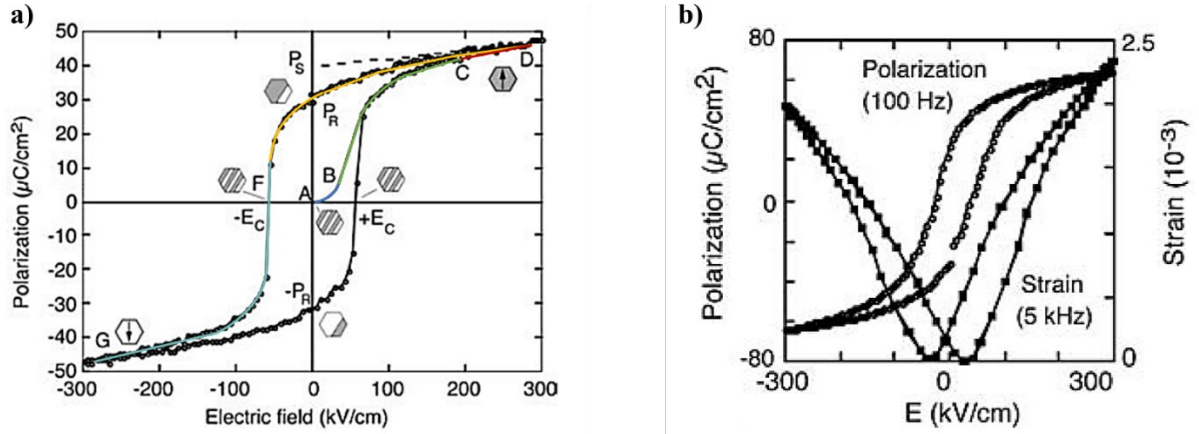
Figure 3.5 a) Ferroelectric polarization hysteresis loop. Hexagon with gray and white regions represents schematically repartition of two polarization states in the material. b) Strain-EF (x-E) hysteresis loop (butterfly loop) in ferroelectrics. Source [142].

An initial unpoled ferroelectric material can be subjected to a different state when increasing the EF at a temperature slightly below its Curie point. The dipoles become increasingly aligned with the field and polarization will follow the curve observed in Figure 3.5 (a). In this curve different segments can be differentiated:

- **AB**: An initial small EF is applied to a ferroelectric material and a linear relationship between polarization and EF is observed owing to the field is not large enough to switch any domain and the material will behave as a normal dielectric material.

- **BC**: The EF increases and the polarization of domains with unfavorable direction of polarization will start to switch along directions that are as close as possible to the direction of the field. The polarization in this region is strongly non-linear.

- **CD**: When all the domains are aligned, the ferroelectric again behaves as a linear dielectric, where the polarization of the material directly increases with the applied EF.

- **DF**: The field strength starts decreasing, some domains will back-switch, but at zero field the polarization is nonzero, obtaining a remanent polarization (P_R). In this segment, the spontaneous polarization (P_S) is located and may be estimated by taking the intercept of the polarization axis with the extrapolated linear segment CD. To reach the zero-polarization state, the field must be reversed, reaching point F. This necessary field to bring polarization to zero is called the coercive field (E_C).

- **FG**: A further increase of the field in the negative direction will cause a new alignment of dipoles and saturation (point G). The field strength is then reduced to zero and reversed to complete the polarization cycle.

It should be mentioned that the coercive field, E_C, that is determined from the intercept of the hysteresis loop with the field axis is not an absolute threshold field;[143] if a low EF is applied over a long period, the polarization will eventually switch. An ideal hysteresis loop is symmetrical, so the positive and negative coercive fields and positive and negative remanent polarizations are equal. The coercive field, spontaneous and remanent polarization, and shape of the loop may be affected by many factors including the thickness of the sample, presence of charged defects, mechanical stresses, preparation conditions, and thermal treatment.

Besides the polarization-EF hysteresis loop, the polarization switching by EF in ferroelectric materials leads to the strain-EF hysteresis as observed in Figure 3.5(b). The strain-EF hysteresis loop, which resembles the shape of a butterfly and is called the butterfly loop, is due to three types of effects. One is the normal converse piezoelectric effect of the lattice, and the other two are due to the switching and movement of domain walls. At zero field the strain of the crystal is taken to be zero. The EF is then applied in the direction of spontaneous polarization. As the field is increased, the crystal expands through the piezoelectric effect. The expansion continues until the maximum field is reached. At this point, the field starts decreasing parallel to P_S. The strain of the sample traces the same line but in the opposite direction. The field then changes its direction, becoming antiparallel to P_S. As the field strength increases in the negative direction, the crystal contracts concerning the initial point. After switching, the polarization becomes parallel to the field, and the strain again becomes positive. During a further increase of the field in the negative direction, strain increases to point F, and then decreases back to the initial point as the field is decreased. Ideally, the strain--field curve is linear, indicating that the strain is purely piezoelectric except at the switching points.[142]

3.1.3. Piezoelectricity

Piezoelectricity is ruled by the piezoelectric coefficients d_{xx} ($pC \cdot N^{-1}$), which correlate the intensity response of the volume charge when a force is applied and vice versa. This value constant is an intrinsic property of the material, where the *xx* values are related to the direction of the dipole orientation and the measured force. As observed in Figure 3.6 (a), when the different forces only have a contribution from one of the axes, this constant gives normal piezoelectricity, however, when more than one axis are involved in the contribution of the forces it is called shear

piezoelectricity. Furthermore, another division depending on the force orientation can be differentiated. When the orientation of the EF (and therefore of the dipoles) is the same that the applied force, we can consider that it is a longitudinal piezoelectric coefficient, while if the EF is in a different direction than the applied force, we obtain a transversal piezoelectric coefficient.[144]
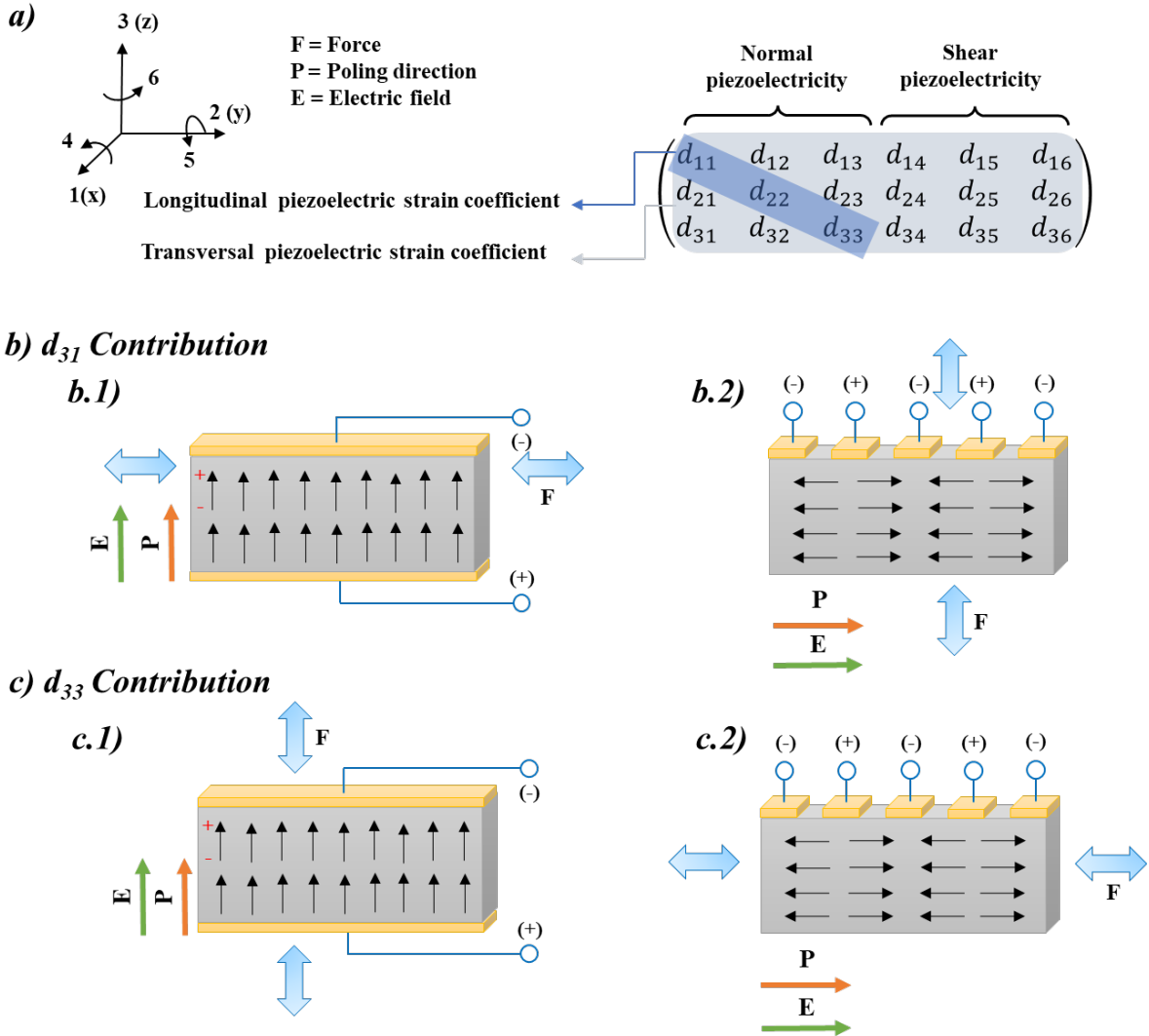
Figure 3.6 a) Definition of the different piezoelectric coefficients depending on the force direction. Schematic design of b) d_{31} contribution with b.1) sandwich electrode structure and b.2) interdigitated electrode structure, and c) d_{31} contribution with c.1) sandwich electrodes structure and c.2) interdigitated electrodes structure.[15]

The most important and singular values for the characterization of piezoelectric materials are the d_{31} and the d_{33}. When the force and the EF are in a perpendicular position it is the d_{31}, and when the vectors are parallel, the used constant is the d_{33}.

The position of the electrodes placed in the piezoelectric layer to achieve, or to proportionate in the case of actuators, plays an important role in the d_{xx} characterization. Depending on the electrode orientation, the scheme of the direction forces involved varies. As shown in Figure 3.6 (b) and Figure 3.6 (c), the applied force to achieve the same contribution changes depending on whether the electrodes are in a sandwich structure or in an interdigitated mode on the same surface of the piezoelectric material. The reason for this effect is that the arrangement of the electrodes will vary the orientation of the internal dipoles in the poling procedure of the piezoelectric material, changing the direction of the EF.

3.1.4. Piezoelectricity limitations

Despite the very stable properties of piezoelectric materials, different parameters limit their application. These aspects are related to electrostriction, depolarization and frequency limitations and those are explained in this section.

Electrostriction
The response of piezoelectric material has a quadratic component that is superposed to the linear behavior and is dependent of an electrostrictive coefficient, which is lower than the piezoelectric constant, but it can be significant when the EF is increased.

Depolarization
After the poling treatment of piezoelectric materials, they will be permanently polarized, however, care must be taken in all subsequent handling to ensure that the material is not depolarized, as this will result in partial or total loss of its piezoelectric properties. Piezoelectric materials may be depolarized in the following ways:

- **Electrical depolarization**: By exposing the material to a strong EF of the opposite polarity of the poling field it will depolarize the material. The field strength required for starting the depolarization depends on the material grade, the time the material is subjected to the depolarization field and the poling temperature.

- **Mechanical depolarization**: By exposing the material to mechanical stress the piezoelectric element becomes high enough to disturb the orientation of the domains and hence destroy the alignment of the dipoles. The limits for mechanical stress vary considerably with material grade.

- **Thermal depolarization**: By exposing the materials to its Curie point, the domains become disordered, and the element becomes completely depolarized. Therefore, the working temperature for a piezoelectric material would normally be between 0 ˚C and their Curie temperature.

Frequency limitations

The fact of being a natural system means that it has an associated natural vibration frequency. When the piezoelectric material is exposed to a periodical impulse (electronics, mechanics or acoustics) with a frequency in the vicinity of the natural frequency, the system will oscillate with very high amplitudes. When this happens to a piezoelectric material, an electrical resonance can be achieved when the material is driven with a mechanical field. Furthermore, high deformations can be produced when the material is electrically driven. Hence, an electrical signal with a frequency very close to the mechanical natural frequency of the system will produce a resonance. This resonant frequency will depend on the characteristics of the piezoelectric material and the mechanical and electrical environmental conditions.

3.2. Piezoelectric devices fabricated with printing technologies

Different types of piezoelectric materials can be found either in nature or processed by humans, however not all of them are suitable to be deposited or fabricated with printed electronics (PE). Using state-of-the-art printing technologies to produce these types of sensors is an exciting concept, given its unique ability to address the issue of low-cost manufacturing. Indeed, PE, of which printed sensors are a subset, is beginning to yield success. The manufacture of sensors using printing techniques is an emerging research and development area.

3.2.1. Paper I: Fully Printed Piezoelectric Devices for Flexible Electronics Applications.

The first paper presented in this Chapter 3, **Paper I**, is a published Progress Report about the use of printing techniques for the fabrication of piezoelectric devices. This Progress Report takes a detailed look at the different printing techniques for PE and more specifically the main ones used for the fabrication of printed electrodes and piezoelectric materials. Furthermore, it explains the current state-of-the-art in piezoelectric devices of the last years, pinpointing the piezoelectric devices that are manufactured through printing techniques.

This article has been reproduced from Advanced Materials Technologies with permission from Wiley*:

Paper I. M. Alique, C. D. Simao, G. Murillo and A. Moya. **Fully Printed Piezoelectric Devices for Flexible Electronics Applications.** Adv. Mater. Technol. 6, (2021), 2001020. doi:10.1002/admt.202001020 (Q1, IF:8.856)

This work has been also presented in different conferences with their corresponding Proceedings:

- Conference **μTAS 2020**: M. Alique, M. Duque, C.D. Simao, P. Lacharmoise, G. Murillo, A. Moya. Fully printed piezoelectric Devices. Poster presentation.

- Conference **JPhD 2020**: M. Alique, A. Moya, G. Murillo, C.D. Simao. Fully printed piezoelectric devices. Oral presentation.

- Conference **LOPEC 2021**: M. Alique, P. Lacharmoise, G. Murillo, A. Moya, C.D. Simao. Advances on fully printed piezoelectric sensors and actuators. Oral presentation.

Note that, equations, tables and figures numbering in the reproduced research article follow the ones of the published version.

Fully printed piezoelectric devices for flexible electronics applications

Marc Alique,[1]† Claudia Delgado Simao[1]*, Gonzalo Murillo[2] and Ana Moya[1]

[1]Eurecat, Centre Tecnològic de Catalunya, Functional Printing and Embedded Devices Unit, 08302 Mataró, Spain.

[2]Instituto de Microelectrónica de Barcelona, IMB-CNM (CSIC), Esfera UAB, Campus Universitat Autònoma de Barcelona, 08193 Bellaterra, Spain.

† Electrical and Telecommunication Engineering Department, Universitat Autònoma de Barcelona (UAB).

Corresponding author

E-mail: claudia.delgado@eurecat.org

Abstract

Recent advances in materials and manufacturing processes pave the way for the establishment of piezoelectric materials via printing techniques as flexible sensors, actuators and generators. Such flexible devices are key building blocks for future advanced robotic skin and conformable medical devices. Herein special focus is given to printed devices for its lightweight, flexibility and manufacturing by high throughput techniques, offering a disruptive advantage in integration technologies and a wide range of opportunities for industrialization routes, where cost-effective applications are required. In this Progress Report, the different system parameters are discussed, pinpointing the ones that affect the production of reliable flexible printed piezoelectric devices and limit this technology to achieve with higher technological maturity. Focus is made on screen and inkjet printing as fabrication techniques and the well-established piezoelectric polymer poly(vinylidene fluoride-co-trifluoroethylene) (PVDF-TrFE). Key limiting factors found for the manufacturing of robust scalable all-printed piezoelectric devices stems mainly from the piezoelectric ink production and processing. Finally, the integration of these materials, via printing technologies, into soft, flexible and even stretchable substrates is analyzed and insights are gathered on the manufacturing trends to achieve low-cost production of flexible piezoelectric devices embedded in electronic skin and smart wearables.

Keywords

piezoelectric materials, printed devices, flexible devices, inkjet printing, screen printing, poling techniques.

3.2.1.1. Introduction

Over the past decades, the fast-growing pace of the printing technology accompanied the emergence of the concept of printed electronics, where electronic circuits or devices may be printed with conventional analog or digital printing techniques.[145], [146] Since its emerging in the mid-20th century, the field of printed electronics has witnessed tremendous progress. New domains in electronic technology related to new materials syntheses,[51] novel devices concepts,[52] new functionalities and new production techniques[50], [147] announce a revolution in microelectronics industry that is usually focusing in silicon and microfabrication techniques.[54]

Printed electronics technology uses an ensemble of additive manufacturing techniques,[50], [147] where stacked layers of functional materials are deposited on a substrate with a certain design or

86

pattern. It is considered relatively simple to implement because it is built over mature technology, which is less time consuming, versatile and customizable, and have less materials waste than typical microfabrication,[54] being suitable to produce cost-effective devices, aiming to niche applications in high-volume market segments where the high performance of conventional electronics is not required. Historically, different types of printing techniques have been employed based on different physic principles, such as lithography or flexography,[56] but the two main groups of techniques that can be differentiated for the development of these systems are with and without the use of a printing mask, also called analog and digital printing, respectively. [57] Each printing technique operates inks and substrates in different manner, limiting the application of one technique or other to the interface relations concerning the materials used and designed pattern structure (thickness and resolution requirements), the physical and chemical properties of the deposited functional inks, and the selected substrate characteristics. The most suitable techniques for almost any application related to the printing electronics field are screen printing (analog) and inkjet (digital) printing. Although screen printing and inkjet printing have different system specifications and requirements, they have both matured in the graphic arts sector before becoming electronic devices manufacturing techniques. Furthermore, their enhanced properties allow the development of customized patterns with complex shapes at low-cost production, making printed electronics very attractive for industrial adoption.[64] Most printed devices target the use of flexible and potentially low-cost substrates to enable large area and/or more rugged products, enabling a higher freedom of design, seamless integration, use of sustainable materials, even recycled or biodegradable,[55] and reduction of metal content in electronic circuits.[148] These characteristics enable the printed materials and devices to be integrated into different soft substrates, like plastics, paper or clothes fabric. Their lightweight character enables them to be placed in locations where conventional sensors or electronics cannot be used due to their rigid characteristics, allowing the creation of innovative designs and applications such as in smart textile,[149], [150] implants onto the human body[151]–[153] or flexible energy devices[154] amongst others.

With the emergence of electronic devices manufactured by printing means, a wide range of conductive, semiconductor and dielectric materials have been developed as inks for the different printed techniques. Electroactive polymers are some of the most promising materials for flexible electronics[22] and amongst them, piezoelectric materials are in the set of accessible printed substances[26] with promising results. The interest of these materials stumbles upon their ability to generate electrical signals as outputs in response to mechanical stress, vibrations or deformations, and vice versa, reversibly. This duality sets the basis for their application in devices such as sensors, actuators or energy harvesters (i.e. direct and indirect piezoelectric effects).[27]–[29] The generated electrical power arises from changes in the internal charge distribution of the

piezoelectric material, produced by random or environmental-driven mechanical movements, e.g. contact from airstreams or liquid flow, or triggered by vicinity vibrations, or also by human motion in their everyday life. Likewise, the application of an external electric field onto a piezoelectric material induces a redistribution of their internal structure, obtaining a controlled mechanical movement. In the case of piezoelectric polymers, their glassy structure creates dispersion of the originated charge upon stimuli, therefore it is required an alignment of the internal charges before it exhibits piezoelectric properties.[155] This treatment is also called *poling* or polarization and is one of the critical parameters in piezoelectric polymers processing. Various reported poling techniques are discussed later in this report, but each one of them has different properties that must be analyzed to choose the right one for every device. There are various piezoelectric materials known nowadays with large d_{33} piezoelectric coefficient, which quantifies the volume change when a piezoelectric material is subject to an electric field, but most of them are bulk inorganic materials with limited printable characteristics, and only polymers and nanoparticles embedded in polymer matrix composite are suitable to be used in printing technologies.[156]

In this Progress Report, an overview about the reported piezoelectric materials apt for printed electronics and the different methodologies followed by the preparation of printed devices are discussed. An initial section provides an analysis of the different printing technologies, focusing on inkjet and screen printing that are the ones more used and useful for printed piezoelectric devices, and the different polarization techniques applied to the materials to induce the piezoelectric characteristics. The content that follows summarizes the main piezoelectric materials with more suitable characteristics in applications (organic, inorganic and composites). The final section discusses different devices focusing on the latest developments, fabricated with the explained printing techniques and materials, to demonstrate the real-life application of the piezoelectric materials as energy harvesters, actuators and sensors.

3.2.1.2. Fabrication methods

3.2.1.2.1. Printing techniques

The capabilities of the piezoelectric materials are promising in the laboratory scale and, to effectively transfer this know-how for mass production and achieve benefits, a promising route is via printed electronics technology. The use of printing techniques for the manufacturing of electronics has several advantages, including the fast and low-cost assemble in large area and flexible substrates. An overview of printing techniques is given in **Figure 1**. Two main printing techniques groups are distinguished, depending if they need a printing mask or not. On one hand,

the ones that require a mask, can be called analogue printing, and include techniques like screen printing,[58] offset,[59] flexography,[60] and gravure.[61] All these techniques share a common feature: the pattern to be printed is embodied in a physical form such as a mask, roll, plate, or screen. This template is transferred during the act of printing through direct or indirect contact with the substrate. Changes in the patterns can only be achieved by changing the master pattern, which involves making physical changes to the template within the printing machine, meaning time consuming and an increase of the device fabrication cost and consequently, of variability to some extent. These master patterns can be produced with different size of the mesh depending on the type of ink used and the weight of their components in order to regulate the size of the printed layer.
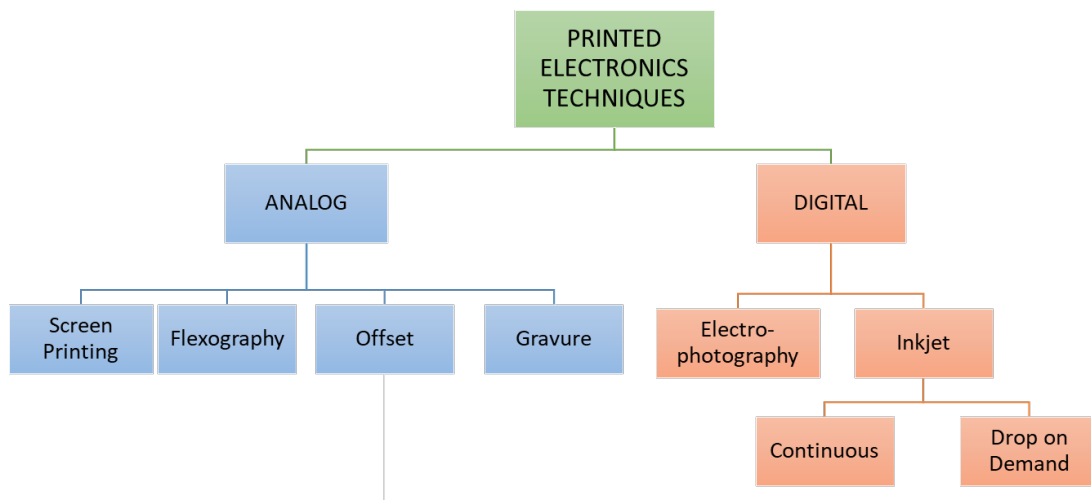

Figure 1. Schematic overview of the different technologies for printing electronics.

In the other hand, there are techniques that do not require a mask, known as digital methods. This term means that the design is controlled by a computer, therefore the printing head is electronically controlled making a translational movement that follows the digital pattern. This results in a contactless selective transfer the ink into the substrate without extra waste, and without force applied onto the substrate or sublayer. The basic premise of digital printing is the accurate positioning of a liquid droplet with small volume directly correlated under digital control with the presence of information at each binary unit of the image to be reproduced. This technique allows the obtaining of thinner layers and a very easy superposition of the deposited ones without masking, being these two the main advantages of the technique. Digital printing has certain drawbacks especially with respect to average throughput when compared to high-end analogue printing technologies. Inkjet printing[62] is the dominant digital technique, but other techniques, like electro-photography,[63] are also used with less reproducibility in industry.

Screen and inkjet printing are the two printing techniques commonly used in printed electronics, and are compatible to process piezoelectric polymers. These two, the most representative of the analog and digital techniques, enable preparing devices composed by different layers in soft and flexible substrates in high throughput. Considering **Figure 2a**, the technique that has been used the longest for the development of the piezoelectric polymers is the screen printing, being first used in the late 20th century. The number of reported publications using inkjet printing is expected to increase in the coming years, thus surpassing those reported using screen printing. Although there is an increasing density of products in the market manufactured using printing techniques, most of printed piezoelectric devices are still under prototype development and basic research. The capability to develop these printed piezoelectric devices (sensors, actuators or energy harvesters) in flexible substrates allows the adhesion in irregular surfaces that conventional devices cannot achieve, thus increasing the number of applications that can be performed. As **Figure 2b** shows, sensors and harvester devices, made with piezoelectric polymers, are currently drawing the most attention in their manufacturing using printing techniques alone.

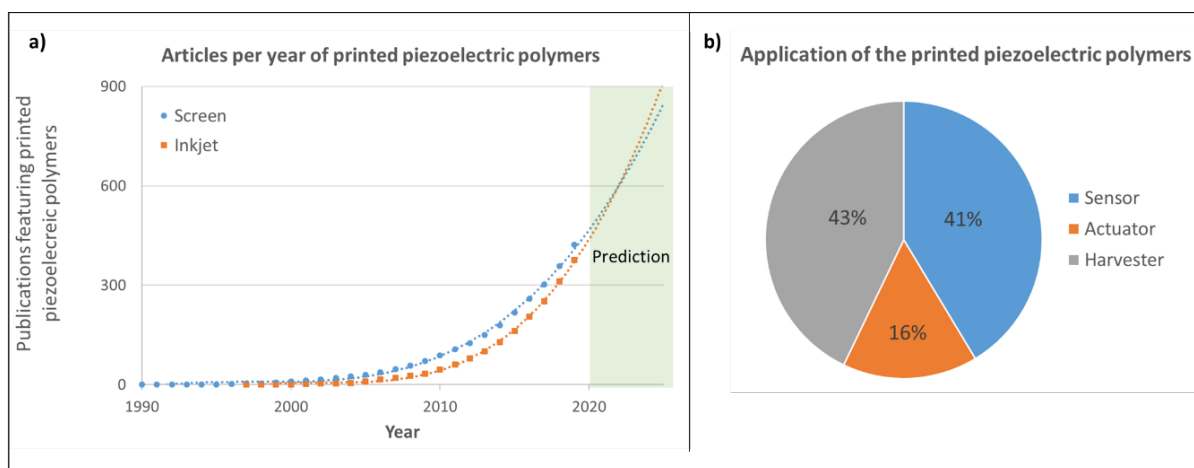**Figure 2.** State of the art of the a) publications about printed piezoelectric polymer devices and b) their applications. Search carried out on April 27, 2020.

Some of the techniques used for printed electronics are schematically summarized in **Figure 3**, where the main parts of their instrumentation are shown. Furthermore, the two main techniques used for printed electronics will be explained more carefully in the section bellow.
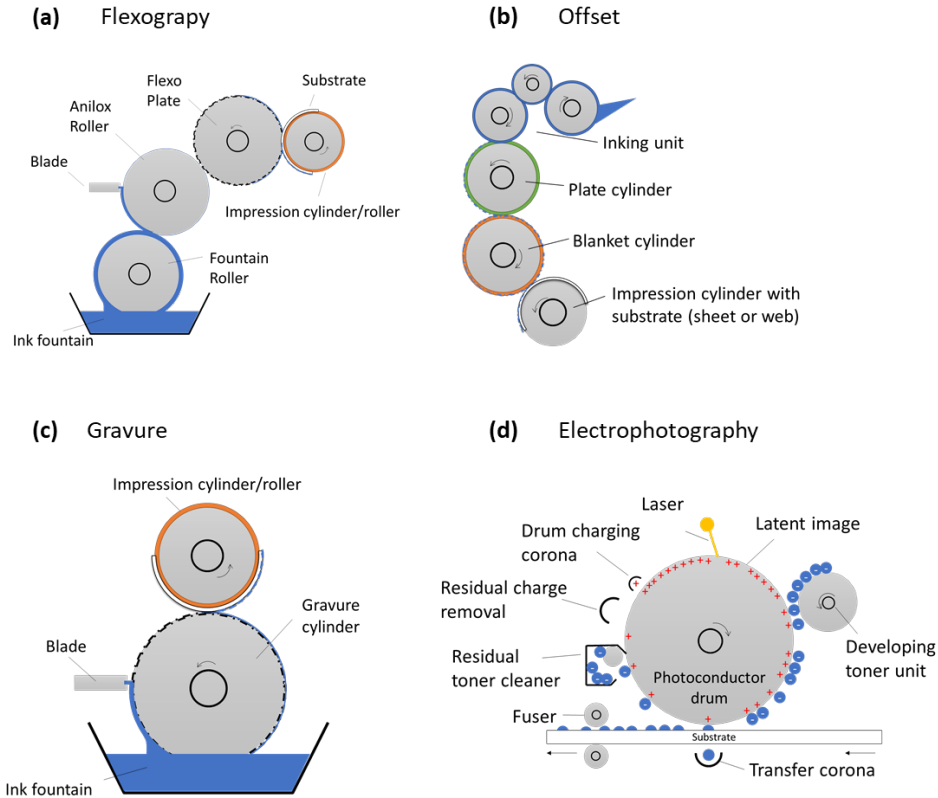
Figure 3. Schematic representation of a) flexography, b) offset, c) gravure and d) electrophotography printing.

Screen printing

Screen printing is the most mature technique in printing electronics. It is a two-dimensional (2D) low-cost manufacturing process able to coat large surface areas, and it is the simplest, most popular, and most economical technique in printed electronics. The fact of being a 2D technique requires the presence of a designed pattern, which provides more versatility than other analog printing tools. A blade, or squeegee, forces the desired ink transfer through the open areas (mesh) of the designed pattern of the mask onto the substrate. A balance of the ink viscosity is needed; the ink has to be liquid enough to slide and pass through the mesh of the mask, but dense enough to be adhered to the substrate surface. Even so, this technique allows the use of a rather high ink viscosity (1-50 Pa/s) and because of this, materials layer up to several μm of thickness can be developed.

There are three different assemblies of screen printing techniques that can be used in 2D round-to-round (R2R) manufacturing based on flatbed and rotary mechanics and a hybrid mechanism mixing both techniques: [57], [157]

- Flat-to-flat method (flatbed): Printing mask and printing substrate are both flat. A movable blade (or squeegee) force the ink to pass through the screen apertures onto the printing substrate (**Figure 4a**).

- Round-to-round (rotary printing): The printing screen is cylindrical with ink inside the printing cylinder. Printing mask, substrate and impression cylinder moves at the same time taking place the ink transfer to the substrate (**Figure 4b**).

- Flat-to-round: Mixture of both techniques, the printing plate is flat and the printing onto the substrate is done by a rotating impression cylinder that moves synchronously. A static blade adapts to the substrate surface transferring the ink.

Inkjet printing

Inkjet printing technique is a digital and non-contact technique that allows the direct pattering of large areas without a physical mask, owing to the precise control of picoliter volumes of materials in form of ink. Furthermore, thanks to the digital pattering, the manufacturing cost is reduced, allowing a fast change in the design without the need for a new set of masks, which enables a more flexible processing flow, and an easy superposition of the layers. It is a suitable technology for a wide range of production scales, with a lower initial investment than other printing techniques. The ink consumption and material wastage are minimal, and it can produce patterned thin films. An important drawback of this technique is concerning that inks have to meet very specific rheological requirements, as viscosity and surface tension, which need to be within narrow margins; 1-30 cP and 24-40 mN·m^{-1} respectively. Inkjet printing has more restrictions in the materials to be printed than other printing techniques, and commercial functional inks are scarce, expensive and have very limited shelf-life. So, more investigation in inks development is required.

The inkjet technique is broadly classified into two categories based on the mechanism of droplet generation: as continuous inkjet and drop-on-demand inkjet printing. Drop-on-demand technique is in turn classified into three types since it can be modulated by thermal, piezo or electrostatic regulators (**Figure 4c-f**): [57], [157]

- Continuous inkjet: a constant flow of selectively charged droplets is generated according to the image and the electronic pattern. The ones that are charged are deflected by an electric field, and the uncharged one's flow onto the substrate. So, only a fraction of the droplets ink is adhered to the substrate (**Figure 4c**).

- Drop-on-demand inkjet: a single drop is only ejected by the cartridge nozzle when required by the image. The drops can be generated thanks to a vaporization of the liquid in the ink chamber (thermal, **Figure 4d**), by a mechanically deformation produced by piezoelectric material under a controlled electric field (piezoelectric, **Figure 4e**), or by the electrostatic force generated by an electric field between the ink and the substrate, pushing the drop through the nozzle (electrostatic, **Figure 4f**).
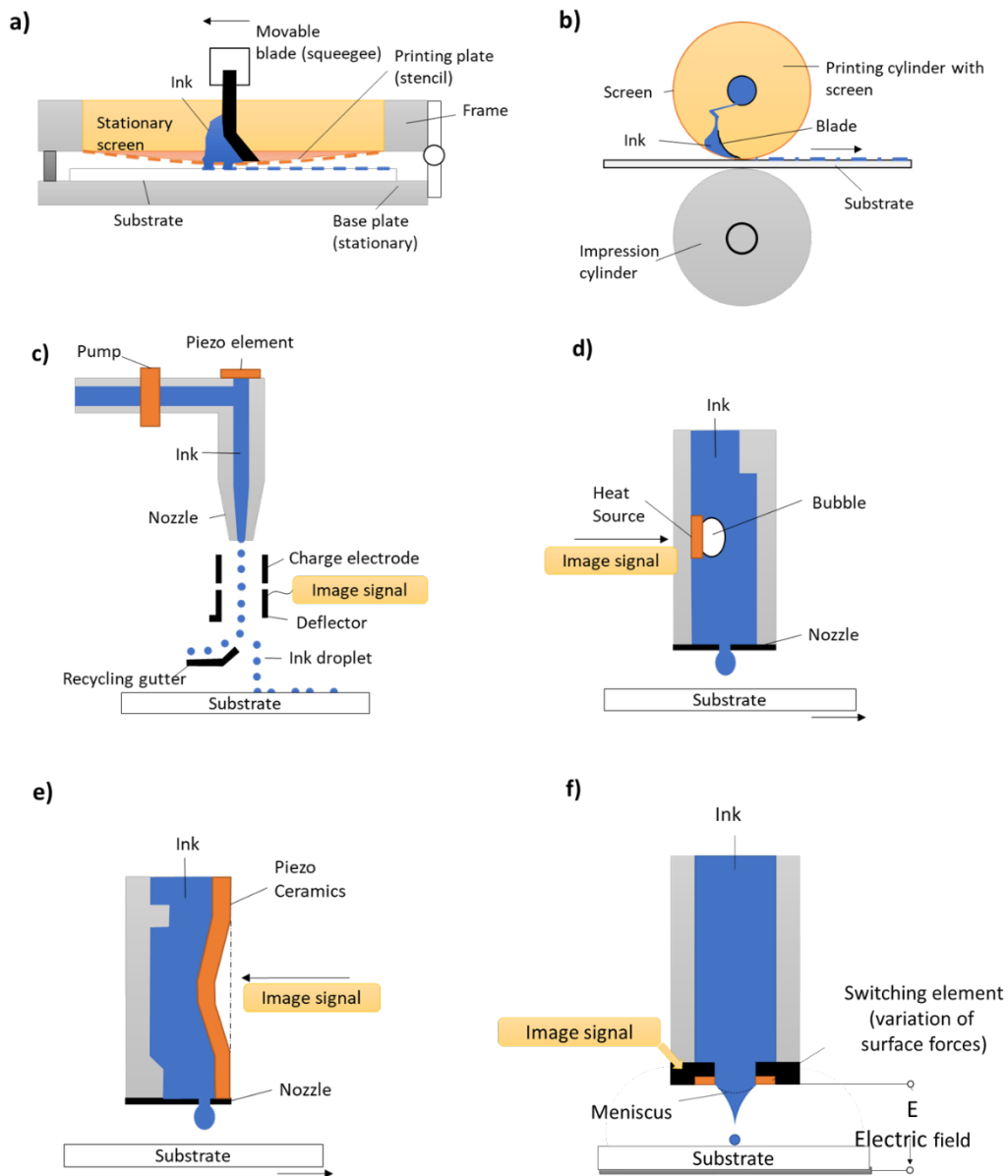

Figure 4. Simplified views of a) flat-to-flat and b) round-to-round screen-printing mechanics. c) Continuous, d) thermal drop-on-demand (bubble jet), e) piezoelectric drop-on-demand and f) electrostatic inkjet printing mechanics.

3.2.1.3. Piezoelectric materials

3.2.1.3.1. Piezoelectric effect

Piezoelectricity is a property that is exhibited by some non-centrosymmetric materials called piezoelectric materials. The piezoelectricity effect occurs when the charge balance within the crystal lattice of those materials is disturbed. When there is no stress applied on the material, the positive and negative charges are evenly distributed so there is no potential difference along the material. When a piezoelectric material is mechanically strained, its internal charge distribution changes, leading to the appearance of an electric potential difference between its outer surfaces that can be detected. Due to this duality, these devices can be used as sensors. Piezoelectric materials also can be used as actuators in presence of the inverse effect. This effect appears when an external field is applied to an actuator device, which causes a realignment of the internal charges of the piezoelectric layer and induces a mechanical strain.

Piezoelectricity is ruled by the piezoelectric coefficients d_{xx} ($pC \cdot N^{-1}$) that relates the force or the volume change when a material is subject to an electric field and vice versa. Typically, the most significant coefficients are the ones where the volume change is parallel to the force applied (d_{33}) or perpendicular to the force applied (d_{31}). A schematic representation of a pressure sensor mechanism is explained in **Figure 5**.
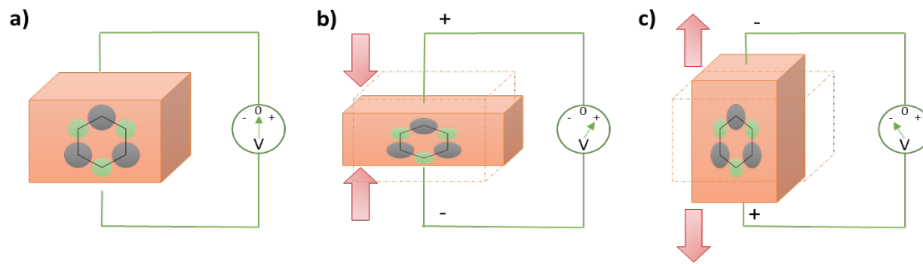

Figure 5. Schematic representation of the piezoelectric effect in a pressure sensor. When the piezoelectric material is compressed (b) it is polarized in one direction generating an electric signal, and when it is expanded (c) it is polarized in the other direction generating an electric signal of the inverse sign.

3.2.1.3.2. Piezoelectric materials

A suitable selection of piezoelectric materials depends on the target mechanical stress-electrical signal ratio. For example, in sensor; inorganic or ceramic piezoelectric layers show a large piezoelectric effect. This amplitude is related to high piezoelectric coefficients d_{33} that can be seen in **Table 1,** which makes possible the detection of low amplitude deformations and forces. Barium titanate ($BaTiO_3$), lead zirconate titanate (PZT) and PMN-PT single crystal (with structure

(1-x) Pb(Mg$_{1/3}$Nb$_{2/3}$)O$_{3-x}$PbTiO$_3$) are the materials with higher piezoelectric constant and, with an optimum manufacturing process, pressure sensors with high levels of sensitivity, in the order of 0.005 Pa, and fast response times (0.1 ms) can be developed.[158] Thus, these materials show promising characteristics to fabricate sensors with real-time response.

Table 1. Piezoelectric constant and Young's modulus of the most used bulk piezoelectric materials.

Piezoelectric material	Material Type	d$_{33}$ coefficient [pC/N]	Young's modulus [GPa]	Ref.
PVDF	Anisotropic, Polymer	- 33	1.0-3.2	[159]
P(VDF-TrFE)	Anisotropic, Copolymer	- 58	1.1-3	[160]
ZnO	Anisotropic, Crystal	27	201	[161]
BaTiO$_3$	Anisotropic (Orthotropic), Ceramic	460	94-120	[162], [163]
PZT	Anisotropic (Orthotropic), Ceramic	593	60	[164]
AlN	Anisotropic, Ceramic	6	308	[165]
PMN-PT	Anisotropic, Single Crystal	2000	1000	[159], [166]

However, because of the high Young's modulus and low solubility, the integration of an isolated layer of these ceramic materials with printing technology into soft and flexible substrates is a challenge that scientists have in mind, trying to dodge the problems of the ink fabrication and application.

Another option for the development of piezoelectric devices is the use of piezoelectric organic materials, such as polymers. Organic polymers, with a low piezoelectric constant, if compared with ceramic piezoelectric materials, have the advantage that can be biocompatible and flexible with relative small Young's modulus, allowing their application into soft substrates and compatible with printed electronics to be applied in places that rigid inorganic piezoelectric sensors cannot be adhered. Polar polymers like polyvinylidene fluoride (PVDF) are a promising alternative for the devices development since their manufacturing is simple and cost-effective.[167] With the adequate morphology and assembly, different sensors,[168]–[170] actuators [171], [172] or generators [173] devices on flexible or stretchable substrates are realized. This polymer is also commercially available with different formulations adapted for conventional printed techniques (both inkjet and screen printing) able to form four types of crystalline phases, phase I (β), phase II (α), phase III (γ), and phase IV. Among these four phases, only the β-phase is the polar phase with a large spontaneous polarization without mechanical orientation. Due to the electronegativity of the β-phase of the PVFD provided by the fluorine atoms, the generated

dipole moment enhances their sensor activity also in vibration sensors, where inorganic piezoelectric materials are the most efficient. The increase of the β-phase of the PVFD has been one of the most challenging investigation since their properties where discovered. The main strategies to increase the β-phase were based on the development of specific post-treatment with regular and expensive results.[174] PVDF-based copolymers have similar properties than the original PVDF polymer but synthetic routes enable achieving compositions with largest contribution of the β-phase. The P(VDF-TrFE) copolymer was obtained with the copolymerization between the VDF building block and the TrFE. Their analysis show that after the annealing at 140 °C, the β-phase was the most predominant structure,[175] obtaining an easy way to increase the contribution of the β-phase, making the P(VDF-TrFE) copolymer a better option for the sensor devices application.[176]
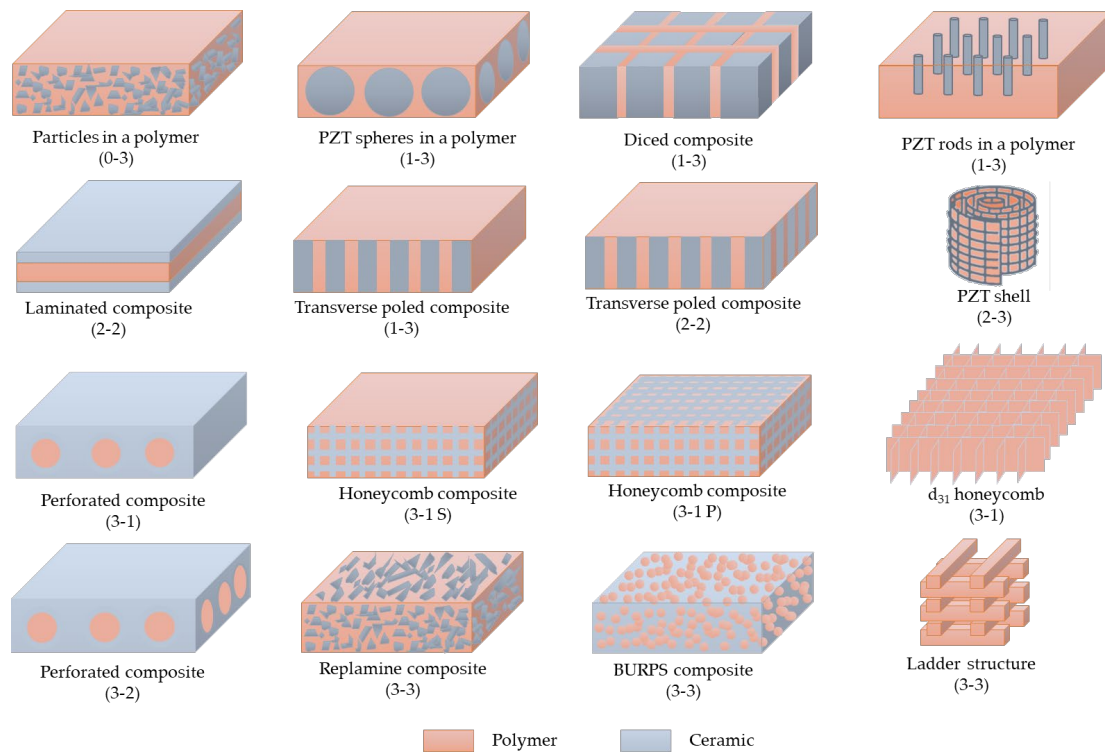

Figure 6. Different structural composition of ceramic-polymer composites. Ceramic materials are represented in blue and polymer materials are represented in orange. Reproduced with permission.[177] Copyright 1999, Elsevier.

Organic and inorganic piezoelectric materials can be combined in hybrid systems improving the mechanical durability of the resultant structure. Going further, these two materials can work closer in composites enhancing their individual lowest properties since the resultant material is flexible with large piezoelectric properties. A schematic of the different constitutions for piezocomposites can be seen in **Figure 6**, where the interaction of the two different phases are shown.[177] The

first number represents the physical connectivity of the active phase and the second one the physical connectivity of the passive phase. For instance, mixing PZT powder in a polydimethylsiloxane (PDMS) matrix produces a stretchable material with very large piezoelectric constant (d_{33} = 26 pC/N) for soft-touch applications.[178]

3.2.1.3.3. Poling techniques

Piezoelectric polymer materials are composed by electric dipoles that are randomly oriented or following a certain alignment. The co-polymer poly(vinylidene fluoride-co-trifluoroethylene) (PVDF–TrFE) became popular in the recent years because of the possibility to be printed, flexible and, because of the presence of the block TrFE, to directly obtain a polar beta phase, if compared with the processing of the homopolymer PVDF alone. However, it is necessary to perform the "poling" process. Such step, also known as thermal poling, consists of applying a high electric field, in combination with temperature, with the aim of aligning (at the nanoscale) all the dipoles with the electric field, which is what eventually yields the piezoelectric response in the material. In the first case, a process called poling is necessary for the dipole alignment to enhance the piezoelectric properties. Poling requires heating the material over the Curie temperature[179] that allows the molecules to move more freely. In that point, a rather high large electric field is applied to the material, causing the dipoles to align themselves in the same direction as the electric field (E), increasing the polarization of the piezoelectric layer. If the material is submitted to the electric field while it cools down, the dipoles are able to remain in that position after removing the electric field, and the material goes back to ambient temperature. Poling process is only relevant for polycrystalline ferroelectric materials, while non-ferroelectric piezoelectric materials, e.g. quartz or AlN, with randomly oriented grains cannot be poled. When measuring the polarization strenght (P) while sweeping an electric field (E), it is usually observed a hysteresis loop from +E to -E (V/μm) increasing each step |E| until it maintains constant and a remnant polarization appears in the piezoelectric layer. A graphical representation of this dipole alignment during the poling mechanism is explained in **Figure 7a** and, in **Figure 7b**, an example of this P-E hysteresis loop is depicted.

Different direct contact poling (DCP) methods can be performed, and in all cases the use of electrodes is required:

- Contact (electrode) poling:[180], [181] The electrodes of the piezoelectric device are electrically connected, and a large electric field (usually higher than 50 V/μm for the piezoelectric polymers[62], [169], [182] and around 10 V/μm for composites[149], [183]) is applied the device. The applied voltage is limited to the dielectric breakdown in

air; therefore, this technique is usually done under inert atmosphere or a vacuum chamber. However, the contact poling through the electrodes is the most used, but two different kind of electrode poling techniques can be distinguished in actuators or cantilevers.[184] When the applied force is perpendicular to the poling direction, the d_{31} piezoelectric coefficient is the most dominant and the piezoelectric material shows unidirectional stretching displacement due to the piezoelectric effect (**Figure 7c** and **7f**). In contrast when the applied force is in-plane to the poling direction, the d_{33} piezoelectric constant is dominant (**Figure 7d** and **7e**).

- Corona poling:[180], [181], [185], [186] This technique usually needs of a high voltage (6-8 kV) with the corona needle electrode located at approximately 2 cm from the piezoelectric layer surface.

- Photothermal poling:[180], [187], [188] This is a variation of the conventional electrode poling, where the material is heated using a laser beam allowing the poling in very localized points in areas in the range of μm^2 size.

- Electron beam poling: [180], [189], [190] The constant current created by a mono-energetic electron beam with energy ranging between 2 keV and 40 keV aligns the dipoles of the material. This technique allows poling very small areas in the range of μm^2.

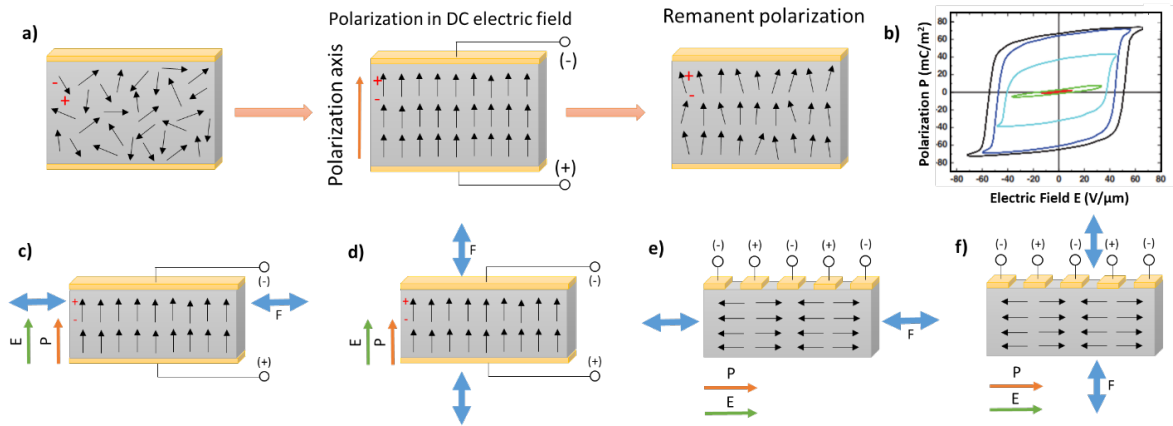**Figure 7.** Schematic representation of a) contact poling effect where the dipoles of the piezoelectric material are aligned, b) example of a typical cyclic P-E curve showing hysteresis, c) d_{31} contribution in sandwiched structure, d) d_{33} contribution in sandwiched structure, e) d_{33} contribution in top electrodes structure and f) d_{31} contribution in top electrodes structure.

3.2.1.4. Fully printed piezoelectric devices

As seen in reported works, the poling conditions are centered in different combinations of electric field and temperature in order to find the ones that allow to obtain the best piezoelectric performances, monitoring device properties like capacitance or piezoelectric constants before and after poling treatment. However, it is not possible to find correlations between the final device characteristics and temperature and electric field only, since the poling process strongly depends of the layers thickness (active piezoelectric polymer and electrodes) and the moisture of the whole printed system and the environment. In this particular point, it is rarely seen being reported the moisture content of the device, since it could be for example characterized by thermogravimetric analysis, or the relative humidity registered in the inert gas chamber, when is the strategy employed. In printed piezoelectric layers, the moisture content has a predominant role in the final piezoelectric characteristics of a printed device. Printed materials are already highly sensitive to the moisture and temperature during the printing process, and the curing process of the inks is clearly insufficient to remove all moisture in the system. Thus, a rigid control and monitoring of moisture seems crucial to define a reproducible protocol for poling a printed piezoelectric device based in PVDF-TrFE.

3.2.1.4.1.   Printed electrodes

As stated before, the motivation for the development of piezoelectric devices using printing techniques and organic/inorganic materials is one of the many ways explored to simplify processing steps, increasing the production speed and reducing manufacturing costs in order to enhance their industrial adoption. Fully printed devices are all-printed multilayer devices, where the printed piezoelectric material is stacked between two printed contact electrodes. The multilayer structure of the piezoelectric device is usually less than 200 μm thick, responsible for a large flexibility, bending or even stretching of the devices, to some extent.[62]

Metal nanoparticles based inks are commonly used for the printed contact electrodes, being the silver nanoparticle inks the ones that is used mostly because its commercial availability, low resistivity and cost-effectiveness. Another type of conductive inks are the organometallic inks, sinter-free inks using metal particles encapsulated with stabilizers capable to produce ink formulations for depositing at low temperature, returning high conductivity metal films, without the need for subsequent sintering treatments.[191] These inks avoid problems of aggregation of the metal particles and clogging in inkjet printing, but are substantially more expensive. They are promising for top electrode applications avoiding permeation through the underlying piezoelectric layer. The conductive ink used to print the bottom and top electrodes do not necessarily have to

be the same, each one will be selected depending on its homogeneity when printing on the different surfaces. Furthermore, it is crucial that the top electrode ink will be compatible with the piezoelectric layer to avoid shortcuts between the top and bottom electrodes.

The shape of the electrodes, and therefore the shape of the device, will depend on the application that is going to be used. If the device will be used as a sensor or actuator, their size will be smaller than if it will be used as energy harvester, because in the first case, the device has to be more precise to be used in the sensing/actuation area. Also, the shape of the sensors and actuators devices trends to be circular or square, while the energy harvester trends to be rectangular as will be discussed later in this section with some examples.

3.2.1.4.2. Printing PVDF based polymers

As stated previously, polymers are the most suitable piezoelectric materials to be used as printable inks owing their flexibility and their relative facility to be solubilized, in comparison with inorganic and crystal materials. PVDF is the most used piezoelectric polymer because it has larger piezoelectric coefficients than other bulk polymers.[156] In addition, PVDF is soluble in acetone and N,N-dimethylformamide (DMF) [192] allowing changing the viscosity and density of the inks to fit the target printing equipment to be employed. Moreover, it can be printed in different soft substrates such as polyethylene terephthalate (PET) or paper, being the mostly used in sensors,[193], [194] but also, in stiffer materials for energy harvesting applications,[195] with a thickness of 3 -10 μm obtaining devices with very good properties. As an example, the all-printed PVDF sensors present a sensitivity of 1.2 V/N when are printed onto PET substrates and 0.3 V/N when are printed onto paper.[193], [194] There is also research done in the addition of piezoelectric inorganic particles with PVDF to selectively enhance the piezoelectric response of the material. This includes $BaTiO_3$, PZT or zinc oxide (ZnO).[196] Almusallam et al. [183] proposed a device based on PZT:P(VDF-TrFE) composite as pressure sensor. They found that the best composition ratio was 50:50 printing the composite in a PET layer followed by a heat treatment for 30 min at 120 °C, successfully achieving a piezoelectric device with a $d_{31} = 17$ pC/N.

The piezoelectric properties of the PVDF are enhanced with the addition of the trifluroethylene (TrEE) which modifies the molecular chain arrangement achieving higher polarization level of piezoelectric coefficient as explained before. Viscosities from 5.4 mPa/s to 0.53 Pa/s of the corresponding ink can be found with a piezoelectric layer thickness ranging from 2 μm to 108 μm respectively. This wide range of thickness allows the printed material to be used in different applications such as stretchable pressure sensors,[62], [197]–[199] actuators for lab-on-chip devices for point-of-care diagnostics [62], [197], [200], [201] or generators.[201]

Besides organic materials, printing piezoelectric composites is also possible thanks to the relative solubility provided by its inherent organic part. Because of the thickness of the piezoelectric layer (from 30 μm to 100 μm in reported works) and the hardness provided by the single crystals the main applications of the printed piezoelectric composites are pressing sensors [183] or energy generators [149], [202] because large elasticity of the piezoelectric material is not needed.

3.2.1.4.3.   Full inkjet-printed piezoelectric devices

Inkjet printing offers a mask less and non-contact deposition of materials onto a wide range of substrates. Nevertheless, the fabrication of fully inkjet-printed devices remains difficult mainly due to the strict parameters that the inks needs to fulfill in terms of viscosity, surface tension and particle size. The success of the inkjet printing technology in piezoelectric device manufacturing strongly depends on the availability of functional materials and suitable post-processing techniques. The main components of these inks are the functional material, the solvent and other additives. These two last components need to be removed after printing through post-processing steps.

A piezoelectric ink made of P(VDF-TrFE) solubilized with cyclopentanone and dimethyl sulfoxide (DMSO) was performed by Tuau et al. [62] with a resulting viscosity of 5.4 $mPs \cdot s^{-1}$ and a contact angle of 9.6 ° with the polyethylene naphthalate (PEN) surface. With these parameters, the ink has an optimal formulation for inkjet printing. This resulted in the successful printing of twelve layers of the piezoelectric compound achieving up to 2 μm thick layer, after the corresponding post-processing steps. This methodology was implemented to prepare a full printed structure, using silver inkjet-printed electrodes. The full inkjet-printed device was studied and able to be used as energy harvesters, sensors and actuators in flexible electronic applications.

Another promising approach was reported by Pabst et al. [200], [201] in 2013. A fully inkjet-printed actuator, with a bending deflection, made of P(VDF-TrFE) onto PEN substrate, also using Ag as a printed contact electrode. They also described that the inkjet-printed piezoelectric layer has a thickness of 9 μm and the complete device showed a promising piezoelectric coefficient d_{31} of about 9 pC/N after thermal treatments (T_{max} = 130 °C) and plasma sintering as post-processing steps. The fabrication method of the actuator proposed [200], [201] is explained in **Figure 8a,** providing a cross-sectional SEM image of the final device. As reported, the actuator has a very thin piezoelectric layer, with a Young's modulus of 2 GPa, but owing to the hardness of the Ag electrodes, which have a Young's modulus of 40 GPa, the flexibility of the final device decreases. A high transversal piezoelectric constant (d_{31} = 7 - 9 pC/N) allows the generation of significant actuator deflections.

Other inkjet-printed device is reported by Lim et al. [202] in 2017. This work presents a flexible piezoelectric energy harvester (f-PEH) made of BaTiO$_3$. The piezoelectric ink used in this device was done by the hybridization of the nano-powder ceramic material with an epoxy thermoset resin in presence of a dispersant and DMF. Printing procedure, SEM images and electrical characteristics can be seen in **Figure 8b**. This hybrid piezoelectric layer has a thickness of 15 µm in the harvesting device with significant properties like current density of 0.21 µA/cm^2 or a power density of 0.42 µW/cm^2.
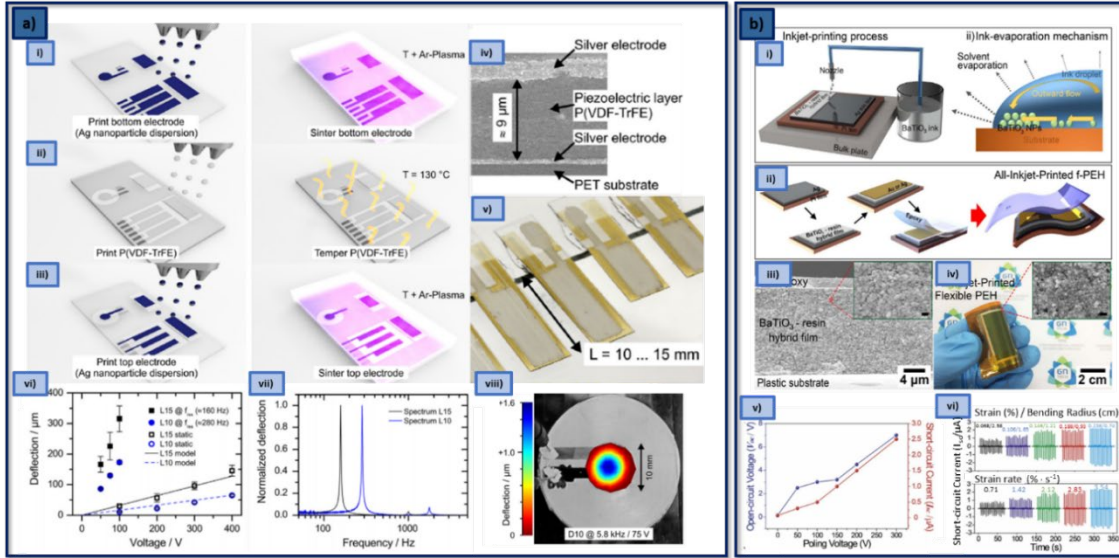

Figure 8. a) Schematic diagram of the fabrication method i) inkjet printing and sintering of Ag bottom electrode onto PET substrate, ii) inkjet printing and tempering of the P(VDF-TrFE) layer and iii) inkjet printing and sintering of Ag top electrode. iv) Cross-sectional SEM image of layer sandwich. v) Cantilever mounted on glass for characterization, vi) static and dynamic deflection behavior of cantilever actuators. The piezoelectric coefficient d$_{31}$ is derived from these measurements and used to model the membrane behavior, vii) resonance spectra of cantilevers actuators and viii) deflected shape of a membrane actuator driven at resonance and measured by a laser scanning vibrometer. Reported with permission [201]. Copyright 2013, Elsevier. b) Schematic illustrations for a facile inkjet printing process and ink solvent-evaporation mechanism in the printed droplet. ii) Schemes of the sequential process for the fabrication of an all-inkjet-printed f-PEH. iii) The cross-sectional SEM images of all-inkjet-printed f-PEH. The inset shows the magnified cross-sectional image of a BaTiO$_3$-resin hybrid film (scale bar: 500 nm). iv) A photograph of the fully f-PEH with a sample size of 5 cm × 5 cm (activation area of 3 cm × 4 cm) achieved by inkjet printing of piezoelectric hybrid film and conductive layers. The inset shows the top surface of inkjet-printed piezoelectric hybrid film (scale bar: 500 nm). v) The output voltage and current increased with the poling voltage. vi) Dependence of the strain (bending radius) and strain rate on the output performance of a f-PEH. Reproduced with permission [202]. Copyright 2017, Elsevier.

3.2.1.4.4. Full screen-printed piezoelectric devices

Because of its simplicity and suitability for mass production, screen printing remains the technology most suitable for industrial scale up of such printed devices. There are several reported full screen printing piezoelectric devices in literature, again combining conductive inks to print the contacts with the printed piezoelectric polymer layer. Lima et al. [71] recently have reported a novel screen-printed and flexible multiferric magnetoelectric (ME) material based on P(VDF-TrFE) as piezoelectric phase and $PVDF/CoFe_2O_4$ as the magnetostrictive phase. The all-printed ME composite exhibits a -26 $pC \cdot N^{-1}$ piezoelectric response at a longitudinal frequency of 16.2 kHz and a voltage coefficient of 164 mV $cm^{-1} \cdot Oe^{-1}$. After the dilution of the ink with DMF, they obtained a 1.13 Pa.s of viscosity at 300 s^{-1} shear rate. Their printing procedure can be seen in **Figure 9a**. Such optimized device reduces cost assembly and an easy integration in large areas for sensors, actuators and energy harvesters.

Also, Zirkl et al. [73] reported a low-cost fully screen-printed smart active matrix sensor array, using P(VDF-TrFE) as piezoelectric material with a thickness of 5 μm printed onto a PET sheet substrate (**Figure 9b**). This sensor has a smaller remnant polarization after hysteresis poling providing the device with a d_{33} = 20 pC/N. A magneto-electric energy harvester based on a PVDF screen-printed polymer deposited on a Metglas® iron-based substrate has been reported by Chlaihawi et al. [195] Silver was screen-printed as top electrode on the printed PVDF layer. This energy harvester had a power density of 639.6 $\mu W/cm^3$ that came from a maximum power generated of 8.41 μW at a load resistant of 100 kΩ and frequency of 100 Hz.

The electrodes and piezoelectric layer of the work by Zirkl et al. was performed by screen printing, but the dielectric layer and the electrolyte ionic conductor were deposited onto the device via inkjet printing. The fabrication of complex devices using just one manufacturing technique limits the architecture to specific resolution or materials, whereas the combination of different techniques offered an advantage due to the need of multilayer assembly of different materials with different rheology.

3.2.1.4.5. Hybrid devices

Hybrid devices use more than one manufacturing technique or combination of materials. Combining printing techniques and materials tends to improve the manufacturability of devices to bridge system mismatch issues, e.g. such as rheology and particle size.[203] As discussed previously, there are some piezoelectric materials that due to their properties cannot be solubilized properly and therefore used as inks in screen nor inkjet printing. However, other manufacturing methods can be performed to fabricate these devices. A promising example of this approach is

with ZnO. Due to its inherent piezoelectricity, good biocompatibility, semiconductor nature and its capability to form multiple piezoelectric nano-objects, this material is compatible with printed technology. [204]–[206] Using an ink with ZnO nanoparticles embedded on a polymer matrix makes this material process compatible with printing steps in a fairly easy way. [18] Posterior hydrothermal method for growing of ZnO nanowires (NWs) from the printed seeds at mild temperatures and aqueous solutions have been successful reported and are one promising piezoelectric device published. [203] A step forward is done in the work reported by Choi et al. [192] where a hybrid piezoelectric structure comprised of ZnO nanowires (NWs) grown on a PVDF polymer matrix is described. In this way, the ink polymer matrix is also piezoelectric. They demonstrate that ZnO NWs growth on a polyimide (PI) substrate is conserved when ZnO is integrated in a PVDF matrix. Although this mixed solution provides internal strain to the PVDF, rising the effective Young's modulus of the device thus its brittleness, it increased gradually the output electrical power of a hybrid nanogenerator whit increasing applied strain (**Figure 9c**). The voltage and current outputs were enhanced approximately 2.7-fold and 6.5-fold, respectively.

Similar work was reported by Kit et al. [207] of a hybrid piezoelectric nanogenerator based in a PVDF-BaTiO$_3$ composite. Eventually, increasing the amount of BaTiO$_3$ increases the Young's modulus until the point of 10 % wt of BaTiO$_3$, where the piezoelectric constant is the highest, indicating that the Young's modulus plays an important role in the piezoelectric power generation. Moreover, finite elements simulations were done to model the stretch where an external strain of 3.2% was applied along an axis. This, reflects a variation of strain from 1% to 11% in the PVDF-BTO composite, however the PVDF display a mean value of 3.2%, neglecting the higher values on the corners of the model, which could reach up to 4.3% as depicted in **Figure 9d**.
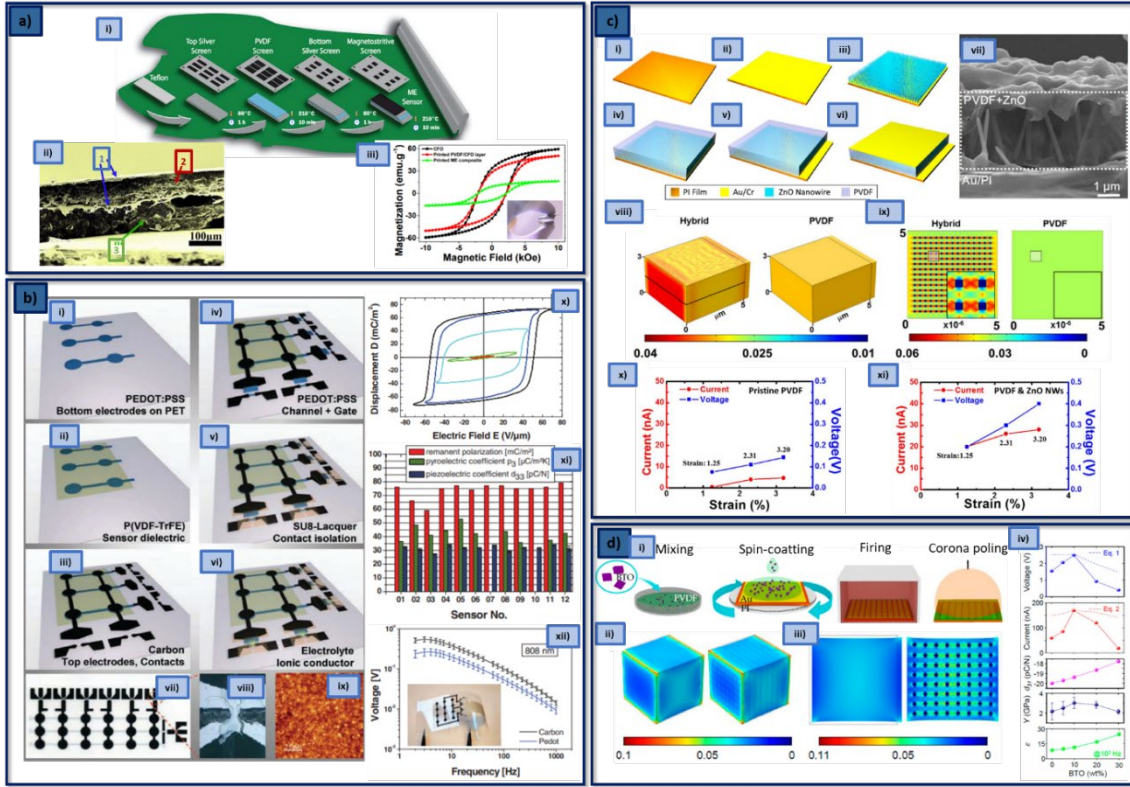
Figure 9. a) i) Schematic representation of the experimental procedure used to obtain the composite, ii) SEM image of the ME sample, iii) Room-temperature magnetic hysteresis loops for the pure CFO nanoparticles, printed PVDF-CFO layer and all-printed ME sample. Reported with permission [197]. Copyright 2019, Royal Society of Chemistry. **b)** Process flow illustrating the fabrication of printed ferroelectric active matrix sensor arrays. i) Screen printing with PEDOT:PSS to form the bottom electrodes of the sensor, ii) screen printing of the ferroelectric P(VDF-TrFE) film, iii) screen printing of carbon to form the top electrodes of the sensor, iv) inkjet printing with PEDOT:PSS to form the gate and channel of the ECTs, v) inkjet printing of the SU-8 separation layer, vi) inkjet printing of the ECT polymeric electrolyte, and vii) layout of an all-printed 3 × 6 sensor array with integrated ECTs. viii) Close-up image of the channel region of the ECT. ix) AFM height image of the screen-printed P(VDF-TrFE) layer. The color map corresponds to a height scale ranging from 0–55 nm. The RMS roughness of the film is 4.5 nm. Characterization of the printed sensor. x) Hysteresis loops of a ferroelectric sensor. The lines illustrate the opening of the loop with increasing electric field amplitude, xi) Variation of P_r, the piezoelectric d_{33} coefficient, and the pyroelectric p_3 coefficient on a 3 × 4 printed sensor array, xii) frequency dependence of the pyroelectric voltage response of a sensor excited by intensity-modulated light from a laser diode emitting at 808 nm for carbon and PEDOT:PSS top electrodes. The error bars illustrate the variation in the pyroelectric response across the 3 × 4 printed sensor array. Reported with permission [199]. Copyright 2011, Wiley-VCH. **c)** Schematic diagram of the fabrication method i) PI as flexible substrate, ii) thermal deposition of the bottom Au/Cr electrode, iii) ZnO NW growth, iv) spin-coating of the PVDF layer, v) cleaning of the top surface and vi) thermal deposition of Au/Cr top-electrode. vii) SEM image of a cross section of the hybrid structure, viii) distribution of strains on surfaces of a hybrid structure and pristine PVDF blocks and ix) distribution of strains in mid-layers of a hybrid structure and PVDF blocks. x) Power output of a PVDF-based NG and xi) power output of NG based on a hybrid structure. Reported with

permission [192]. Copyright 2017, Elsevier. **d)** i) Schematic diagram of the fabrication process of a poly(vinylidene fluorine)-BaTiO$_3$ (PVDF-BTO) composite. Mixing, spin-coating, firing, and corona poling. Finite element simulations of the strain distribution ii) on the surface and iii) in the mid-layers of PVDF and PVDF–BTO blocks. iv) Comparison of the piezoelectric outputs with the predicted piezoelectric coefficient, measured Young's modulus, and dielectric constant. Reported with permission [207]. Copyright 2018, MDPI.

Considering the shape and design of the different devices, a trend is observed. In the devices whose purpose is to generate energy, the rectangular shape is the predominant owing to the devices are made to be used as cantilevers, where thanks to the bending movement the output voltage is higher due to the combination of the piezoelectric constants. In the same perspective, actuator devices also have rectangular shape, remaining in the concept that when applying an AC current, the cantilever moves. In other type of actuator devices, circular shapes are usually reported. In contrast, sensor devices no longer appear with rectangular shapes but usually show square or round shape with smaller electrode area.

The summary of the all-printed piezoelectric devices discussed is shown in **Table 2**. In this table, the referenced papers are ordered according to the different printing technique and the different devices are arranged by their printed material, the printed substrate, the device design, the poling technique applied, and the main properties reported by the authors.

Table 2. Summary of the main works reporting all-printed piezoelectric devices sorted by printing technique.

Printing technique (equipment)	Transducer type	Material	Substrate	Shape & Size	Poling	Characterization	Properties	Application area	Year	Ref
Inkjet Printing (UJ 200 UNIJET)	Generator	BaTiO$_3$ hybrid (resin)	PI	Rectangle 12 cm^2	Different contact poling tests (from 50 to 300 V/µm)	Surface and cross-section (SEM) Morphology (SEM and TEM) Particle size and size distribution (Image J) Crystalline structure (XRD) Vibration modes (Raman)	Output voltage = 7 V $j = 0.21$ µA·cm^{-2} PD = 0.42 µW·cm Thickness [a] = 15 µm	Flexible electronics	(2017)	[202]
Inkjet Printing (NM)	Sensor, actuator and generator	PVDF-TrFE	PEN	Square 4 mm^2 (sensor) Rectangle 5 mm^2 (actuator)	Contact poling at 100 V/µm	Thicknesses (Profilometer) Surface tension (contact angle, goniometer) Viscosity (Rheometer) Dielectric response Piezoelectric properties	Ink Surface tension = 35.6 mN/m Contact angle = 9.6° Viscosity = 5.4 mPa·s Device $d_{31} = 10.4$ pm/V P_r (50 MV/m) = 7.8 µC/cm^2 Thickness [a] = 2 µm	Flexible electronics	(2017)	[62]
Inkjet Printing (Omnijet 100)	Actuator	P(VDF-TrFE)	PET	Circle 1.75 cm^2 (membrane) Rectangle 0.75 cm^2 (cantilever)	Contact poling at 44 V/µm at RT for 1 min	Cross-section (SEM) Static deflection (laser triangulation displacement sensor and high voltage amplifier) Dynamic deflection (laser scanning vibrometer) Calorimetric measurements (Between -20 and 200 C) Morphology (AFM, XRD and NT MDT Solver)	$Y = 40$ GPa $d_{31} = 7 - 9$ pC/N $P_r = 5.8$ µC/cm^2 Thickness [a] = 9 µm	LoC devices for POC diagnostics	(2013, 2014)	[200], [201]

(Continued on next page)

Table 2. (Continued)

Printing technique (equipment)	Transducer type	Material	Substrate	Shape & Size	Poling	Characterization	Properties	Application area	Year	Ref
Screen Printing (NM)	Sensor	PVDF-TrFE	PET	Square 1-3 cm^2	NM	Surface morphology (FE-SEM) Layer structure (EDX)	R_s = 0.09 Ω/sq Thickness [a] = 18 μm	Flexible sensing	(2018)	[198]
Screen Printing (homemade)	Sensor	PVDF-TrFE	PET	Square 2 cm^2	Contact poling at 100 V/μm at 120 °C for 15 min	Data acquisition system (Oscilloscope) Thicknesses Piezoelectric properties	Thickness [a] = 30 μm d_{33} = 19 pC/N	Flexible electronics	(2019)	[208]
Screen Printing (MT320T, Microtech)	Sensor	PVDF-TrFE	PEN	Circle 7 cm^2	Contact poling at 50 V/μm at 140 °C	Data acquisition system Thicknesses	Thickness [a] = 2 μm operating voltage = −3 V	Healthcare monitoring	(2019)	[182]
Screen Printing (AMI MSP 485)	Sensor	PVDF	PET and paper	Squares 1-9 cm^2	NM	Substrate surface energy (Goniometer) Thickness and roughness (scanning interferometer microscope) Sheet resistance Crystallinity & β-phase (XRD)	Sensitivity = 1.2 V/N (PET); 0.3 V/N (paper) Thickness [a] = 10 μm	Flexible electronics	(2015, 2017)	[193], [194]
Screen Printing (HMI MSP-485)	Generator	PVDF	Metglas® iron based	Rectangle 3 cm^2	Contact poling at 80 V/μm for 2 h	Data acquisition system (Oscilloscope) Thicknesses	100 Hz (2 MΩ load resistance) = 2.25 V Thickness [a] = 3 μm PD = 639 μW/m^3	Energy harvester	(2016)	[195]
Screen Printing (DEK Printing Machines Ltd)	Generator	PZT-PVDF (2.57:1) + 0.2% Ag	PI and Woven-fabric	Square 100 cm^2	Contact poling at 3.7 V/μm at 75 °C for 6 min	Dielectric properties Piezoelectric properties Thicknesses	ε_r (ω) = 171 d_{33} = 43.5 pC/N Thickness (total generator) = 100 μm	Textile electronics	(2017)	[149]

(Continued on next page)

Table 2. (Continued)

Printing technique (equipment)	Transducer type	Material	Substrate	Shape & Size	Poling	Characterization	Properties	Application area	Year	Ref
Screen Printing (NM)	Sensor, actuator and generator	PVDF-TrFE	Teflon	Square 12 cm^2	Corona poling at 120 °C	Morphology (FEG/SEM, after gold coated by magnetron sputtering) Piezoelectric properties Thicknesses	Ink Viscosity = 0.53 Pa·s Device Thickness ^{a} = 108 μm d_{33} = -26 pC/N	NM	(2019)	[197]
Screen Printing (TIC SCF-550) Inkjet Printing	Sensor	PVDF-TrFE	PET	Circle 1 cm^2	Contact poling (hysteresis loop at 75 V/μm)	Piezoelectric surface morphology (AFM) Dielectric properties Electric properties Piezoelectric properties	d_{33} = 20 pC/N p_3 = 278 μC/Km^2 P_r (70 V/ μC) = 52 mC/m^2 Thickness ^{a} = 5 μm	NM	(2011)	[199]
Screen Printing electrodes (Dupont 5064H) Doctor Blade technique, composite	Sensor	PVDF-TrFe:PZT (50:50)	PET	Square 1 cm^2	Contact poling at 15 V/μm at RT for 1 h	Dielectric properties Electric properties Piezoelectric properties Thicknesses	ε_r (ω) (1kHz) = 69 P_r (34 MV/m) = 4.8 μC/cm^2 d_{31} = 17 pC/N Thickness ^{a} = 30-60 μm	NM	(2015)	[183]
Roll coating (piezo BTO-carrot composite) and Screen Printing (electrode)	Generator	BaTiO$_3$	Cu electrode	Rectangle 4.5 cm^2	Contact poling at 3.6 V/μm	Cross-section (SEM)	Output voltage = 1 V Thickness ^{a} = 100 μm	Wearable sensor	(2019)	[203]

^{a} Thickness of the total amount of piezoelectric layer

Abbreviations:

ε_r (ω) = Relative Permittivity; P_r = Remnant Polarization; R_s = Sheet Resistance; PD = Power Density; j = Current Density; d_{xy} = Piezoelectric constant;

Y = Young's Modulus; p_3 = Pyroelectric constant; LoC = Lab-on-a-Chip; POC = Point-Of-Care; NM = Non-Mentioned

Each application reported has different target technologies and different adoption barriers, both commercial and technical, and each one is at different stages of technology readiness level.

3.2.1.5. Outlook and conclusions

All printed piezoelectric devices have the singularity to be used in integrated and multi-functional applications, from mechanical energy harvesting, to sensing and actuation. The evolution of printed piezoelectric devices and their applications is closely linked to advances in materials synthesis compatible with printing techniques to reach d_{33} piezoelectric coefficients with at least 15 pC/N. It is noteworthy that the most reported fully printed device is the pressure sensor. Piezoelectric pressure sensor has the capacity to measure pressures as low as 0.1 Pa for applications in robotics and with high sensitivity touch interfaces. However, for applications that do not require sophisticated functionality, such as 3D touch or proximity sensing, [209]–[211] piezoresistive sensors are the widely used due to their low technology complexity, which is more mature technology, longer established, and being used in automotive and medical applications. The main limitation of piezoelectric pressure sensors in some applications is that they are more expensive to manufacture and less straightforward to integrate.

Although printed piezoelectric devices have unique capability with their multi-functionality, their sensing applications are rather niche, and it is expected that with the mature of their use as energy harvesters will increase their application to enable self-powered sensors. There is no doubt that, as the technology matures, the number of applications will keep increasing. As fully printed devices, their field of application is extensive, with great interest in wearables and biomedical systems, this is because of their capabilities in rendering piezoelectric devices in thin and soft formats. Most of the printed devices discussed in the earlier sections are not addressed to a specific application, focusing more in the fabrication, characterization, and performance of the materials and the whole printed device, and just validated in laboratory scale. It is also seen the lack of a critical analysis of device variability and how to tackle it.

In summary, all-printed piezoelectric devices offer promising applications and the ones reported are mainly developed by screen and inkjet printing. The inkjet-printed piezoelectric layers have thickness ranging from 2 μm to 9 μm (with individual layers of 100 nm) in the case of the piezoelectric polymers and up to 15 μm each layer in the case of a hybrid resin of $BaTiO_3$. Moreover, maximum areas of 2 cm^2 and 12 cm^2 for polymer piezoelectric devices and hybrid piezoelectric devices have been found as the maximum inkjet-printed piezoelectric area to our knowledge. The feasibility for scale-up production, and the potential for printing multifunctional materials is increasing, making possible future printed areas in the scale of the squared meters

could be feasible. However, recent developments are done at small scale using desktop printers, exploring new materials, and focusing on getting the best performance of devices. For the screen printing technique, piezoelectric individual layers can have larger thicknesses, from 2 μm to 100 μm, as in the case of PVDF-TrFE and $BaTiO_3$ respectively,[182], [203] owing to the difficulty of processing thin masks for the printing production. In comparison with inkjet-printing, bigger areas of printed devices can be found with screen-printing where maximum areas of 12 cm^2 and 100 cm^2 for polymer piezoelectric devices and hybrid piezoelectric devices respectively. Because of these differences in area and thicknesses, it is more common to use the devices produced by inkjet printing as sensors and the ones made by screen printing for actuator applications. Organic polymers, such as PVDF and its composite P(VDF-TrFE), are the most used piezoelectric materials for printing electronics owing their relative easiness in the ink production. Nevertheless, current research focuses achieving inks and hybrid devices based in piezocomposites composed by ceramic materials such as $BaTiO_3$ or PZT as piezoelectric nanoparticles blended with polymers or resins. These have reported larger piezoelectric constants than the printed piezoelectric polymer alone, up to an order of magnitude, achieving a $d_{33} > 40$ pC/N in a generator made of PZT-PVDF. And finally, but of crucial importance, is the variability of device performance due to lack of control of the poling process of PVDF, being the contact poling while heating under inert atmosphere the most common and effective one still remains an open challenge and with considerable lack of reliability.

Printed piezoelectric devices as key building blocks for their application in smart textiles or flexible electronics require fundamental studies about printed layers homogeneity to conserve their piezoelectric properties obtained in laboratory conditions and when integrated into functional prototypes. Open challenges include that not all the piezoelectric materials are compatible with printing techniques, new methodologies related to the materials and workflow to prepare the printed electrodes in the devices. The techniques and materials presented in this Progress Report show promising candidates to be used in off-the-shelf products of tomorrow. The future mass production of printed piezoelectric devices settles on the combination of different materials and printing techniques and the control of printing parameters in each step. Despite several open challenges, the main bottleneck existing today is still the lack of readily available piezoelectric materials compatible with printing techniques, imposed by high cost, the strict rheological properties that inks need to meet, particularly in terms of viscosity and surface tension and lack of robustness of poling processes. More efforts need to be done in order to increase the compatibility of piezoelectric materials with printing techniques, to facilitate and decrease the cost of the devices production. New printed materials are expected to continue appearing in the coming years.

Acknowledgements

3.3. Application of printed piezoelectric devices

In this section is shown the study of EM tools based on piezoelectric devices. This section is divided in two subsections, where each one corresponds to a published work in a relevant scientific journal. The first one is focused on the fabrication of piezoelectric devices with silver electrodes fully fabricated by PE, combining screen and inkjet printing to increase their properties. The different electrodes inks where fully characterized in terms of printability, morphology and conductivity. Different dimensions of printed electrodes, and therefore of the complete device, are evaluated and validated. The different capabilities of the piezoelectric device, sensor, actuator and energy harvester are evaluated. Furthermore, the poling stages of the printed piezoelectric layer were evaluated obtaining a full control. The second section goes one step further with the integration of a piezoelectric matrix sensor fully fabricated with screen printing (SP) technology on a TPU substrate for wearable applications

3.3.1. Paper II: Controlled poling of fully printed piezoelectric PVDF-TrFE device multifunctional platform with inkjet-printed silver electrodes

The second paper presented in this Chapter 3, **Paper II**, is a published article about the fabrication of a piezoelectric sensor, fully fabricated with printing technologies by the combination of screen and inkjet printing in a polymeric substrate. The article is focused to achieve the best electrical and morphological parameters for the piezoelectric device by doing a complete characterization of the functional inks (silver, PVDF-TrFE, and gold) that can be processed at low temperatures (140 ˚C) for the multilayer fabrication. Different dimensions of inkjet-printed electrodes are fabricated, and their electrical response and validation is presented The characterization and evaluation of the printed piezoelectric device with the different application modes (sensor, actuator and energy harvester) is performed with the same device structure. The poling state of the PVDF-TrFE layer is studied and controlled, being able to achieve polarization cycles with very stable response reproducibility.

This article has been reproduced from Journal of Materials Chemistry C, with permission from RSC*:

Paper II. <u>M. Alique,</u> A. Moya, M. Kreuzer, P. Lacharmoise, G. Murillo, and C. D. Simao. **Controlled poling of fully printed piezoelectric PVDF-TrFE device multifunctional**

platform with inkjet-printed silver electrodes. J. Mater. Chem. C, 2022, doi:10.1039/D2TC01913B (Q1. IF: 8.067)

This work has been also presented in different conferences with their corresponding Proceedings:

- Conference **µTAS 2020**: <u>M. Alique</u>, M. Duque, C.D. Simao, P. Lacharmoise, G. Murillo, A. Moya. Fully printed piezoelectric Devices. Poster presentation.

- Conference **JPhD 2020**: <u>M. Alique</u>, A. Moya, G. Murillo, C.D. Simao. Fully printed piezoelectric devices. Oral presentation.

- Conference **LOPEC 2021**: <u>M. Alique</u>, P. Lacharmoise, G. Murillo, A. Moya, C.D. Simao. Advances on fully printed piezoelectric sensors and actuators. Oral presentation.

- Conference **µTAS 2021**: <u>M. Alique</u>, A. Moya, D. Otero, M. Duque, P. Lacharmoise, G. Murillo, C.D. Simao. A novel multifunctional fully-printed piezoelectric flexible device used as sensor, actuator and energy harvester. Poster presentation.

- Conference **LOPEC 2022**: <u>M. Alique</u>, A. Moya, D. Otero, M. Duque, P. Lacharmoise, G. Murillo, C.D. Simao. Multifunctional fully-printed piezoelectric flexible single device platform for wearable applications. Poster presentation.

* Note that, equations, tables and figures numbering in the reproduced research article follow the ones of the published version.

Fully printed piezoelectric devices for flexible electronics applications

Marc Alique,[1]† Ana Moya,[1] Martin Kreuzer,[2] Paul Lacharmoise,[1] Gonzalo Murillo,[3]

Claudia Delgado Simao,[1]*

[1]Eurecat, Centre Tecnològic de Catalunya, Functional Printing and Embedded Devices

Unit, 08302 Mataró, Spain.

[2]ALBA Synchrotron Light Source, 08290 Cerdanyola del Vallès, Spain

[3]Instituto de Microelectrónica de Barcelona, IMB-CNM (CSIC), Esfera UAB, Campus

Universitat Autònoma de Barcelona, 08193 Bellaterra, Spain.

† Electrical and Telecommunication Engineering Department, Universitat Autònoma de

Barcelona (UAB).

Corresponding author

E-mail: claudia.delgado@eurecat.org

Abstract

Fully printed piezoelectric devices are important components for seamlessly integrated circuits. Here it is reported for the first time, inkjet-printed silver electrodes on screen-printed PVDF-TrFE polymer on flexible film. Different inks and printing conditions studies are performed to select and prepare bottom and top inkjet-printed electrodes on the screen-printed PVDF-TrFE layer. Thermal-assisted electrical poling and unpoling conditions for the device are obtained, with high reproducibility and reversibility in multiple cycles. The fully printed device is investigated as a sensor, actuator, and energy harvester as a single device multifunctional platform. A maximum output voltage of 3.6 V is achieved in the piezoelectric devices when used as a vibrational sensor. The maximum output power of 1.6 µW with a 1.1 MΩ optimum load resistor was obtained when clamped as a cantilever and accelerated at 0.75 G and characterized as a microgenerator

3.3.1.1. Introduction

Printed piezoelectric devices attract a great deal of attention due to their versatility in design, processing, and integration in lightweight electronics applications and flexible form factors. [15], [90] Different printed electronic technologies and approaches have been exploited for the fabrication of printed piezoelectric devices and have demonstrated their applicability to generate low-power, cost-effective and ultra-thin devices in soft substrates. Reports of processing piezoelectric materials using printing techniques have been widely demonstrated on a laboratory scale.[212], [213] [214], [215] Ceramic piezoelectric materials, such as lead zirconate titanate (PZT) or $Pb(Mg_{1/3}Nb_{2/3})O_3$–$PbTiO_3$ (PMN-PT) with large piezoelectric constants (d_{33} or d_{31}) that enable a response with a high signal to noise ratio in sensor devices, for example.[15] However, these materials are rigid and brittle by nature, which hinder their integration in soft wearables or application on curved or irregular surfaces, for example. On the other side of the scale, exist piezoelectric organic polymers. Although polymer materials can be directly processed by printing technologies, ceramic materials can be printed in the form of nanomaterials, in composites with a polymer binder.[183]

Among the organic piezoelectric polymers, polyvinylidene fluoride (PVDF) and its copolymer with trifluoroethylene (PVDF-TrFE), are the polymers with higher piezoelectric constant, thanks to its large polarization owing to the chain arrangement along the carbon axis in its β-phase polymorph.[175], [216] Different fabrication processes of PVDF-based devices have been reported using printing technologies, owing to the relative simplicity of formulating PVDF as ink for screen printing or inkjet printing with promising applications as sensors,[168]–[170] actuators[171], [172] or energy harvesters.[173]

Different conductive materials as printed electrodes have been reported, with silver nanoparticle inks and PEDOT: PSS to create fully printed piezoelectric devices.[199], [200] For the silver nanoparticle-printed electrodes, only an all-inkjet printed device has been reported.[16] When screen-printing electrodes, this has only been achieved with screen-printed PEDOT:PSS over screen-printed PVDF based layer. The main drawback of using PEDOT:PSS as electrodes is that they are more resistive and moisture sensitive,[217] and the main drawback in fully inkjet printed device is that the piezoelectric layer is very thin and higher potentials are required to polarize it.

A key issue with PVDF-based polymers in piezoelectric devices is that they are not as sensitive as piezoelectric ceramics, which present d_{33} as large as 2500 pF·cm^{-1},[166] while the reported for PVDF-TrFE is about 40 pF·cm^{-1}.[218] Moreover, to present the piezoelectric effect, PVDF polymers require a poling step to induce an alignment of the internal dipoles inside the polymer layer. Several poling methodologies are reported in the literature[15], where the most common is the electrical field application, usually 50 V·μm^{-1} of PVDF. After removing the applied field, it is expected to maintain the dipole alignment, thus the dipoles will keep their anisotropic orientation.[62] However, printed piezoelectric devices lose their piezoelectricity with time. How and in which conditions this occurs, is not yet fully understood in reported literature concerning fully printed devices. This lack of control of the piezoelectric behavior of PVDF-TrFE printed devices is the key drawback for their technological adoption.

Herein, we present a novel fully printed piezoelectric device based on screen-printed PVDF-TrFE with inkjet-printed silver electrodes with controllable poled state. The combination of printing techniques aims to take advantage of the screen-printed piezoelectric robustness, and the lateral resolution and stability of silver inkjet-printed electrodes, for integrated circuit applications. The fully printed piezoelectric device is investigated in its morphology and its electromechanical response as an energy harvester, a sensor, an actuator, and a temperature switch in the same device design, to demonstrate its application as a multifunctional device model platform.

3.3.1.2. Experimental section

Materials: 125 μm-thick polyethylene terephthalate (PET) Melinex® 506 was used as substrate. Silver-based inks, organometallic IJ-060-I from Inkte, Sicrys photonic cured I50T-11 from PVNanocell, Silverjet DGP-40LT-15C from Advanced Nano Product, and an organometallic gold ink DryCure Au-J from C-INK were evaluated as top and bottom inkjet-printed electrodes respectively. The PVDF-TrFE screen printing ink (FC25 from Piezotech) based on copolymer with PVDF: TrFE ratio of 75:25 wt% was used as a piezoelectric layer.

Inkjet printing: A piezoelectric Dimatix inkjet printer (DMP 2800 from FUJIFILM-Dimatix, Inc, USA) was employed for the inkjet printing of the metal-based inks. The printer was equipped with fillable 10 pL nominal drop volume printheads having 16 nozzles each with a diameter of 21.5 μm. Printing patterns were made using Inkscape layout software and imported with the Dimatix Bitmap editor software. The printing processes were carried out in a standard laboratory environment in ambient conditions, without non-particulate filtered enclosure systems and without control of temperature or humidity to determine the extent to which the sensor devices could be manufactured on an industrial-scale printing system. The silver nanoparticle ink was printed using a distance between two consecutive drops, called drop spacing (DS) of 40 μm, representing a print resolution of 635 dpi (dots per inch), and the DS was used to print the organometallic silver ink was 35 μm (725.71 dpi). Pulseforge photonic curing (PulseForge 1200 form Novacentrix, USA) was employed for the annealing of the nanoparticle's silver ink.

Screen printing: A semi-automatic flat screen printer with a PU squeegee (AT – 60PDfrom ATMA CHAMP ENT, Corp, Taiwan) was used for the printing of the PVDF-TrFE piezoelectric layer. A mask with 100 mesh/cm was chosen according to supplier information to achieve the desired thickness.

Characterization: The contact angle measure system DSC100 (Krüss GmbH, Germany) was used to investigate the surface energy of the substrates. The thickness of the different printed layers was measured with the profilometer (Dektak 150 form Veeco Instruments, Inc, USA). The same profilometer was used to measure the vibration of the piezoelectric device when employed as an actuator applying an AC source. A high voltage source (Z+650-0.32 from TDK Lambda GmbH, Corp, Germany) was used for the polarization of the piezoelectric layer. Scanning Electron Microscopy (SEM, Auriga-40 from Carl Zeiss, Germany) was used for the morphological characterization of each printed layer. Piezometer (90-2030 from APC International, USA) was employed for the measurement of the d_{33} piezoelectric constant. A Sawyer-Tower circuit was used to measure the piezoelectric activity of the device connecting in series the piezoelectric device with a commercial capacitor and applying a high-voltage AC source while measuring with a Yokogawa DLM2034 oscilloscope. DMA 8000 from Perkin Elmer was used to measure Young's modulus of the piezoelectric sensors and to measure the output voltage at different vibrational frequencies. DSC measurements were done at a 10 ˚C min^{-1} heating rate with thermogravimetric analysis (TGA) and differential scanning calorimetry (DSC) (TGA/DSC STAR^e System from Mettler Toledo). FTIR spectroscopy measurements were performed at MIRAS: The Infrared Synchrotron Radiation Beamline at ALBA.[219] An electrodynamic shaker was used to emulate environmental vibrations at different input acceleration magnitudes (Vibration Testing Controller VR9500, Vibration Research, Jenison, MI,

USA). This was controlled through a MATLAB program that allows automatizing, acquiring, and processing the voltage measurements at different frequencies and acceleration values. All this data is measured by an acquisition system (National Instruments PCI-6132 and BNC-2110, National Instruments, Austin, TX, USA) with very high internal impedance to avoid charge leakages (100 MΩ).

3.3.1.3. Results and discussion

3.3.1.3.1. Inkjet inks for printed electrodes preparation

Four types of commercially available metal-based inks were studied about their morphological and electrical characteristics to select the most suitable ink combination for printed top and bottom electrodes on a screen printed PVDF-TrFE based fully printed device. The inks were firstly evaluated concerning their compatibility with PET substrate and PVDF-TrFE screen printed layer, conductivity, linewidth, and resolution. Another evaluated factor was printability by stable drop ejection conditions evaluation without clogging the nozzles, which affects fabrication yield.

Three different silver inks have been chosen because of their different properties both composition and curing parameters. The silver ANP and PVN are nanoparticles (NPs) based on inks with NPs of 50 nm and 100 nm size respectively, however, the main difference between them is the curing method. The silver INKTEC ink is composed of organometallic silver-based molecules. These molecules contain silver and, thanks to the temperature while curing, the organic cluster releases the anchored silver to the system leaving a homogeneous silver layer. Another ink based on gold nanoparticles was evaluated to compare against the silver-based inks. After establishing the proper parameters of the ink ejection in the inkjet printer (Table S1), different lines were printed at different DS to select the appropriate for each ink. As the DS represents the center-to-center distance between two consecutive drops, a line pattern was designed to print droplets from 5 to 75 μm DS, increasing 5 μm each, to check which is the one that presents a continuous line with the lower amount of ink. Discussion of the DS selection and morphological characterization of the inks can be found in Supporting Information.

Wettability of the bottom electrode inkjet printing ink

To characterize the wettability of the silver inkjet inks on the PET substrate, contact angle measurements were done with the different inks and to control if surface treatment is needed to improve the adhesion. As higher the contact angle, the worst is the wettability of the ink with the surface. As seen in Table 1, each silver ink has contact angles below 15 ° and the gold ink has a

contact angle of about 20 ° which corresponds in both cases to a good wettability of the substrate surface and no treatments were needed to increase the adhesion.

Table 1. The contact angle of the different inks on the PET substrate

Property	Inktec	PVN	ANP	Au
Contact Angle (°)	6.1	12.0	12.0	20.4
DS (µm)	35	40	40	15
Resistivity (Ω·m)	$1.1 \cdot 10^{-7}$	$3.8 \cdot 10^{-8}$	$2.2 \cdot 10^{-7}$	$7.4 \cdot 10^{-7}$
Conductivity (S/m)	$9.2 \cdot 10^{6}$	$2.6 \cdot 10^{7}$	$4.6 \cdot 10^{6}$	$1.4 \cdot 10^{6}$
% Bulk	14.5	41.5	7.2	3.1

Printing resolution of the bottom electrode ink

Once the DS is selected, it's crucial to know which is the minimum line width that can be printed with each ink, and therefore know which is the minimum resolution that can be obtained. Six horizontal and vertical lines with different widths (15, 30, 60, 90, 120, and 150 µm) were printed with only one nozzle of the cartridge to ensure the minimum width.

After printing the pattern with all the inks, the line widths were measured using the optical microscope images and the profilometer. The Ag inks presented a small difference comparing the horizontal with the vertical lines owing to the easiest droplet overlap in the horizontal direction, which is the printing direction. This difference is much lower in the Au ink because the size of the drops ejected by the cartridge is lower, decreasing the width of the line. In Figure S3 all the graphics comparing the design thickness with the real thickness of the printed lines can be seen. Comparing first the Ag inks, the three of them presented a width of about 130 µm in the first horizontal line, however, the vertical lines present different derivations, presenting widths of 117, 130, and 147 µm in the ANP, PVN, and Inktec inks respectively. In the case of the Au ink, the thinner horizontal line had a width of 83 µm, too big compared with the thinner vertical line had a width of 58 µm. Even this difference with the thinner lines in both orientations, with greater line widths, this difference becomes smaller until the point that the width is almost the same.

Conductivity of the bottom electrode ink

Another characterization technique done to evaluate the differences between the inks was the conductivity test in the PET substrate. Electrodes of 0.3 and 0.5 mm of path width have been printed with separation distances of 0.5, 1, 2, and 4 cm (Figure S4). The resistance values were measured between both extremes of each path with a multimeter, and with the value of the

transversal area measured with the profilometer, resistivity and conductivity values were calculated for all the inks.

Table 2 shows the main resume of the different morphological and electrical parameters calculated for the inks. As can be seen, the Au ink is much less conductive than the Ag inks, with an average value of $1.4 \cdot 106$ S/m, the fact that was expected given the different properties of both metals being the bulk Au less conductive than the bulk Ag. Then when comparing the Ag inks, the photonic cured PVN ink is the one that presents lower resistivity with an average of $3.8 \cdot 10\text{-}8$ $\Omega \cdot$m, corresponding to a 41.5 % of the Ag bulk value. ANP and Inktec Ag inks are worse than the PVN in terms of electrical parameters, with resistivity and conductivity values lower than 15 % compared with the bulk material (7.2 % and 14.5 % respectively). Due to its lower resistivity and good printability, PVN silver nanoparticle ink is selected to be used in bottom electrodes for fully printed piezoelectric devices in PET substrates.

PVN		ANP	
12.0°	12.0°	12.0°	12.0°
Inktec		**Au**	
6.1°	6.1°	20.1°	20.1°
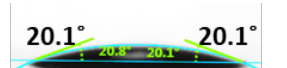
Table 2. Contact angle, DS, and average resistivity and conductivity values were calculated from the resistance of each electrode path distance on the PET substrate.

Morphology and electrical characterization of inkjet-printed top electrode

The same conductive inks tested as bottom electrodes over PET substrate were studied on top of the piezoelectric layer. The challenge of this electrode is to achieve no shortcuts with the bottom electrode through the PVDF-TrFE layer. In this case, the first parameter that was considered to select the appropriate ink is the solvent compatibility with the PVDF-TrFE layer. If the solvent is not compatible with the piezoelectric layer, the top electrode will solubilize the layer and a shortcut will be produced between both the top and bottom electrode, destroying the printed device. For this reason, the Ag Inktec ink was selected as the top electrode.

Therefore, once the ink for the top electrode was selected, the same characterization performed with the inks for the inkjet printing of the bottom electrode, was done to evaluate the printing parameters of the top electrode. Table 3 summarizes all conclusions obtained from these evaluation experiments.

Firstly, to characterize the wettability of the PVDF-TrFE surface, contact angle measurements have been done to control the adhesion of the ink onto the surface and if any treatment to increase this adhesion is needed, but 7.1° of contact angle proves that no treatment is needed.

Then, the same pattern as performed as in the previous section has been printed to determine the minimum DS with which a continuous line is obtained, and given the wettability characteristics of the PVDF-TrFE layer, this DS is 35 µm.

Finally, the patterns to determine the resistivity and conductivity of this organometallic silver ink on the PVDF-TrFE layer are repeated and thus determine that it can be cured homogeneously by providing good conductivity on this layer without producing short circuits between the two electrodes.

Table 3. Parameters of the Ag Inktec ink deposited onto the PVDF-TrFE.

	Contact angle (°)	DS (µm)	Resistivity (Ω·m)	Conductivity (S/m)	% Bulk
Inktec ink on PVDF-TrFE layer	7.1	35	$3.1 \cdot 10^{-7}$	$3.3 \cdot 10^{6}$	5.2

3.3.1.3.2. Fully printed device preparation

Square designs with different areas (3x3, 4x4, and 5x5 mm^2) with two interconnects pads for device contact were used to print bottom and top electrodes to study the correlation of device characteristics with device area. PVDF-TrFE layer was 10 mm x 10 mm in all cases. The full fabrication methodology consists of a sequence of three printing and curing steps, followed by a final poling step, as schematically illustrated in Figure 1a.

The first step in the procedure was inkjet printing the bottom electrode using a PVN silver nanoparticle ink (a_i) over the 125 µm thick PET film. As printed, the bottom electrode was cured by flash sintering. [220] For this purpose, first, it was dried for 5 min at 120 °C in a convection oven to evaporate any ink solvents. Then, it was flash sintered in a photonic curing oven. (a_{ii}). Subsequently, a single layer of PVDF-TrFE (75:25) ink was screen printed over the printed bottom electrode (a_{iii}). This piezoelectric polymer layer was thermally cured to carry out the annealing of the material above its Curie temperature,[221] at 140 °C for 10 min in a convection oven (a_{iv}). Over this layer, the top electrode was printed by inkjet printing organometallic silver ink from Inktec (a_v) and cured in a convection oven for 3 min at 150 °C. Finally, the samples were submitted to a thermal treatment to reduce the organometallic silver material to metallic silver, in

a convection oven for 10 min at 150 °C (a_{vi}). At this stage, the fully printed multilayer device is completed and referred to as "non-poled device". To achieve the piezoelectric form, the non-poled device was submitted to the poling step.[15], [180] The poling conditions found were an electric field of 50 MV·m^{-1}, applied between the top and bottom silver electrodes of the fully printed device, at 95 °C for 15 min (a_{vii}). After this time, the temperature source (hot plate) was removed, and the electric field was maintained until the device cools down to room temperature. At this stage, the fully printed devices are referred to as "poled devices".
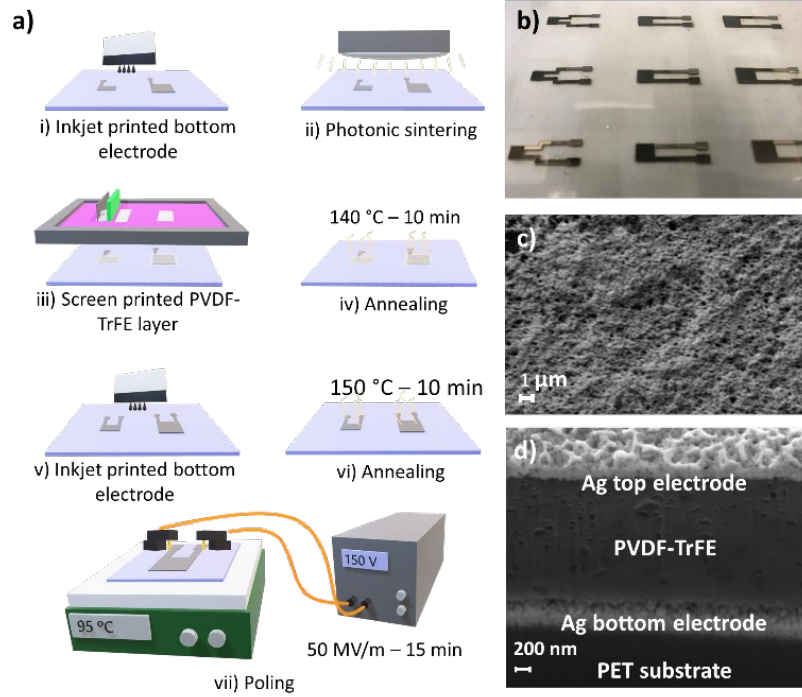
Figure 1. Preparation of fully printed piezoelectric devices and morphological characterization. a) Workflow representation: i) Inkjet printing of silver bottom electrode, ii) photonic sintering of silver bottom electrode, iii) screen printing of piezoelectric PVDF-TrFE layer, iv) thermal annealing of piezoelectric PVDF-TrFE layer at 140 °C for 10 min, v) inkjet printing of the silver top electrode, vi) thermal sintering of silver top electrode at 150 °C for 10 min, vii) poling of the fully printed piezoelectric device with 50 MV/m at 95 °C for 15 min. b) Image of the flexible fully printed piezoelectric device on a 125 μm PET film with the different evaluated areas. SEM images from the surface of the top electrode after thermal curing (c) and SEM images of the FIB cross-section of the printed device (d).

3.3.1.3.3. Printed device characterization

A picture of the fully printed devices with different electrode areas prepared over the PET film is seen in Figure 1b. SEM images were recorded to characterize morphologically the surface of the top electrode of the non-poled device as prepared (observed in Figure 1c).

Figure 1d shows a SEM image of the cross-section of the device made by a focused ion beam (FIB). We can clearly distinguish the three different printed layers, starting over the PET substrate, the Ag bottom electrode, PVDF-TrFE layer, and Ag top electrode, with 450 nm, 3 μm, and 300 nm thickness, respectively. The top and bottom electrodes showed a roughness mean square (RMS), measured by a profilometer of 12 nm and 7 nm, demonstrating the capability of the technique to prepare both silver electrodes for the piezoelectric device. The silver printed electrodes were stable to poling conditions in all experiments performed. Both top and bottom silver electrode resistance was measured before and after each poling step and remains constant over time, having a 5.2±0.4 Ω and a 21.4±2.3 Ω respectively. Therefore, the conductivity does not decrease after the high-temperature process during poling.

To evaluate the electrical characteristics of the printed capacitor, and as quality control capacitance and resistivity between top and bottom printed electrodes were registered at 1 kHz after the poling procedure. The capacitance distribution throughout all samples has a very narrow average capacitance value, which is triggered at 309 ± 22, 539 ± 36, and 833 ± 44 pF for the devices with 3x3, 4x4, and 5x5 mm^2 electrode areas respectively. In Figure S5 the capacitance distribution throughout all samples shows a clear Gaussian behaviour without a very narrow average capacitance value, with more than a 90 % reproducibility. This small standard deviation value elucidates the reproducibility of the proposed fabrication route, where the capacitance values are directly related to the thickness of the piezoelectric material. An increase in the capacitance and a correlated decrease of resistivity between printed electrodes were in accordance with the increasing device area (see Table 4). The mechanical properties of the device were investigated in DMA obtaining a Young's Modulus in the range of 2.3 GPa, (see Figure S6). The Young's modulus of the complete device has a similar value to the Young's modulus of the substrate,[207] showing that the printed layers do not affect the substrate mechanical properties.

FT-IR spectra were registered in reflection geometry, which is perpendicular to the plane, to characterize the printed electrodes and the piezoelectric polymer layer as printed (Figure 2b). The silver electrodes are reflecting surfaces and therefore no peaks were observed. In the polymer layer, CH$_2$ wagging vibration at 1401 cm^{-1} and CF$_2$ symmetry peak at 1182 cm^{-1}, 883 cm$^{-1,}$ and 844 cm^{-1} are observed and known to be related to beta polymorph of PVDF polymer.[222] The FTIR spectra were recorded for both poled and non-poled devices. In situ poling, while applying voltage and temperature, and unpoling of the piezoelectric layer applying temperature were performed while recording the FT-IR spectrum in different polarization lights to characterize the polymer chain orientation during the poling procedure. One observation found is that the printed electrodes served as beam deflectors, which allowed to perform the measurements over the transparent polymer foil (PET). Secondly, it is striking that no differences are observed between

poled and non-poled states, in this experimental configuration, in contrast to reported literature that finds IR as a useful technique to monitor changes in polymer chain orientations after annealing the PVDF-TrFE layer.[222]
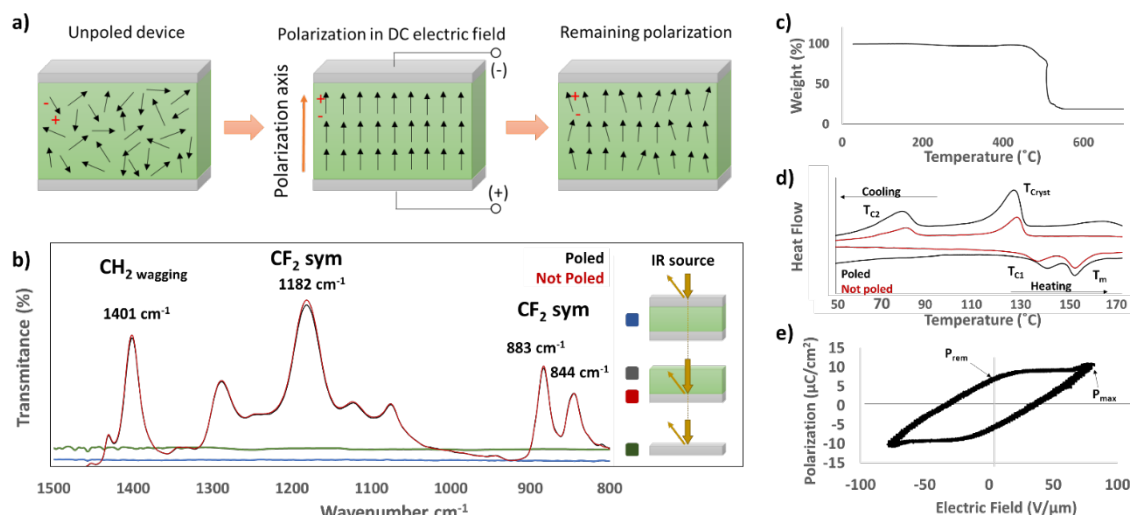

Figure 2. Fully printed PVDF-TrFE device polarization studies. a) Schematic representation of a cross-section of the fully printed device showing the dielectric poles alignment as printed (left), during (middle) and after (right) the poling step conditions. b) MIRAS FTIR spectra layer by layer of the piezoelectric device (in green, the Ag bottom electrode, in red and black the Ag bottom electrode plus the PVDF-TrFE layer poled and no poled respectively, and in blue the Ag bottom electrode + the PVDF-TrFE layer + the Ag top electrode), c) TGA curve of the PVDF-TrFE device, d) DSC measurement of the PVDF-TrFE poled and unpoled and e) hysteresis loop of a printed piezoelectric PVDF-TrFE device.

The prepared devices were also characterized before (as printed) and after poling in DSC and TGA experiments. In Figure 2c, the TGA measurement of the PVDF-TrFE layer shows an initial 2 % weight loss in the first 150 ˚C, related to the water content loss, while material decomposition is registered well above 400 ˚C. The calorimetry analysis (Figure 2d) shows the appearance of a peak at 139 ˚C, related to the Curie temperature, attributed to the formation of the β phase. Both poled and non-poled devices showed the same calorimetric pattern. Both IR and DSC studies results are consistent with the fact that the PVDF-TrFE polymer composition in the commercial screen-print ink is prevalent in β-polymorph and that the poling step induces dipole reorientation aligned perpendicularly to the electrodes, resulting in the activation of the piezoelectric effect of the polymer.

The piezoelectric properties of the printed device with 3x3 cm electrode area were characterized in hysteresis loop measurements as depicted in Figure 2e. The remanent polarization was 6.8 $\mu C \cdot cm^{-2}$ and the coercive field required to switch the piezoelectric polarization was about 45

V·μm^{-1}. d_{33} piezoelectric constant of 34 pC·N^{-1} was measured with a d_{33} piezometer (90-2030 from APC International) in accordance with reported literature.[223]

3.3.1.4. Multifunctional fully printed device platform

3.3.1.4.1. Sensor application

To demonstrate the use of the printed piezoelectric device as a vibrational sensor, two experiments with different setups were evaluated. The first experiment was performed with the DMA equipment, clamping both extremes (the path connection and the piezoelectric part) of the device to evaluate the response under different vibrational frequencies with a controlled displacement of the piezoelectric side. The moving part of the DMA was set to vibrate at different frequencies with a controlled amplitude of 0.5 mm and the output voltage and current generated by the device were measured with an external multimeter. A schematic representation of the measurement with the DMA can be seen in Figure 3a. Measurements were made in devices with and without the poling treatment to demonstrate the piezoelectricity of the poled device. In first experiment, we assessed the stability of the measured signal when the printed piezoelectric sensor was exposed to a long pulse of the same frequency. Figure 3b depicts the output potential signal of the device subjected to a pulse of 15 Hz frequency for 5 minutes, remaining stable at 1.25 V without any voltage loss. The reproducibility of the output potential generated was also investigated. As seen in Figure 3c, by setting the vibration pulse frequency at 15 Hz, the generated output potential remains constant at voltages of about 1.25 V over time without having appreciated changes in the measured value. The small-signal peaks that can be noted when the vibration begins, are caused by initializing the DMA vibration, since it goes from being in a state of "Rest" to a state of "Vibration", generating this small increase in signal. Moreover, to evaluate if the printed vibrational sensor can distinguish between different vibrational frequencies with the same vibration amplitude, different pulses were applied increasing the vibration frequency up to 40 Hz (maximum frequency of the equipment) in steps of 5 Hz. As can be seen in Figure 3d, the potential generated by these pulses at different vibration frequencies increases proportionally up to 40 Hz (the maximum frequency tested at the DMA), which corresponds to a linear sensitivity of 77.2 mV/Hz in the amplitude and range of frequencies tested.

As proof of concept for a wearable application, the flexible device was laminated on the metacarpal's union of a laboratory glove, and an external multimeter was used to evaluate the response of the printed device when bent at different angles with a finger movement. The finger was bent at different angles (180°, 165°, 145°, and 125°) with respect to the flat hand and therefore different displacements of the bending movement.

The output potential measured at each angle is depicted in Figure 3e, where we observed the device output potential gradually increased with the bending angle, being able to distinguish each bending movement with the same bending speed.
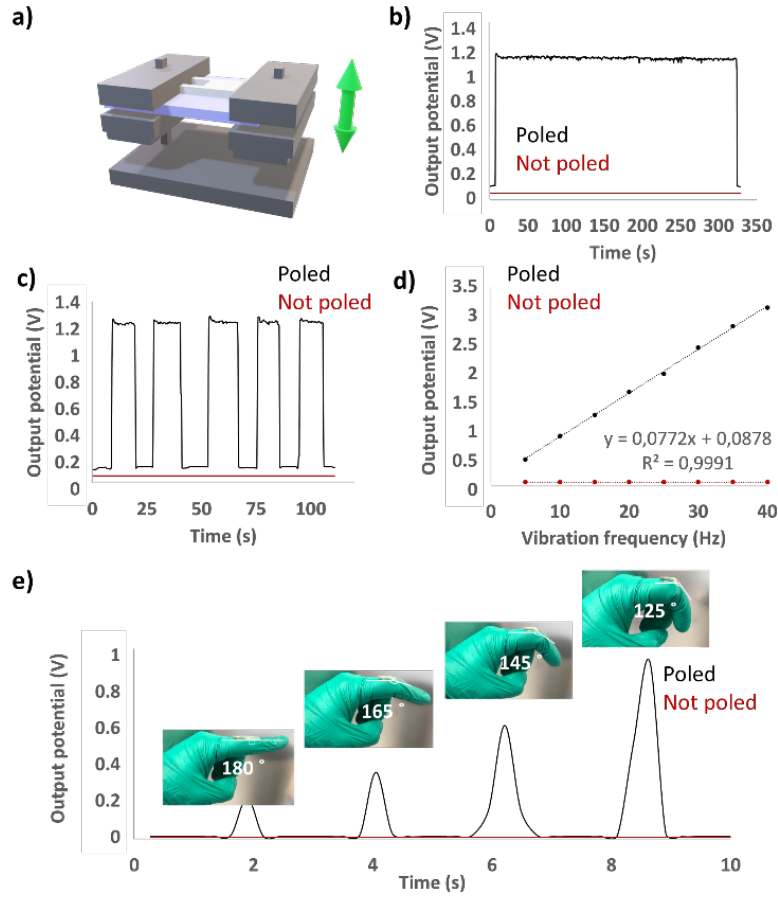

Figure 3. Sensor applications of the fully printed PVDF-TrFE device. a) Schematic representation of the measurements with the DMA. Output voltage(V) generated by the printed piezoelectric device for poled and unpoled PVDF and pulsed actuation of 5 mm amplitude. b) Stability of the measurement signal at 15 Hz of vibration frequency, c) Reproducibility of the measurement signal at 15 Hz of vibration frequency, d) response of the vibrational measurements under different frequencies with the vibrational measurement comparing devices with and without poling treatment and e) response of the printed piezoelectric device at different angles of bending movements

Switching behaviour

It was observed that the poled printed devices remain piezoelectric poled stored in normal environmental conditions after three months. However, it was observed that it was possible to pole the devices again, applying the same poling conditions. To understand the "unpoling mechanism" and exploit this phenomenon for a switch application of our device, we investigated triggering the unpoling of the fully printed devices in a controlled manner. For this purpose, poled

devices (piezoelectric) were studied under different temperature conditions and their piezoelectric properties were monitored through their output voltage as a sensor. Subsequently, after the polling step, poling conditions were applied again to the unpoled devices, in a controlled nitrogen atmosphere, and their piezoelectric state was assessed by measuring their output voltages in sensor mode. This procedure was repeated in several cycles. The two states define the ON (piezoelectric) and OFF (non-piezoelectric) states of the switch. Cycles of poling-unpoling-poling were repeated until there was no recovery of the output potential after applying poling conditions.
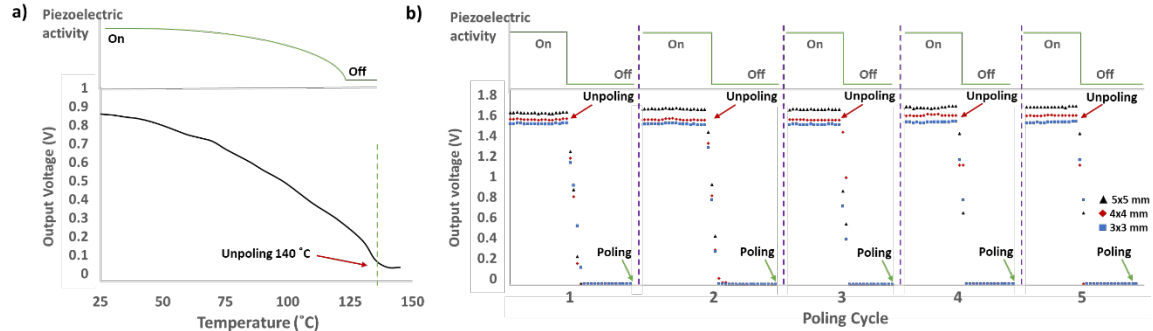
Fig 4. Piezoelectric switching behavior of fully printed PVDF-TrFE device. a) Output potential versus temperature and time on a single device. b) Poling-unpoling-poling cycles of the piezoelectric devices with different area, where the output voltage is represented as a reversible switch triggered by temperature (140 ˚C), while vibrating at 20 Hz with 0.5 mm amplitude.

To find at which temperature the piezoelectric device loses its polarization, the device was hooked to the DMA and the output potential was recorded while increasing the temperature of the chamber. In Figure 4a, the potential curve versus the temperature, while a harmonic vibration is applied, is represented. As observed, while increasing the temperature of the device the output potential gradually decreases until become zero at the temperature of 140 ˚C, a temperature between the Curie and the melting temperatures. This evidences that the initial poled device (piezoelectric) is now unpoled (non-piezoelectric). The unpoling temperature obtained was 140 ˚C and 5 min based on these observations. In Figure 4b, it is seen the output potential recorded in the cycles poling-unpoling applying the unpoling temperature to the device. Is observed a clear recovery of the output potential in each cycle, meaning that this "unpoling mechanism" triggered by temperature is reversible and does not affect neither the PVDF-TrFE layer of the silver electrodes.

3.3.1.4.2.   Actuation

The fully printed PVDF-TrFE devices were also characterized as actuators. For that, a device was placed in a profilometer and connected to an AC source with two actuation modes, as represented in Figure 5a: 1) the device surface fully adhered to a solid support, to monitor actuation via

measuring 3-point vibration of the support, and 2) partially adhered to a solid support and the device area left free-standing, to work as a cantilever. A profilometer tip was put in contact with the device area center, to monitor vibration amplitude (Figure 5b). At each different applied voltage, the frequency of the AC source was adapted to achieve the maximum vibration by the piezoelectric device. Like in the sensor performance, the first experiment was the evaluation of amplitude reproducibility. As seen in Figure 5c, 50-second pulses of 70 V at 80 Hz of the AC source were applied between the printed electrodes of piezoelectric layer. An amplitude deflection of 15 μm was registered in each pulse cycle, indicating a high reproducibility of the system. To validate the stability of the measured vibration. Moreover, a single cycle applying 70 V at 80 Hz of the AC source for 200 s shows a stable deflection of 15 μm as represented in Figure 5d. Finally, to evaluate the response of the devices with different areas and vibration modes, the voltage of the AC source was gradually increased, while the vibration amplitude was recorded with the profilometer as seen in Figure 5e. To corroborate and control the relationship between the applied voltage and the vibration amplitude, an unpoled device was characterized and no electrical response was obtained. In Figure 5e and f, the vibration amplitude of the devices with different areas are represented in response to the applied voltage. As seen, the vibration amplitude is directly proportional to both applied voltage and electrode area with a linear response of the printed piezoelectric device until it deactivates at 160 V. The maximum actuation of the device is obtained with 150 V obtaining deflection values of 37, 30 and 27 μm with the 3-point vibration mode and 43.5, 35 and 26 μm with the cantilever vibration mode for the 5 cm x 5 cm, 4 cm x 4 cm and 3 cm x 3 cm device areas, respectively.
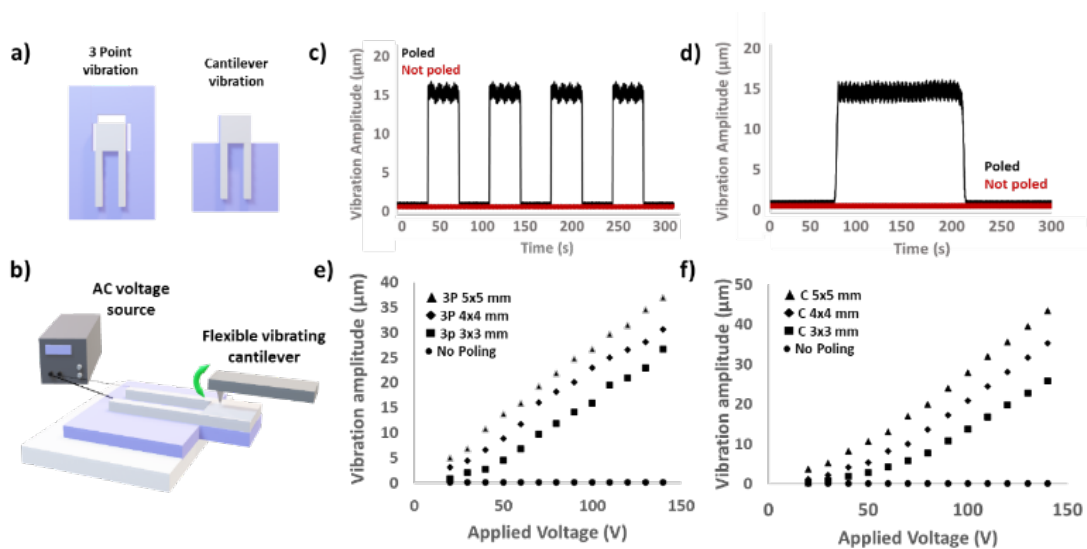

Fig 5. Assessment of fully printed PVDF-TrFE device as actuator. Schematic representation of the two actuator configurations (a) and schematic representation of the measurement with the profilometer (b). Characterization of the printed piezoelectric device as an actuator in 50 s ON-OFF cycles applying 70 V

and 80 Hz of vibration frequency (c) and stability shown in a 200 s cycle (d). Actuation response of the printed piezoelectric device in 3-point vibration mode (e) and cantilever mode at different voltages of the AC source (f).

3.3.1.4.3. Energy Harvester

As seen in the previous sections, exciting the device at different frequencies of vibration and different displacement generates an output potential and an output current. Therefore, to evaluate their performance as an energy harvester, the device with 5x5 mm^2 area was clamped in a single cantilever mode in a shaker, and an inertial mass of 0.42 g was attached at the opposite side of the cantilever to favor the bending of the device with the simulated vibrations. Figure 6a-c shows images of the device excited at 0.25, 0.5 and 0.75 G respectively.

The generated piezoelectric potential from the piezoelectric energy harvester device depends on the piezoelectric coefficient and can be expressed as: [224]

$$V_{OC} = g_{33} \sigma Y t \tag{1}$$

where g_{33} is the piezoelectric voltage constant ($g_{33} = d_{33}/(\varepsilon_0 K)$), in which d_{33} is the piezoelectric charge constant, ε_0 is the permittivity of free space and K is the dielectric constant or relative permittivity), σ is the strain in the perpendicular direction, Y is the Young's modulus of the device, and t is the thickness of the device. According to Eq 1, the Young's modulus is one of the key parameters to obtain high piezoelectric potential from de device. Due to the low Young's modulus provided by the substrate and by the PVDF-TrFE layer, the maximum internal stress will be achieved with high displacements of the device.

The resonance frequency of the device was measured at different acceleration ranges from 0.1G to 0.75G, resulting an applying force between 0.042 mN to 0.315 mN. As can be seen in Figure 6d, the resonance frequency of the devices increases a little with the acceleration, and therefore with the displacement, but always keeping it at low vibrational frequencies < 100 Hz.

According to the fundamental piezoelectric theory,[225] the short circuit current can be described as:

$$I = d_{33} Y A \varepsilon \tag{2}$$

Where I is the generated current, d_{33} is the piezoelectric coefficient, Y is the Young's modulus, A is the cross-sectional area, and ε is the applied strain. According with Eq 1 and 2, the energy

conversion efficiency of the printed piezoelectric device is the ratio of generated electrical energy and applied electrical energy.[224] Subsequently, the output voltage and power of the printed piezoelectric device was measured by measuring the output voltage across the load resistors range from 47 kΩ to 1.9 MΩ (0.047, 0.312, 0.593, 0.858, 1.12, 1.38, 1.64 and 1.9 MΩ). As observed in Figure 6e-f, the output voltage and power increases with the acceleration as can be expected. The maximum voltage is observed across the load resistance of 1.9 MΩ meanwhile the maximum output power is observed across the load resistor of 1.12 MΩ, with a maximum output power value of 1.6 µW with an acceleration of 0.75G.
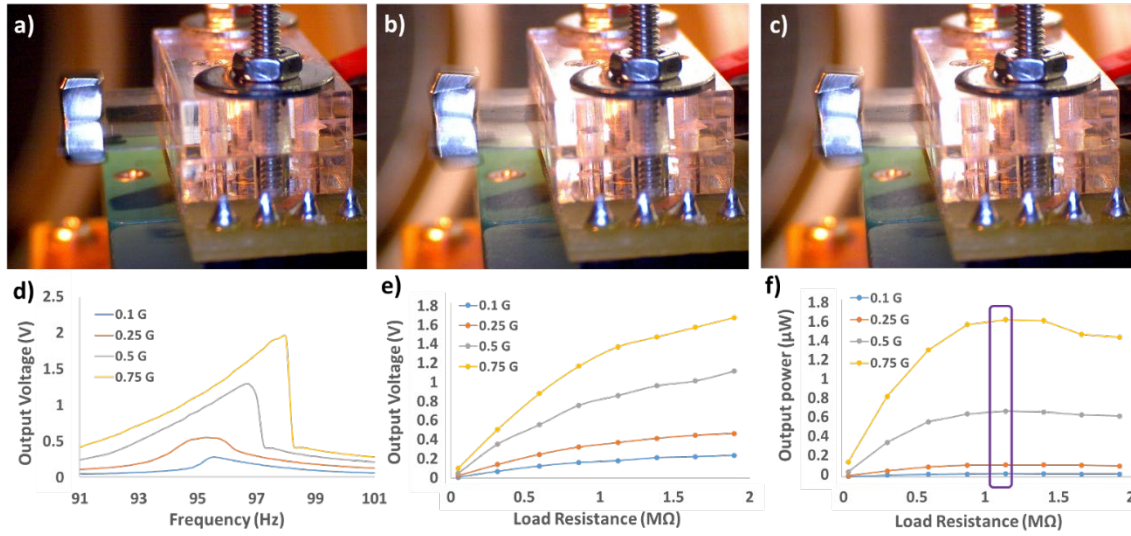
Fig 6. Characterization of the printed piezoelectric device as energy harvester. Image of the vibrational set-up for the energy harvesting with accelerations of a) 0.25 G, b) 0.5 G and c) 0.75 G. d) Output voltage (V) generated at each resonance frequency for different accelerations, e) output voltage (V) and f) output power (µW) with the different load resistance values at each different acceleration

In Table 4, it is summarized the overall characteristics of the fully printed piezoelectric devices prepared in this study and characterized as sensor, actuator and energy harvester. It is striking the reproducibility of the results found for piezoelectric constant, Young's modulus and dielectric constant for the three different electrode areas. The capacitance, output potential, current and vibration amplitude are increasing with increasing electrodes area, while the resistance between electrodes decreases.

Table 4. Summary of the device characteristics of the sensors with different electrode area.

Area (mm²)	Cp (pF)	Rs (MΩ)	d_{33} (pC/N)	Young's modulus (GPa)	Dielectric constant	Output potential (V)[a]	Output current (µA)	Vibration amplitude (µm)
3x3	309± 22	16.1± 2.4	34	2.3	8.8	3.1	0.08[b] 1.1[c]	27[d] 26[e]
4x4	539± 36	8.0± 1.6	34	2.3	8.8	3.4	0.1[b] 1.7[c]	30[d] 35[e]
5x5	833± 44	3.0± 1.1	34	2.3	8.8	3.6	0.125[b] 2.3[c]	37[d] 43[e]

[a]Potential generated at 40 Hz frequency vibration with 0.5 mm displacement
[b]Output current generated by a single tap with 6 mm displacement
[c]Output current generated by a 40 Hz frequency vibration with 0.5 mm displacement
[d]Vibration amplitude of the piezoelectric layer in 3-point mode
[e]Vibration amplitude of the piezoelectric layer in cantilever mode

3.3.1.4.4. Conclusions

In summary, here it is presented a novel fabrication route of a fully printed piezoelectric device based on PVDF-TrFE copolymer. The combination of inks and printing conditions found, allowed to create a robust capacitor structure with well-defined interfaces between inkjet printed silver electrodes and a PVDF-TrFE screen printed layer. Poling conditions of the fully printed device found were 50 MV·m^{-1} at 95 ˚C for 15 min, being reproducible for all devices prepared. The piezoelectric d_{33} coefficient for the fully printed PVDF-TrFE devices were found to be of 34 pC · N^{-1} with a remanent polarization of 6.8 µC · cm$^{-2.}$ Controlled unpoling conditions was found for a thermal exposure at 140 ˚C and, and after poling conditions are applied again to the same device, the device completely recovers its piezoelectric characteristics. Multiple poling-unpoling cycles performed showed the fully reversible mechanism. Maximum output voltages of 3.6 V and output currents of 2.3 µA were obtained in the 5 mm x 5 mm device measured as a vibrational sensor. Maximum displacements of 43 µm when the device was used as actuator under applied voltage of 140 V and output power of 1.6 µW with 1.12 MΩ of load resistor were achieved when was used as energy harvester, and structure-property correlation was found for different electrode areas. The presented study brings novel insights that contribute to fill the gap in materials combinations, preparation methodologies and poling mechanism control of fully printed piezoelectric devices.

Author Contributions

M.A. designed and developed the concept of the research study. M.A. carried out the main experiments, analyzed the results and constructed the figures. M.A., A.M., M.K., P.L., G.M. and

C.D. interpreted the data. M.A., A.M., M.K., P.L., G.M. and C.D wrote the manuscript. All authors have given approval to the final version of the manuscript.

Conflicts of interest

There are no conflicts to declare.

Acknowledgements

Supporting Information

Controlled poling of fully printed piezoelectric PVDF-TrFE device multifunctional platform with inkjet printed silver electrodes

Marc Alique,[a†] Ana Moya,[a] Martin Kreuzer,[c] Paul Lacharmoise,[a] Gonzalo Murillo[b], Claudia Delgado Simao[a*]
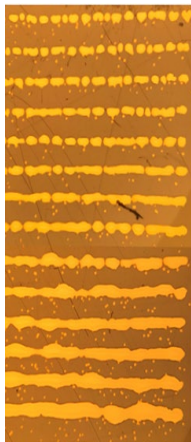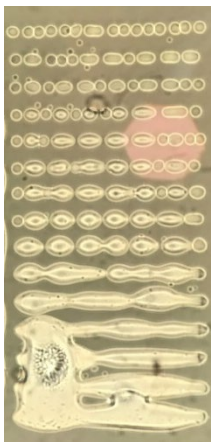
Table S1. Jetting parameters of the different inks.

	Ag ANP	Ag Inktec	Ag PVN	Au
Platen temperature [°C]	40	-	-	-
Cartridge temperature [°C]	35	38	39	30
Jetting frequency [kHz]	5	3	5	5
Meniscus Setpoint	5.0	2.0	5.0	5.0
Initial cleaning	None	SplitPurgueSplit	SplitPurgueSplit	SplitPurgueSplit
Printing cleaning	None	SplitPurgueSplit (50 Bands)	SplitPurgueSplit (70 Bands)	None
ΔV [V]	30	40	30	30
Drop spacing [μm]	40	35	40	15
Δt_1 [μs]	2.560	2.816	2.560	2.560
Δt_2 [μs]	2.560	3.712	2.560	2.560
Δt_3 [μs]	2.560	3.392	2.560	2.560
Δt_4 [μs]	-	0.832	-	-
Level V_1	7 %	20 %	7 %	7 %
Level V_2	100 %	100 %	100 %	100 %
Level V_3	27 %	67 %	27 %	100 %
Level V_4	-	40 %	-	-
Slew rate 1	1.00	0.65	1.00	1.00
Slew rate 2	1.00	0.93	1.00	1.00
Slew rate 3	1.00	0.60	1.00	1.00
Slew rate 4	-	0.80	-	-

Drop spacing selection and morphology for the bottom electrode

After stablishing the proper parameters of the ink ejection in the inkjet printer (Table S1) different lines were printed at different DS (Figure S1). The DS represents the center-to-center distance between the printed droplets from 5 to 75 μm, increasing 5 μm each, to check which is the one that presents a continuous line with the lower amount of ink. Then, to know the thickness of the continuous lines printed at each DS a profilometric analysis has been done. The images of the pattern of each ink and the profile of the continuous lines are shown in the Table S2. As can be seen, each ink presents different pattern in the PET surface, therefore the DS selected will be correlated with the different properties of the inks. Also, in Figures S1 and S2, can be observed that ANP and PVN Ag inks have bigger thickness in comparison with the Ag Inktec or the Au ink and it can be attributed to the wettability properties of the ink in the substrate, because the ones that wet less have a worst distribution of the, pilling up at one point instead of being homogeneously distributed. Analyzing all of this features, the DSs selected are: 40 μm, 40 μm, 35 μm and 20 μm for the ANP, PVN, Inktec and Au inks respectively.

Table S2. Drop spacing pattern of the different inks

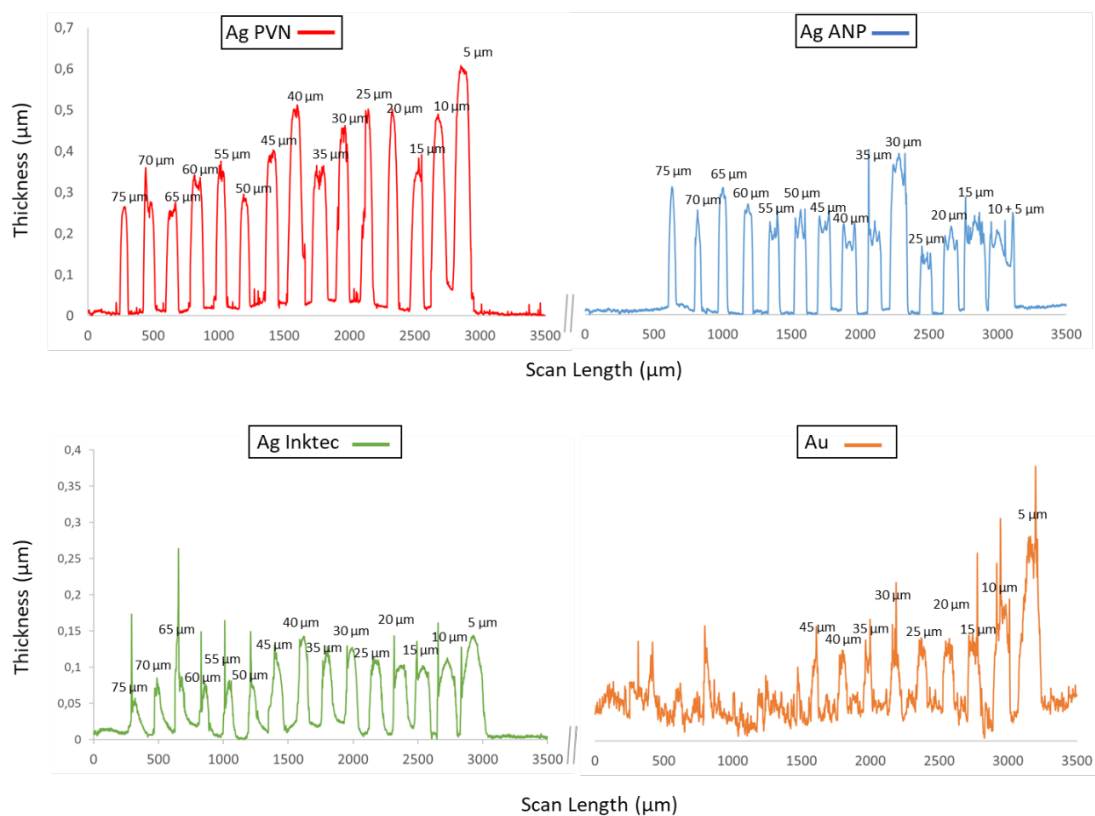| Design	PVN	ANP	Inktec	Au
	40	40	35	35

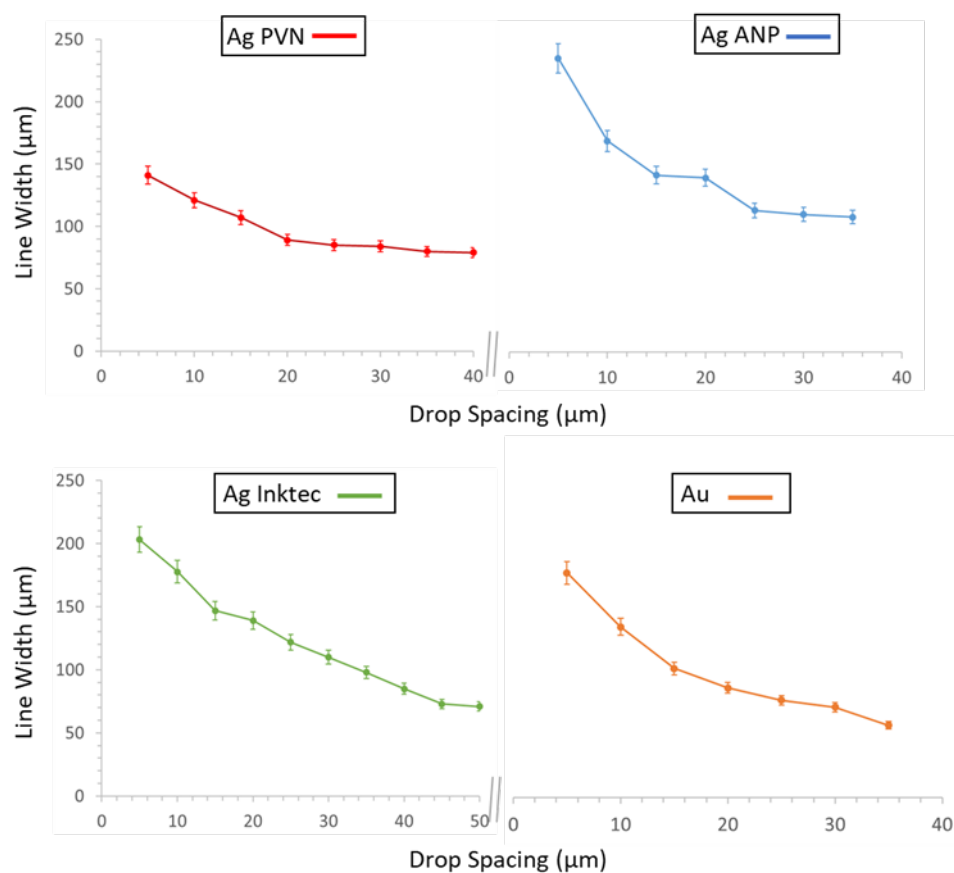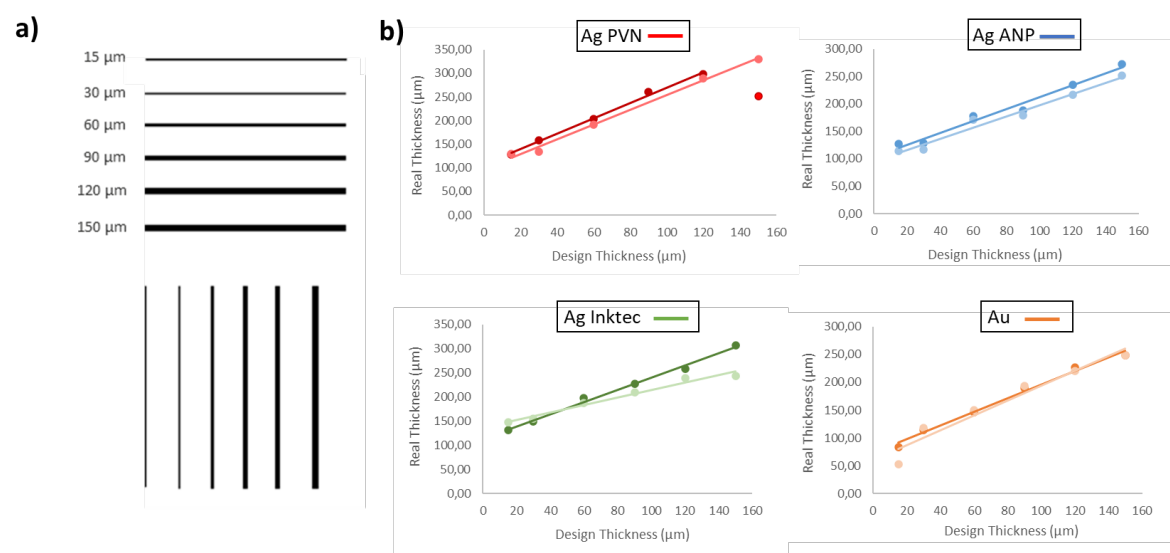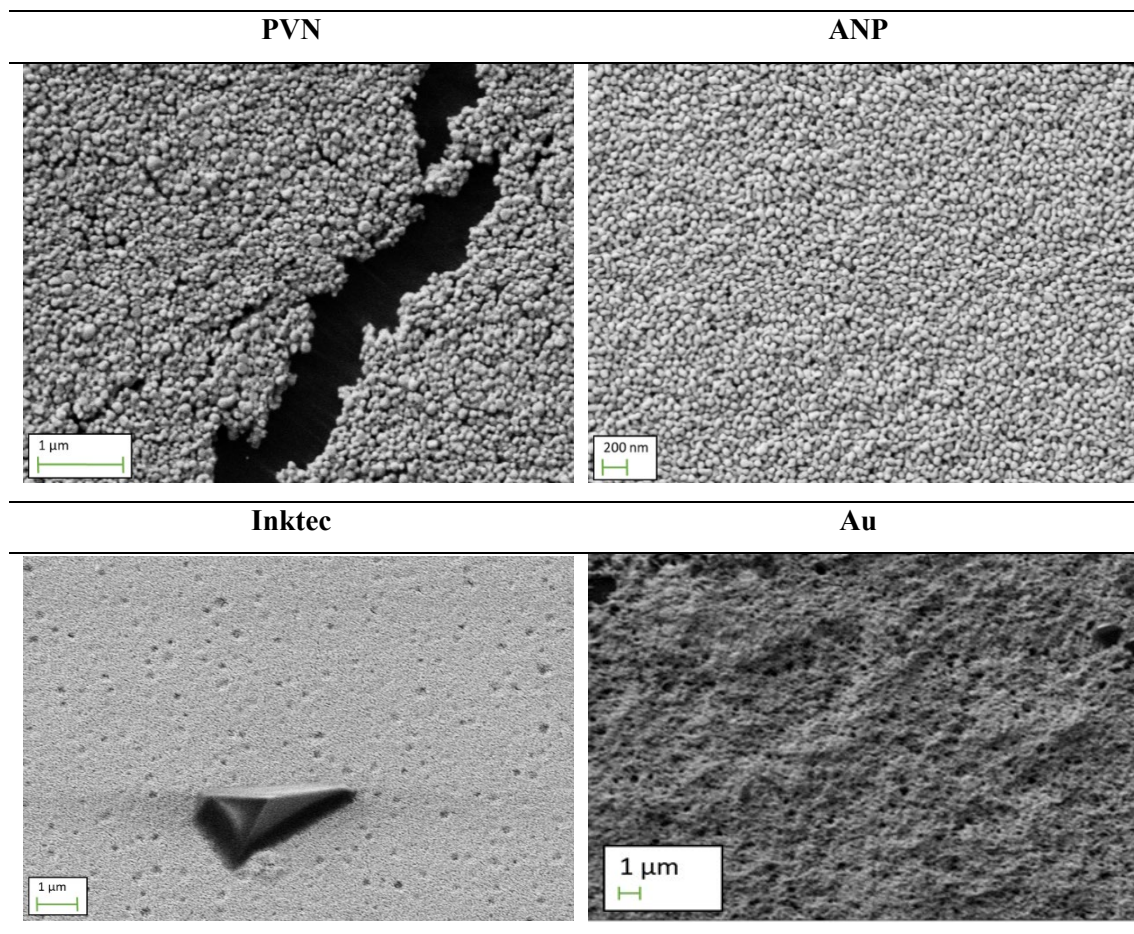**Figure S1.** Profilometric analysis of the printed lines at different drop spacing

Figure S2. Line width of each line printed at different drop spacing (n=3)

Table S3. SEM images of the different inks surface layers.

PVN	ANP

Inktec	Au

Figure S3. a) Line pattern printed to know the resolution of each ink. b) Representation of the line width in vertical and horizontal lines.
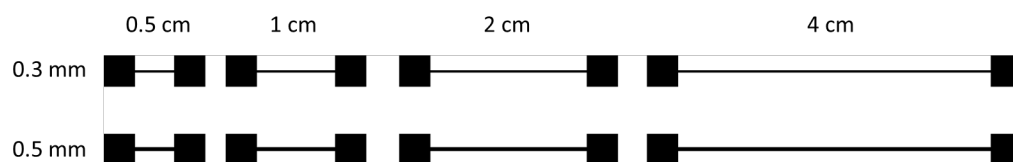
Figure S4. Line pattern designed to characterize the electrical parameters of the inks
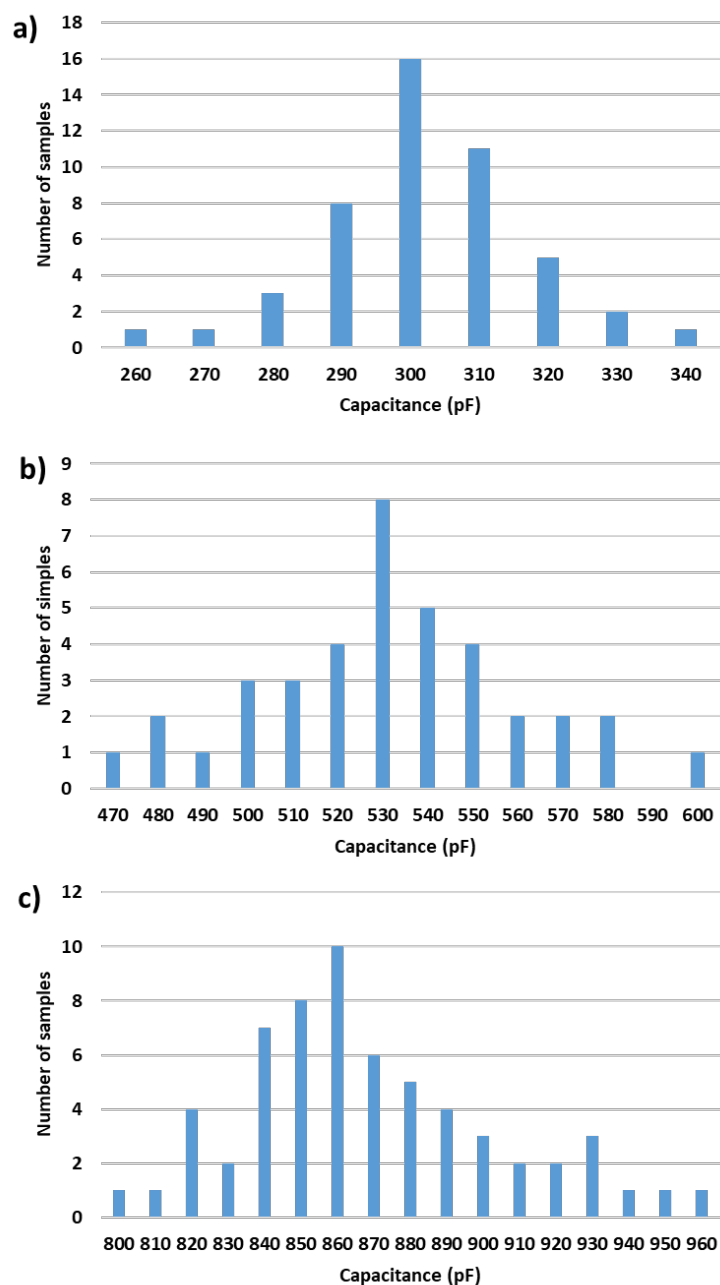

Figure S5. Gaussian distribution of the printed piezoelectric samples for the a) 3x3, b) 4x4) and c) 5x5 mm^2 printed electrodes area.
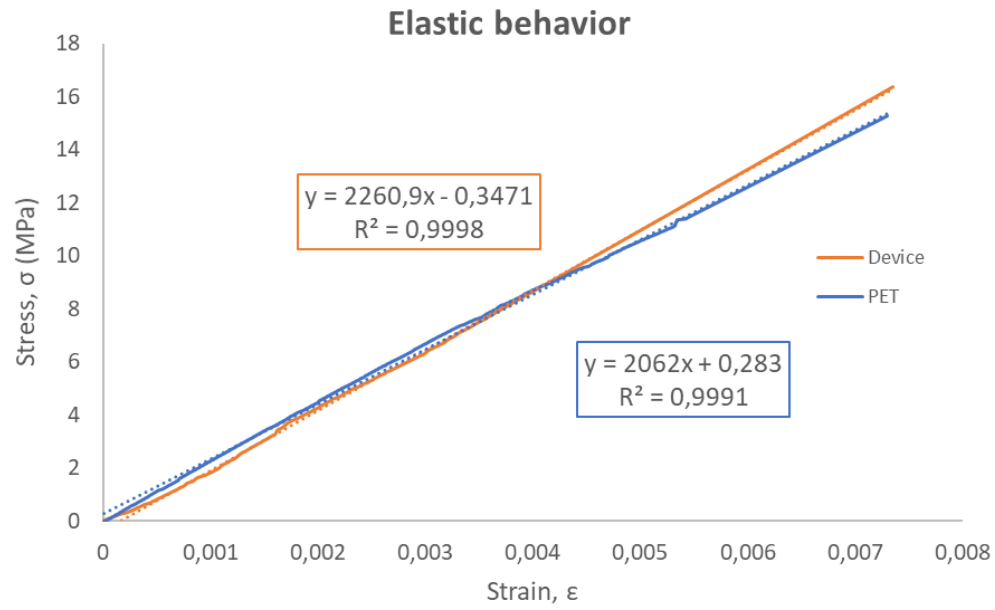
Figure S5. Elastic behavior of the stress-strain diagram to calculate the Young's modulus.

3.3.2. Paper III: Multiparametric sensing electronic skin based on seamless fully printed stretchable piezoelectric devices

The third paper present in this Chapter 3, **Paper III**, is an article about the integration of piezoelectric sensors, fully fabricated with SP in a TPU substrate. For the first time, these printed sensors were printed on a stretchable substrate that is compatible with wearable applications to achieve a human motion monitoring. The stretchable properties of the printed material as well of the structure characterization is performed as single device and in a matrix. The composition of these printed piezoelectric matrix is used for a low-cost, real-time monitoring of a human hand movements.

This article has been sent to an Advanced Science journal and currently is under review*:

Paper III. M. Alique, A. Moya, D. Otero, M. Kreuzer, P. Lacharmoise, G. Murillo, and C. D. Simao. **Multiparametric sensing electronic skin based on seamless fully printed stretchable piezoelectric devices**. The article has been SUBMITTED to Advanced Science journal in July 2022. (Q1, IF:17.521).

Note that, equations, tables and figures numbering in the reproduced research article follow the ones of the published version.

Multiparametric sensing electronic skin based on seamless fully printed stretchable piezoelectric devices

Marc Alique,[1]† Ana Moya,[1] David Otero,[1] Martin Kreuzer,[2] Paul Lacharmoise,[1] Gonzalo Murillo,[3] Claudia Delgado Simao,[1]*

[1]Eurecat, Centre Tecnològic de Catalunya, Functional Printing and Embedded Devices Unit, 08302 Mataró, Spain.

[2]Instituto de Microelectrónica de Barcelona, IMB-CNM (CSIC), Esfera UAB, Campus Universitat Autònoma de Barcelona, 08193 Bellaterra, Spain.

[3]ALBA Synchrotron Light Source, 08290 Cerdanyola del Vallès, Spain

† Electrical and Telecommunication Engineering Department, Universitat Autònoma de Barcelona (UAB).

Corresponding author

E-mail: claudia.delgado@eurecat.org

Abstract

Wearable skin mountable devices, more than flexibility, require conformability, stretchability, and high vapor transmission rate, so that the perspiration processes are not blocked, to assure comfort and stability of use in contact with living bodies. Skin mountable stretchable devices with piezoelectric devices have been reported, based on the integration of PVDF foils with discrete electrodes and stretchable substrates, and show potential in revolutionizing medical devices for remote monitoring applications. However, the electrodes and active layer are never stretchable, only the carrier substrate. Our work reports the full description of novel fully printed stretchable piezoelectric devices, printed directly over a stretchable polymer foil of thermoplastic polyurethane. The stability of the response of the stretchable piezoelectric devices was used as movement sensors through their output potential. An electronic skin based on a fully printed circuit with a matrix of 15 all-printed piezoelectric devices was prepared and investigated and used directly mounted on different body parts, and the real-time monitoring of movements were recorded and analyzed.

3.3.2.1. Introduction

Wearable electronics with integrated sensing devices draw an important deal of attention for their big impact in human society for their potential to delivering trustworthy, comfortable, cost-effective, personalized medicine devices for real time continuous monitoring of patients, for remote health monitoring[226]–[228] to human-machine interaction.[229]–[231] One of the key elements for wearable electronics is the capability to be fabricated in stretchable and conformable substrates such as thermoplastic polyurethanes (TPU),[15], [232] for the later integration and characterization in textile or human-like surfaces. Printed electronics has been a key technology for the over the past decades, owing to the versatility of the technique to prepare devices[15] on textile, conformable and/or stretchable substrates and the advances related with new printable materials.[51] There are several devices that can be manufactured thanks to printing electronics, from conductive and semiconductive elements to dielectric or electroactive polymers. These last ones are some of the most promising elements for wearable electronics[22] and among them, piezoelectric materials are in the set of accessible printed substances with promising results. Reported literature on stretchable piezoelectric devices are usually referring to multilaminate PVDF polymer foils with patterned discrete metal electrodes. Sun et. al.[233] reported a

stretchable piezoelectric device based on PVDF polymer foil laminated in a multilayer fashion with discrete metal electrodes but refer only to the description of the sensing results, without correlating to the fundamental piezoelectric mechanisms. Ha et. al.[234] reported a similar work with discrete metal electrodes and 28 micrometer PVDF polymer foil, in an e-tattoo as a multilayer laminate form, demonstrating ECG and SCG sensing. Khan et. al.[90] obtained a pressure sensor based on polyvinylidene fluoride with trifluoroethylene (PVDF-TrFE) with multi-walled carbon nanotubes (MWCNTs) with flexible properties owing to the polyethylene substrate. Reported literature have been published previously around similar topics (stretchable sensor devices, piezoelectric devices) but we did not find any work that offers a complete study with preparation, fundamental characterization, and device demonstration however, further investigation in stretchable piezoelectric sensors is required. The versatility of piezoelectric materials to generate electrical signals provided from mechanical movements or deformations, and vice versa, owing to the direct and the inverse piezoelectric effect allows their exploitation in movement[235]–[237] and strain sensors.[238]–[240] From the different piezoelectric materials that are commonly combined with printing technology we found the piezoelectric polymers, which have lower piezoelectric constant than piezoelectric crystals, but allows a simple integration in soft wearables substrates by printed technologies for their application in curved or irregular surfaces, being more compatible with stretchable applications.[15] From the existing piezoelectric polymers, the copolymer of PVDF-TrFE is the one that has larger piezoelectric constant of organic materials, owing to its β-phase polymorph, which provides piezoelectric activity to the polymer,[175], [176] and is available as a commercial ink, both for screen-print and inkjet printing.[241] These inks are based on the β-phase polymorph but require a polarization step, to align dipoles and thus activate the piezoelectric effect in the material. Accurate details of the poling step have been largely missing in the different printed PVDF-TrFE devices found in literature, [review] but recently we have reported new insights on the control and reversible switching of the poled state of screen-printed PVDF-TrFE.[25]

However, for practical wearable applications, rigid or merely flexible devices have limited mechanical stability, and is require a high degree of conformability which is usually achieved in stretchable systems. Until now, the integration of ceramic and polymeric piezoelectric materials with stretchable substrates have been hindered owing to lack of compatibility of materials and processes, eg, the high processing temperatures of ceramic materials with soft wearable substrates found in wearable applications, or the difficulty to achieve complex shapes to adapt to body shape and volume. There are a few publications concerning the preparation of piezoelectric sensors in stretchable substrates, being mostly the PVDF itself the substrate used to print the electrodes.[234], [240], [242] However, none of these reports are related to a device (electrodes and piezoelectric layer) printed directly in a stretchable functional substrate. Herein, in this study

we demonstrate a step forward for the first time to our knowledge the fully printing of a PVDF-TrFE piezoelectric sensor on a flexible TPU substrate. This fully printed device has been investigated as a stretchable sensor, integrated as a single sensor in different parts of the body (fingers, knee and elbow) and its response has been correlated to the movement of the body. In a second stage, a fully printed circuit design that included an array of fully printed PVDF-TrFE with PEDOT:PSS electrodes and silver nanoparticle interconnects, was prepared and investigated as a wearable piezoelectric e-skin system capable to monitor the different movements of the human body.

3.3.2.2. Experimental Part

All materials were used as purchased. Rectangular design with 4x15 mm2 area with two interconnects pads for device contact was used to print bottom and top electrodes. PVDF-TrFE layer was 6x17 mm^2 in all cases. The full fabrication methodology, which consists of a sequence of 5 printing steps and one poling step, is schematically illustrated in Figure 1a. The first step was to screen print the electrical connections using a silver ink (Ag 125-28 from Creative Materials) over 150 µm thick TPU film (GenioTex MB from Novogenio). Subsequently, the silver ink was thermally sintered for 10 min at 120 °C to achieve electrical conductivity of the material. Afterwards, bottom electrode was printed using a PEDOT:PSS ink (CLEVIOS SV3 from HC STARCK). After the deposition process, the bottom electrode was thermally cured for 10 min at 130 °C in a convection oven to evaporate the solvent of the ink. Subsequently, a single layer of PVDF-TrFE (80:20) ink was screen printed over the printed bottom electrode. This layer was thermally cured to carry out the annealing of the material above its Curie temperature,[221] at 140 °C for 10 min in a convection oven. The final PVDF-TrFE layer was 4 µm thick. The next step consists of the screen printing of the top electrode. To achieve a homogeneous top electrode layer, the conductive ink was thus investigated to be chemically compatible with the PVDF-TrFE layer to avoid dissolving with the undesired effect of creating a short circuit between the printed electrodes. The same PEDOT:PSS ink was finally used owing its compatibility with the polymeric piezoelectric layer and thermally cured 10 min at 130 °C. The final step dwell in the printing of the isolation layer with a polydimethylsiloxane (PDMS) elastomer ink. This silicone material is biocompatible and the most studied implantable polymer, being perfect for wearable and stretchable applications. Afterwards, solvent evaporation and polymerization of the printable ink was done at 80 °C for 30 min. At this stage, the fully printed multilayer device is complete and mechanically and chemically stable, showing to conserve the full flexibility of the TPU substrate, since no delamination occurs upon bending. The device as prepared is refereed as "non-poled device" from now on. Finally, the poling conditions were investigated to induce the piezoelectric polymorph of the PVDF-TrFE layer following reported literature.[15], [180] To achieve the

correct poled device, an electric field of 75 MV·m^{-1} was applied between the top and bottom electrodes of the fully printed device for 1 min. To avoid the shock of the applied high electric field, and therefore the spark production that can destroy the electrodes, the voltage was applied by means of a ramp, reaching its maximum in 2 min. Figure 1b shows an image of the final device where the different printed layers can be observed without any delamination and the stretching properties provided by the TPU substrate. Scanning electron microscope (SEM) (Auriga-40 from Carl Zeiss) images were taken to characterize morphologically the surface of the top electrode and the cross-section as observed in Figure 1c and d.
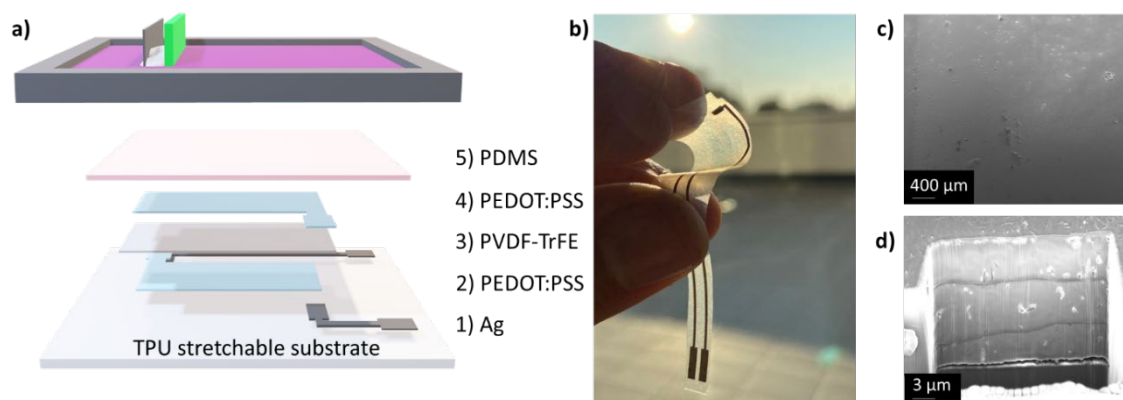

Figure 1. a) Schematic illustration of the screen-printing procedure for the stretchable piezoelectric sensor. b) Image of the conformable printed piezoelectric sensor. SEM images of the piezoelectric device form c) top view and d) cross-section, where the 3 different printed layers that conform the main electrode can be observed.

3.3.2.3. Results and discussion

3.3.2.3.1. Printed device characterization

Hysteresis loop measurements were done with the Sawyer-Tower circuit to characterize the piezoelectrical properties of the printed capacitor. The measurement has been done at a frequency of 30 Hz, obtaining a remanent polarization of 8.7 µC·cm^{-2} and a coercive field about 75 V·µm^{-1}, value with which it is possible to switch the piezoelectric polarization as observed in Figure 2a. d_{33} piezoelectric constant of 42 pC·N^{-1} was measured with a d_{33} piezometer (90-2030 from APC International) being a value in accordance with the literature.[15] As quality control after the poling process, the capacitance of the printed individual capacitor was measured and recorded. As can be observed in Figure 2b, the capacitance distribution throughout all samples shows a clear Gaussian behavior with a very narrow average capacitance value, which is triggered at 755 ± 30 pF with more than 90 % reproducibility. This small standard deviation value elucidates the

reproducibility of the proposed fabrication route, where the capacitance values are directly related to the thickness of the piezoelectric material.

As previously reported, the piezoelectric activity of the PVDF-TrFE is determined by their dipole orientation,[25] however, their crystallinity is an important factor that can affect the device performance.[243] Grazing-Incidence Wide-Angle X-ray Scattering (GIWAXS) was performed to investigate the molecular and crystal arrangement of the PVDF-TrFE layer. As observed in the 2D spectrum of Figure 2c, the piezoelectric layer displays the arced strong reflection near q = 1.3 Å^{-1} following Eq. 1, with symmetry on the meridian which corresponds to both {110} and {200} reflections of orthorhombic PVDF-TrFE crystals, being in concordance with literature.[244]–[246]

$$q = 4\pi \, sin\theta/\lambda \qquad\qquad \text{Eq. 1}$$

This preferential orientation in the γ axis indicates the orientation of the molecular chain parallel to the surface substrate owing to the inertial force of the screen-printing technique. In this situation, both α and β chains can rotate around the γ axis randomly. Thanks to the external electric field applied in the polarization step, a preferential orientation of the polar β axis is induced towards the electric field direction, which is responsible for the large polarization of the PVDF-TrFE.[245]

Furthermore, IR structural characterization of the piezoelectric polymer was done to evaluate the robustness of the printed layer through the stretching process. To further evaluate the piezoelectric layer, polarized light at 0˚ and 90˚ was used for the IR measurement. In Figure 2d IR spectrum of the PVDF-TrFE through the PEDOT:PSS electrodes can be observed before and after stretching with 20 mm displacement. In the polymer layer, CH2 wagging vibration at 1401 cm^{-1} and CF2 symmetry peak at 1182 cm^{-1}, 883 cm^{-1} and 844 cm^{-1} are observed and known to be related to beta polymorph of PVDF polymer.[222] As depicted, no several changes appear in the structure of the printed polymer, demonstrating that the piezoelectric activity became from the dipole alignment as explained in literature.[25]
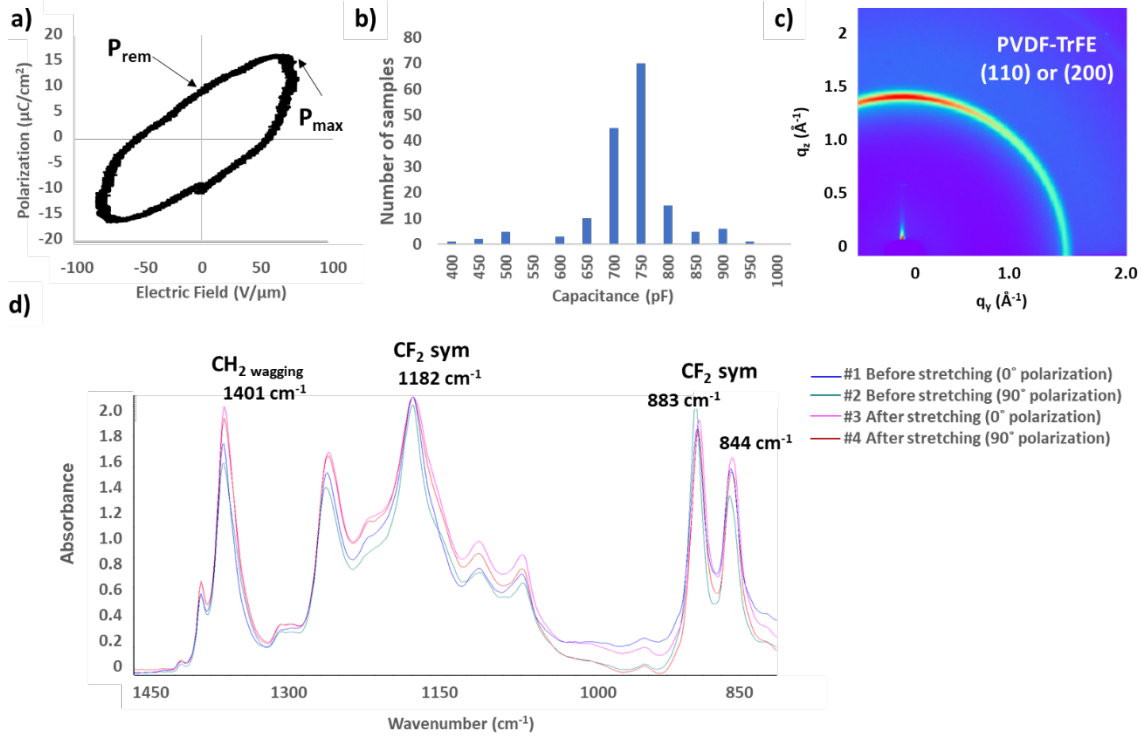
Figure 3. a) Hysteresis loop of a stretchable piezoelectric PVDF-TrFE sensor. b) distribution of the capacitance value and c) synchrotron source GIWAXS spectra of the PVDF-TrFE layer and d) synchroton source FT-IR spectra of the PVDF-TrFE piezoelectric layer before and after reaching their maximum stretchablility with different polarized lights.

3.3.2.3.2. Stretchability characterization

After the electrical characterization of the device was done, the device was placed in a uniaxial motor and its characteristics as stretchable piezoelectric device were evaluated. As first evaluation, capacitance and resistance of the full device were monitored at different displacements with 0.5 mm increments. In Figure 3a the variation of the capacitance is represented over time. As can be seen, the trend of both parameters is to decrease as the applied displacement increases, since the thickness of the piezoelectric layer is expected to decrease when the device is stretched. Furthermore, capacitance and resistance values are inversely proportional considering that the considering that the device behaves as a capacitor. When the displacement value is higher than 3 mm, the resistance of the printed device highly decreases, obtaining less potential response, until the strain is 153%, an adequate value according to the literature,[247] arriving to their maximum stretchability (ε) response, breaking the piezoelectric properties and reaching their limit stretch performance. With these values, the slope of the relative change in the capacitance the Gauge Factor (GF) was calculated. In this piezoelectric stretchable sensor, the electrical response can be characterized though the capacitance value according to Eq. 1

$$GFs = \frac{(1 + \varepsilon)C_0 - C_0}{\varepsilon C_0}$$
Eq. 2

With this capacitive approach, the GFs of the stretchable piezoelectric sensor is 1, due to the theoretical limitations of the capacitive-type sensors.[248], [249]

After defining the stretching limit of the device, their piezoelectric response has been characterized in terms of output voltage while stretching and relaxing the materials. To stablish the linear response of the sensor, their characterization was divided in two main parts: 1) output voltage measured with a fixed acceleration, but different displacements and 2) output voltage measured with fixed displacement but with different accelerations (Figure 3b). With a fixed acceleration it can be observed how the output voltage increases as displacement increases up to 1.5 mm. From this point, the maximum displacement speed is achieved and there is no acceleration, therefore the output voltage remains constant as the displacement continues to increase.

Afterwards, the response and relaxation time of the printed stretchable sensor, the output voltage was recorded while the stretching movements were performed and the time was recorded to know a 90 % time constant (as standard response time value for stretchable sensors).[250] As seen in Figure 3c, the stretchable sensor presents a fast response time of 200 ms. Recovery time is another important parameter of stretchable strain sensors under dynamic loads. In this case, the piezoelectric response of the sensor presents a recovery time of 1.2 s a value near to the polymer-based sensors.[251]

Finally, the dynamic durability of the stretchable piezoelectric sensor was measured by monitoring the output voltage in the long-term stretching/releasing cycles. As seen in Figure 3d the piezoelectric response in constant up to 360 cycles (with a maximum error of a 20 %). From this point the response starts to decay up to 450 cycles, where becomes more unstable until it breaks at 1300 cycles.
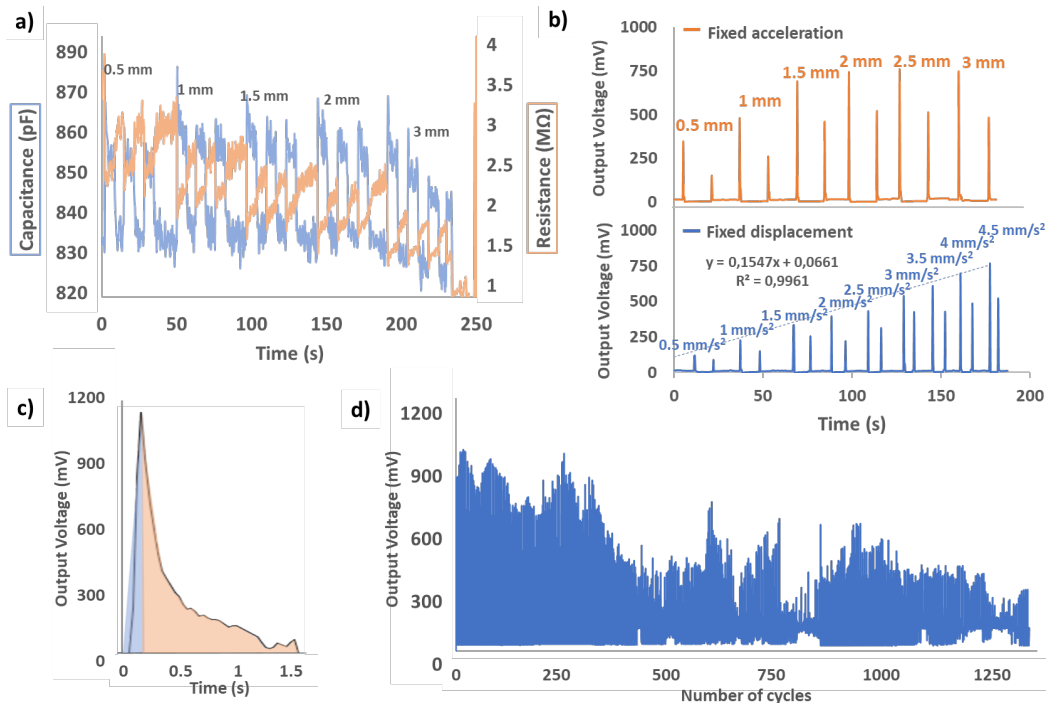
Figure 3. a) Capacitance and resistance characterization of the piezoelectric device under different stretching displacement values, b) Graphical representation of the output voltage versus the stretching and relaxing displacements with fixed acceleration and displacement respectively, c) response and recovery time of the stretchable piezoelectric sensor and d) graphical representation of the dynamic durability of the stretchable printed sensor for several stretching cycles.

As summary, Table 1 elucidates the characteristics of the PVDF-TrFE printed piezoelectric sensor:

Table 1. Stretchable characteristics of the fully printed piezoelectric device.

d_{33} Piezoelectric constant	42 pC·N^{-1}
Remanent polarization	8.7 µC·cm^{-2}
Coercive field	75 V·µm^{-1}
Capacitance	755 ± 30 pF
Stretchability	153 %
Gauge Factor	1
Response time	200 ms
Recovery time	1.2 s
Dynamic durability	1300 cycles
Linear range	Up to 4.5 mm·s^{-2} with fixed displacement

3.3.2.3.3. Fully printed stretchable single device sensor characterization

As proof of concept for the wearable application, the printed piezoelectric sensor was attached to different body parts to monitor movement as function of the str. An image of the stretchable sensor and the measurement positions (chest, elbow, knee, and the five metacarps) are schematically illustrated in **Figure 4a**. The AC output voltage produced by the stretchable piezoelectric sensor was measured for different reproducible movements. In **Figure 4b-f**, the stretchable sensor was placed in the metacarpal's union and the finger bending movement was performed in a reproducible way. As observed, the intensity of the output signal maintains constant over time either in the movement of shrinking or stretching the fingers, since the signal is taken in alternating current, demonstrating the reproducibility of the piezoelectric performance. In **Figure 4g**, the stretchable sensor was placed in the elbow olecranon bursa, and the movement of stretching and contracting the arm was repeated with the same frequency and intensity. As elucidated, the measured output voltage remains constant over time, demonstrating again the reproducibility of the measured signal. Following with the characterization of the piezoelectric stretchable sensor, the flexible band was placed in the middle of the patella.
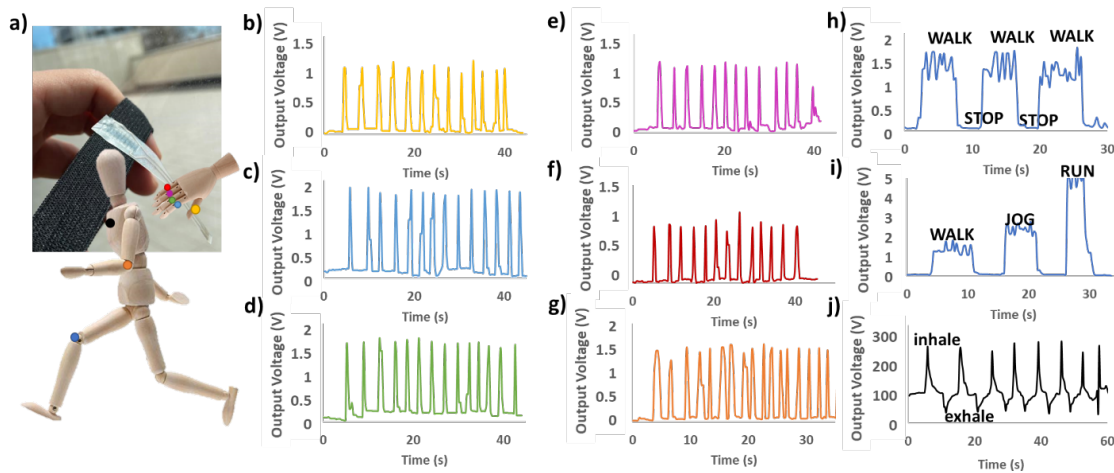

Figure 4. a) Image of the piezoelectric stretchable sensor and a schematic color ilustration of the sensor location for the motion measurements. AC output voltage measurement of the same bending movement for the b) thumb, c) index, d) middle, e) ring, f) pinkie and g) elbow. h) AC output voltage measurement with the stretchable sensor located in the kwee while walking and stoping with the same speed and i) while walking and stoping with different speeds. j) DC output voltage measurement of inhalation and exhalation in respiration monitoring.

3.3.2.3.4. Sensing electronic skin with fully printed stretchable matrix device circuit

Once the fabrication conditions were optimized and the single unit of the stretchable printed sensor was characterized, we had changed the design to integrate a matrix of 15 units of the stretchable sensors for the monitoring of the hand movement. The desing was optimized to integrate the sensors in the metacarpal's union of all the hand fingers and in the wrist joint to monitor the different dynamic moves. To asegurate that the printed sensor matrix keeps the same characteristics than the individual unit, the same area and the same printed layers and conditions were used. In Figure 5a, an image of the printed design on TPU, which includes the design for both hands, can be observed. After the printing, the piezoelectric sensors were poled with the same poling conditions and the hand profile was delimited with laser cutting. As with the individual sensors, quality control by capacitance measurement was done after the poling, obtaining an average value of 734 ± 12 pC. This small standard deviation value despites the high reproducibility of the printing technique for the matrix fabrication, obtaining very symilar thickness values of the piezoelectric layer. Figure 5b shows the integration of the stretchable exoskeleton with the hand. Thanks to the sticky surface and the biocompatibility of the PDMS layer the wearable unit can be addhered to the skin without further effort.

Evaluation of the piezoelectric matrix was performed by measuring the output voltage upon different bending movements. In this example, the signals from the piezoelectric sensors were measured and transformed through an Arduino UNO board, which was flashed with a code that uses the analog to digital converter (ADC) to read the signals comming from the printed glove. As a result, the microcontroller can modulate the intensity of two LEDs that are connected to two pulse-with modulation (PWM) outputs, one for the blue LED and the other for the yellow LED. In Figure 5c we can observe that both LEDs are turned off and in Figure 5d, when a bending motion was produced by the hand fingers, both LEDs produces a light signal directly related to the output voltage produced by the dinamic movement. Finally, in Figure 5e, the correlation of the piezoelectric response with the intensity generated by the LEDs is correlated regarding time. As observed, the signal of the LED matxes with the response of the piezoelectric sensor. After the bending movement was produced, a 3 seconds atenuation time was observed in the signal, corresponding to the dinamic response of the piezoelectric stretchable sensor. A signal peak of output voltage was produced when they detected a deflection, with an intensity directly related to the motion speed, and afterwards this signal needs a relaxation time to come back to its initial state.
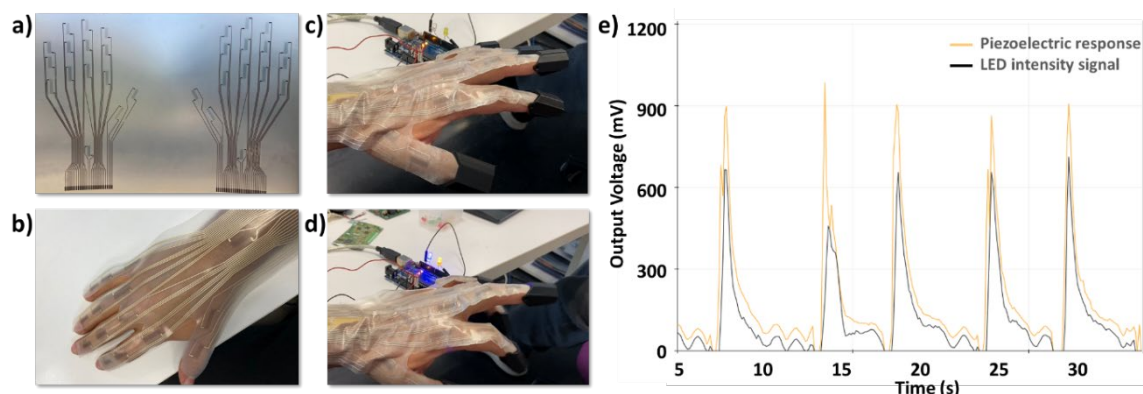
Figure 5. Images of the piezoelectric matrix on a stretchable TPU substrate where a) is the image of the printed design and b) the stretchable piezoelectric matrix integrated in the hand. Images with the printed matrix integrated with a light as a response in the back while c) on relax and d) bending the fingers. e) AC output voltage response of the stretchable piezoelectric matrix, correlated with the intensity of the LED, for each finger bending.

3.3.2.4.   Conclusions

A fully printed stretchable piezoelectric device based on PVDF-TrFE copolymer was prepared directly on a TPU stretchable foil. Maximum d_{33} piezoelectric constant of 42 pC·N^{-1} reported for the polymer was also obtained in this stretchable device form. A remanent polarization of 8.7 μC·cm^{-2} and a coercive field about 75 V·μm^{-1}. This novel stretchable sensor presents a dynamic response with a 3 mm of maximum displacement without losing its piezoelectric activity and returning to its original state with a maximum stretchability of 153%. The stability of the piezoelectric response allowed to use this stretchable fully printed devices as body movement monitoring sensors, correlating their output potential variation as a function of the strain. In a step further, exploiting the scalability of printed electronics preparation methodology presented, a fully printed stretchable piezoelectric matrix composed by 15 individual sensor units, was prepared, and directly used as an electronic skin device.

3.3.2.5.   Experimental Section

Materials: 150 μm-thick TPU (GenioTex MB from Novogenio) was used as stretchable substrate. The PEDOT:PSS electrodes were based on the Clevios SV3 screen printing ink from HC STARCK. The PVDF-TrFE screen printing ink (FC20 from Piezotech) was based on a copolymer with PVDF:TrFE ratio of 80:20 wt%. The Ag current collector pads were based on the 125-28 Ag ink from Creative Materials. PDMS encapsulation layer was developed with Sylgard 184, a bicomponent ink from Ellsworth Ibérica

Screen printing: A semi-automatic flat screen printer with a PU squeegee (AT – 60PDfrom ATMA CHAMP ENT, Corp, Taiwan) was used for the printing of the different layers. The mesh dimensions were chosen individually for each printing material in order to achieve the desired thickness. For the PEDOT:PSS electrodes, a 140T mesh produces enough thickness for good homogeneity and conductivity. For the PVDF-TrFE layer, a 100T mesh was chosen to achieve a desired thickness of 4 μm.

Characterization: High voltage source (Z+650-0.32 from TDK Lambda GmbH, Corp, Germany) was used for the polarization of the piezoelectric layer. Scanning Electron Microscopy (SEM, Auriga-40 from Carl Zeiss, Germany) was used for the morphological characterization of each printed layer. A piezometer (90-2030 from APC International, USA) was employed for the measurement of the d_{33} piezoelectric constant. A Sawyer-Tower circuit was used to measure the piezoelectric activity of the device connecting in series the piezoelectric device with a commercial capacitor and applying a high-voltage AC source while measuring with a Yokogawa DLM2034 oscilloscope with an input impedance of 1 MOhm. FTIR spectrum measurements were performed in reflection geometry at the MIRAS beamline of the ALBA synchrotron. Infrared light has been polarized parallel (0°) and perpendicular (90°) to stretching direction. GIWAXS spectrum measurements were performed at the NCD-SWEET beamline of the ALBA synchrotron.

Supporting Information

Supporting Information is available from the Wiley Online Library or from the author.

Acknowledgements

4. Fully Printed Electrochemical Sensors for Water Monitoring Systems

In this chapter, it is presented the general characteristics of electrochemical techniques, followed by an overview of electrochemical sensors. In addition, the miniaturization routes through printing techniques for these electrochemical sensors are presented. Then, two different electrochemical devices are presented. The first one is a fully printed solid-state iridium oxide (IrOx)-based pH sensor for medical and environmental applications with a single device, which can be used as single-use thanks to the novel fabrication route. The second device presents a novel approach for water quality monitoring based on the Lab-on-a-Chip (LoC) approach, where seven different sensors (free chlorine (FC), dissolved oxygen (DO), pH, redox, conductivity, temperature and flow) are included, combining all the different printing techniques to obtain the best fabrication route.

4.1. Overview of electrochemical sensors

The use of electroactive materials to construct smart devices for environmental monitoring (EM) is a key point to control the vast majority of interferences, playing an important role in the fields of environmental conservation and monitoring, disaster and disease prevention, and industrial analysis.[252] If we perform a closer look at the use of sensors for water monitoring, we can determine that the main uses are based on electrochemical sensors. With the increase of new fabrication technology and the development of new functional materials, the miniaturization of these types of sensors has provided useful tools widely used for the fabrication of Lab-on-a-Chip (LoC) for Point-of-Need (PoN) monitoring.

Electrochemical sensors start with the invention of the glass electrode by Cremer in 1906.[253] This idea was used by Haber and Klemensiewicz in 1909, performing the basis for analytical applications.[254] Their interest in society is continuously increasing owing to the wide range of potential applications that can afford, being very close in daily life, where they continue to meet the expanding need for rapid, simple and economic methods of determination of numerous analytes.

The sensors used in this Chapter 4 are based on electrochemical transduction (amperometric, potentiometric or impedimetric sensors). These types of measuring methods are ideal for their miniaturization owing to the easy fabrication of the electrodes. This miniaturization involves a decrease in the reagent consumption and the sensor size, allowing low limits of detection and a wide response range. In this thesis work their use has been focused on the analysis of water monitoring.

In the following section, it is described the working principle of the electrochemical sensors used in this thesis work. A summary about; potentiometric, amperometric and impedimetric techniques are introduced, centering on their use for the studied and performed: pH, redox, DO, FC and conductivity sensors.

4.1.1. Potentiometric sensors

In these type of sensors, the information is obtained by converting the recognition process into a potential signal, which is logarithmically proportional to the concentration (activity) of species generated or consumed in the recognition event.[252] The Nernst equation (Equation 4.1) logarithmically relates the measured electrode potential, E, to the relative activities of the redox species of interest:

$$E = E^0 - \frac{RT}{nF} ln \frac{a_0}{a_R}$$

Equation 4.1

Where E^0 is the standard electrode potential and a_0 and a_R are the activities of the oxidized and reduced species, R is the universal gas constant; T is the absolute temperature; F is the Faraday constant and n is the number of moles of electrons exchanged in the electrochemical reaction.

The main structure of a potentiometric sensor has two electrodes, where one electrode is the indicator, and the other is the reference. Normally, the potentiometric measurement relies onto zero current value. The potentiometric measurement involves the determination of the potential difference between the indicator electrode (IE) and the reference electrode (RE). The importance of the stability of the RE is crucial to obtain a reliable measurement, and their long-term stability relies on their good performance. Depending on the selectivity of the IE, different analytes can be measured.

The simplicity of necessary equipment for potentiometric measurement and data acquisition and the low effort for maintenance and calibration makes potentiometric sensors very easy to use, being able to obtain signals in real-time measurement. Despite their simplicity, potentiometric sensors present different influences that can affect depending on the measuring conditions such as: pressure, temperature and chemical composition of the signal, determining the limits of the application.

Ion-selective electrodes (ISEs) are the most representative potentiometric sensors. These type of sensors uses an IE which selectively measures the activity of a particular analyte ion. This electrical response is provided by the RE and the potential signal is generated by a charge separation between the ion-selective membrane and the solution due to selective partitioning of the ionic species between these two phases. The electrical response to an ISE is provided by a RE in contact with the internal solution that contains chloride ions at a constant concentration.[255]

ISEs have evolved throughout history. As previously mentioned, the first ISE was developed by Cremer in 1906 [253] and it was based on glass membranes as pH sensors, where the selective material was doped on the membrane (Figure 4.1 (a)). The concept of liquid membrane was introduced half a century later by Ross. [256] this type of ISEs are based on a water-immiscible liquid substance produced in a polymeric membrane (Figure 4.1 (b)). Thanks to this concept, Simon reported the first liquid membrane[257] and prompted Bloch to develop the ionophore membrane on polyvinyl chloride,[258] being a key point for their later miniaturization (Figure 4.1 (c)).
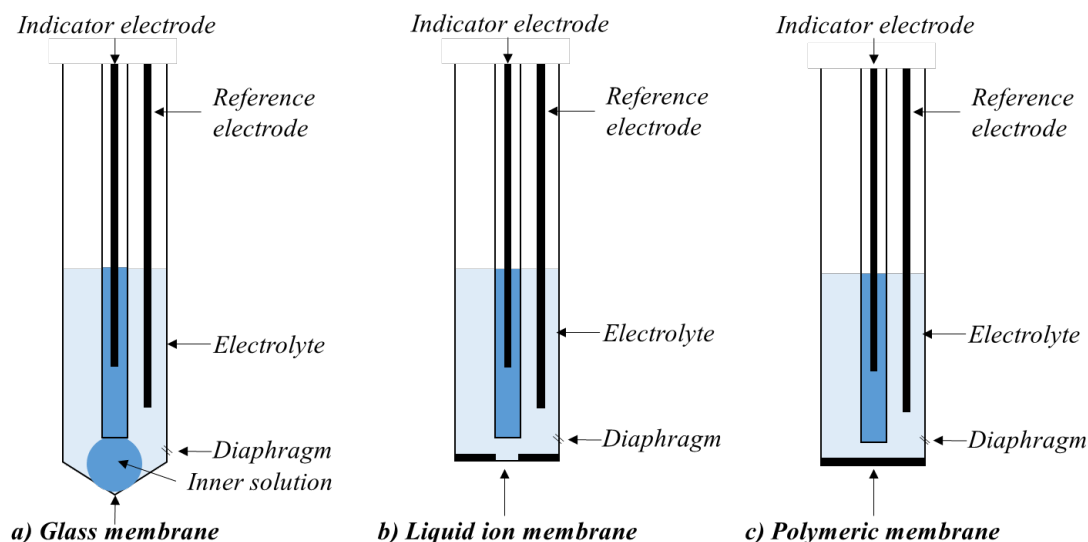
160

Indicator electrode *Indicator electrode* *Indicator electrode*

Reference electrode *Reference electrode* *Reference electrode*

Electrolyte *Electrolyte* *Electrolyte*

Diaphragm *Diaphragm* *Diaphragm*
Inner solution

a) Glass membrane **b) Liquid ion membrane** **c) Polymeric membrane**

Figure 4.1 | Liquid junction potentiometric ISE in a combination with the RE with a) glass membrane, b) liquid ion membrane and c) polymeric membrane.

All these conventional systems described are based on the junction-liquid connection, where one side of the ISE membrane is in contact with the sample and the other with the electrolyte to obtain the signals. In this thesis work, the miniaturization of these sensors for the fabrication and study of pH and redox sensors is performed. This miniaturization is based on a planar solid-state construction approach and is further explained in Section 4.2.

4.1.2. Amperometic sensor

The amperometry technique is one of the methods available from voltammetry. This is an electroanalytical method where the current is linearly dependent upon the concentration of the electroactive species (analyte) involved in a chemical or biological recognition process. There are different methods available in the voltammetry technique depending on which way this potential is applied. When the applied potential is fixed during the time, the technique is called amperometry. In the amperometry technique, the continuous measured current results from the oxidation or reduction of an electroactive species in a chemical reaction,[259] and this current is related to the concentration of the analyte presented. Thus, if a redox active specie is reduced at the electrode surface, the reaction can be written as:

$$Ox + ne^- \rightarrow Red^-$$

Equation 4.2

where Ox is the oxidized form and Red is the reduced form of the analyte. At standard conditions, this redox reaction has the standard potential E^o. This potential this potential is the one applied to

measure the desired species and the obtained current value follows the Cottrell equation for a planar electrode:

$$I = nFA \sqrt{\frac{D}{\pi t}} \, C$$

where n is the number of electrons needed to reduce and oxidize a molecule, F is the Faraday constant, A is the area of the working electrode, D is the diffusion constant of the specie, t is the time and C is the concentration of the analyte.

The first amperometric sensor was the oxygen electrode developed by Clark for their measurement in blood.[260] This first version of the amperometric sensor was composed of two electrodes acting as working electrode (WE) and RE in an electrolyte solution and separated from the medium by a gas-permeable membrane (Figure 4.2 (a)). When the oxygen enters to the system through the membrane is reduced to water in the WE, which is a noble metal. However, the typical structure of a voltammetric sensor is composed of three electrodes: a RE, a WE and a counter electrode (CE), this configuration allows the application of the desired potential between the WE and the RE, and the obtained current is measured through the WE and the CE (Figure 4.2 (b)). The addition of this third CE to the system helps to maintain a constant applied potential while is measured the generated current.
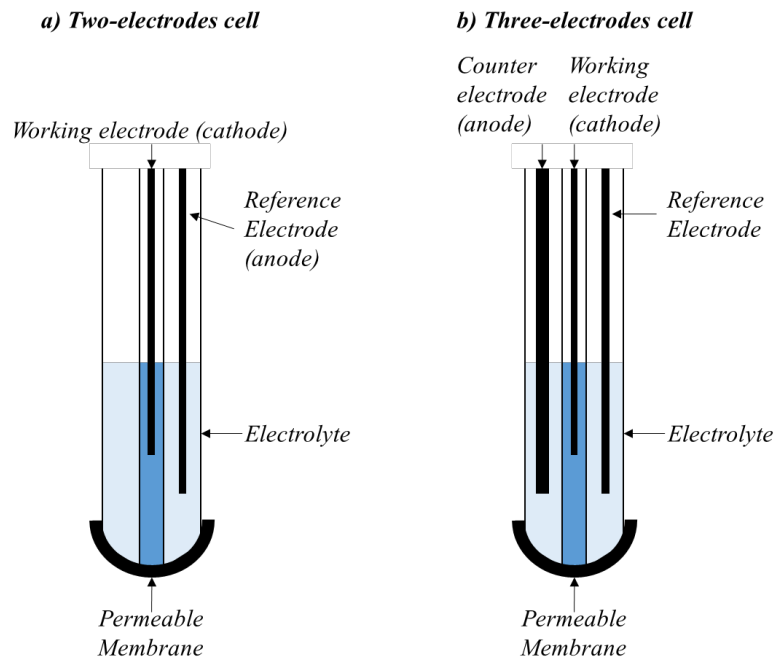

a) Two-electrodes cell

Working electrode (cathode)

Reference Electrode (anode)

Electrolyte

Permeable Membrane

b) Three-electrodes cell

Counter electrode (anode) *Working electrode (cathode)*

Reference Electrode

Electrolyte

Permeable Membrane

Figure 4.2 Clark-type amperometric sensor in a) two electrodes cell configuration and b) three-electrodes cell configuration.

Amperometric techniques are predominantly based on the use of mercury, carbonaceous materials and noble metals as working electrodes. However, the toxicity of mercury, the inconvenience of working with liquid hanging drop electrodes, and a limited range of potentials for mercury for anodic reactions have essentially eliminated mercury from this list. Carbon–based working electrode materials include all allotropic forms of carbons - graphite, glassy carbon, amorphous carbon, fullerenes and, nanotubes are all used as important electrode materials in electroanalytical chemistry.

As mentioned, in this thesis work the miniaturization of these sensors for the fabrication and study of DO and FC sensors is also performed. This miniaturization is based on a planar solid-state construction approach and is further explained in Section 4.2.

4.1.3. Impedimetric sensor

Impedance is one of the most important electrochemical techniques. In there, the measured sample is treated like an electric circuit and their resistance is measured. Over the other electrochemical technique, impedance measurement offers several advantages reliant on the fact that it is a steady-state technique, that it utilizes small signal analysis, and that it is able to probe signal relaxations over a very wide range of applied frequency, from less than 1 mHz to greater than 1 MHz, using commercially available electrochemical working stations.[261]

This technique recognizes the intrinsic properties of the different present species and are characterized by an electrical circuit that consists of resistances, capacitors, or constant phase elements that are connected in parallel or in a series to form an equivalent circuit, therefore is an excellent technique to explore mass-transfer, charge-transfer, and diffusion processes.

Practically, impedance is measured by applying a potential wave to the electrodes and recording the resulting current wave. From these two waves, Z, Φ, Z_{real}, and Z_{imag} are extracted and sketched, where Z is the impedance value and Φ is the phase shift. The spectrum is obtained by measuring these parameters for potential waves with different frequencies.[262]

The electrochemical probe most similar to the impedance measurement is the conductivity cell. This has the same electrode structure, but instead of applying a potential and measuring the current, a current is applied and the generated potential is measured. Conductivity measurements are generally performed with an AC supply. During this process, the cations migrate to the negative electrode, the anions to the positive electrode and the solution acts as an electrical

conductor. The conductivity is a linear function of the ion concentration; therefore, it can be used for sensor applications.

There are two types of conductivity cells depending on the number of electrodes it contains: 2-pole cell (Figure 4.3 (a)) and 4-pole cell (Figure 4.3 (b)). In a traditional 2-pole cell, an alternating current is applied between the 2 poles and the resulting voltage is measured. The aim is to measure the solution resistance (R_{sol}) only. However, the resistance (R_{el}) caused by polarization of the electrodes and the field effect interferes with the measurement, and both R_{sol} and R_{el} are measured. In a 4-pole cell, a current is applied to the outer rings in such a way that a constant potential difference is maintained between the inner rings. As this voltage measurement takes place with a negligible current, these two electrodes are not polarized. The conductivity will be directly proportional to the applied current. This geometry minimizes the beaker field effect, therefore the position or the volume of the sample does not influence on the measurement. A comparison of the main advantages and limitations of both cell configurations are elucidated in Table 4.1.[263]

Table 4.1. Advantages and limitations of the 2-pole and 4-pole conductivity cells. Source [263]

Advantages	Limitations
2-pole cell	
Easier to maintain.	Field effects – cell must be positioned in the center of the measuring vessel.
Use with sample changer (no carryover).	Only cells with no bridge between the plates.
Economical.	Polarization in high conductivity samples.
Recommended for viscous media or samples with suspension.	Calibrate using a standard with a value close to the measuring value. Measurement accurate over 2 decades.
4-pole cell	
Linear over a very large conductivity range.	Unsuitable for micro samples; depth of immersion 3 to 4 cm.
Calibration and measurement in different ranges.	Unsuitable for use with a sample changer.
Flow-through or immersion-type cells.	
Ideal for high conductivity measurements.	
Can be used for low conductivity measurement if cell capacitance is compensated.	

a) 2-pole cell

b) 4-pole cell

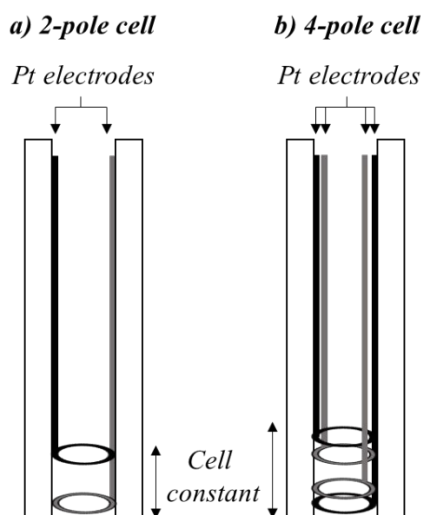*Pt electrodes*

Pt electrodes

Cell constant

Figure 4.3 Impedimetric type conductivity sensor with a) two-pole cell and b) four-pole cell configurations.

4.2. Electrochemical sensors fabricated with printing technologies

As mentioned in the previous sections, electrochemical sensors enable the measurement of several analytes for EM. However, due to the high demand for PoN applications to increase this monitoring of in-field sensing, their miniaturization to make it simple, portable and compatible with LoC technology is crucial to continue growing in this direction. Printing techniques are in the set of these technologies that allows the miniaturization of these devices owing to their capability for the deposition of several types of functional materials. Printing technologies offer high-volume production with extremely inexpensive sensors. Other advantages of printing technologies are the variability of used materials, their flexibility, accessibility, non-vacuum and ecological friendly fabrication processes, their good reproducibility and good compatibility with electronic devices and circuits, and their good mechanical and electrical resistivity.

It is therefore that in this thesis work, the study of the miniaturization, through printing techniques, of the different electrochemical sensors is performed, evaluating the relationship of their design, as well as the investigation of new materials for this manufacturing process to obtain portable analytical devices with small sample volumes, easy maintenance simple operation, and low-cost. In this miniaturization process, the liquid contact that enables the connection in regular electrochemical sensors is replaced by solid elements.

All the printed electrochemical sensors have different properties such as transduction materials or electrode design, however, there are some common points with whom they can relate. The design of this printed electrochemical sensor is composed of three parts: the sensing area, the electrical connection, and the contact pads, being the first one dependent on the sensors and the two seconds the common element. This electrical connection is usually made with silver and connects the sensing area with the electronics, meanwhile, the connection pads are made of carbon and are responsible for protecting this silver both from oxidation caused by the environment and from scratches when making contacts. Apart from this there is another element in common and it is the presence of a dielectric material; this has the function of defining the active area of the electrode and protecting the silver in the areas where there is no carbon, avoiding oxidation or damage.

In many cases, the miniaturization is limited because of the necessary functional elements. In summary, to construct a successful microsensor, a number of aspects must be taken into account:

- The design of the sensor to reduce the electrochemical crosstalk between the different electrodes.
- The fabrication of a reliable RE with potential stability and a long lifetime.
- The replacement of internal electrolytes using different hydrogels or polymers.
- The bonding strategies and durability of the deposited membranes.

The second point deserves special attention. Traditional RE cannot be completely miniaturized owing to the need for a chlorine solution to keep constant the chlorine concentration in the Ag/AgCl electrode and maintain the potential. Despite the well-known behavior of Ag/AgCl, when these electrodes are printed, they typically have a very short lifetime due to the dissolution of the thin AgCl layer, and when the chloride coating is dissolved, the standard potential radically changes.[264] Currently, the integration of a reliable pseudo-RE represents a key challenge for electrochemical microsensors,[265], [266] and their miniaturization is not easy and not completely solved nowadays.

4.2.1. Printed Potentiometric sensor

The miniaturization of potentiometric sensors is the one schematically illustrated in Figure 4.4. As observed, the two-electrode structure is maintained, with a printed pseudo-RE and an IE. The membrane that is present in the regular potentiometric electrodes can be replaced by polymers or metal oxides in solid-state sensors IE a sensing membrane or metal is placed on an electron-conducting layer of the IE, replacing the liquid contact.
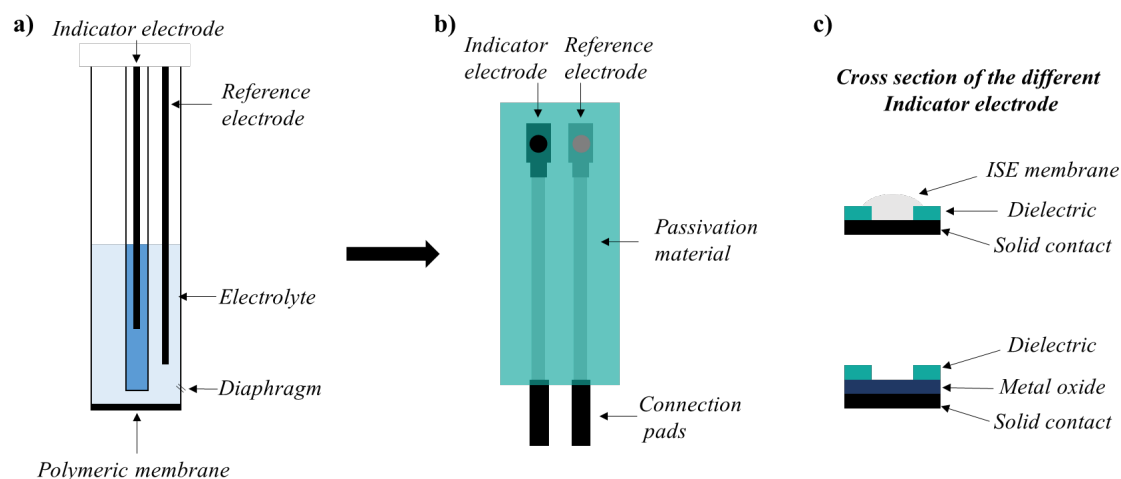
Figure 4.4. | Miniaturization of a potentiometric sensor. a) Schematic image of a potentiometric sensor with a polymeric membrane, b) scheme of a printed potentiometric sensor and c) cross-section of the IE, which can be functionalized with an ISE membrane or with a metal oxide.

4.2.1.1. Printed pH sensor

As mentioned, the pH sensor was the first potentiometric sensor based on the glass electrode, being a pioneer in biological applications. therefore

The pH of an aqueous solution is defined as the negative common logarithm of the molar concentration of hydronium ions (H_3O^+), given by pH = -log $[H_3O^+]$. The usual range of pH is 0 to 14, where pH = 7 is the neutral value. Two possible mechanisms for pH sensing can be found: redox reactions and ion-selective permeation:

- **Redox reaction**: The material over the sensing electrode can be reduced or oxidized with $H3O^+$ and a potential difference is generated by the free energy change a reversible chemical reaction approaching their equilibrium conditions.

- **ISE permeation**: The sensing material acts as an ion-selective membrane and the concentration gradient of $[H3O^+]$ ions at both sides of the membrane also generates a potential difference.

In this thesis work, a metal oxide pH sensor has been proposed and studied, specifically with an Iridium oxide (IrOx) material. Among all the pH-sensitive metal oxides, IrOx is an outstanding material for pH measurements over wide ranges, with fast response, and high durability and

stability even for chemical interferences; furthermore, IrOx has the main advantage that can work both at high temperatures and pressures, as well as in a wide variety of aqueous and non-aqueous media, being perfect for fluidic systems or biological applications since its biocompatibility. Several approaches for the preparation of the IrOx sensor fabrication can be used: iridium thermal oxidation, electroplating, anodization, sputtering and sol-gel processing. These deposition techniques lead to pH sensors with super-Nerstian response (sensitivities greater than 59 mV·pH[-1]) with a sensitivity of around 70 mV·pH^{-1}. Potentiometric response of the IrOx to pH is a function of the transition effect between two oxidation states Ir^{3+}oxide and Ir^{4+} oxide, which can be explained following Equation 4.4, where a change in the iridium ion valence occurs during the reversible reaction from Ir^{3+} to Ir^{4+}.[267]
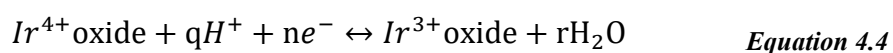
$$Ir^{4+}\text{oxide} + qH^+ + ne^- \leftrightarrow Ir^{3+}\text{oxide} + rH_2O \qquad \textit{Equation 4.4}$$

Other recent works are beginning to work with the large scalable deposition of IrOx as a pH electrode using inkjet printing (IJP),[268] however, and even being a very promising approximation, the need for polymeric multilayer to increase stability and their Nernstian sensitivity, instead of super-Nernstian as reported in the literature, indicates that more work needs to be done to improve sensor performance. It is, therefore, in this thesis work the manufacturing of a new fully printed pH sensor is demonstrated with a fabrication method involving IrOx as a sensing element onto graphite layers over a flexible polyethylene terephthalate (PET) substrate.

4.2.2. Printed Amperometric sensor

Following the same strategy as with potentiometric sensors, the miniaturization of amperometric sensors leads to the replacement of traditional electrochemical cells and bulk electrodes with solid-state planar electrodes. The miniaturization of an amperometric sensor is schematically illustrated in Figure 4.5. With amperometric sensors, in the simplest configuration, it is possible to work without the use of a membrane, exposing the electrodes to the analyte sample. This 'membrane-free' construction improves the response time and sensitivity of the sensor however, only can be used in a few applications since the active electrodes are influenced by interfering compounds.[269] The implementation of the membrane and electrolyte as a polymer makes the system more robust and prolongs its lifetime.[270], [271]
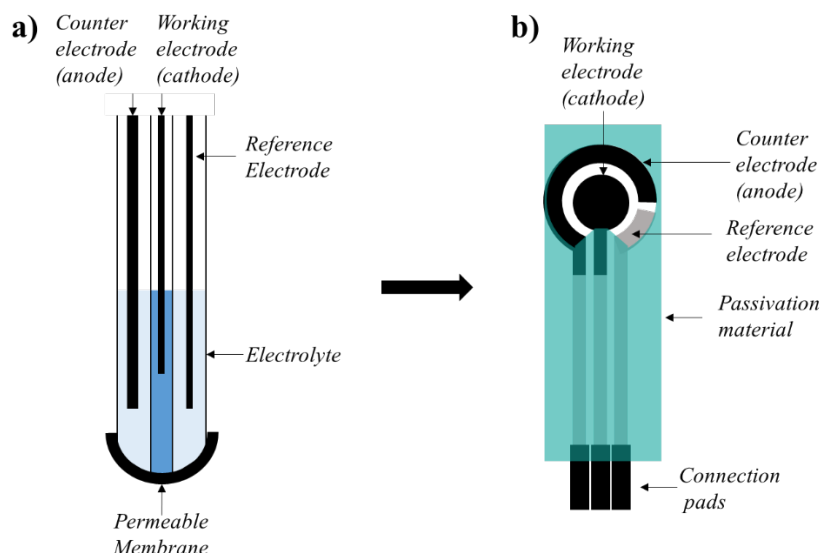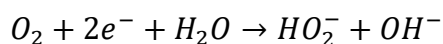
Figure 4.5 | Miniaturization of an amperometric sensor. a) Schematic image of an amperometric sensor with a permeable membrane and b) scheme of a solid-state printed 3-electrode amperometric sensor.

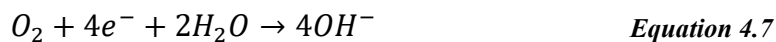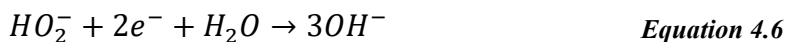## 4.2.2.1. Printed Dissolved Oxygen sensor

As mentioned, the DO was the first amperometric sensor developed by Clark.[260] The miniaturization of this type of sensor constructed in this thesis work is based on a Clark-type 3-electrodes sensor, with a WE, a CE and a pRE.

As described in the literature, its working principle is based on the diffusion of the oxygen through a gas-permeable membrane to an oxygen reduced at the WE (cathode), which typically is a noble metal electrode like platinum or gold, related to an Ag/AgCl RE (anode) at a fixed potential. However, since one of the goals is to study the fabrication of these printed sensors with scalable techniques, the membrane is eliminated, and the 3-electrode sensor is developed to increase their sensitivity.

Since no membranes are used for the measurement of amperometric DO and the electrodes are exposed to the solution, we must optimize the applied potential to obtain a more precise response and thus not be affected by interferents.

$$O_2 + 2e^- + H_2O \rightarrow HO_2^- + OH^-$$

Equation 4.5

$$HO_2^- + 2e^- + H_2O \rightarrow 3OH^-$$

<div align="right">*Equation 4.6*</div>

$$O_2 + 4e^- + 2H_2O \rightarrow 4OH^-$$

<div align="right">*Equation 4.7*</div>

In an alkaline solution, the oxygen reduction equation that takes place in the WE can be divided into two semi-reactions (Equation 4.5 and Equation 4.6); corresponding to each of the reduction procedures of the oxygen. Each equation has its reduction potential, being those the ones that we must optimize with the printed pRE to perform the DO measurement of the final balanced redox reaction can be observed in Equation 4.7.

Clark-type sensors measure oxygen partial pressure and not its concentration, for this reason, to know the concentration value, it is necessary to know the temperature and salinity of the analyte when the measurement takes place.

4.2.2.2.   Printed Free chlorine sensor

When chlorine is added to raw or wastewater, a series of reactions occur that have been extensively studied over the last century.[272]–[275] Depending on the compounds initially present in the water, the chlorine will dissociate and generate chemical aggregates that will have different disinfection abilities, but the compound with the highest disinfection capacity is undoubtedly the residual FC. [274]
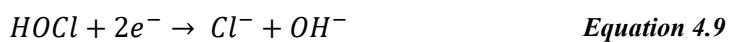
To correctly control these standards, traditionally, the colorimetric method was used. In this analysis, a DPD indicator is applied, which oxidizes in contact with FC, forming a stable semiquinoid that adsorbs light in the red region of the visible spectrum (wavelength of 515 nm). The concentration of FC present in the water is directly related to the intensity of the resulting color once the DPD solution is applied.[276]

Amperometry is another detection method for the FC measurement. Following the structure of the DO sensor, the amperometric FC sensor proposed in this thesis is also a Clark-type 3-electrodes sensor, with a WE, a CE and a pRE. In the same way, this printed FC sensor will not have a polymeric membrane on the WE surface, being the Au electrode used directly in contact with the medium.

When a compound with one (or two) chlorine molecules is added to the water, it dissociates, generating FC, together with other oxidizing compounds such as hypochlorous acid, which, in any case, ends up dissociating to hypochlorite ion (OCl⁻) and a proton (H⁺) according to Equation 4.8.

<div align="center">170</div>

$$HOCl \leftrightarrow OCl^- + H^+ \qquad\qquad \textbf{\textit{Equation 4.8}}$$

The HOCl and OCl⁻ compounds are the ones that are controlled through the colorimetric or amperometric measurements described above and would be the molecules that we refer to as FC or residual FC. By applying a known potential on the surface of the WE, the species of HOCl and OCl⁻ are reduced by reduction Equation 4.9 and Equation 4.10, being these:

$$HOCl + 2e^- \rightarrow Cl^- + OH^- \qquad\qquad \textbf{\textit{Equation 4.9}}$$

$$OCl^- + H_2O + 2e^- \rightarrow Cl^- + 2OH^- \qquad\qquad \textbf{\textit{Equation 4.10}}$$

As mentioned, Clark-type electrodes without the use of a membrane have different interferents in the measurement. Furthermore, if it will be performed in a microfluidic LoC device, pH, temperature, conductivity and flow are parameters that must be controlled.

4.2.3. Printed Impedimetric sensor

The miniaturization of the impedimetric sensor performed in this thesis work is focused to construct a printed conductivity sensor using silver electrodes. A schematic approach to the miniaturization of the conductivity sensor through printing techniques is illustrated in Figure 4.6.

The fabrication of this type of sensor with printing technologies does not imply the use of different materials for the electrode performance, however, their measurement is not a trivial procedure since the conductivity constant cannot be easily calculated for planar electrodes. Thanks to their capacitance behavior, the conductivity measurement can be performed with an impedance system, applying a voltage in the inner electrodes and obtaining the resistance by the current measured in the outer electrodes. The obtained resistance can be related with capacitance following Equation 4.11.

$$C = \frac{1}{2\pi R f_c} \qquad\qquad \textbf{\textit{Equation 4.11}}$$

Where C is the capacitance, R is the real value of the measured resistance and f_c is the frequency of the applied signal used for the measurement.
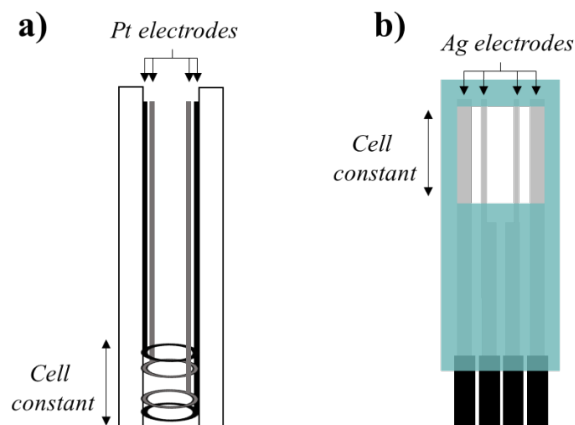
Figure 4.6 | Miniaturization of an impedimetric sensor. a) Conductivity type conductivity sensor with four pole cell and b) scheme of a printed 4-pole type conductivity sensor.

It is well known that conductivity measurement depends on the solution temperature. If the temperature increases, the conductivity decreases. In moderate and highly conductive solutions, a temperature correction can be applied based on a linear equation involving a temperature coefficient θ. This correction can be observed in Equation 4.12:

$$\kappa_{Tref} = \frac{100}{100 + \theta \cdot \left(T - T_{ref}\right)} \cdot \kappa_T \qquad \qquad \textbf{\textit{Equation 4.12}}$$

Where κ_{Tref} is the conductivity at a T_{ref}, κ_T is the conductivity at T, T_{ref} the reference temperature, T is the sample temperature and θ is the temperature coefficient. This temperature correction is accurate within the application of electrochemical sensors for water quality monitoring

4.3. Application of printed electrochemical devices for water monitoring systems

In this section is shown the study and fabrication of monitoring tools using different printing technologies, addressed to monitor different parameters for water monitoring. This section is divided into two subsections, where each one corresponds to submitted works in a relevant scientific journal. The first one is focused on the study of IrOx pH sensors fully fabricated by printing techniques onto a polymeric polyethylene naphthalate (PEN) substrate. The used inks are completely characterized in terms of printability, morphology and conductivity, comparing the performance of printed IrOx with the regular electrodeposited, validating the performance of this new approach. The second work goes one step further with the integration of seven printed sensors

inside a LoC system for controlled, smart and automatic water monitoring. The array of fully printed sensors, which includes DO, FC, pH, redox, temperature, conductivity and flow were laminated in a polymethylmethacrylate (PMMA) matrix with the microfluidic channels and their performance was evaluated with different real water conditions.

4.3.1. Paper IV: Large-scale fully printed iridium oxide-based pH sensor

The first paper presented in this Chapter 4, **Paper IV**, is a scientific article about the study of IrOx-based pH sensors, fully fabricated with scalable printing techniques in a plastic substrate. The article is focused on a complete characterization of the functional inks (silver, graphite, Ag/AgCl, and IrOx) that can be processed at low temperatures (80 – 130 ˚C) to be compatible with polymeric substrates.

This article has been submitted to Advanced Functional Materials journal and is currently under review*:

Paper IV. M. Alique, P. Lacharmoise, C. D. Simao, and A. Moya. **Large-scale fully printed iridium oxide-based pH sensor**. The article has been SUBMITTED to Advanced Materials Technologies journal in September 2022. (Q1, IF: 8.856).

Note that equations, tables and figures numbering in the reproduced research article follow the ones of the submitted version.

Large-scale fully printed iridium oxide-based pH sensor

Marc Alique,[1]† Claudia Delgado Simao[1], Paul Lacharmoise[1] and Ana Moya[1]*

[1]Eurecat, Centre Tecnològic de Catalunya, Functional Printing and Embedded Devices Unit, 08302 Mataró, Spain.

† Electrical and Telecommunication Engineering Department, Universitat Autònoma de Barcelona (UAB).

Corresponding author

E-mail: ana.moya@eurecat.org

ABSTRACT:

An all-solid-state pH sensor based on a novel Iridium Oxide (IrOx) has been constructed and its performance was investigated and compared against an electrodeposited IrOx-based pH sensor. This work presents for the first time to our knowledge a novel approach for the printed IrOx sensor fabrication route, using large-scale printing techniques, combining screen printing and spray coating over a polymeric polyethylene terephthalate (PET) substrate to obtain in a very fast way a low-cost and flexible pH sensor for a wide range of applications. The IrOx solution was formulated and directly spray coated over a commercial graphite ink, which has a high surface roughness, promoting the adhesion of deposited sensing material, increasing the sensor stability and sensitivity and showing an excellent reproducibility with a linear super-Nernstian response (69.4 ± 1.0 mV·pH^{-1}) in a wide pH range (pH 2 – 12). This novel additive manufacturing fabrication route through large-scale printing techniques on a polymeric substrate opens new opportunities for low-cost pH sensing in medical and environmental applications with a single device, which can be used as single-use either in Point of Care (PoC) or Point of Need (PoN) applications or for continuous monitoring in a wide pH range in Lab-on-Chip systems (LoC).

Keywords

IrOx, pH, sensor, printing, spray, large-scale

4.3.1.1. Introduction

For many years, the miniaturization of electrochemical sensors has been a challenge that scientists are facing, with the aim to obtain robust low-cost sensors with the capability to measure in different aqueous media. Low-cost sensors, in lightweight and more sustainable forms, enable massification of data collection in environmental and medical applications, which play an important role in acquiring relevant datasets for environmental phenomena mapping and disease monitoring.[19], [20] This need for low-cost miniaturization has led to the growth of the functional printing technology industry.[15], [25] This technology has been known for many years, and thanks to the increase in functional materials that can be processed as inks, it is on the rise, as it allows large-scale manufacturing on flexible substrates[277], [278] while greatly reducing cost.[57], [279] Within the enormous group that makes up the different printing techniques, screen printing is one of the best known at an industrial level, since it allows the scalable deposition of the desired material over large and soft surface areas, obtaining the desired low-cost devices.[15]

Regular commercial sensors are commonly performed using glass-type electrodes, which have good sensitivities, high stabilities, and lifetime. However, these rigid sensors have several disadvantages owing to the intrinsic properties of the glass, such as their interferences in alkaline solutions or their brittle nature, being limited to a lot of applications where miniaturization is needed, like biomedical or clinical applications. In addition, they are not useful for Point of Care (PoC) applications where mostly low-cost and single-use sensors are needed.

Different solid-state sensors have been studied for pH sensing, including different ion-sensitive materials like polymers,[280] ion selective electrodes (ISEs)[281], [282] or metal oxides,[283]–[286] to overcome the sensing limitations and to expand their application field. These potentiometric sensors are composed of two electrodes: an indicative electrode (IE), with the pH-sensitive material, and the reference electrode (RE), which maintains a constant potential and is usually made up of Ag/AgCl material. Selective hydrogen ionophore materials in polymeric membranes working as transducers in the IE are very promising PoC applications since they have working ranges between pH 4-10 and their low manufacturing cost makes them perfect for single-use applications, working as transducers in the IE.[281], [287]–[289] However, their low sensitivity to low pH levels and the incapability of plasticizers with some complex aqueous medias are the main drawbacks that limits their application field.[290] For the metal options, a big number of metal oxide pH sensors have been developed to functionalize the IE, being RuO_2, SnO_2 and Sb_2O_3 the ones that present a higher sensor performance in different application fields. [286], [291]–[293] Even so, the big sensitivity of these materials is overshadowed by their potential drift, leading to an unstable response unable to reproduce or characterize.[285], [294] Among all the pH-sensitive metal oxides, IrOx is an outstanding material for pH measurements over wide ranges, with fast response, high durability, and stability even for chemical interferences.[293], [295] Within the large number of advantages that IrOx has over other metal oxides, it can work both at high temperatures and pressures,[296], [297] as well as in a wide variety of aqueous and non-aqueous media, being perfect for fluidic systems or biological applications since its biocompatibility.[298]–[300]

However, despite having a multitude of advantages that make it a great material for the manufacture of low-cost pH sensors for many applications, its great limitation is the IrOx deposition method. Several methods are well known including electrodeposition (ED) or thermal oxidation; however, all these techniques are not properly scalable in the industry of printed sensors, being a bottleneck for the large-scale sensor fabrication. Therefore, increasing the scalability of the IrOx coating process would make printed pH sensors more relevant in all their application areas.

Spray coating is a well-established printing technique in graphic arts or industrial coating. The functional material is supplied by means of a controlled pump that injects the ink at the desired speed through an ultrasonic nozzle where an aerosol is formed, and the material is deposited with the help of a carrier gas.[98]–[100] In printing electronics this technique has not received much attention owing to the difficulty concerning the homogeneous control of deposition thickness and roughness, however, for this application where a functional material is deposited on a very rough surface such as carbon is an ideal technique.[101], [102]

In Table 1, a summary of the most relevant works in relation to solid-state pH sensors, with IrOx as the sensing element of the IE can be observed. As can be observed, very few works are done using printing techniques. Most reported works make the fabrication of the electrodes using clean room manufacturing techniques,[301], [302] obtaining chemically pure materials, but making their manufacturing scalability very complicated over polymeric substrates at an affordable cost. As depicted, the vast majority of reported works do not use a fully scalable IrOx deposition method, being the electrodeposition the most used owing to its reproducibility. Recently reported works are starting to use more rapid and scalable printing techniques such as inkjet printing for the development of the printed electrodes, obtaining sensitivities of 71.3 mV·pH^{-1}, a very good value compared to the reported literature.[284] However, the IrOx coating is still by electrodeposition, decreasing the scalability of the technique. Other recent works are beginning to work with the large scalable deposition of IrOx as a pH electrode using inkjet printing,[268] however, and even being a very promising approximation, the need for a polymeric multilayer using inkjet printing to increase stability that is very time-consuming approach compared with our work, together with their Nernstian sensitivity, instead of super-Nernstian as reported in literature, indicates that only one stochiometric form of the ion is present in the electrode sensing mechanism, therefore reducing its sensibility.

Table 1. Comparison of different printed pH sensors with IrOx as the sensing material.

Fabrication method	IrOx deposition technique	Sensor substrate	Electrode material	Sensitivity (mV·pH^{-1})	pH	Author, Year [Ref]
Screen printing	Spray coating	PET	C	69.9	2-12	This work, 2022
Inkjet printing	Electrodeposition	PEN	Pt	71.3	2-11	M. Zea, 2019 [284]
Inkjet printing	Inkjet printing	PET	ITO	59	3-11	M. Jović, 2018[268]
e-beam vacuum evaporation	Electrodeposition	Glass	Pt	77.6	4-11	I. Ges, 2005[303]
Photolithography	Oxygen plasma	Glass	Au/Cr	60.6	4-12	J. Wang, 2015 [301]

Photolithography	Sol-gel	PI	Au/Cr	71.6	3-11	W. Huang, 2008[302]
Photolithography	Electrodeposition	PI	Au	70.0	4-9	P.Marsh, 2020[283]
Photolithography	Electrodeposition	Silicon	Au	69.5	4-10	S. Carroll, 2010[304]
Photolithography	Electrodeposition	PI	Pt	63.5	2-10	S. Marzouk, 1998[295]

Herein, in this study, we demonstrate a new fully printed pH sensor fabrication method involving IrOx as a sensing element onto graphite layers on a flexible PET substrate. Optimal thickness in the printing process has been also evaluated for every printed layer to obtain the best electrical parameters that favor the sensor performance. After the full printing methodology, the electrodes have been fully characterized to obtain their sensibility, stability and response time, as well as corroborate the IrOx species present in the electrode to obtain a reliable fabrication condition, the details of which are described in the following sections. Finally, the performance of this fully printed IrOx pH sensor has been evaluated by measuring the pH in different water conditions.

4.3.1.2. Results and discussion

Characterization of the prepared IrOx solutions was performed by the monitorization of the UV-vis absorption spectra. Figure 1 shows the effect of the reaction evolution at pH 10. With the course of the reaction, the solution color goes from a yellowish green to blue, and the peak correlated with the IrOx formation increases in the 520 nm wavelength. The UV-vis spectra after the reaction completely exhibited two characteristic absorption peaks at 312 and 570 nm. The first peak at 312 nm is assigned to the hydrolysis product of $[Ir(OH)_6]^{3-}$.[305] The second broad absorption at 570 nm is the characteristic peak for IrOx particles, which results in the appearance of the blue color in the dispersion[306], [307] and corroborates the formation of IrOx particles. While advancing the reaction, both peak intensities become sharper, which is correlated with the kinetics of the reaction related to the product formation. The absorbance band of 312 become sharper in the first hours of the reaction in the alkaline media, indicating that the $IrCl_3$ is continuously hydrolyzed and converted to $[Ir(OH)_6]^{3-}$, being this the first step of the IrOx formation according to Eq. 1. Then, when the concentration of the $[Ir(OH)_6]^{3-}$ monomers are at sufficiently high concentration, partially polymerize to generate the Ir_2O_3 following the procedure explained in Eq. 2. Afterwards, Ir^{3+} partially oxidizes to Ir^{4+} oxide in alkaline solution thanks to the dissolved oxygen present in the solution, and after their deposition on the electrode, thanks to

the curing temperature and the atmosphere oxygen, the reaction present in Eq. 3 was completed obtaining the IrOx particles at the top of the electrode.
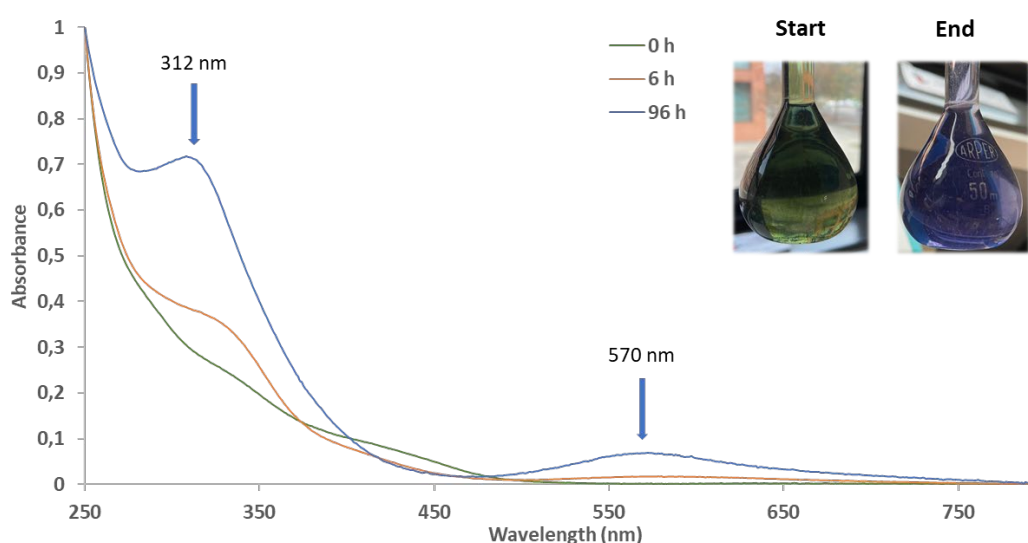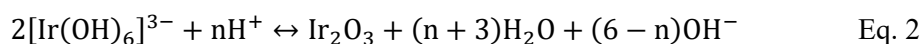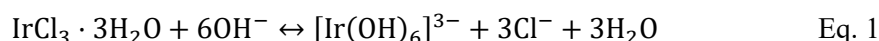
$$IrCl_3 \cdot 3H_2O + 6OH^- \leftrightarrow [Ir(OH)_6]^{3-} + 3Cl^- + 3H_2O \qquad \text{Eq. 1}$$

$$2[Ir(OH)_6]^{3-} + nH^+ \leftrightarrow Ir_2O_3 + (n+3)H_2O + (6-n)OH^- \qquad \text{Eq. 2}$$

$$Ir_2O_3 + O_2 \leftrightarrow 4IrO_2 \qquad \text{Eq. 3}$$

Figure 1. UV-vis absorbance spectrum of the IrOx solution comparing the color, and therefore the coordination sphere of the Ir complex, at the beginning and the end of the IrOx reaction formation.

Figure 2a schematically illustrates the automatized and scalable printed fabrication process. The full fabrication methodology, which consists of a sequence of 5 printing and curing steps, is detailed in Experimental Section. The printed inks were carefully selected to obtain the best electrical and morphological characteristics for the fabrication of this electrochemical sensor, such as stability and long-term response. After the fabrication, the fully printed pH sensor seemed mechanically and chemically stable since no delamination occurs upon bending. An image of the fully printed IrOx sensor can be observed in Figure 2a$_{vi}$. Thanks to the deposition of the functional material at the top of the printed electrode through the spray coating technique, we optimize the fabrication route by using scalable and automatized printing methods, obtaining a robust device with high reproducibility and repetitivity between these low-cost printed sensors for the pH monitoring.

In Figure 2b, the color change in the IE after deposition of the IrOx solution can be appreciated. This color change goes from a light black, corresponding to the graphite layer, to a very dark blue, given by the IrOx particles at the top of the electrode surface. Furthermore, Figure 2c shows an image example of the highly scalable production of this IrOx-based pH sensor thanks to the printing technique production.
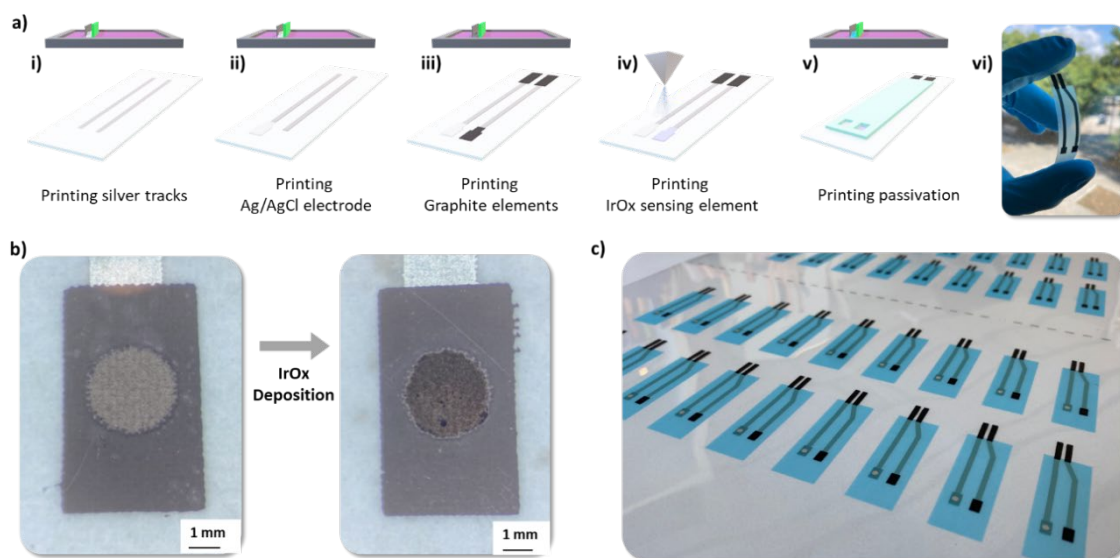
Figure 2. a) Schematic ilustration of the printing procedure for the IrOx based printed pH sensor: i) printing of Ag tracks, ii) printing of Ag/AgCl RE, iii) printing of graphite for the IE and the contact pads, iv) IrOx deposition on the IE, v) printing of a dielectric pasivation layer and vi) image of the final printed pH sensor. b) Images of the IE before and after the deposition of the IrOx ink and c) example image of the A3 size scalability of the printed sensors.

To characterize the different oxidation states of the IrOx at the top of the printed electrode X-ray photoelectron spectroscopy (XPS) was performed and compared to an electrodeposited IrOx sensor. The XPS spectra of the Ir4f core levels of both sensors can be observed in Figure 3, indicating the different compositions of IrO_2 and Ir_2O_3 on the surface. The two peaks' positions of the spectra are clearly indicating the presence of Ir_2O_3 $4f_{7/2}$ and Ir_2O_3 $4f_{5/2}$ spin orbital components with peak energies centered at approximately 61.92 and 64.61 eV respectively. The peak binding energies of the IrO_2 $4f_{7/2}$ and IrO_2 $4f_{5/2}$ doublets are centered at approximately 63.26 and approximately 65.96 eV, respectively.[308], [309] The IrO_2 peak intensity is smaller than that of the Ir_2O_3, which evidently proves the presence of IrOx on the electrode surface. Comparing the relationship between the different intensities of the Ir_2O_3 (Ir^{3+}) and IrO_2 (Ir^{4+}) peaks we can clearly observe that the composition of the electrodeposited sensor is very similar to the printed sensor, having a relationship between both Ir species of 1.29 and 1.18 respectively. Thus, the printed IrOx

sensor has a lower percentage of Ir^{4+} which may affect sensitivity, which will be studied in the next sections.
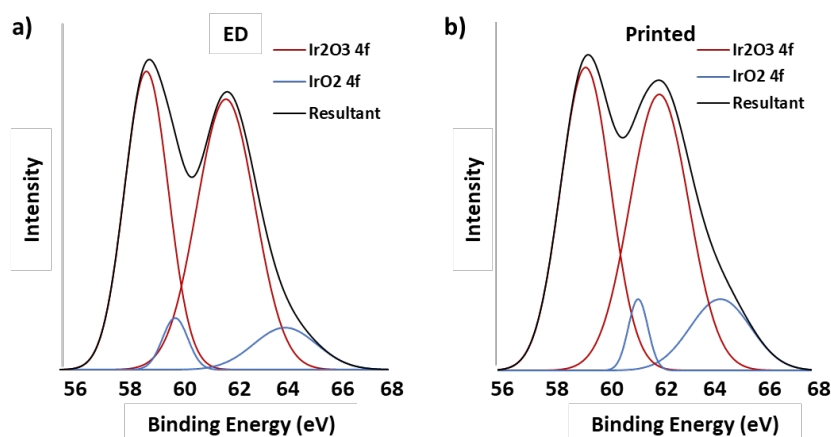

Figure 3. XPS spectra of the IrOx IE where the different species can be differentiated on a) the ED electrode and b) the printed electrode.

Thickness and rugosity of each screen printed layer were measured with a profilometer to characterize their morphology, and the obtained results are summarized in Figure 4. As can be observed, the printed layers present a uniform thickness, being silver the one that presents a smaller deviation and, therefore, a smaller roughness as can be seen in Figure 4a. The graphite layer (Figure 4c) has a higher roughness in comparison with the silver layer due to its intrinsic characteristics. Finally, the Ag/AgCl ink is the one that has a higher roughness on its surface as depicted in Figure 4b. This bigger roughness is caused by its solvent composition since when it dries quickly, part of the ink remains in the printing mask. That is why a higher layer thickness is needed to cover the RE surface with a minimum amount of material.

Cyclic voltammetries (CVs) obtained in PBS of the printed sensor before and after IrOx deposition are compared in Figure 4d. The voltammograms for the printed graphite IE (Figure 4d, black) show an approximately rectangular shape, which is expected for electrodes exhibiting only a double-layer capacitance, suggesting a capacitance behavior.[284] The measured CVs for the deposited IrOx electrodes (Figure 3d, red) correspond to a typical electrodeposited IrOx electrode, where the different peaks associated with the reduction of IrOx (Ir^{3+}/Ir^{4+}) can be observed, independent of the graphite electrodes.[310] The printed IrOx electrode has more than 5.5 times the available charge for the same printed electrodes without the metal oxide. The charge storage capacity (CSC) of the electrodes in Figure 4d, calculated from the integral of the cathodic current over the potential sweep, were 0.61 and 3.36 mC·cm^{-2} for the printed graphite and the deposited

IrOx electrodes respectively. These relationship values are in good agreement according to the results obtained from literature on electrodeposited IrOx electrodes.[310], [311]
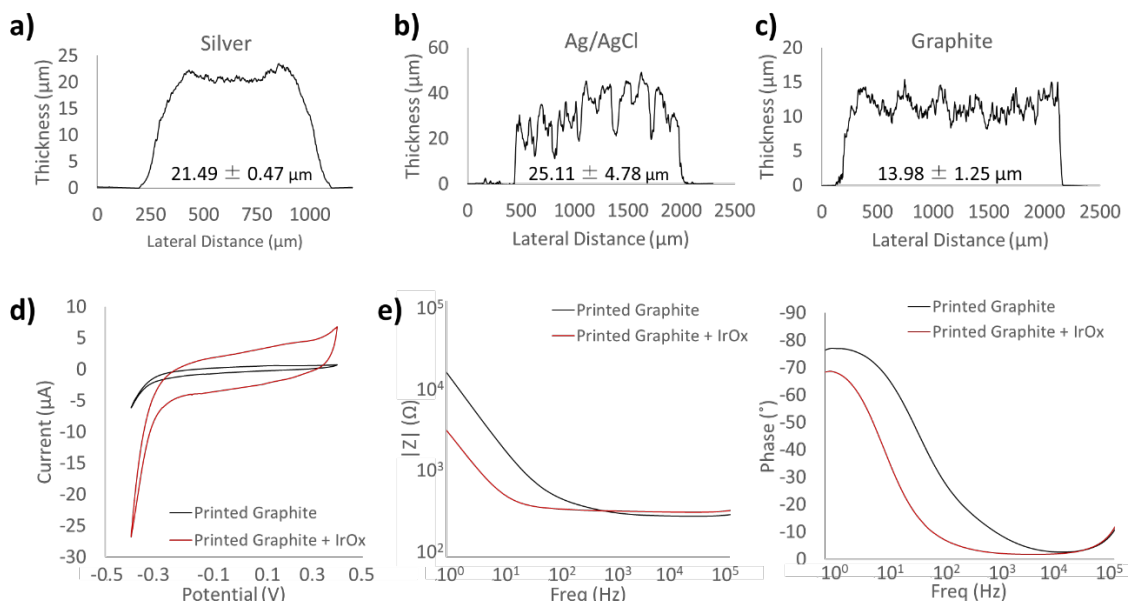

Figure 4. Cross section profile measured with the profilometer of the printed layers being a) silver, b) silver/silver chloride and c) graphite layers. d) Comparison of CVs of the printed sensor before and after IrOx deposition in PBS and scan rate of 20 mV·s^{-1}. e) EIS measurements comparison of the printed sensor before and after the IrOx deposition. CV and EIS data are representative of 10 samples in each group.

Electrochemical impedance spectroscopy (EIS) was used to investigate electrode-electrolyte properties. The benefit of high CSC coatings to reduce the charge-transfer resistance of the electrodes is also observed in Figure 4e for the printed graphite and the deposited IrOx electrodes. Both electrodes exhibited very similar high-frequency ($10^3 – 10^6$ Hz) impedance, exhibiting a near-resistive phase angle (approaching 0°) and an impedance modulus (|Z|) that was the value of the PBS solution resistance. In the low-frequency region ($1 – 10^3$), the increase of the surface area of the electrode owing to the deposition of IrOx can be observed, decreasing the phase angle and the impedance modulus compared with the bare graphite electrode. This impedance response is in good accordance with the roughness profiles presented and with the CSCs values, owing to the impedance improvement after the IrOx deposition in the graphite electrode.

Potentiometric response of the IrOx to pH is a function of the transition effect between two oxidation states Ir^{3+}oxide and Ir^{4+} oxide, which can be explained following Eq. 4.[267] A change in the iridium ion valence occurs during the reversible reaction from Ir^{3+} to Ir^{4+}. Several models have been suggested for the sensing mechanism of the IrOx electrodes, leading all of them to super-Nernstian responses ranging from 60 to 90 mV·pH^{-1},[267], [283], [293], [312], [313] depending on the equilibrium on each IrOx layer, produced from differences in the fabrication conditions.

$$Ir^{4+}\text{oxide} + qH^+ + ne^- \leftrightarrow Ir^{3+}\text{oxide} + rH_2O \qquad\qquad \text{Eq. 4}$$
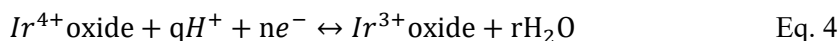
Sensitivities greater than 59 mV·pH^{-1} were observed for the IrOx printed electrodes as depicted in Figure 5a. The potentiometric response of the printed pH sensor was carried out by measuring the Open Circuit Potential (OCP) at room temperature of the IrOx IE vs the Ag/AgCl RE, and it is represented in a pH range of 2-12. Each sensor was tested three times in the same buffer solutions to characterize its super-Nernstian response and repeatability. Average sensitivity of -69.4 mv·pH^{-1} was obtained with a high correlation coefficient r^2 value greater than 0.999, being in good agreement with other reported electrochemical deposited IrOx electrodes.[283], [284]

The complete evaluation of the IrOx printed sensor includes the reproducibility study of the printed IE on the top of the graphite electrode to demonstrate the robustness of the sensor with the described automatic and scalable deposition technique. Different printed electrodes were evaluated with sequential immersions in commercial buffer solutions while measuring the OCP at room temperature of the IrOx IE vs the integrated Ag/AgCl RE, followed by a cleaning step with MilliQ water to avoid cross-contamination. As observed in Figure 5b, the potentiometric response of the printed sensors shows excellent reproducibility. The average sensitivity of the evaluated electrodes was -69.4 mV·pH^{-1} with a relative standard deviation (RSD) of 1.011 %, confirming the excellent reproducibility of the printed IrOx pH sensors.

The response time, calculated as the time needed to reach 90 % transition of the total potential step, was studied in a transition from pH 4 to 6 by adding the desired KOH, and the OCP response in time was monitored. The pH variation was done at room temperature and without conditioning the electrode. As seen in Figure 5c, the sensor response reaches the equilibrium after 45 s. This time depends on the electrode area, it would be possible to reduce it by reducing the IE diameter.

It is well known that the adhesion of the electrodeposited IrOx films is rather poor, being a big problem for the electrodes when are exposed for long times in liquid media since delamination of the IrOx pH-sensitive layer can occur. Several reported methods have been tried to increase this adhesion,[314], [315] such as surface treatment to increase the roughness of the electrode, and therefore increase the electrode area, to oxidize the iridium surface at 300 ˚C, thing that it is impossible owing to the transition temperature of the PET plastic substrate. However, thanks to the intrinsic roughness of the graphite layer, as explained in the previous sections, the adhesion of the IrOx particles to the electrode surface highly increases, thus obtaining a stable layer of IrOx. To evaluate the stability of the IE, the sensor was dipped in a commercial pH 7 buffer for 24 hours and the OCP in time was recorded using a commercial Ag/AgCl RE keeping the

temperature constant at 25 ˚C to avoid potential fluctuations caused by the temperature change. As observed in Figure 5d the recorded voltage remains constant for at least 24 h of measurement. After the validation, impedance measurement was performed, obtaining the same initial values. With these results, we demonstrate the reliability of this novel fabrication procedure for the IrOx electrodes.
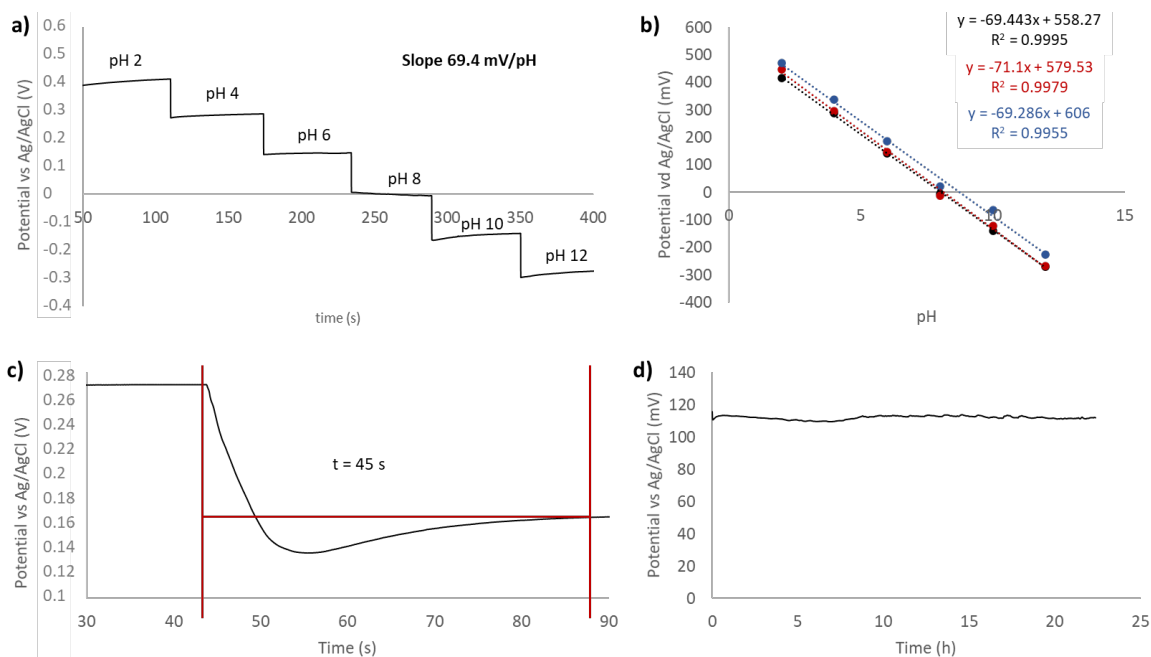

Figure 5. a) Sensor sensitivity of the deposited IrOx electrodes on screen printed electrodes in the pH range of 2-12 using the integrated RE. b) Sensor reproducibility of the IrOx electrode at different pH values from 2-12. c) Response time of the printed sensor to reach the equilibrium after a pH change from 4 to 6. d) Stability in time of the IrOx printed electrode in a pH 7 buffer solution.

Until this point, the different electrochemical characterizations performed with the printed sensor were done in a controlled ionic environment with laboratory conditions. However, in real-life waters, several parameters can interfere with the pH potentiometric measurement, such as temperature, conductivity, ionic concentration, or free chlorine, depending on the location in which the pH measurement is made. In this article, the validation of the printed IrOx pH sensors was performed in three different water conditions: tap water, saltwater and chlorinated water. In saltwater and chlorinated water, we can locate different interferents that could affect the measurement and the tap water is the closest chemically to the conditions previously tested. The pH value obtained from the printed sensors was calculated from an initial calibration using commercial buffers at pH 4.01 and 9.21. Table 2 shows a summary of the characteristics of the different waters tested as well as the measured pH value and its error and deviation from the reference pH value measured with a conventional pH-meter. As observed from the obtained data,

the printed IrOx sensor has high accuracy and precision in its measurement, being the seawater the medium in which the response was most similar to the pH reference value. This high accuracy in the measurement can be attributed to the high conductivity of this type of water, making the OCP reading a more stable value. The measurement in chorinated water was the one that presents a bigger deviation compared to the real pH value, as well as a bigger drift in the measurement. This error and drift read by the sensor is related to the presence of free chlorine in the solution, an oxidizing agent that can change the oxidation state of the IrOx complex, changing the potential on the surface. However, the measurement obtained at first is the one we use to obtain the pH value.

Table 2. Sample parameters for the pH measurements. Each measurement was reproduced with 5 different sensors to obtain the pH and the error value.

Sample	Tap Water	Saltwater	Chlorinated Water
Conductivity (mS·cm^{-1})	0.47	61.5	1.09
Free chlorine (ppm)	0.55	0.00	2.05
Temperature (˚C)	25	25	25
pH	8.3	8.1	7.5
Measured pH	8.4±0.2	8.1±0.1	7.7±0.1
% Error	1.2	0.4	2.7

4.3.1.3. Conclusions

This work presents a novel approach to prepare reproducible and stable fully printed IrOx pH sensor for mass production of a using graphite as electrical collector for the IE on a polymeric substrate, improving the device scalability and, therefore, their application range. The proposed fabrication technology is based on additive manufacturing where printing techniques have a high impact interest; the IrOx deposition using spray coating is compatible with any electrode design and can be deposited in a very fast way over a large number of conductive materials with excellent chemical and mechanical stability. The pH sensors exhibit a linear super-Nernstian response of 69.4±1.0 mV·pH-1 in a wide range of pH between 2-12, with excellent reproducibility, and high stability of the potential drift over time. The high mechanical stability of the printed IrOx coating over the printed graphite layer can be attributed to the high roughness of this printed layer. This presented approach of directly printing the IrOx sensing element on the surface of the electrode, could lead to the manufacture of the pH printed sensors over a large scale with low-cost techniques on a huge variety of polymeric substrates, which is a very interesting alternative to other established non-easily scalable deposition methods, and it can suppose a step further for the adoption of low-cost pH sensors in large scale data acquisition applications.

4.3.1.4. Experimental Section

Materials and chemicals: $IrCl_3 \cdot H_2O$ (Sigma Aldrich 99.9 %), oxalic acid, $H_2C_2O_4 \cdot 2\ H_2O$ (Sigma Aldrich 99%), and K_2CO_3 (Sigma Aldrich 99%) were used for the IrOx preparation. For the development of the printed sensor, we use four commercially available inks. A silver conductive ink (5065 from DuPont™, EEUU), a silver/silver chloride ink (LOCTITE EDAG 7019 E&C from Henkel, Germany), a carbon graphite ink (C2030519P4 from SunChemical, EEUU) and a dielectric ink (90960359 from SunChemical, EEUU). Polyethylene terephthalate (PET, Melinex® 506, Hi-Fi inductrial Film Ldt, United Kingdom) was used as substrate to print the printed sensors. Commercial buffer solutions of pH 2-12 (Panreac) were used for the pH calibration.

IrOx synthesis: The IrOx solution was prepared with an adapted method from literature.[316] 4 mmol of $IrCl_3 \cdot H_2O$, 30 mmol of oxalic acid, $H_2C_2O_4 \cdot 2\ H_2O$, and 0.1 mol of K_2CO_3 were dissolved in MilliQ water in that sequence. The final 50 mL solution was kept at 37 ˚C for 4 days and stored at 4 ˚C prior to use. During this waiting period, the solution has a notable color change from green to blue, showing a change in the iridium ion coordination sphere and demonstrating the formation of the IrOx particles. No precipitation was seen at the bottom of the solution flask after the reaction was completed.

Printing methodology: For the fabrication of the fully printed sensor, the first step was to screen print (AT-60PD from ATMA) the electrical connections with the silver ink and the annealing at 130 ˚C for 10 min. The next step was the screen print of the silver/silver chloride for the reference electrode, and the printed layer was cured at 130 ˚C for 10 min. Then, a graphite layer was screen printed to have the electrical base for the indicative electrode and to protect the silver connections from oxidation and give robustness during the connection process. The printed layer was also cured at 130 ˚C for 10 min. Afterwhile, the customized IrOx ink was spray coated on the printed electrode. For this process, 3 layers of the ink were sprayed on the graphite electrodes and the ink was cured at 80 ˚C for 10 min more. Finally, the last printing step was the passivation of the electrodes with a dielectric ink. 1 layers of the ink were screen printed and the surface was UV cured to obtain the final device.

Characterization: The prepared solution was characterized by the monitorization of their color change while reacting and with the monitorization of the UV-vis absorption spectra (LAMBDA 950 from Perkin Elmer). With the course of the reaction, the solution color goes from a yellowish green to blue, and the peak correlated with the IrOx formation increases in the 520 nm wavelength.

The printed layers were analyzed using a profilometer (DEKTAK 150 Surface profiler from Veeco) and an optical microscope (Eclipse LV100D from Nikon) to evaluate the morphology of the different printed layers. An XPS measurement (PHI ESCA-5500) was performed to characterize the IrOx composition at the top of the graphite electrode. The electrical conductivity was evaluated using a commercial multimeter (Agilent 34410A) connected to a computer with a software to collect the data (Keysight BenchVue).

The electrochemical characterization of the printed electrodes was done by cyclic voltammetry (CV) and electrochemical impedance spectroscopy (EIS). A standard three-electrode cell arrangement was used with printed Graphite-IrOx as IE, a commercial Pt electrode (Metrohm, Germany) as CE and Ag/AgCl (3 M KCl) (Metrohm, Germany) electrode as RE. CVs and EIS measurements were conducted in PBS (15.5 mS·cm^{-1}). CVs were performed with 20 mV·s^{-1} of scan rate and EIS were measured in the range of 1 Hz to 1 MHz.

The open-circuit potential (OCP) of the printed electrodes was measured by an Autolab (Metrohm, Germany). Measurements were carried out in various commercial pH buffer solutions ranging from pH 2 to 12. The pH change was induced by switching the sensor from one buffer to another. Furthermore, after the printed sensor calibration the pH measurement was carried out in different real-life waters such as saltwater, chlorinated water and tap water.

Supporting Information

Supplementary data to this article can be found online…

Acknowledgements

4.3.2. Paper V: Fully printed novel approach for Lab-on-a-Chip smart water monitoring

The second paper presented in this Chapter 4, **Paper V**, is an article about the integration of a single low-cost microfluidic LoC multisensing platform that can be used as an automated and smart novel approach for a water monitoring. The platform proposed in this work allows the simultaneous measurement of DO, FC, pH, redox, temperature, flow and conductivity values. This platform is fully fabricated with printing techniques in a polymeric PEN substrate, incorporating the microfluidic part fabricated through rapid prototyping techniques in a PMMA substrate. Although their applicability is addressed to any type of microfluidic system, here it is validated for the specific case of monitoring tap water, while monitoring its limit of detection (LOD) and limit of quantification (LOQ).

This article was submitted to Chemical Engineering Journal and is currently under review*:

Paper V. M. Alique, P. Lacharmoise, C. D. Simao, and A. Moya. **Fully printed novel approach for Lab-on-a-Chip smart water monitoring**. The article has been SUBMITTED to Chemical Engineering Journal in September 2022. (Q1, IF:16.744).

Note that equations, tables and figures numbering in the reproduced research article follow the ones of the submitted version

Fully printed novel approach for Lab-on-a-Chip smart water monitoring

Marc Alique,[1]† Claudia Delgado Simao[1]*, Paul Lacharmoise[1] and Ana Moya[1]

[1]Eurecat, Centre Tecnològic de Catalunya, Functional Printing and Embedded Devices Unit, 08302 Mataró, Spain.

† Electrical and Telecommunication Engineering Department, Universitat Autònoma de Barcelona (UAB).

Corresponding author

E-mail: ana.moya@eurecat.org

Abstract

The concern for environmental monitoring has been increasing in society along with the technological growth produced in the last century. Water is one of the fields from which a greater source of data can be obtained for society healthcare, thanks to the measurement of different electrochemical parameters, being free chlorine (FC) and dissolved oxygen (DO) key for bioactivity development. The need to be able to obtain a large amount of data autonomously means that the use of conventional technology is not efficient enough. This work presents a novel monitoring approach for the printed sensors fabrication route to obtain a low-cost and autonomous multisensing platform with a "Lab-on-a-Chip" (LoC) approach. Seven sensors; FC, DO, pH, redox, temperature, conductivity and flow, were included in the multiplatform development thanks to functional inks specially deposited through printing techniques on a polymeric polyethylene naphthalate (PEN) substrate. The printed platform presents very high stability and linearity when real tap water samples were measured and compared with commercial sensors, demonstrating the reliability of this LoC approach for the single or continuous monitoring in Point-of-Need (PoN) applications in environmental measurements.

Keywords

Electrochemical sensor, free chlorine sensor, PVDF-TrFE, screen printing, Lab-on-a-Chip, water monitoring.

4.3.2.1. Introduction

The increase of urbanization and industrialization has led society to have continuous monitoring of pollution to ensure society wellness.[317], [318] Among the different detected hazardous, chemical factors are those that can affect more types of species, especially those found in the water. [8], [319], [320] Conventional sensors are being largely used for these measurements; however, these systems are not easy to translate to *in-vivo* scenarios due to the difficult integration and the laborious data processing and transmission. Furthermore, these sensors usually require a continuous maintenance to calibrate the obtained signal or to develop a sophisticated sample treatment before the measurement, as well as its high cost to obtain a signal from a single point. It is at this point that microfluidic systems and more advanced "Lab-on-a-Chip" (LoC) systems have emerged to automatize the required procedures to obtain a measurement.[40], [43], [321]–[324]

In the field of water monitoring, the interest in integrating sensors for *in-situ* measurements has increased in the last decade, being free chlorine (FC) one of the most interesting owing to its difficult characterization.[273], [274] The principal different types of FC measurement methods are colorimetric and electrochemical. The colorimetric methods are present with the use of N, N'-diethyl-p-phenylenediamine (DPD) reagent as the redox colorimetric indicator, and the intensity of a specific wavelength is correlated with the free chlorine concentration.[275], [276] For the electrochemical FC measurement, the amperometric measurement is performed with gold or platinum as working electrodes (WE).[325]–[327] The high cost and the need for sample treatment make these methods incompatible as we know them. However, if they can be carried out with low-cost techniques and with the possibility of automatized processes this will suppose a game-changing in the environmental measurement as we know.

Printing techniques are perfect for this application. Their capability to print different functional materials over large areas of polymeric substrates make it possible the manufacturing of these low-cost sensors. Different scalable printing techniques can be afforded, such as screen printing, inkjet printing or spray coating; the combination of their unique properties makes it possible to deposit and manufacture an almost unlimited number of functional materials with very different designs and functions.[15] Furthermore, the use of printing techniques for the fabrication of the sensors, and rapid manufacturing techniques, such as laser cutting or milling, for the microchannels fabrication on polymeric substrates, make it possible their combination for the LoC fabrication and automatization of the measuring process.[36]

 It is well known that interferents such as temperature, pH, redox potential or conductivity affect the amperometric FC measurement.[325] Furthermore, the fact of encapsulating the sensors in microfluidic channels means that the flow is also a parameter that must be considered for the FC measurement. Besides FC, other parameters such as dissolved oxygen (DO) are also important in monitoring water to have information on biological activity, being essential for cell cultures systems since is vital in the energy metabolism of cells.[36]

In this contribution, we present a double-side low-cost multisensing platform based on a polyethylene naphtalate (PEN) substrate and encapsulated on a microfluidic device using laminated techniques by means of rapid prototyping techniques. Different scalable printing techniques, such as screen printing, inkjet printing and spray coating were used for the deposition of the different materials. The platform incorporates seven different sensors that are necessary for water quality monitoring in LoC conditions: conductivity, pH, redox, FC, DO, temperature and flow.

Special care has been taken with the combination and integration of all different sensors because the different fabrication steps need to be compatible for the materials deposition and electrode functionalization. Our efforts have been focused on developing a more realistic device that combines low-volume microfluidics with multi-analyte sensing, allowing the detection of real water samples. Simplicity in the design and miniaturization of multisensing platform will facilitate adapting the platform to sense other interferents for different water compositions.

4.3.2.2. Materials and methods

4.3.2.2.1. Reagents

Pt on graphitized carbon (40 wt% loading, Merck), H2O/2-propanol (LC-MS CHROMASOLV®, Fluka Analytical) and Nafion® perfluorinated resin solution (Aldrich Chemistry) were used for the Pt/C ink solution. $IrCl_3 \cdot H_2O$ (Sigma Aldrich 99.9 %), oxalic acid, $H_2C_2O_4 \cdot 2\ H_2O$ (Sigma Aldrich 99%), and K_2CO_3 (Sigma Aldrich 99%) were used for the IrOx preparation, together with 20 % Nafion® perfluorinated resin solution (Aldrich Chemistry) and 2-propanol (Merck).

For the development of the printed sensor, we use six commercially available inks. A silver conductive ink (ELG, EEUU), a silver/silver chloride ink (LOCTITE EDAG 7019 E&C from Henkel, Germany), a graphite ink (C2030519P4 from SunChemical, EEUU), a PEDOT:PSS ink (CLEVIOS SV3 from HC STARCK), a piezoelectric ink (FC20 from Piezotech), a gold ink (Colloidal Au from C-Ink) and a dielectric ink (90960359 from SunChemical, EEUU). Every commercial ink was printed with a semi-automatic screen printer, except gold ink which was printed with a desktop inkjet printer. Polyethylene naphthalate (PEN Q65HA from Inabata) was used as substrate to print the printed sensors. Commercial buffer solutions of pH 2-12 (Panreac) were used for the pH calibration.

4.3.2.2.2. Equipment

The printed layers were analyzed using a profilometer (DEKTAK 150 Surface profiler from Veeco) and an optical microscope (Eclipse LV100D from Nikon) to evaluate the morphology of the different printed layers. The electrical conductivity was evaluated using a commercial multimeter (Agilent 34410A) connected to a computer with a software to collect the data (Keysight BenchVue).

All electrochemical characterization was carried out with an Autolab PGSTAT101 (Metrohm Autolab, Utrecht, Netherlands) operated by Nova v2.0 software (Metrohm Autolab, Utrecht,

Netherlands). The electrochemical characterization of the printed electrodes was done by cyclic voltammetry (CV) and electrochemical impedance spectroscopy (EIS). A standard three-electrode cell arrangement was used to evaluate the printed Graphite-IrOx and the Graphite-Pt/C as WE, a commercial Pt electrode (Metrohm, Germany) as CE and Ag/AgCl (3 M KCl) (Metrohm, Germany) electrode as RE. CVs were conducted in a ferro/ferricyanide (10^{-2} M) solution and EIS measurements were conducted in PBS (15.5 mS·cm^{-1}). CVs were performed with 20 mV·s^{-1} of scan rate and EIS were measured in the range of 1 Hz to 1 MHz.

4.3.2.2.3. Microfluidic printed platform fabrication

Pt/C ink production

Pt/C catalyst ink was prepared following an adapted method from literature by mixing 62.5 mg of Pt on graphitized carbon, 1.50 g of distilled H2O/2-propanol 1:1 w/w as solvents with 1.563 g of 5 wt% Nafion® perfluorinated resin solution as the binder.

IrOx ink synthesis

The IrOx solution was prepared following the previously reported method.[316] 4 mmol of IrCl$_3$ · H$_2$O, 30 mmol of oxalic acid, H$_2$C$_2$O$_4$ · 2 H$_2$O, and 0.1 mol of K$_2$CO$_3$ were dissolved in MilliQ water in that sequence. The final 50 mL solution was kept at 37 ˚C for 4 days and stored at 4 ˚C prior to use. During this waiting period, the solution has a notable color change from green to blue, showing a change in the iridium ion coordination sphere and demonstrating the formation of the IrOx particles. No precipitation was seen at the bottom of the solution flask after the reaction was completed. After the reaction, the solution was mixed with 2-propanol as solvent with a 20 % Nafion® perfluorinated resin solution as the binder. The ink composition is protected by patent

LoC fabrication methodology

The LoC platform is composed of 3 different polymeric layers. The bottom and top are a 4 mm thick polymethyl methacrylate (PMMA) that is used for the microfluidic encapsulation, where the channels, the inlet and the outlet are defined. The second layer is a 125 μm PEN film that incorporates all the electroactive sensors. The array of chemical sensors is composed by a gold electrode for the WE and a graphite electrode for the counter electrode

) on the amperometric measurements, a common integrated Ag/AgCl pseudoreference electrode (pRE), an IrOx electrode for the indicative electrode (IE) on the pH sensor and a Pt/C graphite

supported electrode for the IE on the redox sensor for the potential measurement, and Ag 4-electrode array for the impedance conductivity measurement. The back side is composed of a Ag resistive track for the temperature sensor and a printed PVDF-TrFE piezoelectric sensor for the flow measurements. The middle layer is an acrylic adhesive, which joins and encapsulates the microfluidic part with the printed sensors. The full fabrication methodology is schematically illustrated in Figure 1a-d.

The first steps were the preparation of the polymeric substrate. A thermal pre-treatment was performed at 150 ˚C to avoid later deformations of the material that difficult the printing steps. Afterward, drilling holes were performed to electrically connect both sides of the platform. The second step was to screen print the back side layers. Firstly, the temperature sensor was printed using a silver ink over 125 μm thick PEN film. Subsequently, the silver ink was UV-cured to achieve the electrical conductivity of the material (Figure 1b$_1$). Afterwards, the bottom electrode of the flow sensor was printed using a PEDOT:PSS ink. After the deposition process, the bottom electrode was thermally cured for 10 min at 130 °C in a convection oven to evaporate the solvent of the ink (Figure 1b$_2$). Subsequently, a single layer of PVDF-TrFE (80:20) ink was screen printed over the printed bottom electrode. This layer was thermally cured to carry out the annealing of the material above its Curie temperature,[221] at 140 °C for 10 min in a convection oven (Figure 1b$_3$). The final PVDF-TrFE layer thickness was 6 μm thick. The last step of the back side consisted of the screen printing of the top electrode. As reported, in our previous work,[328] to achieve a homogeneous top electrode the same PEDOT:PSS ink was finally used owing to its compatibility with the polymeric piezoelectric layer and thermally cured for 10 min at 130 °C (Figure 1b$_4$). From this point, the front layers were printed, so the first step was to inkjet print Au electrodes, followed by the annealing process at 150 ˚C for 30 min (Figure 1c$_1$). Afterward, the electrical connections and the four electrodes for the conductivity sensor were screen printed with the same Ag ink and the same annealing conditions (Figure 1c$_2$). The next step was the screen print of the Ag/AgCl ink for the pRE, and this printed layer was cured at 130 ˚C for 10 min (Figure 1c$_3$). Then, a graphite layer was screen printed to have the counter electrode, the base for the pH sensor and to protect the connections. The printed layer was also cured at 130 ˚C for 10 min (Figure 1c$_4$). Afterwhile, the customized selective inks were spray coated on the printed electrodes. First, 3 layers of the Pt/C ink was sprayed on one of the gold electrodes and the ink was cured at 80 ˚C for 10 min (Figure 1c$_5$). Then, 2 layers of the IrOx ink were sprayed on one of the graphite electrodes and the ink was cured at 80 ˚C for 10 min more (Figure 1c$_6$). Finally, the last printing step was the passivation of the multiplatform with a dielectric ink. 1 layer of the ink was screen printed and the surface was UV cured to obtain the final device (Figure 1c$_7$). At this stage, the fully printed multiplatform is complete and seemed mechanically and chemically stable, since no

delamination occurs upon bending. The device as prepared is referred as "non-poled device" from now on. A final polarization step of the PVDF-TrFE layer must be done to obtain its piezoelectric activity.[15], [180] To achieve the correct poled device, an electric field of 75 MV·m^{-1} was applied between the top and bottom electrodes of the fully printed device for 1 min (Figure 1c$_8$). To avoid the shock of the applied high electric field, and therefore the spark production that can destroy the electrodes, the voltage was applied using a ramp, reaching its maximum in 2 min.
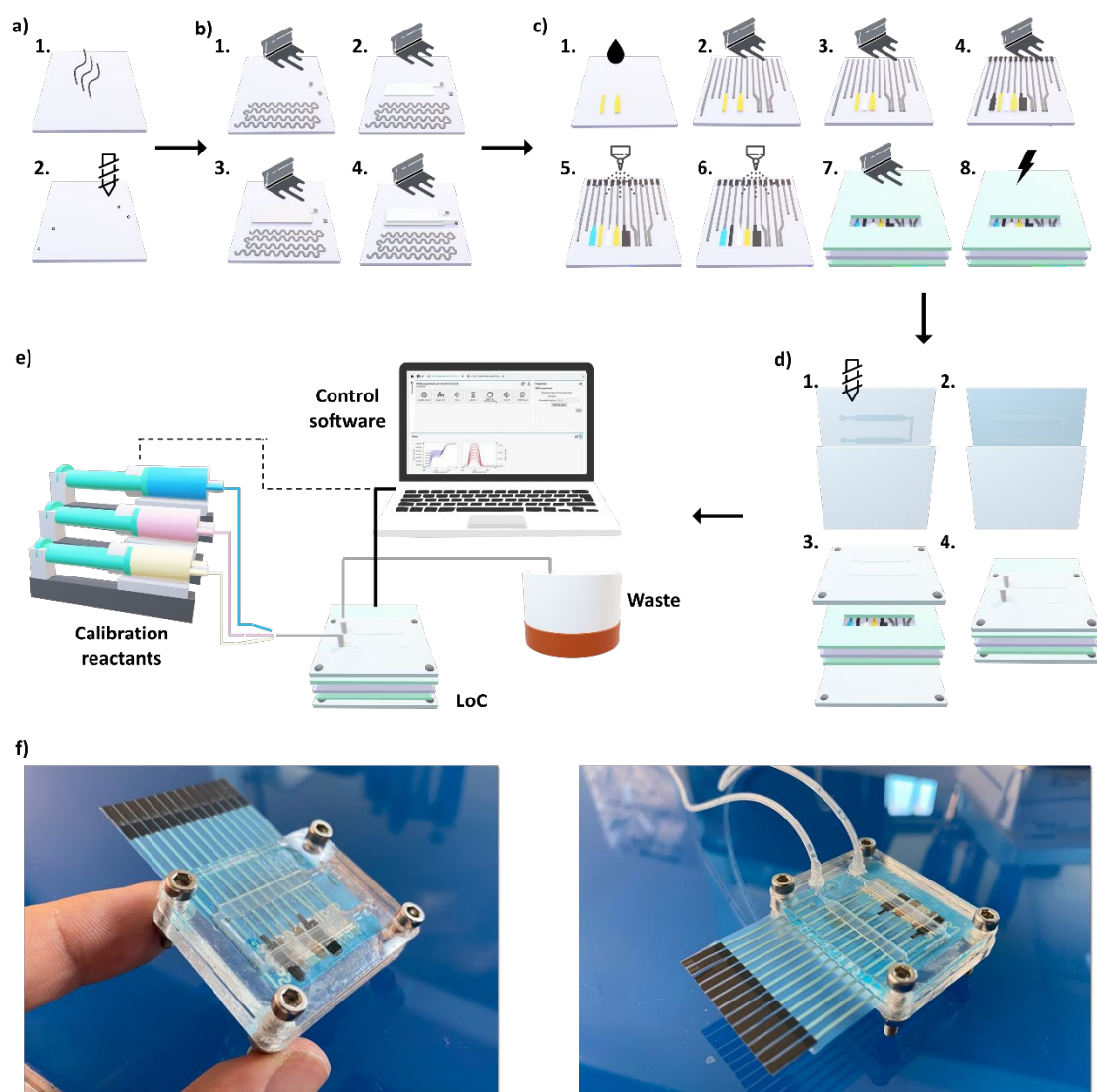
Figure 1. Schematic illustration of the LoC fabrication and measurement. a) Substrate treatment: a.1) Temperature pre-treatment and a.2) Drill perforation. b) Printing of the back side: b.1) Ag screen printing, b.2) PEDOT:PSS screen printing, b.4) PVDF-TrFE screen printing and b.4) PEDOT:PSS screen printing. c) Printing of the front side: c.1) Au inkjet printing, c.2) Ag screen printing, c.3) Ag/AgCl screen printing, c.4) graphite screen printing, c.5) IrOx spray coating, c.6) Pt/C spray coating, c.7) Dielectric screen printing and c.8) PVDF-TrFE Poling. d) Microfluidic integration: d.1) microfluidic channels milling on PMMA,

d.2) structural adhesive, d.3) LoC lamination and d.4) fluidic connection. e) System measurement set-up. f) Integration of the printed platform with the microfluidic device and the final image of the LoC concept.

The connection to the electrode pads was done by using a flexible printed circuit (FPC) connector. This strategy reduces the costs and the fabrication time and, also allows the reusability of the connectors. Finally, a custom holder fabricated in PMMA was used for easy handling of the chip as shown in Figure 1d. The holder was designed in order to have both fluidic and electrical access to the electrodes in a reliable and simple manner and with the possibility to place and remove the chip in an easy way. The final set-up measurement with the LoC device is schematically illustrated in Figure 1e.

4.3.2.2.4. Sensors development

Amperometric printed sensors

The amperometric printed sensor is composed of a gold WE, a graphite CE and an Ag/AgCl pRE. This three-electrodes sensor structure is used for the FC and DO measurements. The active area of the WE measure 21 mm^2. During an amperometric measurement, a polarized potential is applied to the WE and the reduction of the current generated is directly proportional to the analyte concentration in the solution. The FC sensors were calibrated in a FC concentration between 0 and 2.5 mg·L^{-1}, and the DO sensors in a DO concentration between 0 and 8 mg·L^{-1}, polarizing the sensors at 0.1 and - 0.95 V as optimal potential values for the FC and DO measurement respectively. The FC concentration was adjusted by controlled additions of a hypochlorite solution (14% FC) and the DO concentration was adjusted by bubbling different nitrogen (O$_2$ free) through a PBS (10 mM) solution, and a magnetic stirrer was used to ensure better mixing of the solution. A standard colorimetric DPD method and a commercial DO probe were used to correlate the FC and DO response of our printed sensor in order to build the calibration curves.

Potentiometric printed sensors

pH and redox values were measured with a potentiometric method. Different functionalized graphite IE were used for each measurement sharing the same Ag/AgCl pRE for both sensors. For the pH sensor, we functionalized a graphite conductive printed surface with a deposited IrOx ink, meanwhile, for the redox sensor the electrode was functionalized with a Pt/C ink. The functionalization of both IE was performed through a scalable spray coating printing technique. The response of the potentiometric sensors was studied in terms of open circuit potential (OCP). The pH sensor was calibrated over a pH range between 3 and 11, monitoring the

changes in parallel using a commercial pH-meter. The redox response was characterized by adding controlled additions of a hypochlorite solution (14% FC) and using a commercial redox probe to perform the calibration curve.

Impedimetric printed sensor

Typical solid-state conductivity sensor was fabricated through a 4-pole electrode with the silver ink, and the conductivity measurements were performed with a frequency response analyzer (FRA) impedance potentiostatic measurement. The obtained capacitance value, extracted from the impedance measured, is proportional to the conductivity of the solution. The sensor was calibrated in conductivities between 0.017 and 13 mS·cm^{-1} with an optimized sinusoidal pulse with frequency of 10 kHz and 0.01 V$_{RMS}$ amplitude between the inner electrodes. The solution conductivity was increased with controlled additions of a potassium chloride solution (0.1 mM KCl) and the response was monitored in parallel using a commercial conductometer.

Resistance printed sensor

A resistive silver track was used for the temperature sensor. The longitude of the track was optimized to obtain the maximum resistance inside the microfluidic channel. The measurement was performed by measuring the resistance change of the printed track while changing the temperature of the solution. The obtained resistance change is proportional to the temperature change. The sensor was calibrated between a temperature range of 10-40 ˚C while measuring with a commercial thermometer to obtain the calibration curves.

Flow printed sensor

The flow sensor was developed by a PVDF-TrFE piezoelectric material in a sandwich structure with PEDOT:PSS electrodes. As previously reported, the measurement was performed by monitoring the output potential of the piezoelectric sensor.[25] When the piezoelectric material is deflected by the fluidic flow detects a vibration and generates an electrical signal. The measured output potential is directly related to the flow rate. The sensor was calibrated in flow rates between 1-6 mL·min^{-1}, varying the rate with a peristaltic pump. The value of the rate generated by the pump is used to obtain the calibration curve.

4.3.2.3. Results and discussion

The full fabrication methodology of the multisensing platform, which consists of a sequence of 12 printing and one poling steps, is completely detailed in the Experimental Section. The printed inks were carefully selected to obtain the best electrical and morphological characteristics for the fabrication of the sensors. The best fabrication route to integrate the different materials in the same printed platform was optimized to reduce interferences between sensors. After the fabrication, the multisensing platform seemed mechanically and chemically stable since no delamination occurs upon bending. An image of the fully printed platform and its microfluidic integration can be observed in Figure 1f. In there, the multisensing platform as a single device and with the LoC connection can be observed. The combination of different printing techniques allows the deposition of different metals for the electrodes sensing, as well as their functionalization with the manufactured ink to obtain a scalable and automated routine for the fabrication of these low-cost printed sensors for the monitoring of sever parameters.

4.3.2.3.1. Amperometric calibration

In order to check the correct response of the printed electrodes, CVs were carried out in a ferro/ferricyanide (10^{-2} M) solution with external CE and RE and compared with the integrated CE and pRE configuration. Figure 2a shows the CV comparison responses of gold electrodes with consistent peak definition in both cases. With external electrodes, the peak-to-peak separation (ΔE_p) is about 89 mV, a significant value according to literature, and when measured with integrated pRE a with CE, the separation decreases up to 82 mV, decreasing the sensibility of the sensor owing to the lower stability of the pRE in comparison with a commercial Ag/AgCl probe, but with a very good performance.

Free chlorine calibration

The amperometric FC response of the Au WE was studied with the integrated CE and pRE configuration owing to the good performance obtained in the CV characterization. The reduction potential was studied for the FC sensor by means of a linear sweep voltammetry (LSV) as shown in Figure 2b. The final selected potential for the calibration measurement of the FC concentration was 0.15 V. Figure 2d shows the calibration curve of the current measured for different FC concentrations in the range between 0 and 2.5 mg·L^{-1}. Our amperometric printed sensor showed excellent sensibility in the FC measurement with very high linearity in all the FC concentrations range. The FC sensor exhibited a sensibility of 0.15 µA(mg·L^{-1}) and a correlation

factor of 0.9994 using the integrated three-electrode configuration. LOD and LOQ were also measured, resulting in 0.15 and 0.3 ppm respectively.

DO calibration

The amperometric DO response of the Au WE was studied with the integrated CE and pRE configuration. The same electrodes were used than for the FC sensor but optimizing the applied potential for the reduction reaction of the oxygen for the DO measurement. After the LSV characterization, the selected potential for the calibration measurement of the DO concentration was -0.95 V, coinciding with the second oxygen reduction potential (Figure 2c). Figure 2e shows the calibration curve of the current measured for different DO concentrations in the range between 0 and 7 mg·L^{-1}. The sensor exhibited an excellent performance, displaying very stable linearity in all DO concentrations range. The DO sensor exhibited a sensibility of 0.51±0.01 µA(mg·L^{-1}) and a correlation factor of 0.9996 using the integrated three-electrode configuration. LOD and LOQ were also estimated, resulting in 0.28 and 0.75 ppm respectively.
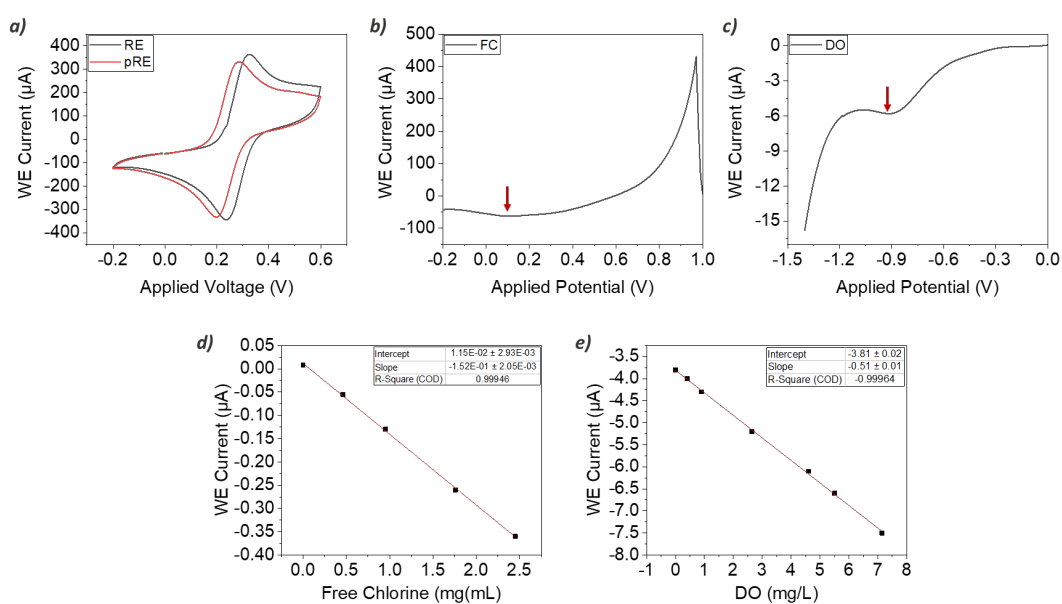
Figure 2 a) Cyclic voltammetry measurement of the amperometric electrode with external electrodes and printed pRE with printed CE. Linear sweep voltammetry to characterize the b) free chlorine and c) dissolved oxygen printed sensors. Calibration curves of amperometric d) printed free chlorine sensor and e) printed dissolved oxygen sensor.

4.3.2.3.2.   **Potentiometric calibration**

To check the correct functionalization of the potentiometric IE, CV and EIS measurements were performed on a PBS buffer (15.5 mS·cm^{-1}). The measured CVs for the modified electrodes correspond to a typical IrOx and Pt/C electrode, where the intensity of the current value directly increases as the resistance of the electrode decreases, owing to the presence of the printed metal/metal oxide layer (Figure 3a). The functionalized printed electrodes have more than 7.1 times the available charge for the same printed electrodes without the metal oxide and more than 65 times larger for the electrodes with the Pt/C. The charge storage capacity (CSC$_c$) of the electrodes in Figure 3a, calculated from the integral of the cathodic current over the potential sweep, were 0.13, 0.94 and 8.65 mC·cm^{-2} for the printed graphite and the functionalized IrOx and Pt/C electrodes respectively.

EIS was used to investigate electrode-electrolyte properties. The benefit of high CSCc coatings to reduce the charge-transfer resistance of the electrodes is also observed in Figures 3b and 3c. The printed electrodes exhibited similar high-frequency ($10^3 - 10^6$ Hz) impedance, exhibiting a near-resistive phase angle (approaching 0˚) and an impedance modulus (|Z|) that was the value of the PBS solution resistance for the IrOx and C electrodes. The Pt/C printed electrode exhibited a decrease of the |Z| owing to ins better CSC value. In the low-frequency region ($1 - 10^3$), the increase of the surface area of the electrode owing to the deposition of IrOx and Pt/C can be observed, decreasing the phase angle and the impedance modulus compared with the graphite electrode. Those values are in good concordance with the reported CSCs values owing to the impedance improvement after the IrOx and Pt/C deposition in the graphite electrode

pH calibration

IrOx layers were prepared by deposition of a functionalized ink, where the pH sensitivity depends on the oxidation state of the IrOx. The potentiometric pH response of an IrOx deposited layer was studied in our previous work,[329] where sensitivities greater than 59 mV·pH^{-1} were obtained, meaning that more than one hydrogen ions can be transferred in the redox reaction. In this work, the sensor was directly calibrated using the pRE configuration owing to the known stability. The sensor exhibits a super-Nernstian linear response between pH ranging from 2 to 11, with an average slope of 72.2±0.8 mV·pH^{-1}. Figure 3d shows the obtained calibration curve. The response time of the sensor was fast, with 40 s to reach the desired signal (Figure 4e). The obtained results were compared with our previous reported response time, linear pH range and slope values, and were adequate for the determination of pH in the experimental water samples.

Redox calibration

Pt/C layers of the IE were prepared by deposition of a functionalized ink, where the Pt act as a novel metal for the potential measurement. In this work, the sensor was calibrated by using the Ag/AgCl pRE configuration and comparing the obtained potential with a commercial sensor. The printed sensor exhibited a linear response in comparison with the commercial redox probe with a linear relationship of 0.2 and a deviation of 182 mV as elucidated in Figure 3f.
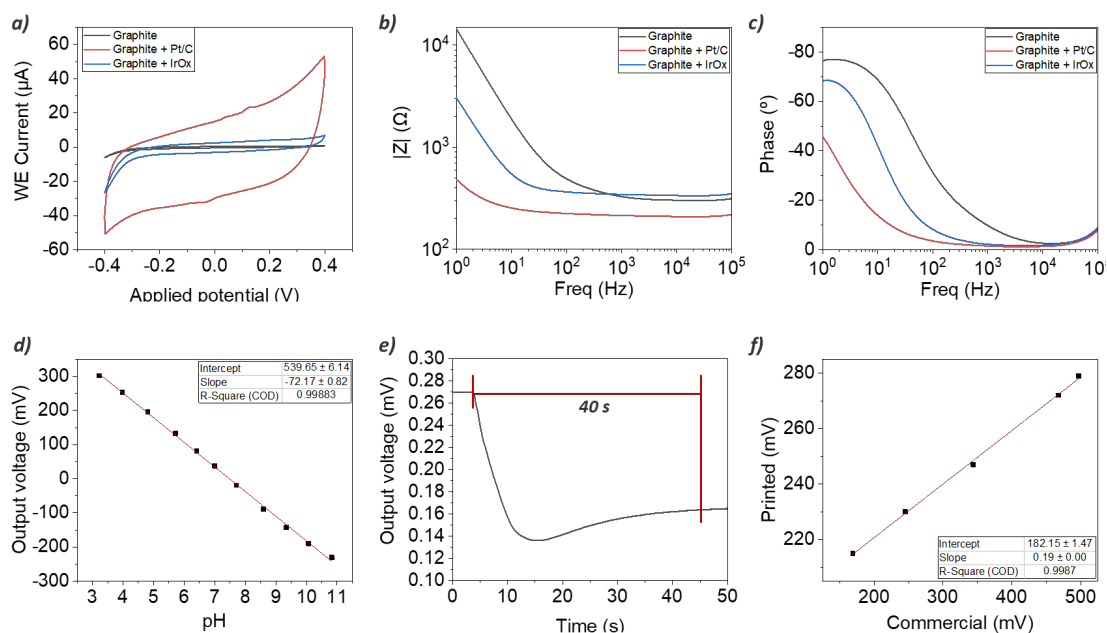

Figure 3. a) Comparison of CVs of the printed sensor before and after IrOx and Pt/C deposition in PBS and scan rate of 20 mV·s^{-1}. EIS measurements comparison of the printed sensor before and after the IrOx and Pt/c deposition representing b) resistance and c) phase. CV and EIS data are representative of 10 samples in each group. d) Calibration curve of potentiometric printed IrOx based pH sensor and e) response time of the printed pH IrOx sensor. f) Calibration curve of potentiometric printed Pt-based redox sensor vs a commercial redox probe.

4.3.2.3.3. Electrical sensors calibration

Conductivity calibration

The response of the conductivity sensor was studied with the integrated 4-pole electrode. After the frequency optimization observed in Figure 4a, impedance measurement was performed at 10kHz with 0.01 V$_{RMS}$. The chosen frequency was used since it corresponds to a linear response zone for the different conductivities and frequencies measured (Figure 4a). The presence of the 4-pole electrode allows the measurement avoiding polarization effects and without the need of a

stable cell distance. Thanks to the capacitive behavior of the printed electrodes, the capacitance measurement shows an excellent relationship with the resistance values of the solution as shown in Figure 4b, with an average slope of 0.15 mF(mS·cm^{-1}) and a correlation factor greater than 0.999. The LOD and LOQ were also estimated, resulting in 0.016 and 0.018 mS·cm^{-1} respectively.

Temperature calibration

The resistive temperature sensor was calibrated with the printed resistive track at the bottom of the printed platform. Samples at different temperatures were passed through the microfluidic channels while measuring the resistance of the printed sensors. Thanks to the changes in the resistance provided by the UV-curable ink, after the calibration of the printed sensor exhibited a linear relationship against the temperature of 85 mΩ·°C^{-1} with a correlation factor greater than 0.999 (Figure 4c).

Flow calibration

The flow sensors were developed with a printed piezoelectric PVDF-TrFE layer in a sandwich structure with PEDOT:PSS as top and bottom electrodes. After printing, a piezoelectric layer with 6 μm thick was obtained and a poling procedure was performed by applying an electric field of 75 MV·m^{-1} was applied between the top and bottom electrodes for 1 min. After the procedure, a d_{33} piezoelectric constant of 34 pC·N^{-1} was obtained, a value in relationship with literature.[25] In this work, the sensor was placed at the entrance of the microfluidic channel, and different flow rates were applied with a controlled peristaltic pump. As observed in Figure 4d, the output potential of the piezoelectric layer is directly related to the flow rate, obtaining a sensibility of 5.07 mV(mL·min^{-1}) and a correlation factor of 0.9972. LOD and LOQ were also measured obtaining values of 0.1 and 0.5 mL·min^{-1} respectively.

Table 2 summarizes the main specification of the different sensors that composes the printed platform. As can be observed, the different sensors present very high linearity to the analyzed samples in the microfluidic platform, with a broad linear range for that allows the measurement of several water conditions. Furthermore, the measured LOD and LOQ enhance this hypothesis, with values very close to the lower limit, obtaining very reliable values.
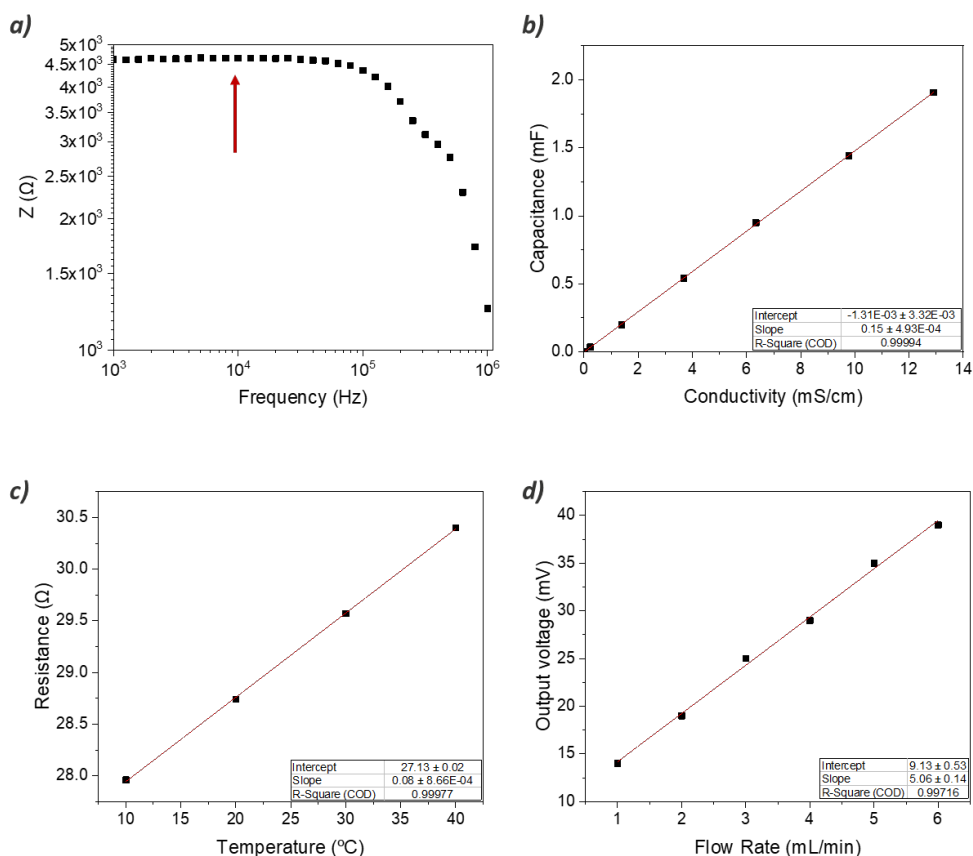
Figure 4. Calibration curves of a) printed conductivity sensor, b) printed temperature sensor and c) printed piezoelectric flow sensor.

Table 2. Specifications of the different printed sensors.

Sensor	Sensibility	Linear Range	Response Time (s)	LOD	LOQ
Free Chlorine	0.1520 µA(mg·L^{-1})	0-2.5 ppm	60	0.15 ppm	0.3 ppm
Dissolved Oxygen	0.5113 µA(mg·L^{-1})	0-8 ppm	40	0.28 ppm	0.75 ppm
pH	72.1 mV·pH^{-1}	3-11	25	-	-
Redox	-	-	60	-	-
Conductivity	0.1479 mF(mS·cm^{-1})	0-13 mS/cm	10	0.016 mS·cm^{-1}	0.018 mS·cm^{-1}
Temperature	84.7 mΩ·˚C^{-1}	10-40 ˚C	-	-	-
Flow	5.05 mV(mL·min^{-1})	0-6 mL/min	0.7	0.1 mL·min^{-1}	0.5 mL·min^{-1}

4.3.2.3.4. Real sample analysis

To provide an initial evaluation of the LoC performance for the analysis of tap water we analyzed real samples obtained from different locations. Prior to measurement, automated calibration of the electrochemical sensors was performed inside the microfluidic chamber and thus obtaining the real concentration value of the analyzed data. The characteristics parameters of the analyzed tap water and the error of the obtained values with the printed sensors compared with those obtained from commercial probes are parametrized in Table 3.

As can be observed, errors lower than 2.5 % were obtained with the FC, DO, pH, redox, conductivity and temperature sensors, and a maximum error of 5.2 % was obtained with the piezoelectric flow sensor. These small errors observed, where the deviation appears in the second decimal place, show us the reliability of the electrical and electrochemical printed sensors of the multiparametric LoC platform for measurements of real samples of tap water after calibration is performed. Furthermore, thanks to the LoC approach, automatic calibrations of the microfluidic system can be performed to increase the lifetime of the printed platform.

Table 3. Tap water characterization and measurement deviation obtained with the printed platform.

Parameter	Tap Water Value	Measured error vs real samples (%)
Free Chlorine	0.56 ppm	1.9
Dissolved Oxygen	6.31 ppm	2.3
pH	6.8	1.2
Redox	626 mV	2.5
Conductivity	0.642 mS·cm^{-1}	1.1
Temperature	22 ˚C	0.2
Flow	1 ml/min	5.2

4.3.2.4. Conclusions

In summary, a compact analytical microfluidic platform for LoC monitoring that is fully fabricated with printing technology and rapid prototyping techniques for smart water monitoring is here presented. Different types of electrochemical and electrical sensor compositions and configurations were produced showing excellent performance compared with commercial sensors. This multisensing platform includes seven different sensors for water quality monitoring

in a LoC system such as FC, DO, pH, redox, temperature, conductivity and flow rate. Thanks to the different employed printing techniques different materials can be deposited to obtain the desired electrode configurations. The amperometric sensors are based on a Au-colloidal ink as a WE material, which provides great stability to the measurement, being able to obtain the measurement of FC and DO with great sensitivity. The novel approach to deposit by spray coating IrOx and Pt/C solutions onto graphite electrodes for the potentiometric measurements provides bigger stability to the printed sensors, being able to measure in different water backgrounds with high performance. Thanks to the versatility of the rapid prototyping techniques, an easy and compact design can be obtained, optimizing the surface taking advantage of both sides of the polymeric substrate. Thanks to the microfluidic approach, the calibration of the printed sensors can be performed automatically increasing the lifetime of the multiparametric LoC device. Real samples were collected from tap water and analyzed with the multisensing platform. The obtained values were in good agreement with the values obtained by commercial sensors including electrochemical or colorimetric with the DPD method. These results demonstrate the potential of printing technologies and rapid manufacturing techniques for the fabrication of electrochemical and electrical sensors for the analysis of water samples in environmental monitoring.

Supplementary Information

Supplementary information to this article can be found online…

Acknowledgements

Supplementary Information

Fully printed novel approach for Lab-on-a-Chip smart water monitoring

Marc Alique,† Claudia Delgado Simao, Paul Lacharmoise, Ana Moya *

Table S.1. Parameters of the measured tap water.

Parameter	Value
Free Chlorine	0.56 ppm
Dissolved Oxygen	6.31 ppm
pH	6.8
Redox	626 mV
Conductivity	0.642 mS·cm^{-1}
Temperature	22 ˚C
Flow	1 ml·min^{-1}

5. Conclusions and Future Work

In this chapter, the main conclusions of this thesis work are presented. The key findings of the work achieved throughout the whole dissertation are exposed, including the detailed results on each topic. Moreover, an overview of the remaining open challenges and potential future research directions in the area following this research are identified and described

5.1. Overview and general conclusions

The main purpose of this thesis dissertation was to investigate new materials and their combination, methodologies and devices architectures to create and characterize novel fully printed electroactive devices (ED) for monitoring environmental physical and electrochemical parameters addressed to help the understanding of the role of printed sensors in environmental monitoring (EM) field for the study and fabrication of autonomous, low-cost and reliable tools, for novel and disruptive approaches for the EM field. The use of printed electronics (PE) to construct these monitoring tools allows their obtention through robust and scalable fabrication methods, using diverse functional materials deposited in micrometric-thick multilayer systems.

To accomplish this overarching goal, a common approach was obtained transversally in all chapters that was to investigate the different materials used, and their combination and compatibility within the multilayered printed structures, and the printing techniques sequence to obtain functional devices. **An overarching key result of the thesis work, and underlying pillar of all chapters of this dissertation, is the finding of a transversal methodology workflow** to prepare electroactive printed devices, culminating in a patent application entitled *"Additive manufacturing of sensors"* filed at the end of this thesis work. It was found that respecting this methodology sequence is critical to achieve operational fully printed sensors and is best appreciated during the preparation of printed multiparametric electrochemical sensing platform, due to its high complexity and extensive preparation workflow. However, it is also applicable and still critical in the simplest devices designed, this is the planar capacitors printed piezoelectric devices, either with screen printing (SP) or inkjet printing (IJP) electrodes. The relevance of this finding is such that an universal methodology was created and can be adapted to use and combining any type of functional inks investigated in this dissertation, with different designs to create novel functions.

All objectives set in Chapter 1 have been successfully addressed. Concretely, different proof-of-concept devices for EM have been designed, prepared and studied for different monitoring applications at the Point-of-Need (PoN). The two types of devices proposed for the monitoring, **multifunctional piezoelectric device and multiparametric electrochemical sensor for PoN applications**, have been prepared and studied with different device architectures, successfully achieving reproducible and reliable devices. The first has been based on the use of printed piezoelectric devices that can act as sensors, actuators or energy harvesters to monitor different aspects of the environment related to motion. The second type of devices included the manufacturing of electrochemical sensors for a smart and low-cost approach to water quality monitoring.

Four different electroactive printed proof-of-concept demonstrators have been investigated and developed as observed in Figure 5.1. The first two were based on piezoelectric devices on different polymeric substrates for vibration and movement monitoring, including their use as actuators and energy harvesters. The second two were focused on the research and fabrication of electrochemical sensors with the aim of monitoring different water parameters, inside of a Lab-on-a-Chip (LoC) system as observed in Figure 5.1 (d). This last device also includes a piezoelectric sensor for flow monitoring in the LoC system, integrating in the same platform the different approaches studied in the first stage.

a) Printed piezoelectric device **b) Stretchable piezoelectric sensor** **c) Printed IrOx pH sensor** **d) Printed LoC multiplatform**
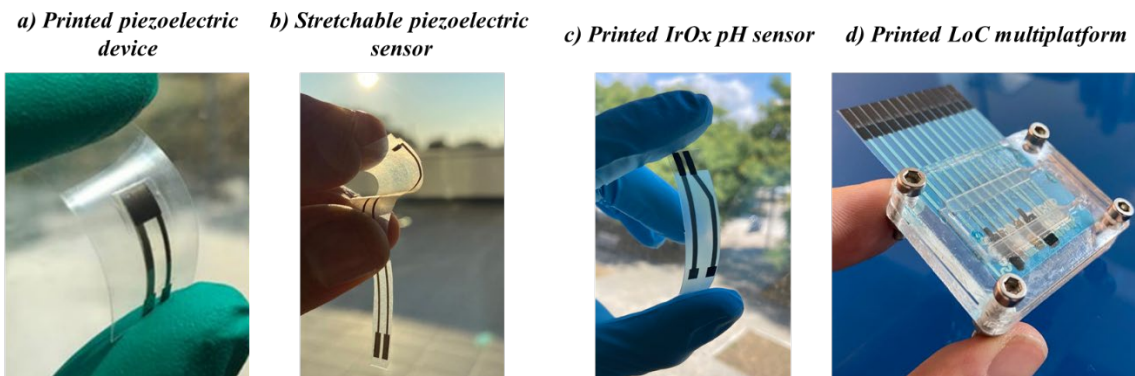
Figure 5.1 Images of the printed devices developed as proof-of-concept in this thesis work. a) versatile piezoelectric device, b) stretchable piezoelectric sensor. c) Fully printed IrOx pH sensor and d) Fully printed LoC multisensing platform.

5.2. Specific conclusions

More in detail, different specific conclusions have been reached after the fabrication and characterization of each proof-of-concept demonstrator. Figure 5.2 summarizes the main key points of evolution based on device, materials, structure, deposition method and innovation investigated in this thesis work. In general terms, the evolution of the work has been always looking for simple, scalable and autonomous devices while adapting these technologies to the requirements of each system.
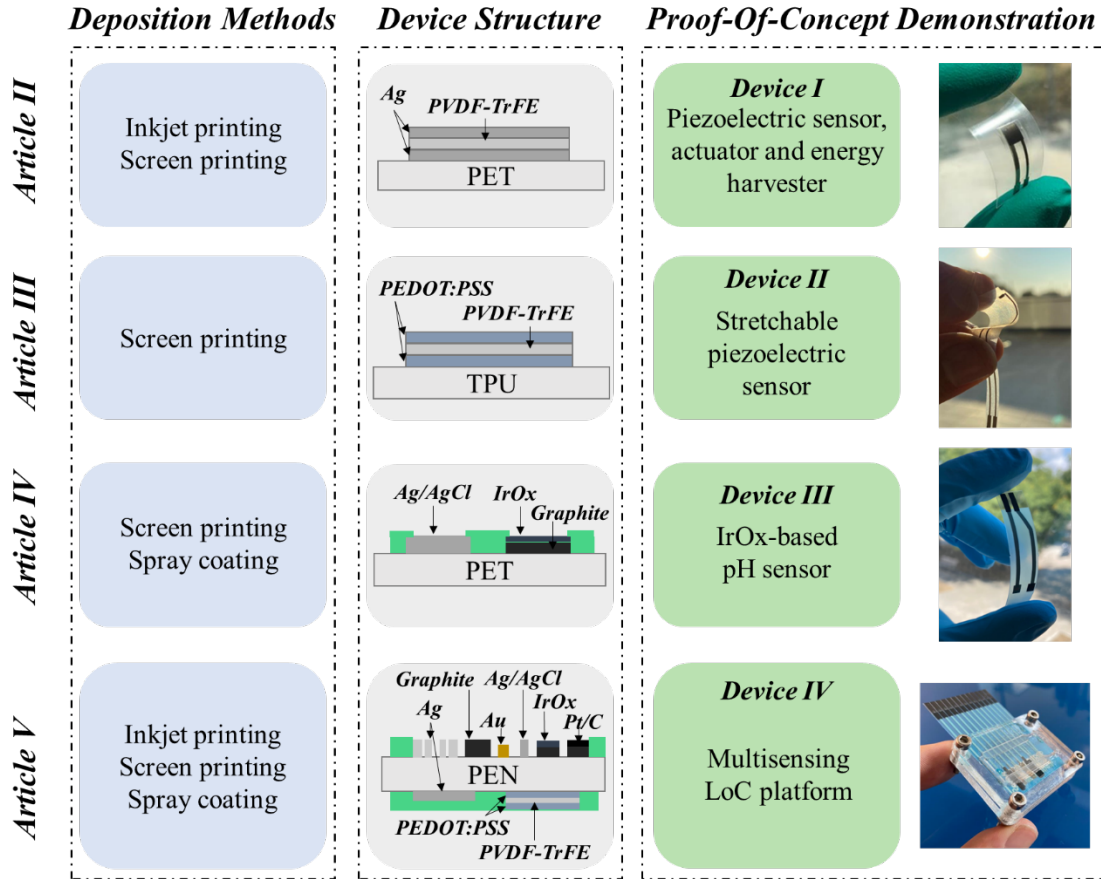
Figure 5.2 | Evolution of the thesis work shows the main key advances to solve different EM necessities.

Following, specific conclusions of each printed device are presented.

Device I. The first printed platform has been addressed with the study of a polyvinylidene fluoride trifluoroethylene (PVDF-TrFE) printed piezoelectric device structure on a flexible polyethylene terephthalate (PET) substrate for its application as a sensor, actuator and energy harvester, while studying their poling properties. A review about the fabrication of piezoelectric materials with printing technologies has been presented in **Paper I**. In **Paper II** the complete fabrication, characterization and study of the printed PVDF-TrFE piezoelectric device have been explored. The specific results of the work can be summarized as:

- A novel fabrication route for the printed piezoelectric PVDF-TrFE piezoelectric device was demonstrated for their versatile application demonstration. The device was fabricated with a combination of SP and IJP techniques to obtain the best morphological and electrical parameters obtaining a piezoelectric thickness of 3 µm fabricated through SP technology.

- Four different inks were characterized in terms of printability, morphology, compatibility and conductivity for the study of the IJP electrodes. After the study, the best materials were selected, obtaining for the first-time stable printing conditions and providing reliable capacitor fabrication without shortcuts between electrodes. A silver nanoparticle and silver organometallic inks were selected for their use as bottom and top electrodes respectively. Scanning Electron Microscope (SEM) images showed good sintering of the particles after their curing process with an excellent definition between layers. The nanoparticle ink shows a conductivity of $2.6 \cdot 10^7$ S·m^{-1} after photonic sintering and the organometallic ink shows a conductivity of $9.2 \cdot 10^6$ S·m^{-1} after a sintering process of 150 ˚C for 30 min. Their high conductivity and their solvent compatibility with the polymeric PVDF-TrFE layer make these inks the bests for the fabrication of the printed piezoelectric device. After the optimization of printing conditions, layers of 500 nm thickness were obtained for the inkjet printed electrodes.

- Polarization of the printed piezoelectric layer was studied. The best poling conditions were obtained by application of 50 MV·m^{-1} at 95 ˚C for 15 min, achieving a piezoelectric d$_{33}$ coefficient of 34 pC · N^{-1} with a remanent polarization of 6.8 µC · cm^{-2}. Controlled unpoling conditions were found for a thermal exposure at 140 ˚C and after poling conditions are applied again to the same device, the device completely recovers its piezoelectric characteristics. The multiple poling-unpoling cycles performed showed a fully reversible mechanism.

- The performance of the piezoelectric device was studied for its application as a vibrational sensor, actuator and energy harvester. Different electrode areas of 3x3, 4x4 and 5x5 mm^2 were also evaluated. By increasing the area of the electrode, the resistance of the device decreases while the capacitance increases, obtaining values of 3.0± 1.1 MΩ and 833± 44 pF respectively. The best performance was obtained with the largest electrode area and structure-property correlation was found for different electrode areas. Maximum output voltages of 3.6 V and output currents of 2.3 µA were obtained in the 5 mm x 5 mm device measured as a vibrational sensor. Maximum displacements of 43 µm when the device was used as an actuator under an applied voltage of 140 V and an output power of 1.6 µW with a value of 1.12 MΩ of load resistor were achieved when the device was used as an energy harvester.

Device II. The second monitoring device has been addressed with the fabrication of a stretchable piezoelectric sensor through printing techniques for the monitoring of human movements. This work has been explained in **Paper III** and its specific results can be summarized as:

- It was constructed a PVDF-TrFE piezoelectric sensor on a stretchable polymeric TPU substrate using SP technology. The sensors were fabricated using commercially available inks that can be processed at low temperatures (< 140 ˚C). Polymeric PEDOT:PSS was used for the fabrication of top and bottom electrodes of the piezoelectric system, obtaining a thickness of 3 μm for each polymeric layer. Silver ink was used for the electrical connections and the dielectric polydimethylsiloxane (PDMS) was applied as a passivation layer for the conductive materials. Poling conditions were optimized for this system and an electric field of 75 MV·m^{-1} was applied between the top and bottom electrodes of the fully printed device for 1 min.

- The single stretchable piezoelectric sensor was fabricated with an area of 6x17 mm^2 and exhibits a d_{33} piezoelectric constant of 42 pC · N^{-1} with a remanent polarization of 8.7 μC · cm^{-2} and a coercive field of 75 V·μm^{-1} was obtained. Capacitance value was used as quality control after the scalable fabrication and a value of 755 ± 30 pF was obtained as standard.

- The novel stretchable sensor presents a dynamic response with a 3 mm of maximum displacement without losing its piezoelectric activity and returning to its original state with a maximum stretchability of 153%. The stability of the piezoelectric response and the fast response time of 200 ms allowed us to use these stretchable fully printed devices as body motion monitoring sensors, correlating their output electric potential variation as a function of the mechanical strain. The stretchable sensor allows the monitoring of all the carpals of the hand, the elbow, knee and chest, being able to distinguish between walking and running and the inhale and exhale respiration mechanism.

- A further approach was performed by exploiting the scalability of the PE preparation methodology presented. A fully printed stretchable piezoelectric matrix composed of 15 individual sensor units was prepared and directly used as an electronic skin device for the monitoring of hand movement. The e-skin devices exhibit the same characteristics as the individual stretchable sensor, being able to distinguish the different movements of the fingers from the hand.

Device III. The third monitoring tool has been addressed with the scalable fabrication of an Iridium oxide (IrOx)-based pH sensor in a polymeric substrate through different printing techniques in a cost-effective, simple and fast way. The description of the technological steps and the characterization of the printed sensor has been presented in **Paper III**, and the specific conclusions of the work can be summarized as:

- It was studied a printed sensor based on an IrOx material for the measurement of pH in water applications. The main parts of the printed sensor were fabricated with the SP technique and the IrOx functionalization was performed with spray coating (SC). The use of SC for the functionalization of the indicative electrode (IE) allows greater scalability of these types of sensors, rather than the standard electrodeposition method.

- Low temperature curing inks (<130 ˚C) were used for the fabrication of the sensor. The selected inks exhibit excellent chemical and mechanical stability. The printed sensor includes the use of silver for the electrical connections, Ag/AgCl as a transductor element for the reference electrode (RE), graphite as an interlayer for the transductor element in the IE and contact pads protection and a UV-curable dielectric material used for the passivation.

- The electrochemical pH sensor exhibited a linear super-Nernstian response of 69.4 ± 1.0 $mV\cdot pH^{-1}$ in a wide range of pH between 2-12. The printed sensors were tested in different water conditions: tap, chlorinated and saltwater, exhibiting excellent reproducibility and high stability of the potential drift over time.

- The novel additive manufacturing fabrication route through large-scale printing techniques on a polymeric PET substrate opens new opportunities for pH sensing in several applications with a single device, which can be used for single use in a Point-of-Care (PoC) or continuous monitoring in a wide pH range in systems LoC.

Device IV. The fourth monitoring tool, that is the biggest challenge faced in this work, has been addressed with the study and fabrication of a printed multisensing platform for the monitoring of free chlorine (FC), dissolved oxygen (DO), pH, redox, conductivity, temperature and flow inside a LoC system to allow the automatic water quality measurement. The sensors have been characterized in terms of linearity, limit of detection (LOD) and limit of quantification (LOQ) This work has been presented in **Paper V** and its specific results can be summarized as:

- Sever printed sensors were fabricated in the same sensing platform in a polymeric polyethylene naphthalate (PEN) substrate using SP, IJP and SC scalable fabrication techniques. The array of sensors integrates FC, DO, pH, redox, conductivity, temperature and flow and was embedded in a polymethylmethacrylate (PMMA) holder with the microfluidic system fabricated through rapid prototyping techniques. The sensing platform incorporates a common gold working electrode (WE), a common Ag/AgCl pRE, a common graphite counter electrode (CE), an IrOx and a Pt/C IE for the potentiometric measurements, four silver electrodes, a silver resistive track, two PEDOT:PSS electrodes integrated with the PVDF-TrFE piezoelectric layer.

- The amperometric FC sensor exhibited a sensibility of 0.15 $\mu A(mg \cdot L^{-1})$ in a range of concentrations of 0-2.5 ppm with a LOD of 0.15 $mg \cdot L^{-1}$ and LOQ of 0.3 $mg \cdot L^{-1}$. The amperometric DO sensor exhibited a sensibility of 0.51 $\mu A(mg \cdot L^{-1})$ in the range between 0 and 7 $mg \cdot L^{-1}$ with a LOD of 0.28 $mg \cdot L^{-1}$ and a LOQ of 0.75 $mg \cdot L^{-1}$. The potentiometric pH sensor exhibited a linear super-Nernstian response of 72.1 $mV \cdot pH^{-1}$ in a wide range of pH between 3-11 with a response time of 25 s. The redox sensor exhibited a correlation factor of 0.2 against the commercial Pt sensor. Impedimetric conductivity sensor presents a sensibility of 0.15 $mF(mS \cdot cm^{-1})$ in a range of 0-13 $mS \cdot cm^{-1}$ with a LOD of 0.016 $mS \cdot cm^{-1}$ and a LOQ of 0.018 $mS \cdot cm^{-1}$. Temperature resistive sensor exhibits a linear relationship against the temperature of 85 $m\Omega \cdot °C^{-1}$ between 10-40 °C with a correlation factor of 0.9998. Flow piezoelectric sensor shows a linear relation of 5.05 $mV(mL \cdot min^{-1})$ in a range of 0-6 $mL \cdot min^{-1}$ with a LOD of 0.1 $mL \cdot min^{-1}$ and a LOQ of 0.5 $mL \cdot min^{-1}$.

- Values of FC, DO, pH, redox, conductivity, temperature and flow were successfully determined in real tap water demonstrating that sensors responses were in good agreement with results obtained with commercial sensors. The printed platform presents very high stability and linearity when real tap water samples were measured and compared with commercial sensors, demonstrating the reliability of this LoC approach for single or continuous monitoring in PoN applications in environmental measurements. Thanks to the microfluidic approach, the calibration of the printed sensors can be performed automatically increasing the lifetime of the multiparametric LoC device.

5.3. Open issues and future work

This work represents an advancement towards understanding and the correlation of structure and functionality, making use of printing technologies as a versatile fabrication approach to create novel printed devices and sensors. The combination of materials, multilayer structure and topographic design allows many different adaptations for integrating novel functional materials.

Significant results of the different studied proof-of-concept prototypes were obtained by measuring real signals, such the body movements with the piezoelectric systems, or real water samples from tap, saltwater or chlorinated water with the printed electrochemical sensors. Printed sensors best serve the application of single-use sensors, in the line with healthcare applications at the point of care (PoC). However, it was demonstrated that in the LoC approach, the sensors may be reused and have an extended lifetime demonstrating its capability for continuous, real-time measurements in PoN applications. In the last, further investigation of the functional materials chemical stability, within their printed multilayered structure is necessary to understand and control device degradation patterns. This is another crucial point for future research, both in printed device design, but also in microfluidic system investigation that may allow mitigation of the degradation of the functional devices, to extend their lifetime and increase their sustainability.

Another key aspect that the printed platforms need for their application in PoN applications is in terms of compact, autonomous control and automation modules. The electroactive systems require an electronic control unit, and the lab on chip microfluidic system require a compact pump system for fluid control. Research in electronic modules for data acquisition, signal processing and data transfer are fundamental to cope with the reliability need for adoption of the printed devices.

The printed sensor system approach completes and complements the concept to advance reliability and intelligibility of the interrelationships of the acquired data, making it enter the world of Internet-of-Things (IoT) devices. To improve reliability and be comparable to conventional sensor systems, the LoC platform must be provided of autonomy and connectivity, by developing a wireless communication method. Moreover, printed sensors have the ability to be massively produced thus able to generate high resolution, spatial and/or temporal, which is a disruptive characteristic to create datasets for Big Data and artificial intelligence (AI) modeling of the environmental occurrences. AI-driven approaches based on federated learning, or other techniques relying on massive distributed measurements and knowledge generation, to increase fault tolerance to field conditions thanks to a better understanding of the data, with its key

interferents and the autonomous and collaborative decision-making, and to reduce response time at the edge and network traffic needs, being able to perform wireless sensor networks (WSNs).
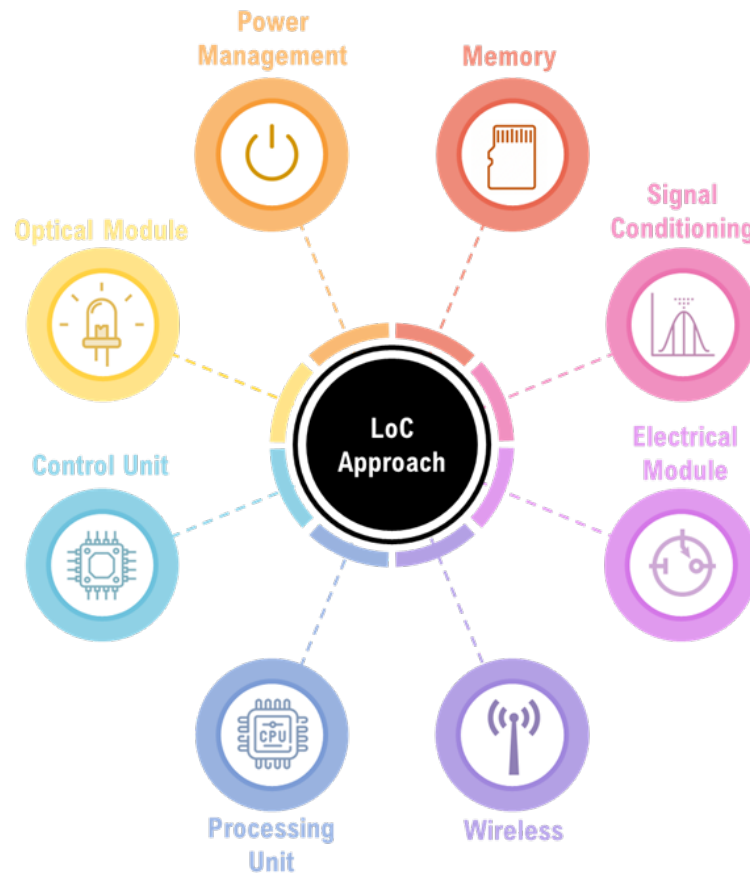
Figure 5.3 | Schematic approach of the modules for a IoT-based LoC application.

An schematic approach of these IoT-based system with the LoC devices can be observed in Figure 5.3. To provide a better efficiency, stability, durability and autonomy to the world of printed sensors it must be necessary the use of a specific electronic control unit that can manage and transmit the obtained data but with the enough capacity to kwon how to act according to the situation. Furthermore, the study and implementation of self-powered devices to increase the autonomy of LoC devices is crucial for its continuous evolution. Printed piezoelectric materials are one example, among other technologies, that pave the way to develop energy harvesting devices that, once optimized for the ambient energy sources, could help to allow an energy autonomy of the IoT.

The contributions made during this thesis work extend the understanding of the needs for EM processes, allowing the continuous improvement of the role of low-cost printed sensors which replace regular sensors, increasing the monitoring capabilities for PoN applications.

References

[1]   G. Klečka, C. Persoon, and R. Currie, *Chemicals of emerging concern in the Great Lakes Basin: An analysis of environmental exposures*, vol. 207. 2010.

[2]   C. C. Conrad and K. G. Hilchey, "A review of citizen science and community-based environmental monitoring: Issues and opportunities," *Environ. Monit. Assess.*, vol. 176, no. 1–4, pp. 273–291, 2011, doi: 10.1007/s10661-010-1582-5.

[3]   F. J. Kelly, G. W. Fuller, H. A. Walton, and J. C. Fussell, "Monitoring air pollution: Use of early warning systems for public health," *Respirology*, vol. 17, no. 1, pp. 7–19, 2012, doi: 10.1111/j.1440-1843.2011.02065.x.

[4]   X. yan Xue, R. Cheng, L. Shi, Z. Ma, and X. Zheng, "Nanomaterials for water pollution monitoring and remediation," *Environ. Chem. Lett.*, vol. 15, no. 1, pp. 23–27, 2017, doi: 10.1007/s10311-016-0595-x.

[5]   P. C. Brookes, "The use of microbial parameters in monitoring soil pollution by heavy metals," *Biol. Fertil. Soils*, vol. 19, no. 4, pp. 269–279, 1995, doi: 10.1007/BF00336094.

[6]   Y. Wei, Y. Jiao, D. An, D. Li, W. Li, and Q. Wei, "Review of dissolved oxygen detection technology: From laboratory analysis to online intelligent detection," *Sensors (Switzerland)*, vol. 19, no. 18, 2019, doi: 10.3390/s19183995.

[7]   Y. Qin, H.-J. Kwon, M. M. R. Howladera, and M. J. Deen, "Microfabricated electrochemical pH and free chlorine sensors for water quality monitoring: Recent advances and research challenges," *RSC Adv.*, vol. 2019-Novem, 2019, doi: 10.1039/x0xx00000x.

[8]   F. R. Burden, D. Donnert, T. Godish, and I. McKelvie, *Environmental Monitoring Handbook*. McGraw-Hill, 2002.

[9]   S. G. Evans and K. B. Delaney, *Catastrophic Mass Flows in the Mountain Glacial Environment*. Elsevier Inc., 2015.

[10]   H. Kulah and K. Najafi, "An Electromagnetic Micro Power Generator For Low-Frequency Environmental Vibrations," *17th IEEE Int. Conf. Micro Electro Mech. Syst.*, pp. 237–240, 2004.

[11]   B. Bayat, N. Crasta, A. Crespi, A. M. Pascoal, and A. Ijspeert, "Environmental monitoring using autonomous vehicles: a survey of recent searching techniques," *Curr. Opin. Biotechnol.*, vol. 45, pp. 76–84, 2017, doi: 10.1016/j.copbio.2017.01.009.

[12]   J. S. Chang, A. F. Facchetti, and R. Reuss, "A Circuits and Systems Perspective of Organic/Printed Electronics: Review, Challenges, and Contemporary and Emerging Design Approaches," *IEEE J. Emerg. Sel. Top. Circuits Syst.*, vol. 7, no. 1, pp. 7–26,

2017, doi: 10.1109/JETCAS.2017.2673863.

[13]   J. Barton *et al.*, "Screen-printed electrodes for environmental monitoring of heavy metal ions: a review," *Microchim. Acta*, vol. 183, no. 2, pp. 503–517, 2016, doi: 10.1007/s00604-015-1651-0.

[14]   A. Hayat and J. L. Marty, "Disposable Screen Printed Electrochemical Sensors: Tools for Environmental Monitoring," *Sensors*, vol. 14, pp. 10432–10453, 2014.

[15]   M. Alique, C. Delgado Simao, A. Moya, and G. Murillo, "Fully-Printed Piezoelectric Devices for Flexible Electronics Applications," *Adv. Mater. Technol.*, vol. 6, no. 3, 2021, doi: 10.1002/admt.202001020.

[16]   S. L. Ullo and G. R. Sinha, "Advances in smart environment monitoring systems using iot and sensors," *Sensors (Switzerland)*, vol. 20, no. 11, 2020, doi: 10.3390/s20113113.

[17]   C. Bazilo, A. Zagorskis, O. Petrishchev, Y. Bondarenko, V. Zaika, and Y. Petrushko, "Modelling of piezoelectric transducers for environmental monitoring," *10th Int. Conf. Environ. Eng. ICEE 2017*, no. August, 2017, doi: 10.3846/enviro.2017.008.

[18]   K. Yan, P. Karthick Kannan, D. Doonyapisut, K. Wu, C. H. Chung, and J. Zhang, "Advanced Functional Electroactive and Photoactive Materials for Monitoring the Environmental Pollutants," *Adv. Funct. Mater.*, vol. 31, no. 12, pp. 1–28, 2021, doi: 10.1002/adfm.202008227.

[19]   Y. Himeur, B. Rimal, A. Tiwary, and A. Amira, "Using artificial intelligence and data fusion for environmental monitoring: A review and future perspectives," *Inf. Fusion*, vol. 86–87, no. December 2021, pp. 44–75, 2022, doi: 10.1016/j.inffus.2022.06.003.

[20]   S. Bahri, N. Zoghlami, M. Abed, and J. M. R. S. Tavares, "BIG DATA for Healthcare: A Survey," *IEEE Access*, vol. 7, pp. 7397–7408, 2019, doi: 10.1109/ACCESS.2018.2889180.

[21]   M. S. Jamil, M. A. Jamil, A. Mazhar, A. Ikram, A. Ahmed, and U. Munawar, "Smart Environment Monitoring System by Employing Wireless Sensor Networks on Vehicles for Pollution Free Smart Cities," *Procedia Eng.*, vol. 107, pp. 480–484, 2015, doi: 10.1016/j.proeng.2015.06.106.

[22]   P. Clément *et al.*, "Gas discrimination using screen-printed piezoelectric cantilevers coated with carbon nanotubes," *Sensors Actuators, B Chem.*, vol. 237, no. August 2018, pp. 1056–1065, 2016, [Online]. Available: http://dx.doi.org/10.1016/j.snb.2016.07.163.

[23]   V. T. Rathod, D. R. Mahapatra, A. Jain, and A. Gayathri, "Characterization of a large-area PVDF thin film for electro-mechanical and ultrasonic sensing applications," *Sensors Actuators, A Phys.*, vol. 163, no. 1, pp. 164–171, 2010, doi: 10.1016/j.sna.2010.08.017.

[24]   T. Sharma, S. S. Je, B. Gill, and J. X. J. Zhang, "Patterning piezoelectric thin film PVDF-TrFE based pressure sensor for catheter application," *Sensors Actuators, A Phys.*, vol. 177, pp. 87–92, 2012, doi: 10.1016/j.sna.2011.08.019.

[25]   M. Alique, A. Moya, M. Kreuzer, P. Lacharmoise, G. Murillo, and C. Delgado Simao, "Controlled poling of fully printed piezoelectric PVDF-TrFE device multifunctional platform with inkjet-printed silver electrodes," *J. Mater. Chem. C*, vol. XX, 2022, doi: 10.1039/d2tc01913b.

[26]   S. Khan, L. Lorenzelli, and R. S. Dahiya, "Technologies for printing sensors and electronics over large flexible substrates: A review," *IEEE Sens. J.*, vol. 15, pp. 3164–3185, 2015.

[27]   M. Duque, E. Leon-Salguero, J. Sacristán, J. Esteve, and G. Murillo, "Optimization of a

piezoelectric energy harvester and design of a charge pump converter for CMOS-MEMS monolithic integration," *Sensors (Switzerland)*, vol. 19, no. 8, p. 1895, 2019.

[28] G. Murillo *et al.*, "Electromechanical Nanogenerator–Cell Interaction Modulates Cell Activity," *Adv. Mater.*, vol. 29, no. 24, pp. 1–7, 2017.

[29] I. J. Gomez, B. Arnaiz, M. Cacioppo, F. Arcudi, and M. Prato, "Nitrogen-doped Carbon Nanodots for bioimaging and delivery of paclitaxel," *J. Mater. Chem. B*, vol. 6, no. 35, pp. 5540–5548, 2018.

[30] W. Heywanh, K. Lubitz, and W. Wersing, *Piezoelectricity: Evolution and Future of a Technology*. Springer Series in Materials Science, 2008.

[31] J. R. Stetter, W. R. Penrose, and S. Yao, "Sensors, Chemical Sensors, Electrochemical Sensors, and ECS," *J. Electrochem. Soc.*, vol. 150, no. 2, p. S11, 2003, doi: 10.1149/1.1539051.

[32] A. HULANICKI, S. GEAB, and F. INGMAN, "Chemical Sensors Definition and Classification," *Pure Appl. Chem.*, vol. 63, no. 9, pp. 1247–1250, 1991, doi: doi:10.1351/pac199163091247.

[33] D. R. Thévenot, K. Toth, R. A. Durst, and G. S. Wilson, "Electrochemical Biosensors: Recomended Definitions ans Classification," *Pure Appl. Chem.*, vol. 71, no. 12, pp. 2333–2348, 1999, [Online]. Available: http://iupac.org/publications/pac/71/12/2333/.

[34] C. Dixon, J. Lamanna, and A. R. Wheeler, "Printed Microfluidics," *Adv. Funct. Mater.*, vol. 27, no. 11, 2017, doi: 10.1002/adfm.201604824.

[35] N. G. Di Novo, E. Cantù, S. Tonello, E. Sardini, and M. Serpelloni, "Support-material-free microfluidics on an electrochemical sensors platform by aerosol jet printing," *Sensors (Switzerland)*, vol. 19, no. 8, 2019, doi: 10.3390/s19081842.

[36] A. Moya *et al.*, "Miniaturized multiparametric flexible platform for the simultaneous monitoring of ionic: Application in real urine," *Sensors Actuators, B Chem.*, vol. 255, pp. 2861–2870, 2018, doi: 10.1016/j.snb.2017.09.104.

[37] A. MANZ, N. GRABER, and H. M. WIDMER, "Miniaturized Total Chemical Analysis Systems: a Novel Concept for Chemical Sensing," *Sensors Actuators B1*, pp. 244–248, 1990, doi: 10.1109/34.387509.

[38] S. Ramírez-García *et al.*, "Towards the development of a fully integrated polymeric microfluidic platform for environmental analysis," *Talanta*, vol. 77, no. 2, pp. 463–467, 2008, doi: 10.1016/j.talanta.2008.04.002.

[39] G. Quantification, "Lab on Chip PCR." https://www.gene-quantification.de/lab-on-chip-index.html (accessed Aug. 06, 2022).

[40] H. F. Li and J. M. Lin, "Applications of microfluidic systems in environmental analysis," *Anal. Bioanal. Chem.*, vol. 393, no. 2, pp. 555–567, 2009, doi: 10.1007/s00216-008-2439-4.

[41] E. Samiei, M. Tabrizian, and M. Hoorfar, "A review of digital microfluidics as portable platforms for lab-on a-chip applications," *Lab Chip*, vol. 16, no. 13, pp. 2376–2396, 2016, doi: 10.1039/c6lc00387g.

[42] A. Economou, C. Kokkinos, and M. Prodromidis, "Flexible plastic, paper and textile lab-on-a chip platforms for electrochemical biosensing," *Lab Chip*, vol. 18, no. 13, pp. 1812–1830, 2018, doi: 10.1039/c8lc00025e.

[43] R. Pol, F. Céspedes, D. Gabriel, and M. Baeza, "Microfluidic lab-on-a-chip platforms for environmental monitoring," *TrAC - Trends Anal. Chem.*, vol. 95, pp. 62–68, 2017, doi:

10.1016/j.trac.2017.08.001.

[44]   C. B. Freitas, R. C. Moreira, M. G. De Oliveira Tavares, and W. K. T. Coltro, "Monitoring of nitrite, nitrate, chloride and sulfate in environmental samples using electrophoresis microchips coupled with contactless conductivity detection," *Talanta*, vol. 147, pp. 335–341, 2016, doi: 10.1016/j.talanta.2015.09.075.

[45]   C. E. Stanley, G. Grossmann, X. CasadevallI Solvas, and A. J. DeMello, "Soil-on-a-Chip: Microfluidic platforms for environmental organismal studies," *Lab Chip*, vol. 16, no. 2, pp. 228–241, 2016, doi: 10.1039/c5lc01285f.

[46]   A. Moya Lara, "Integrated Sensors for Overcoming Organ-on-a-Chip Monitoring Challenges," Universitat Autònoma de Barcelona, 2017.

[47]   J. Höflin, S. M. T. Delgado, F. S. Sandovalb, J. G. Korvink, and D. Mager, "Electrifying the disk: A modular rotating platform for wireless power and data transmission for Lab on a Disk application," *Lab Chip*, vol. 3, pp. 10715–10722, 2015, doi: 10.1039/b000000x.

[48]   G. Lippmann, "The principle of the conservation of electricity," *Ann. chim. phys*, vol. 24, no. 5, pp. 145–179, 1881, doi: 10.5840/monist190414314.

[49]   H. Klank, J. P. Kutter, and O. Geschke, "CO2-laser micromachining and back-end processing for rapid production of PMMA-based microfluidic systems," *Lab Chip*, vol. 2, no. 4, pp. 242–246, 2002, doi: 10.1039/b206409j.

[50]   K. Suganuma, *Introduction to Printed Electronics*. Springer, 2014.

[51]   W. Wu, "Inorganic nanomaterials for printed electronics: A review," *Nanoscale*, vol. 9, no. 22, pp. 7342–7372, 2017.

[52]   M. G. Mohammed and R. Kramer, "All-Printed Flexible and Stretchable Electronics," *Adv. Mater.*, vol. 29, no. 19, 2017.

[53]   Z. Cui *et al.*, *Printed Electronics: Materials, Technologies and Applications*, 1 edition. Wiley, 2016.

[54]   M. Graf, A. Gurlo, N. Bârsan, U. Weimar, and A. Hierlemann, "Microfabricated gas sensor systems with sensitive nanocrystalline metal-oxide films," *J. Nanoparticle Res.*, vol. 8, no. 6, pp. 823–839, 2006.

[55]   D. J. Kang, Y. Jüttke, L. González-García, A. Escudero, M. Haft, and T. Kraus, "Reversible Conductive Inkjet Printing of Healable and Recyclable Electrodes on Cardboard and Paper," *Small*, vol. 2000928, pp. 1–7, 2020.

[56]   B. Michel *et al.*, "Printing meets lithography: Soft approaches to high-resolution patterning," *Chimia (Aarau).*, vol. 56, pp. 527–542, 2002.

[57]   H. Kipphan, *Handbook Of Print Media*. Springer-Verlag Berlin, 2001.

[58]   R. Soukup, A. Hamáček, and J. Řeboun, "Organic based sensors: Novel screen printing technique for sensing layers deposition," *Proc. Int. Spring Semin. Electron. Technol.*, pp. 19–24, 2012.

[59]   M. Pudas, J. Hagberg, and S. Leppa, "Printing parameters and ink components affecting ultra-fine-line gravure-offset printing for electronics applications," *J. ofthe Eur. Ceram. Soc.*, vol. 24, pp. 2943–2950, 2004.

[60]   H. Kempa *et al.*, "Complementary Ring Oscillator Exclusively Prepared by Means of Gravure and Flexographic Printing," *IEEE Trans. Electron Devices*, vol. 58, no. 8, pp. 2765–2769, 2011.

[61]   E. B. Secor, S. Lim, H. Zhang, C. D. Frisbie, L. F. Francis, and M. C. Hersam, "Gravure printing of graphene for large-area flexible electronics," *Adv. Mater.*, vol. 26, pp. 4533–4538, 2014.

[62]   D. Thuau, K. Kallitsis, F. D. Dos Santos, and G. Hadziioannou, "All inkjet-printed piezoelectric electronic devices: Energy generators, sensors and actuators," *J. Mater. Chem. C*, vol. 5, pp. 9963–9966, 2017.

[63]   H. Gleskova and S. Wagner, "Electrophotographically printed insulator," *Mater. Lett.*, vol. 52, pp. 150–153, 2002.

[64]   B. R. F. Pease and S. Y. Chou, "Lithography and Other Patterning Techniques for Future Electronics," *Proc. IEEE*, vol. 96, pp. 248–270, 2008.

[65]   R. Larson, *OE-A roadmap for organic and printed electronics*, 8th Editio. 2018.

[66]   H. Becker and C. Gärtner, "Polymer microfabrication methods for microfluidic analytical applications," *Electrophoresis*, vol. 21, no. 1, pp. 12–26, 2000, doi: 10.1002/(sici)1522-2683(20000101)21:1<12::aid-elps12>3.3.co;2-z.

[67]   J. Wiklund *et al.*, "A review on printed electronics: Fabrication methods, inks, substrates, applications and environmental impacts," *J. Manuf. Mater. Process.*, vol. 5, no. 3, 2021, doi: 10.3390/jmmp5030089.

[68]   S. Li, R. Li, O. G. González, T. Chen, and X. Xiao, "Highly sensitive and flexible piezoresistive sensor based on c-MWCNTs decorated TPU electrospun fibrous network for human motion detection," *Compos. Sci. Technol.*, vol. 203, no. May, pp. 2020–2022, 2021, doi: 10.1016/j.compscitech.2020.108617.

[69]   Y. Zhao *et al.*, "Ultra-sensitive and durable strain sensor with sandwich structure and excellent anti-interference ability for wearable electronic skins," *Compos. Sci. Technol.*, vol. 200, no. July, p. 108448, 2020, doi: 10.1016/j.compscitech.2020.108448.

[70]   A. K. Bose *et al.*, "Screen Printed Silver/Carbon Composite Strain Gauge on a TPU Platform for Wearable Applications," *FLEPS 2020 - IEEE Int. Conf. Flex. Printable Sensors Syst.*, pp. 18–22, 2020, doi: 10.1109/FLEPS49123.2020.9239547.

[71]   A. A. F. Husain, W. Z. W. Hasan, S. Shafie, M. N. Hamidon, and S. S. Pandey, "A review of transparent solar photovoltaic technologies," *Renew. Sustain. Energy Rev.*, vol. 94, no. June, pp. 779–791, 2018, doi: 10.1016/j.rser.2018.06.031.

[72]   T. Yoshida, "Photovoltaic Properties of Screen-Printed CdTe / CdS Solar Cells on Indium-Tin-Oxide Coated Glass Substrates," *J. Electrochem. Soc.*, vol. 142, no. 9, pp. 3232–3237, 1995, doi: 10.1149/1.2048720.

[73]   V. Beedasy and P. J. Smith, "Printed electronics as prepared by inkjet printing," *Materials (Basel).*, vol. 13, no. 3, pp. 1–23, 2020, doi: 10.3390/ma13030704.

[74]   M. Neophytou, E. Georgiou, M. M. Fyrillas, and S. A. Choulis, "Two step sintering process and metal grid design optimization for highly efficient ITO free organic photovoltaics," *Sol. Energy Mater. Sol. Cells*, vol. 122, pp. 1–7, 2014, doi: 10.1016/j.solmat.2013.11.021.

[75]   J. Kim, J. Hwang, K. Song, N. Kim, J. C. Shin, and J. Lee, "Ultra-thin flexible GaAs photovoltaics in vertical forms printed on metal surfaces without interlayer adhesives," *Appl. Phys. Lett.*, vol. 108, no. 25, 2016, doi: 10.1063/1.4954039.

[76]   X. Li, D. R. Ballerini, and W. Shen, "A perspective on paper-based microfluidics: Current status and future trends," *Biomicrofluidics*, vol. 6, no. 1, 2012, doi: 10.1063/1.3687398.

[77]   H. Z. Sheng Huang, Peng Huang, Lei Wang, Junbo Han, Yu Chen, "Halogenated-Methylammonium based Three Dimensional Halide Perovskites," *Adv. Mater.*, no. 25, pp. 1–24, 2016, doi: 10.1002/)).

[78]   Y. Wang *et al.*, "Flexible RFID Tag Metal Antenna on Paper-Based Substrate by Inkjet Printing Technology," *Adv. Funct. Mater.*, vol. 29, no. 29, pp. 1–11, 2019, doi: 10.1002/adfm.201902579.

[79]   L. Yang, A. Rida, R. Vyas, and M. M. Tentzeris, "RFID tag and RF structures on a paper substrate using inkjet-printing technology," *IEEE Trans. Microw. Theory Tech.*, vol. 55, no. 12, pp. 2894–2901, 2007, doi: 10.1109/TMTT.2007.909886.

[80]   T. Tuhkala, T. Tuhkala, T. Tuomaala, and H. Määttä, "Practical guide to screen printing in printed electronics," 2019. [Online]. Available: https://oamk.finna.fi/Record/leevi.218210%0Ahttps://oamk.finna.fi/Record/leevi.218210 .

[81]   M. Palencia, "Surface free energy of solids by contact angle measurements.," *J. Sci. with Technol. Appl.*, vol. 2, no. 2017, pp. 84–93, 2017, doi: 10.34294/j.jsta.17.2.17.

[82]   A. A. Tyuftin and J. P. Kerry, "Review of surface treatment methods for polyamide films for potential application as smart packaging materials: surface structure, antimicrobial and spectral properties," *Food Packag. Shelf Life*, vol. 24, 2020, doi: 10.1016/j.fpsl.2020.100475.

[83]   L. Podgorski, B. Chevet, L. Onic, and A. Merlin, "Modification of wood wettability by plasma and corona treatments," *Int. J. Adhes. Adhes.*, vol. 20, no. 2, pp. 103–111, 2000, doi: 10.1016/S0143-7496(99)00043-3.

[84]   R. Wolf and A. C. Sparavigna, "Role of Plasma Surface Treatments on Wetting and Adhesion," *Engineering*, vol. 02, no. 06, pp. 397–402, 2010, doi: 10.4236/eng.2010.26052.

[85]   J. M. Farley and P. Meka, "Heat sealing of semicrystalline polymer films. III. Effect of corona discharge treatment of LLDPE," *J. Appl. Polym. Sci.*, vol. 51, no. 1, pp. 121–131, 1994, doi: 10.1002/app.1994.070510113.

[86]   I. Novák and Š. Florián, "Influence of processing additives on adhesive properties of surface-modified low-density polyethylene," *Macromol. Mater. Eng.*, vol. 289, no. 3, pp. 269–274, 2004, doi: 10.1002/mame.200300166.

[87]   H. Chtourou, B. Rield, and B. V. Kokta, "ESCA and FTIR Study of Synthetic Pulp Fiber Modified by Fluorinated Gases and Corona Discharge," *J. Colloid Interface Sci.*, vol. 158, 1993.

[88]   D. J. Carlsson and D. M. Wiles, "Surface studies by attenuated total reflection spectroscopy. I. Corona treatment of polypropylene," *Can. J. Chem.*, vol. 48, no. 15, pp. 2397–2406, 1970, doi: 10.1139/v70-401.

[89]   E. C. Onyiriuka, "The effects of high-energy radiation on the surface chemistry of polystyrene: A mechanistic study," *J. Appl. Polym. Sci.*, vol. 47, no. 12, pp. 2187–2194, 1993, doi: 10.1002/app.1993.070471213.

[90]   S. Khan, W. Dang, L. Lorenzelli, and R. Dahiya, "Flexible Pressure Sensors Based on Screen-Printed P(VDF-TrFE) and P(VDF-TrFE)/MWCNTs," *IEEE Trans. Semicond. Manuf.*, vol. 28, no. 4, pp. 486–493, 2015, doi: 10.1109/TSM.2015.2468053.

[91]   I. Gibson, D. Rosen, and B. Stucker, *Additive Manufacturing Technologies 3D Printing, Rapid Prototyping, and Direct Digital Manufacturing*, 2nd Editio. Springer, 2015.

[92] Y. J. Kwon, Y. D. Park, and W. H. Lee, "Inkjet-printed organic transistors based on organic semiconductor/insulating polymer blends," *Materials (Basel).*, vol. 9, no. 8, 2016, doi: 10.3390/ma9080650.

[93] G. C. Dubey, "The squeegee in printing of electronic circuits," *Microelectron. Reliab.*, vol. 14, no. 5–6, pp. 427–429, 1975, doi: 10.1016/0026-2714(75)90151-1.

[94] N. Board, *Screen Prinitng Technology Hand Book*. Asia Pacific Business Press Inc., 2003.

[95] M. S. Rusdi *et al.*, "Numerical Investigation on the Effect of Squeegee Angle during Stencil Printing Process," *J. Phys. Conf. Ser.*, vol. 1082, no. 1, 2018, doi: 10.1088/1742-6596/1082/1/012057.

[96] C. O. Phillips, D. G. Beynon, S. M. Hamblyn, G. R. Davies, D. T. Gethin, and T. C. Claypole, "A study of the abrasion of squeegees used in screen printing and its effect on performance with application in printed electronics," *Coatings*, vol. 4, no. 2, pp. 356–379, 2014, doi: 10.3390/coatings4020356.

[97] *Digital Electric Flat Screen Printer AT-GOPD Instruction Manual*. China, 2016.

[98] S. Park *et al.*, "Spray-coated organic solar cells with large-area of 12.25 cm2," *Sol. Energy Mater. Sol. Cells*, vol. 95, no. 3, pp. 852–855, 2011, doi: 10.1016/j.solmat.2010.10.033.

[99] G. Susanna, L. Salamandra, T. M. Brown, A. Di Carlo, F. Brunetti, and A. Reale, "Airbrush spray-coating of polymer bulk-heterojunction solar cells Gianpaolo," *Sol. Energy Mater. Sol. Cells*, vol. 95, no. 7, pp. 1775–1778, 2011, doi: 10.1016/j.solmat.2011.01.047.

[100] J. Kang *et al.*, "Fully spray-coated inverted organic solar cells," *Sol. Energy Mater. Sol. Cells*, vol. 103, pp. 76–79, 2012, doi: 10.1016/j.solmat.2012.04.027.

[101] F. Aziz and A. F. Ismail, "Spray coating methods for polymer solar cells fabrication : A review," *Mater. Sci. Semicond. Process.*, vol. 39, pp. 416–425, 2015, doi: 10.1016/j.mssp.2015.05.019.

[102] F. C. Krebs, "Fabrication and processing of polymer solar cells : A review of printing and coating techniques," *Sol. Energy Mater. Sol. Cells*, vol. 93, pp. 394–412, 2009, doi: 10.1016/j.solmat.2008.10.004.

[103] M. M. Deshmukh, D. C. Ralph, M. Thomas, and J. Silcox, "Nanofabrication using a stencil mask," *Appl. Phys. Lett.*, vol. 75, no. 11, pp. 1631–1633, 1999.

[104] A. Greve *et al.*, "Wafer scale coating of polymer cantilever fabricated by nanoimprint lithography WAFER SCALE COATING OF POLYMER CANTILEVER FABRICATED BY NANOIMPRINT LITHOGRAPHY," *IEEE 23rd Int. Conf. Micro Electro Mech. Syst.*, pp. 612–614, 2010, doi: 10.1109/MEMSYS.2010.5442334.

[105] J. Brugger, J. W. Berenschot, S. Kuiper, W. Nijdam, B. Otter, and M. Elwenspoek, "Resistless patterning of sub-micron structures by evaporation through nanostencils," *Microelectron. Eng.*, vol. 53, pp. 403–405, 2000.

[106] G. Kim, B. Kim, and J. Brugger, "All-photoplastic microstencil with self-alignment for multiple layer shadow-mask patterning," *Sensors Actuators, A Phys.*, vol. 107, pp. 132–136, 2003, doi: 10.1016/S0924-4247(03)00298-X.

[107] S. Selvarasah, S. H. Chao, C. Chen, S. Sridhar, and A. Busnaina, "A reusable high aspect ratio parylene-C shadow mask technology for diverse micropatterning applications," *Sensors Actuators, A Phys.*, 2007, doi: 10.1016/j.sna.2007.10.053.

[108] R. J. Jackman, D. C. Duffy, O. Cherniavskaya, and G. M. Whitesides, "Using Elastomeric Membranes as Dry Resists and for Dry Lift-Off," *Langmuir*, no. 4, pp. 2973–2984, 1999.

[109] D. V Muyres *et al.*, "Polymeric aperture masks for high performance organic integrated circuits Polymeric aperture masks for high performance organic integrated circuits *," *J. Vac. Sci. Technol. B Microelectron. Nanom. Struct.*, vol. 22, pp. 1892–1895, 2004, doi: 10.1116/1.1766304.

[110] L. La Notte *et al.*, "Airbrush spray coating of amorphous titanium dioxide for inverted polymer solar cells," *Int. J. Photoenergy*, vol. 2012, 2012, doi: 10.1155/2012/897595.

[111] R. Green, A. Morfa, A. J. Ferguson, N. Kopidakis, G. Rumbles, and S. E. Shaheen, "Performance of bulk heterojunction photovoltaic devices prepared by airbrush spray deposition," *Appl. Phys. Lett.*, vol. 92, no. 3, 2008, doi: 10.1063/1.2836267.

[112] Sono-tek, "Precise Control with Patented Spray Shaping Systems." https://www.sono-tek.com/ultrasonic-coating/spray-shaping-systems/ (accessed Aug. 01, 2022).

[113] D. Vak *et al.*, "Fabrication of organic bulk heterojunction solar cells by a spray deposition method for low-cost power generation Fabrication of organic bulk heterojunction solar cells by a spray deposition method for low-cost power generation," *Appl. Phys. Lett.*, vol. 081102, no. 2007, 2014, doi: 10.1063/1.2772766.

[114] W. Nie *et al.*, "Exploring spray-coating techniques for organic solar cell applications," *Int. J. Photoenergy*, vol. 2012, pp. 1–8, 2012, doi: 10.1155/2012/175610.

[115] I. M. HUTCHINGS and G. D. MARTIN, *Inkjet technology for Digital Fabrication*, vol. 2a. 2013.

[116] D. B. Bogy and F. E. Talke, "Experimental and Theoretical Study of Wave Propagation Phenomena in Drop-on-Demand Ink Jet Devices.," *IBM J. Res. Dev.*, vol. 28, no. 3, pp. 314–321, 1984, doi: 10.1147/rd.283.0314.

[117] K. S. Kwon, "Experimental analysis of waveform effects on satellite and ligament behavior via in situ measurement of the drop-on-demand drop formation curve and the instantaneous jetting speed curve," *J. Micromechanics Microengineering*, vol. 20, no. 11, 2010, doi: 10.1088/0960-1317/20/11/115005.

[118] H. C. Wu, T. R. Shan, W. S. Hwang, and H. J. Lin, "Study of micro-droplet behavior for a piezoelectric inkjet printing device using a single pulse voltage pattern," *Mater. Trans.*, vol. 45, no. 5, pp. 1794–1801, 2004, doi: 10.2320/matertrans.45.1794.

[119] I. FUJIFILM Dimatix, "Dimatix Materials Printer DMP-2800 Series User Manual," *FUJIFILM Dimatix*, pp. 1–93, 2006, [Online]. Available: https://www.lcinet.kent.edu/images/user_images/cpip/1418077287_18795DMP-2800 User Manual v1.3.pdf.

[120] B. J. De Gans, P. C. Duineveld, and U. S. Schubert, "Inkjet printing of polymers: State of the art and future developments," *Adv. Mater.*, vol. 16, no. 3, pp. 203–213, 2004, doi: 10.1002/adma.200300385.

[121] S. D. Hoath, *Fundamentals of Inkjet Printing*. Weinheim, Germany All, 2016.

[122] D. F. Elger, B. A. LeBret, C. T. Crowe, and J. A. Roberson, *Engineering Fluid Mechanical*. John Wiley & Sons, 2020.

[123] C. J. Seeton, "Viscosity-Temperature Correlation for Liquids," *Am. Soc. Mech. Eng. Digit. Collect.*, pp. 131–142, 2008, doi: https://doi.org/10.1115/IJTC2006-12139.

[124] B. Derby, "Inkjet printing of functional and structural materials: Fluid property

requirements, feature stability, and resolution," *Annu. Rev. Mater. Res.*, vol. 40, pp. 395–414, 2010, doi: 10.1146/annurev-matsci-070909-104502.

[125] J. Alamán, R. Alicante, J. I. Peña, and C. Sánchez-Somolinos, "Inkjet printing of functional materials for optical and photonic applications," *Materials (Basel).*, vol. 9, no. 11, 2016, doi: 10.3390/ma9110910.

[126] G. H. McKinley and M. Renardy, "Wolfgang von Ohnesorge," *Phys. Fluids*, vol. 23, no. 12, 2011, doi: 10.1063/1.3663616.

[127] I. Burgués-Ceballos, M. Stella, P. Lacharmoisea, and E. Martinez-Ferrero, "Towards industrialization of polymer solar cells: material processing for upscaling," *J. Mater. Chem. A*, vol. 3, pp. 10715–10722, 2014, doi: 10.1039/b000000x.

[128] R. D. Deegan, O. Bakajin, and T. F. Dupont, "Capillary flow as the cause of ring stains from dried liquid drops," *Nature*, vol. 389, pp. 827–829, 1997.

[129] D. Soltman and V. Subramanian, "Inkjet-Printed Line Morphologies and Temperature Control of the," *Langmuir*, vol. 24, no. 5, pp. 2224–2231, 2008.

[130] D. Kim, S. Jeong, B. K. Park, and J. Moon, "Direct writing of silver conductive patterns: Improvement of film morphology and conductance by controlling solvent compositions," *Appl. Phys. Lett.*, vol. 89, no. 26, pp. 87–90, 2006, doi: 10.1063/1.2424671.

[131] H. Hu and R. G. Larson, "Marangoni effect reverses coffee-ring depositions," *J. Phys. Chem. B*, vol. 110, no. 14, pp. 7090–7094, 2006, doi: 10.1021/jp0609232.

[132] E. C. M. Friend, "Smart materials and structures: The emerging technology," *Interdiscip. Sci. Rev.*, vol. 21, no. 3, pp. 195–198, 1996, doi: 10.1179/isr.1996.21.3.195.

[133] A. Sir, "Smart Materials and Their Classification," *Can. Mil. J.*, 2000.

[134] J. Sun, Q. Guan, Y. Liu, and J. Leng, "Morphing aircraft based on smart materials and structures: A state-of-the-art review," *J. Intell. Mater. Syst. Struct.*, vol. 27, no. 17, pp. 2289–2312, 2016, doi: 10.1177/1045389X16629569.

[135] B. Koc, S. Cagatay, and K. Uchino, "A Piezoelectric Motor Using Two Orthogonal," *IEEE Trans. Ultrason. Ferroelectr. Freq. Control*, vol. 49, no. 4, pp. 495–500, 2002.

[136] H. J. Kim, W. S. Yang, and K. No, "Improvement of low-frequency characteristics of piezoelectric speakers based on acoustic diaphragms," *IEEE Trans. Ultrason. Ferroelectr. Freq. Control*, vol. 59, no. 9, pp. 2027–2035, 2012, doi: 10.1109/TUFFC.2012.2423.

[137] J. Curie and P. Curie, "Development by Pressure of Polar Electricity in Hemihedral Crystals with Inclined Faces," *Bull. la Société minéralogique Fr.*, vol. 3, no. 4, pp. 90–93, 1880, [Online]. Available: https://www.persee.fr/doc/bulmi_0150-9640_1880_num_3_4_1564.

[138] S. Priya *et al.*, "A Review on Piezoelectric Energy Harvesting: Materials, Methods, and Circuits," *Energy Harvest. Syst.*, vol. 4, no. 1, pp. 3–39, 2017.

[139] D. W. Lee *et al.*, "Polarization-controlled PVDF-based hybrid nanogenerator for an effective vibrational energy harvesting from human foot," *Nano Energy*, vol. 76, no. May, p. 105066, 2020, doi: 10.1016/j.nanoen.2020.105066.

[140] Q. Li and Q. Wang, "Ferroelectric Polymers and Their Energy-Related Applications," *Macromol. Chem. Phys.*, vol. 217, no. 11, pp. 1228–1244, 2016, doi: 10.1002/macp.201500503.

[141]   S. Trolier-McKinstry and P. Muralt, "Thin Film Piezoelectrics for MEMS," *J. Electroceramics*, vol. 12, pp. 7–17, 2004, doi: 10.1023/B.

[142]   D. Damjanovic, *Hysteresis in piezoelectric and ferroelectric materials*, vol. 3. 2006.

[143]   J. C. Burfoot and G. W. Taylor, *Polar Dielectric and Their Application*. London: Macmillan, 1979.

[144]   M. T. Chorsi *et al.*, "Piezoelectric Biomaterials for Sensors and Actuators," *Adv. Mater.*, vol. 31, no. 1, pp. 1–15, 2019, doi: 10.1002/adma.201802084.

[145]   K. S. Kim, Y. C. Lee, J. W. Kim, and S. B. Jung, "Flexibility of silver conductive circuits screen-printed on a polyimide substrate," *J. Nanosci. Nanotechnol.*, vol. 11, no. 2, pp. 1493–1498, 2011.

[146]   S. Chung, J. Lee, H. Song, S. Kim, J. Jeong, and Y. Hong, "Inkjet-printed stretchable silver electrode on wave structured elastomeric substrate," *Appl. Phys. Lett.*, vol. 98, no. 15, pp. 2011–2014, 2011.

[147]   Z. Cui *et al.*, *Printed Electronics: Materials, Technologies and Applications*. Wiley, 2016.

[148]   W. Yang, E. J. W. List-Kratochvil, and C. Wang, "Metal particle-free inks for printed flexible electronics," *J. Mater. Chem. C*, vol. 7, no. 48, pp. 15098–15117, 2019.

[149]   A. Almusallam *et al.*, "Flexible piezoelectric nano-composite films for kinetic energy harvesting from textiles," *Nano Energy*, vol. 33, pp. 146–156, 2017.

[150]   N. Matsuhisa *et al.*, "Printable elastic conductors with a high conductivity for electronic textile applications," *Nat. Commun.*, vol. 6, 2015.

[151]   J. Sato *et al.*, "Ferroelectric polymer-based fully printed flexible strain rate sensors and their application for human motion capture," *Sensors Actuators, A Phys.*, vol. 295, pp. 93–98, 2019.

[152]   T. Sekine *et al.*, "Fully Printed Wearable Vital Sensor for Human Pulse Rate Monitoring using Ferroelectric Polymer," *Sci. Rep.*, vol. 8, pp. 1–10, 2018.

[153]   C. Dagdeviren *et al.*, "Conformal piezoelectric systems for clinical and experimental characterization of soft tissue biomechanics," *Nat. Mater.*, vol. 14, pp. 728–736, 2015.

[154]   D. Garcia *et al.*, "Large-Area Paper Batteries with Ag and Zn/Ag Screen-Printed Electrodes´," *ACS Omega*, vol. 4, pp. 16781–16788, 2019.

[155]   P. H. Ducrot, I. Dufour, and C. Ayela, "Optimization of PVDF-TrFE Processing Conditions for the Fabrication of Organic MEMS Resonators," *Sci. Rep.*, vol. 6, no. December 2015, pp. 1–7, 2016.

[156]   J. S. Harrison and Z. Ounaies, *Piezoelectric polymers Encyclopedia of Polymer Science and Technology*. 2002.

[157]   P. F. Moonen, I. Yakimets, and J. Huskens, "Fabrication of transistors on flexible substrates: From mass-printing to high-resolution alternative lithography strategies," *Adv. Mater.*, vol. 24, pp. 5526–5541, 2012.

[158]   C. Dagdeviren *et al.*, "Conformable amplified lead zirconate titanate sensors with enhanced piezoelectric response for cutaneous pressure monitoring," *Nat. Commun.*, vol. 5, 2014, doi: 10.1038/ncomms5496.

[159]   T. Someya, Ed., *Stretchable Electronics*. Weinheim, Germany: Wiley-VCH, 2013.

[160]   Z. H. Liu, C. T. Pan, L. W. Lin, J. C. Huang, and Z. Y. Ou, "Direct-write PVDF

nonwoven fiber fabric energy harvesters via the hollow cylindrical near-field electrospinning process," *Smart Mater. Struct.*, vol. 23, 2014.

[161] H. J. Xiang, J. Yang, J. G. Hou, and Q. Zhu, "Piezoelectricity in ZnO nanowires : A first-principles study Piezoelectricity in ZnO nanowires : A first-principles study," *Appl. Phys. Lett.*, vol. 223111, pp. 1–4, 2006.

[162] Y. Tan *et al.*, "Unfolding grain size effects in barium titanate ferroelectric ceramics," *Sci. Rep.*, vol. 5, pp. 15–21, 2015.

[163] A. C. Dent, C. R. Bowen, R. Stevens, M. G. Cain, and M. Stewart, "Effective elastic properties for unpoled barium titanate," *J. Eur. Ceram. Soc.*, vol. 27, pp. 3739–3743, 2007.

[164] V. Bystrov *et al.*, *Piezoelectric Nanomaterials for Biomedical Applications*. New York: Springer, 2012.

[165] I. L. Guy, S. Muensit, E. M. Goldys, and D. Interna-, "Extensional piezoelectric coefficients of gallium nitride and aluminum nitride," *Appl. Phys. Lett.*, vol. 75, pp. 4133–4135, 1999.

[166] A. Ciubotariu, "Design, Modeling, Fabrication and Control of PMN-PT Piezoelectric Systems," Université de Franche-Comté, 2016.

[167] S. Crossley, R. A. Whiter, and S. Kar-Narayan, "Polymer-based nanopiezoelectric generators for energy harvesting applications," *Energy Mater. Mater. Sci. Eng. Energy Syst.*, vol. 9, pp. 1613–1624, 2014.

[168] I. Murat Koç and E. Akça, "Design of a piezoelectric based tactile sensor with bio-inspired micro/nano-pillars," *Tribol. Int.*, vol. 59, pp. 321–331, 2013.

[169] G. H. Feng and M. Y. Tsai, "Acoustic emission sensor with structure-enhanced sensing mechanism based on micro-embossed piezoelectric polymer," *Sensors Actuators, A Phys.*, vol. 162, pp. 100–106, 2010.

[170] D. H. Kim, B. Kim, and H. Kang, "Development of a piezoelectric polymer-based sensorized microgripper for microassembly and micromanipulation," *Microsyst. Technol.*, vol. 10, pp. 275–280, 2004.

[171] J. Pu, X. Yan, Y. Jiang, C. Chang, and L. Lin, "Piezoelectric actuation of direct-write electrospun fibers," *Sensors Actuators, A Phys.*, vol. 164, pp. 131–136, 2010, [Online]. Available: http://dx.doi.org/10.1016/j.sna.2010.09.019.

[172] Y. Zhang, H. Niu, S. Xie, and X. Zhang, "Numerical and experimental investigation of active vibration control in a cylindrical shell partially covered by a laminated PVDF actuator," *Smart Mater. Struct.*, vol. 17, p. 035024, 2008.

[173] J. Fang, X. Wang, and T. Lin, "Electrical power generator from randomly oriented electrospun poly(vinylidene fluoride) nanofibre membranes," *J. Mater. Chem.*, vol. 21, pp. 11088–11091, 2011.

[174] K. F. Lei, Y. Z. Hsieh, Y. Y. Chiu, and M. H. Wu, "The structure design of piezoelectric poly(vinylidene fluoride) (PVDF) polymer-based sensor patch for the respiration monitoring under dynamic walking conditions," *Sensors (Switzerland)*, vol. 15, pp. 18801–18812, 2015.

[175] D. Song, D. Yang, and Z. Feng, "Formation of β-phase microcrystals from the melt of PVF 2 -PMMA blends induced by quenching," *J. Mater. Sci.*, vol. 25, pp. 57–64, 1990.

[176] C. Li, P. M. Wu, L. A. Shutter, and R. K. Narayan, "Dual-mode operation of flexible piezoelectric polymer diaphragm for intracranial pressure measurement," *Appl. Phys.*

Lett., vol. 96, pp. 1–4, 2010.

[177] J. F. Tressler, S. Alkoy, A. Dogan, and R. E. Newnham, "Functional composites for sensors, actuators and transducers," *Compos. Part A*, vol. 39, pp. 477–482, 1999.

[178] I. Babu and G. de With, "Highly flexible piezoelectric 0-3 PZT-PDMS composites with high filler content," *Compos. Sci. Technol.*, vol. 91, pp. 91–97, 2014.

[179] M. Latour, R. Almairac, and R. L. Moreira, "Contribution of Defects to the Ferroelectric to Paraelectric Phase Transition in Polyvinylidenefluoride Trifluoroethylene Copolymers," *IEEE Trans. Electr. Insul.*, vol. 24, no. 3, pp. 443–448, 1989.

[180] F. Kajzar and J.-M. Nunzi, *Molecule Orientation Techniques*. 2006.

[181] R. A. Hill, A. Knoesen, and M. A. Mortazavi, "Corona poling of nonlinear polymer thin films for electro-optic modulators," *Appl. Phys. Lett.*, vol. 65, pp. 1733–1735, 1994.

[182] T. Sekine *et al.*, "Low Operating Voltage and Highly Pressure-Sensitive Printed Sensor for Healthcare Monitoring with Analogic Amplifier Circuit," *ACS Appl. Electron. Mater.*, vol. 1, no. 2, pp. 246–252, 2019.

[183] T. Siponkoski *et al.*, "Electromechanical properties of PZT/P(VDF-TrFE) composite ink printed on a flexible organic substrate," *Compos. Part B Eng.*, vol. 80, pp. 217–222, 2015.

[184] Q. Q. Zhang, S. J. Gross, S. Tadigadapa, T. N. Jackson, F. T. Djuth, and S. Trolier-McKinstry, "Lead zirconate titanate films for d33 mode cantilever actuators," *Sensors Actuators, A Phys.*, vol. 105, pp. 91–97, 2003.

[185] R. B. Comizzoli, "Uses of Corona Discharges in the Semiconductor Industry," *J. Electrochem. Soc.*, vol. 134, pp. 424–429, 1987.

[186] K. D. Singer *et al.*, "Electro-optic phase modulation and optical second-harmonic generation in corona-poled polymer films," *Appl. Phys. Lett.*, vol. 53, pp. 1800–1802, 1988.

[187] T. Yamaguchi, A. Kojima, and I. Shibata, "Opto-ferroelectric Memories using Vinylidene Fluoride and Trifluoroethylene Copolymers," *IEEE Trans. Electr. Insul.*, vol. 24, pp. 537–540, 1989.

[188] Ş. Yilmaz, S. Bauer, and R. Gerhard-Multhaupt, "Photothermal poling of nonlinear optical polymer films," *Appl. Phys. Lett.*, vol. 64, pp. 2770–2772, 1994.

[189] B. Gross, R. Gerhard-Multhaupt, A. Berraissoul, and G. M. Sessler, "Electron-beam poling of piezoelectric polymer electrets," *J. Appl. Phys.*, vol. 62, pp. 1429–1432, 1987.

[190] S. Bauer, "Poled polymers for sensors and photonic applications," *J. Appl. Phys.*, vol. 80, pp. 5531–5558, 1996.

[191] K. Black, J. Singh, D. Mehta, S. Sung, C. J. Sutcliffe, and P. R. Chalker, "Silver Ink Formulations for Sinter-free Printing of Conductive Films," *Sci. Rep.*, vol. 6, no. 1, pp. 1–7, Feb. 2016, doi: 10.1038/srep20814.

[192] M. Choi *et al.*, "Mechanical and electrical characterization of PVDF-ZnO hybrid structure for application to nanogenerator," *Nano Energy*, vol. 33, pp. 462–468, 2017.

[193] S. Emamian *et al.*, "Fully printed and flexible piezoelectric based touch sensitive skin," *2015 IEEE SENSORS - Proc.*, 2015.

[194] S. Emamian, B. B. Narakathu, A. A. Chlaihawi, B. J. Bazuin, and M. Z. Atashbar, "Screen printing of flexible piezoelectric based device on polyethylene terephthalate

(PET) and paper for touch and force sensing applications," *Sensors Actuators, A Phys.*, vol. 263, pp. 639–647, 2017.

[195] A. A. Chlaihawi, S. Emamian, B. B. Narakathu, B. J. Bazuin, and M. Z. Atashbar, "Novel screen printed and flexible low frequency magneto-electric energy harvester," *Proc. IEEE Sensors*, pp. 13–15, 2016.

[196] J. S. Dodds, F. N. Meyers, and K. J. Loh, "Piezoelectric Characterization of PVDF-TrFE Thin Films Enhanced With ZnO Nanoparticles," *IEEE Sens. J.*, no. June, pp. 1889–1890, 2012.

[197] A. C. Lima *et al.*, "All-printed multilayer materials with improved magnetoelectric response," *J. Mater. Chem. C*, vol. 7, pp. 5394–5400, 2019.

[198] K. K. Chow, S. L. Kok, and K. T. Lau, "Study of screen printed polymer and ceramic based electrode on P(VDF-TrFE) flexible film," *J. Telecommun. Electron. Comput. Eng.*, vol. 10, pp. 93–96, 2018.

[199] M. Zirkl *et al.*, "An all-printed ferroelectric active matrix sensor network based on only five functional materials forming a touchless control interface," *Adv. Mater.*, vol. 23, pp. 2069–2074, 2011.

[200] O. Pabst *et al.*, "Inkjet printed micropump actuator based on piezoelectric polymers: Device performance and morphology studies," *Org. Electron. physics, Mater. Appl.*, vol. 15, pp. 3306–3315, 2014, [Online]. Available: http://dx.doi.org/10.1016/j.orgel.2014.09.007.

[201] O. Pabst, J. Perelaer, E. Beckert, U. S. Schubert, R. Eberhardt, and A. Tünnermann, "All inkjet-printed piezoelectric polymer actuators: Characterization and applications for micropumps in lab-on-a-chip systems," *Org. Electron. physics, Mater. Appl.*, vol. 14, pp. 3423–3429, 2013.

[202] J. Lim *et al.*, "All-inkjet-printed flexible piezoelectric generator made of solvent evaporation assisted BaTiO 3 hybrid material," *Nano Energy*, vol. 41, pp. 337–343, 2017.

[203] Y. Ba, J. Bao, R. Song, C. Zhu, and X. Zhang, "Printing Paper-Like Piezoelectric Energy Harvesters Based on Natural Cellulose Nanofibrils," *2019 20th Int. Conf. Solid-State Sensors, Actuators Microsystems Eurosensors XXXIII (TRANSDUCERS EUROSENSORS XXXIII)*, vol. 1, pp. 1451–1454, 2019.

[204] G. Murillo, I. Rodríguez-Ruiz, and J. Esteve, "Selective Area Growth of High-Quality ZnO Nanosheets Assisted by Patternable AlN Seed Layer for Wafer-Level Integration," *Cryst. Growth Des.*, vol. 16, no. 9, pp. 5059–5066, 2016.

[205] G. Murillo, H. Lozano, J. Cases-Utrera, M. Lee, and J. Esteve, "Improving Morphological Quality and Uniformity of Hydrothermally Grown ZnO Nanowires by Surface Activation of Catalyst Layer," *Nanoscale Res. Lett.*, vol. 12, no. 1, pp. 4–11, 2017, [Online]. Available: http://dx.doi.org/10.1186/s11671-017-1838-x.

[206] Z. L. Wang, "ZnO nanowire and nanobelt platform for nanotechnology," *Mater. Sci. Eng. R Reports*, vol. 64, no. 3–4, pp. 33–71, 2009.

[207] H. S. Kim *et al.*, "Dominant Role of Young ' s Modulus for Electric Power Generation in PVDF – BaTiO 3 Composite-Based Piezoelectric Nanogenerator," *Nanomaterials*, vol. 8, no. 10, p. 777, 2018.

[208] S. Gonçalves *et al.*, "Environmentally Friendly Printable Piezoelectric Inks and Their Application in the Development of All-Printed Touch Screens," *ACS Appl. Electron. Mater.*, vol. 1, no. 8, pp. 1678–1687, 2019.

[209] H. F. Castro, V. Correia, N. Pereira, P. Costab, J. Oliveiraa, and S. Lanceros-Méndez, "Printed Wheatstone bridge with embedded polymer based piezoresistive sensors for strain sensing applications," *Addit. Manuf.*, vol. 20, no. March 2017, pp. 119–125, 2018, [Online]. Available: https://doi.org/10.1016/j.addma.2018.01.004.

[210] H. K. Kim *et al.*, "Transparent and flexible tactile sensor for multi touch screen application with force sensing," *TRANSDUCERS 2009 - 15th Int. Conf. Solid-State Sensors, Actuators Microsystems*, pp. 1146–1149, 2009.

[211] V. Correia *et al.*, "All-Printed Piezoresistive Sensor Matrix with Organic Thin-Film Transistors as a Switch for Crosstalk Reduction," *ACS Appl. Electron. Mater.*, vol. 2, no. 5, pp. 1470–1477, 2020.

[212] S. Xu, Y. W. Yeh, G. Poirier, M. C. McAlpine, R. A. Register, and N. Yao, "Flexible piezoelectric PMN-PT nanowire-based nanocomposite and device," *Nano Lett.*, vol. 13, pp. 2393–2398, 2013.

[213] N. Godard, S. Glinšek, A. Matavž, V. Bobnar, and E. Defay, "Direct Patterning of Piezoelectric Thin Films by Inkjet Printing," *Adv. Mater. Technol.*, vol. 4, no. 2, pp. 1–8, 2019, doi: 10.1002/admt.201800168.

[214] R. Maas, M. Koch, N. R. Harris, N. M. White, and A. G. R. Evans, "Thick-film printing of PZT onto silicon," *Mater. Lett.*, vol. 31, no. 1–2, pp. 109–112, 1997.

[215] J. Li, X. Yan, B. Zhu, J. Xu, J. Ou-Yang, and X. Yang, "Synthesis of cylindrically-concaved PMN–PT thick films by pad printing process," *J. Alloys Compd.*, vol. 695, pp. 859–862, 2017.

[216] R. Gregorio and E. M. Ueno, "Effect of crystalline phase, orientation and temperature on the dielectric properties of poly (vinylidene fluoride) (PVDF)," *J. Mater. Sci.*, vol. 34, no. 18, pp. 4489–4500, 1999.

[217] L. Bießmann, L. P. Kreuzer, T. Widmann, N. Hohn, J. F. Moulin, and P. Müller-Buschbaum, "Monitoring the Swelling Behavior of PEDOT:PSS Electrodes under High Humidity Conditions," *ACS Appl. Mater. Interfaces*, vol. 10, no. 11, pp. 9865–9872, 2018, doi: 10.1021/acsami.8b00446.

[218] T. Furukawa and N. Seo, "Electrostriction as the Origin of Piezoelectricity in Ferroelectric Polymers," *Jpn. J. Appl. Phys.*, vol. 26, p. 675, 1990.

[219] I. Yousef *et al.*, "MIRAS: The Infrared Synchrotron Radiation Beamline at ALBA," *Synchrotron Radiat. News*, vol. 30, no. 4, pp. 4–6, 2017, doi: 10.1080/08940886.2017.1338410.

[220] J. West, J. W. Sears, S. Smith, and M. Carter, "Photonic sintering – an example: photonic curing of silver nanoparticles," *Sinter. Adv. Mater.*, vol. 1, pp. 275–288, Jan. 2010, doi: 10.1533/9781845699949.2.275.

[221] K. Lau, Y. Liu, H. Chen, and R. L. Withers, "Effect of annealing temperature on the morphology and piezoresponse characterisation of poly(vinylidene fluoride-trifluoroethylene) films via Scanning Probe Microscopy," *Adv. Condens. Matter Phys.*, vol. 2013, pp. 1–5, 2013.

[222] K. J. Kim, N. M. Reynolds, and S. L. Hsu, "Spectroscopic Analysis of the Crystalline and Amorphous Phases in a Vinylidene Fluoride/Trifluoroethylene Copolymer," *Macromolecules*, vol. 22, no. 12, pp. 4395–4401, 1989.

[223] A. J. Lovinger, "Ferroelectric Polymers," *Science (80-.).*, vol. 220, no. 4602, pp. 1115–1121, 1983, [Online]. Available: http://www.sciencemag.org/content/220/4602/1115.short.

[224] N. R. Alluri, B. Saravanakumar, and S. Kim, "Nanogenerator as a Self-Powered Fluid Velocity Sensor," *ACS Appl. Mater. Interfaces*, vol. 7, pp. 9831–9840, 2015.

[225] A. Gessow, "Fundamental Understanding of Piezoelectric Strain Sensors," *J. Intell. Mater. Syst. Struct.*, vol. 11, pp. 246–257, 2001.

[226] A. M. Zamarayeva *et al.*, "Optimization of printed sensors to monitor sodium, ammonium, and lactate in sweat," *APL Mater.*, vol. 8, no. 10, 2020, doi: 10.1063/5.0014836.

[227] Y. Yamamoto *et al.*, "Printed multifunctional flexible device with an integrated motion sensor for health care monitoring," *Sci. Adv.*, vol. 2, no. 11, 2016, doi: 10.1126/sciadv.1601473.

[228] C. Gerlach *et al.*, "Printed MWCNT-PDMS-Composite Pressure Sensor System for Plantar Pressure Monitoring in Ulcer Prevention," *IEEE Sens. J.*, vol. 15, no. 7, pp. 3647–3656, 2015, doi: 10.1109/JSEN.2015.2392084.

[229] R. Cao *et al.*, "Screen-Printed Washable Electronic Textiles as Self-Powered Touch/Gesture Tribo-Sensors for Intelligent Human-Machine Interaction," *ACS Nano*, vol. 12, no. 6, pp. 5190–5196, 2018, doi: 10.1021/acsnano.8b02477.

[230] Z. Zhou *et al.*, "Supersensitive all-fabric pressure sensors using printed textile electrode arrays for human motion monitoring and human-machine interaction," *J. Mater. Chem. C*, vol. 6, no. 48, pp. 13120–13127, 2018, doi: 10.1039/c8tc02716a.

[231] T. Sekine *et al.*, "Microporous Induced Fully Printed Pressure Sensor for Wearable Soft Robotics Machine Interfaces," *Adv. Intell. Syst.*, vol. 2, no. 12, p. 2000179, 2020, doi: 10.1002/aisy.202000179.

[232] Y. Li *et al.*, "Flexible TPU strain sensors with tunable sensitivity and stretchability by coupling AgNWs with rGO," *J. Mater. Chem. C*, vol. 8, no. 12, pp. 4040–4048, 2020, doi: 10.1039/d0tc00029a.

[233] R. Sun *et al.*, "Stretchable Piezoelectric Sensing Systems for Self-Powered and Wireless Health Monitoring," *Adv. Mater. Technol.*, vol. 4, no. 1900100, 2019, doi: DOI: 10.1002/admt.201900100.

[234] T. Ha *et al.*, "A Chest-Laminated Ultrathin and Stretchable E-Tattoo for the Measurement of Electrocardiogram, Seism," *Adv. Sci.*, vol. 6, 2019.

[235] N. I. Kim *et al.*, "Highly-Sensitive Skin-Attachable Eye-Movement Sensor Using Flexible Nonhazardous Piezoelectric Thin Film," *Adv. Funct. Mater.*, vol. 31, no. 8, pp. 1–11, 2021, doi: 10.1002/adfm.202008242.

[236] X. Wang, B. Yang, J. Liu, and C. Yang, "A transparent and biocompatible single-friction-surface triboelectric and piezoelectric generator and body movement sensor," *J. Mater. Chem. A*, vol. 5, no. 3, pp. 1176–1183, 2017, doi: 10.1039/C6TA09501A.

[237] Y. Y. Chiu, W. Y. Lin, H. Y. Wang, S. Bin Huang, and M. H. Wu, "Development of a piezoelectric polyvinylidene fluoride (PVDF) polymer-based sensor patch for simultaneous heartbeat and respiration monitoring," *Sensors Actuators, A Phys.*, vol. 189, pp. 328–334, 2013, doi: 10.1016/j.sna.2012.10.021.

[238] H. Khan, A. Razmjou, M. E. Warkiani, A. Kottapalli, and M. Asadnia, "Sensitive and flexible polymeric strain sensor for accurate human motion monitoring," *Sensors (Switzerland)*, vol. 18, no. 2, pp. 1–10, 2018, doi: 10.3390/s18020418.

[239] C. Sun *et al.*, "Design and fabrication of flexible strain sensor based on ZnO-decorated PVDF via atomic layer deposition," *Appl. Surf. Sci.*, vol. 562, no. March, p. 150126,

2021, doi: 10.1016/j.apsusc.2021.150126.

[240] G.-F. Yu *et al.*, "Patterned, highly stretchable and conductive nanofibrous PANI/PVDF strain sensors based on electrospinning and in situ polymerization," *Nanoscale*, vol. 00, pp. 1–7, 2016, doi: 10.1039/x0xx00000x.

[241] X. Chen, X. Han, and Q. D. Shen, "PVDF-Based Ferroelectric Polymers in Modern Flexible Electronics," *Adv. Electron. Mater.*, vol. 3, no. 5, 2017, doi: 10.1002/aelm.201600460.

[242] R. Guo, H. Zhang, S. Cao, X. Cui, Z. Yan, and S. Sang, "A self-powered stretchable sensor fabricated by serpentine PVDF film for multiple dynamic monitoring," *Mater. Des.*, vol. 182, p. 108025, 2019, doi: 10.1016/j.matdes.2019.108025.

[243] S. B. Kang, W. J. Park, M. H. Jeong, S. H. Kang, C. Yang, and K. J. Choi, "Ambipolar Passivated Back Surface Field Layer for Silicon Photovoltaics," *Adv. Funct. Mater.*, vol. 30, no. 50, pp. 1–11, 2020, doi: 10.1002/adfm.202004943.

[244] K. L. Kim *et al.*, "Epitaxial Growth of Thin Ferroelectric Polymer Films on Graphene Layer for Fully Transparent and Flexible Nonvolatile Memory," *Nano Lett.*, vol. 16, no. 1, pp. 334–340, 2016, doi: 10.1021/acs.nanolett.5b03882.

[245] Y. J. Park *et al.*, "Irreversible extinction of ferroelectric polarization in P(VDF-TrFE) thin films upon melting and recrystallization," *Appl. Phys. Lett.*, vol. 88, no. 24, pp. 6–9, 2006, doi: 10.1063/1.2207831.

[246] Y. J. Park, S. J. Kang, B. Lotz, M. Brinkmann, and C. Park, "High throughput epitaxy of ferroelectric PVDF-TrFE thin films on molecularly ordered PTEF surface for non-volatile polymer memory," *Proc. - Int. Symp. Electrets*, pp. 8648–8654, 2008, doi: 10.1109/ISE.2008.4814003.

[247] M. Amjadi, K. U. Kyung, I. Park, and M. Sitti, "Stretchable, Skin-Mountable, and Wearable Strain Sensors and Their Potential Applications: A Review," *Adv. Funct. Mater.*, vol. 26, no. 11, pp. 1678–1698, 2016, doi: 10.1002/adfm.201504755.

[248] S. Yao and Y. Zhu, "Wearable multifunctional sensors using printed stretchable conductors made of silver nanowires," *Nanoscale*, vol. 6, no. 4, pp. 2345–2352, 2014, doi: 10.1039/c3nr05496a.

[249] F. Xu and Y. Zhu, "Highly conductive and stretchable silver nanowire conductors," *Adv. Mater.*, vol. 24, no. 37, pp. 5117–5122, 2012, doi: 10.1002/adma.201201886.

[250] M. Amjadi, A. Pichitpajongkit, S. Lee, S. Ryu, and I. Park, "Highly stretchable and sensitive strain sensor based on silver nanowire-elastomer nanocomposite," *ACS Nano*, vol. 8, no. 5, pp. 5154–5163, 2014, doi: 10.1021/nn501204t.

[251] T. Yamada *et al.*, "A stretchable carbon nanotube strain sensor for human-motion detection," *Nat. Nanotechnol.*, vol. 6, no. 5, pp. 296–301, 2011, doi: 10.1038/nnano.2011.36.

[252] A. C. Power and A. Morrin, *Electroanalytical Sensor Technology*. 2013.

[253] M. Cremer, "Über die Ursache der elektromotorischen Eigenschaften der Gewebe, zugleich ein Beitrag zur Lehre von den polyphasischen Elektrolytketten," *Z. Biol.*, vol. 47, pp. 562–608, 1906.

[254] F. Haber and Z. Klemensiewicz, "Über elektrische Phasengrenzkräfte," vol. 67, pp. 385–431, 1909.

[255] S. Alegret, M. del Valle, and A. Merkoçi, "Sensores electroquímicos: introducción a los quimiosenspres y biosensores: curso teórico-práctico," *Univ. Autònoma Barcelona*,

2004.

[256] J. W. Ross, "Calcium-Selective Electrode with Liquid Ion Exchanger," *Science (80-.).*, vol. 156, no. 3780, pp. 1378–1379, 1967, doi: doi:10.1126/science.156.3780.1378.

[257] L. A. R. Pioda, V. Stankova, and W. Simon, "Highly Selective Potassium Ion Responsive Liquid-Membrane Electrode," *Anal. Lett.*, vol. 2, no. 12, pp. 665–674, 1969, doi: 10.1080/00032716908051343.

[258] R. Bloch, A. Shatkay, and H. A. Saroff, "Fabrication and Evaluation of Membranes as Specific Electrodes for Calcium ions," *Biophys. J.*, vol. 7, no. 6, pp. 865–877, 1967, doi: 10.1016/S0006-3495(67)86626-8.

[259] B. R. Eggind, "Chemical sensors and Biosensors," *West Sussex*, 2002.

[260] L. C. Clark, "Monitor and control of blood and tissue oxygen tensions," 1956.

[261] J. . MacDonald, *Imprdance spectroscopy*. 1991.

[262] H. S. Magar, R. Y. A. Hassan, and A. Mulchandani, "Electrochemical impedance spectroscopy (EIS): Principles, construction, and biosensing applications," *Sensors*, vol. 21, no. 19, 2021, doi: 10.3390/s21196578.

[263] Radiometer analytical, "Conductivity-Theory and Practice," *Anal. Radiom.*, vol. D61M002, pp. 1–50, 2004, [Online]. Available: http://scholar.google.com/scholar?hl=en&btnG=Search&q=intitle:Conductivity+Theory +and+Practice#4%5Cnhttp://scholar.google.com/scholar?hl=en&btnG=Search&q=intitle :Conductivity-theory+and+practice#0.

[264] H. Suzuki, A. Hiratsuka, S. Sasaki, and I. Karube, "Problems associated with the thin-film Ag/AgCl reference electrode and a novel structure with improved durability," *Sensors Actuators, B Chem.*, vol. 46, no. 2–3, pp. 104–113, 1998, doi: 10.1016/S0925-4005(98)00043-4.

[265] T. Guinovart, G. A. Crespo, F. X. Rius, and F. J. Andrade, "A reference electrode based on polyvinyl butyral (PVB) polymer for decentralized chemical measurements," *Anal. Chim. Acta*, vol. 821, pp. 72–80, 2014, doi: 10.1016/j.aca.2014.02.028.

[266] U. Guth, F. Gerlach, M. Decker, W. Oelßner, and W. Vonau, "Solid-state reference electrodes for potentiometric sensors," *J. Solid State Electrochem.*, vol. 13, no. 1, pp. 27–39, 2009, doi: 10.1007/s10008-008-0574-7.

[267] Y. J. Kim, Y. C. Lee, B. K. Sohn, J. H. Lee, and C. S. Kim, "A Novel pH Microsensor with a Built-in Reference Electrode," *J. Korean Phys. Soc.*, vol. 43, no. 5 I, pp. 769–772, 2003, doi: 10.3938/jkps.43.769.

[268] M. Jović *et al.*, "Large-scale layer-by-layer inkjet printing of flexible iridium-oxide based pH sensors," *J. Electroanal. Chem.*, vol. 819, no. 0, pp. 384–390, 2018, doi: 10.1016/j.jelechem.2017.11.032.

[269] D. S. Silvester and L. Aldous, "Chapter 10:electrochemical detection using ionic liquids.," in *Electrochemical Strategies in Detection Science*, 2015, pp. 341–386.

[270] G. Jobst *et al.*, "Thin-film Clark-type oxygen sensor based on novel polymer membrane systems for in vivo and biosensor applications," *Biosens. Bioelectron.*, vol. 8, no. 3–4, pp. 123–128, 1993, doi: 10.1016/0956-5663(93)85024-I.

[271] M. Nádherná, F. Opekar, J. Reiter, and K. Štulík, "A planar, solid-state amperometric sensor for nitrogen dioxide, employing an ionic liquid electrolyte contained in a polymeric matrix," *Sensors Actuators, B Chem.*, vol. 161, no. 1, pp. 811–817, 2012, doi: 10.1016/j.snb.2011.11.037.

[272] J. T. Stock, "Amperometric, Bipotentiometric, and Coulometric Titrations.," *Anal. Chem.*, vol. 50, no. 5, 1978, doi: 10.1021/ac50028a001.

[273] A. Badalyan, J. Buff, M. Holmes, C. W. K. Chow, and D. Vitanage, "On-line free-chlorine/total-chlorine monitors' evaluation - A step towards a correct choice of residual disinfectant monitor," *J. Water Supply Res. Technol. - AQUA*, vol. 58, no. 3, pp. 181–190, 2009, doi: 10.2166/aqua.2009.037.

[274] D. G. Wahman, M. T. Alexander, and A. G. Dugan, "Chlorinated cyanurates in drinking water: Measurement bias, stability, and disinfectant byproduct formation," *AWWA Water Sci.*, vol. 1, no. 2, pp. 1–19, 2019, doi: 10.1002/aws2.1133.

[275] J. N. Jensen and D. J. Johnson, "Specificity of the DPD and amperometric titration methods for free available chlorine. A review," *J. / Am. Water Work. Assoc.*, vol. 81, no. 12, pp. 59–64, 1989, doi: 10.1002/j.1551-8833.1989.tb06894.x.

[276] R. B. Baird, A. D. Eaton, and E. W. Rice, *Standard Methods for the Examination of Water and Wastewater*. 2017.

[277] A. J. Bandodkar, R. Nuñez-Flores, W. Jia, and J. Wang, "All-printed stretchable electrochemical devices," *Adv. Mater.*, vol. 27, no. 19, pp. 3060–3065, 2015, doi: 10.1002/adma.201500768.

[278] R. Zhong *et al.*, "Self-Assembly of Enzyme-Like Nanofibrous G-Molecular Hydrogel for Printed Flexible Electrochemical Sensors," *Adv. Mater.*, vol. 30, no. 12, pp. 1–8, 2018, doi: 10.1002/adma.201706887.

[279] T. Wu, A. Alharbi, R. Kiani, and D. Shahrjerdi, "Quantitative Principles for Precise Engineering of Sensitivity in Graphene Electrochemical Sensors," *Adv. Mater.*, vol. 31, no. 6, pp. 1–35, 2019, doi: 10.1002/adma.201805752.

[280] M. Zea, R. Texidó, R. Villa, S. Borrós, and G. Gabriel, "Specially Designed Polyaniline/Polypyrrole Ink for a Fully Printed Highly Sensitive pH Microsensor," *ACS Appl. Mater. Interfaces*, vol. 13, no. 28, pp. 33524–33535, 2021, doi: 10.1021/acsami.1c08043.

[281] N. Zine *et al.*, "All-solid-state hydrogen sensing microelectrodes based on novel PPy[3,3′-Co(1,2-C2B9H11)2] as a solid internal contact," *Mater. Sci. Eng. C*, vol. 26, no. 2–3, pp. 399–404, 2006, doi: 10.1016/j.msec.2005.10.073.

[282] A. Moya *et al.*, "Flexible microfluidic bio-lab-on-a-chip multi-sensor platform for electrochemical measurements," *Proc. IEEE Sensors*, vol. 2014-Decem, no. December, pp. 1018–1021, 2014, doi: 10.1109/ICSENS.2014.6985176.

[283] P. Marsh *et al.*, "Flexible Iridium Oxide Based pH Sensor Integrated with Inductively Coupled Wireless Transmission System for Wearable Applications," *IEEE Sens. J.*, vol. 20, no. 10, pp. 5130–5138, 2020, doi: 10.1109/JSEN.2020.2970926.

[284] M. Zea, A. Moya, M. Fritsch, E. Ramon, R. Villa, and G. Gabriel, "Enhanced Performance Stability of Iridium Oxide-Based pH Sensors Fabricated on Rough Inkjet-Printed Platinum," *ACS Appl. Mater. Interfaces*, vol. 11, no. 16, pp. 15160–15169, 2019, doi: 10.1021/acsami.9b03085.

[285] Y. H. Liao and J. C. Chou, "Preparation and characteristics of ruthenium dioxide for pH array sensors with real-time measurement system," *Sensors Actuators, B Chem.*, vol. 128, no. 2, pp. 603–612, 2008, doi: 10.1016/j.snb.2007.07.023.

[286] C. Colombo, T. Kappes, and P. C. Hauser, "Coulometric micro-titrator with a ruthenium dioxide pH-electrode," *Anal. Chim. Acta*, vol. 412, no. 1–2, pp. 69–75, 2000, doi: 10.1016/S0003-2670(00)00765-0.

[287] D. H. Cho, K. C. Chung, S. S. Jeong, and M. Y. Park, "Potentiometric behavior of N,N,N',N'-tetrabenzylmethylenediamine-based hydrogen ion-selective electrodes," *Talanta*, vol. 51, no. 4, pp. 761–767, 2000, doi: 10.1016/S0039-9140(99)00350-1.

[288] E. Lindner *et al.*, "Electroanalytical and biocompatibility studies on microfabricated array sensors," *Electroanalysis*, vol. 7, no. 9, pp. 864–870, 1995, doi: 10.1002/elan.1140070913.

[289] V. V. Cosofret, M. Erdosy, T. A. Johnson, R. P. Buck, R. B. Ash, and M. R. Neuman, "Microfabricated Sensor Arrays Sensitive to pH and K+ for Ionic Distribution Measurements in the Beating Heart," *Anal. Chem.*, vol. 67, no. 10, pp. 1647–1653, 1995.

[290] B. H. van der Schoot and P. Bergveld, "ISFET based enzyme sensors," *Biosensors*, vol. 3, no. 3, pp. 161–186, 1987, doi: 10.1016/0265-928X(87)80025-1.

[291] A. Fog and R. P. Buck, "Electronic semiconducting oxides as pH sensors," *Sensors and Actuators*, vol. 5, no. 2, pp. 137–146, 1984, doi: 10.1016/0250-6874(84)80004-9.

[292] J. A. Mihell and J. K. Atkinson, "Planar thick-film pH electrodes based on ruthenium dioxide hydrate," *Sensors Actuators, B Chem.*, vol. 48, no. 1–3, pp. 505–511, 1998, doi: 10.1016/S0925-4005(98)00090-2.

[293] S. Yao, M. Wang, and M. Madou, "A pH Electrode Based on Melt-Oxidized Iridium Oxide," *J. Electrochem. Soc.*, vol. 148, no. 4, p. H29, 2001, doi: 10.1149/1.1353582.

[294] C. N. Tsai, J. C. Chou, T. P. Sun, and S. K. Hsiung, "Study on the sensing characteristics and hysteresis effect of the tin oxide pH electrode," *Sensors Actuators, B Chem.*, vol. 108, no. 1-2 SPEC. ISS., pp. 877–882, 2005, doi: 10.1016/j.snb.2004.11.050.

[295] S. A. M. Marzouk, S. Ufer, R. P. Buck, T. A. Johnson, L. A. Dunlap, and W. E. Cascio, "Electrodeposited iridium oxide pH electrode for measurement of extracellular myocardial acidosis during acute ischemia," *Anal. Chem.*, vol. 70, no. 23, pp. 5054–5061, 1998, doi: 10.1021/ac980608e.

[296] T. Katsube, I. Lauks, and J. N. Zemel, "pH-sensitive sputtered iridium oxide films," *Sensors and Actuators*, vol. 2, no. C, pp. 399–410, 1981, doi: 10.1016/0250-6874(81)80060-1.

[297] J. V. Dobson, P. R. Snodin, and H. R. Thirsk, "EMF measurements of cells employing metal-metal oxide electrodes in aqueous chloride and sulphate electrolytes at temperatures between 25-250°C," *Electrochim. Acta*, vol. 21, no. 7, pp. 527–533, 1976, doi: 10.1016/0013-4686(76)85143-2.

[298] K. Izutsu and H. Yamamoto, "Response of an Iridium Oxide pH-sensor in Nonaqueous Solutions. Comparison with Other Oxide," *Anal. Sci.*, vol. 12, no. December, pp. 905–909, 1996.

[299] H. Cao *et al.*, "An implantable, batteryless, and wireless capsule with integrated impedance and pH sensors for gastroesophageal reflux monitoring," *IEEE Trans. Biomed. Eng.*, vol. 59, no. 12 PART2, pp. 3131–3139, 2012, doi: 10.1109/TBME.2012.2214773.

[300] C. Ratanapromcharoen *et al.*, "pH Mapping on Tooth Surfaces for Quantitative Caries Diagnosis Using Micro Ir/IrOx pH Sensor," *Anal. Chem.*, vol. 90, no. 7, pp. 4925–4931, 2018, doi: 10.1021/acs.analchem.8b00867.

[301] J. Wang, M. Yokokawa, T. Satake, and H. Suzuki, "A micro IrOx potentiometric sensor for direct determination of organophosphate pesticides," *Sensors Actuators, B Chem.*, vol. 220, pp. 859–863, 2015, doi: 10.1016/j.snb.2015.05.115.

[302] W.-D. Huang, J. Wang, T. Ativanichayaphong, M. Chiao, and J. C. Chiao, "Development of an IrO x micro pH sensor array on flexible polymer substrate," *Nanosensors Microsens. Bio-Systems 2008*, vol. 6931, p. 693104, 2008, doi: 10.1117/12.775856.

[303] I. A. Ges, B. L. Ivanov, D. K. Schaffer, E. A. Lima, A. A. Werdich, and F. J. Baudenbacher, "Thin-film IrOx pH microelectrode for microfluidic-based microsystems," *Biosens. Bioelectron.*, vol. 21, no. 2, pp. 248–256, 2005, doi: 10.1016/j.bios.2004.09.021.

[304] S. Carroll and R. P. Baldwin, "Self-calibrating microfabricated iridium oxide pH electrode array for remote monitoring," *Anal. Chem.*, vol. 82, no. 3, pp. 878–885, 2010, doi: 10.1021/ac9020374.

[305] S. R. Mellsop, A. Gardiner, and A. T. Marshall, "Spontaneous Deposition of Iridium onto Nickel Substrates for the Oxygen Evolution Reaction," *Electrocatalysis*, vol. 7, no. 3, pp. 226–234, 2016, doi: 10.1007/s12678-016-0299-9.

[306] M. Yagi, E. Tomita, and T. Kuwabara, "Remarkably high activity of electrodeposited IrO2 film for electrocatalytic water oxidation," *J. Electroanal. Chem.*, vol. 579, no. 1, pp. 83–88, 2005, doi: 10.1016/j.jelechem.2005.01.030.

[307] Y. Zhao, E. A. Hernandez-Pagan, N. M. Vargas-Barbosa, J. L. Dysart, and T. E. Mallouk, "A high yield synthesis of ligand-free iridium oxide nanoparticles with high electrocatalytic activity," *J. Phys. Chem. Lett.*, vol. 2, no. 5, pp. 402–406, 2011, doi: 10.1021/jz200051c.

[308] W. Banerjee *et al.*, "Formation polarity dependent improved resistive switching memory characteristics using nanoscale (1.3 nm) core-shell IrOx nanodots," *Nanoscale Res. Lett.*, vol. 7, no. 1, p. 194, 2012, doi: 10.1186/1556-276X-7-194.

[309] A. Touni, A. Papaderakis, D. Karfaridis, G. Vourlias, and S. Sotiropoulos, "Oxygen evolution reaction at IrO2/Ir(Ni) film electrodes prepared by galvanic replacement and anodization: Effect of precursor Ni film thickness," *Molecules*, vol. 24, no. 11, pp. 1–16, 2019, doi: 10.3390/molecules24112095.

[310] Y. Lu, T. Wang, Z. Cai, Y. Cao, H. Yang, and Y. Y. Duan, "Anodically electrodeposited iridium oxide films microelectrodes for neural microstimulation and recording," *Sensors Actuators, B Chem.*, vol. 137, no. 1, pp. 334–339, 2009, doi: 10.1016/j.snb.2008.11.036.

[311] T. Y. Kim and S. Yang, "Fabrication method and characterization of electrodeposited and heat-treated iridium oxide films for pH sensing," *Sensors Actuators, B Chem.*, vol. 196, pp. 31–38, 2014, doi: 10.1016/j.snb.2014.02.004.

[312] S. Kakooei, M. C. Ismail, and B. Ari-wahjoedi, "An overview of pH Sensors Based on Iridium Oxide : Fabrication and Application," *Int. J. Mater. Sci. Innov.*, vol. 1, no. 1, pp. 62–72, 2013.

[313] W. D. Huang, H. Cao, S. Deb, M. Chiao, and J. C. Chiao, "A flexible pH sensor based on the iridium oxide sensing film," *Sensors Actuators, A Phys.*, vol. 169, no. 1, pp. 1–11, 2011, doi: 10.1016/j.sna.2011.05.016.

[314] E. Jan *et al.*, "Layered carbon nanotube-polyelectrolyte electrodes outperform traditional neural interface materials," *Nano Lett.*, vol. 9, no. 12, pp. 4012–4018, 2009, doi: 10.1021/nl902187z.

[315] F. Huang, Y. Jin, L. Wen, D. Mu, and M. Cui, " Effects of Thermal Oxidation Cycle Numbers and Hydration on IrO x pH Sensor ," *J. Electrochem. Soc.*, vol. 160, no. 10, pp. B184–B191, 2013, doi: 10.1149/2.006310jes.

[316] K. Yamanaka, "Anodically electrodeposited Iridium Oxide Films," *Japanese Journal of Applied Physics*, vol. 28, no. 4. pp. 632–637, 1989.

[317] A. Kumar, H. Kim, and G. P. Hancke, "Environmental Monitoring Systems: A Review," *IEEE*, vol. 7, no. 1, pp. 37–72, 2015, [Online]. Available: https://www.researchgate.net/publication/269107473_What_is_governance/link/548173 090cf22525dcb61443/download%0Ahttp://www.econ.upf.edu/~reynal/Civil wars_12December2010.pdf%0Ahttps://think-asia.org/handle/11540/8282%0Ahttps://www.jstor.org/stable/41857625.

[318] C. K. Ho, A. Robinson, D. R. Miller, and M. J. Davis, "Overview of sensors and needs for environmental monitoring," *Sensors*, vol. 5, no. 1–2, pp. 4–37, 2005, doi: 10.3390/s5010004.

[319] G. Hanrahan, D. G. Patil, and J. Wang, "Electrochemical sensors for environmental monitoring: Design, development and applications," *J. Environ. Monit.*, vol. 6, no. 8, pp. 657–664, 2004, doi: 10.1039/b403975k.

[320] C. M. A. Brett, "Electrochemical sensors for environmental monitoring. Strategy and examples," *Pure Appl. Chem.*, vol. 73, no. 12, pp. 1969–1977, 2001, doi: 10.1351/pac200173121969.

[321] L. Marle and G. M. Greenway, "Microfluidic devices for environmental monitoring," *TrAC - Trends Anal. Chem.*, vol. 24, no. 9, pp. 795–802, 2005, doi: 10.1016/j.trac.2005.08.003.

[322] W. Duan, M. Gunes, A. Baldi, and M. Gich, "Compact fluidic electrochemical sensor platform for on-line monitoring of chemical oxygen demand in urban wastewater," *Chem. Eng. J.*, vol. 449, 2022, doi: 10.1016/j.cej.2022.137837.

[323] P. N. Nge, C. I. Rogers, and A. T. Woolley, "Advances in Microfluidic Materials, Functions, Integration, and Applications," *Chem. Rev.*, vol. 113, pp. 2550–2583, 2013.

[324] S. Hansen and A. A. El Wahed, "Point-of-care or point-of-need diagnostic tests: time to change outbreak investigation and pathogen detection," *Trop. Med. Infect. Dis.*, vol. 5, no. 4, 2020, doi: 10.3390/tropicalmed5040151.

[325] Y. Qin *et al.*, "Integrated water quality monitoring system with pH, free chlorine, and temperature sensors," *Sensors Actuators, B Chem.*, vol. 255, pp. 781–790, 2018, doi: 10.1016/j.snb.2017.07.188.

[326] Y. Qin, H. J. Kwon, M. M. R. Howlader, and M. J. Deen, "Microfabricated electrochemical pH and free chlorine sensors for water quality monitoring: Recent advances and research challenges," *RSC Adv.*, vol. 5, no. 85, pp. 69086–69109, 2015, doi: 10.1039/c5ra11291e.

[327] A. U. Alam, D. Clyne, W. Lush, and M. J. Deen, "A reusable, reagent-less free chlorine sensor using gold thin film electrode," *Analyst*, vol. 146, no. 8, pp. 2626–2631, 2021, doi: 10.1039/d1an00038a.

[328] M. Alique *et al.*, "Multiparametric sensing electronic skin based on seamless fully printed stretchable piezoelectric devices," *Artic. Prep.*, 2022.

[329] M. Alique, P. Lacharmoise, C. D. Simao, and A. Moya, "Large-scale fully printed iridium oxide-based pH sensor," *Artic. Prep.*, 2022.

List of Figures

247